

# **The wind driven property variability of the Denmark Strait Overflow**

Jacob Opher

A thesis presented for the degree of  
Doctor of Philosophy

University of East Anglia

School of Environmental Sciences

January 2021

© This copy of the thesis has been supplied on condition that anyone who consults it is understood to recognise that its copyright rests with the author and that use of any information derived therefrom must be in accordance with current UK Copyright Law. In addition, any quotation or extract must include full attribution.



## Abstract

The Denmark Strait Overflow (DSO) is the densest component of the Atlantic Meridional Overturning Circulation (AMOC) in the subpolar North Atlantic. This thesis demonstrates, for the first time, that the DSO exhibits a statistically significant seasonal salinity cycle. Sustained freshening of the DSO, which occurs in late winter and spring, is intensified upslope, in lighter classes of DSO ( $27.88 \text{ kg m}^{-3} < \sigma_{\theta} < 27.91 \text{ kg m}^{-3}$ ) and is weaker downslope, in denser classes ( $\sigma_{\theta} \approx 27.94 \text{ kg m}^{-3}$ ). The downstream evolution of fresh signals could shed light on the mixing between different water mass components of the AMOC. The freshening originates from advection of fresh water lenses, termed lids, present in the lighter classes of the DSO above the deep trough at Denmark Strait in spring, and hitherto not detected by moored observations. The freshening is linked to wintertime freshening and enhancement of the Shelfbreak East Greenland Current (EGC) 200 km to the north of Denmark Strait, driven in part by barrier winds, increasing the volume transport of fresh pycnocline water within the Shelfbreak EGC towards Denmark Strait, which forms the fresh lid. It is also shown that seasonality of Shelfbreak EGC volume transports in 2011-12 may explain around 50% of the DSO salinity seasonality. The DSO salinity is strongly controlled by northerly/northeasterly winds over the east Greenland shelfbreak around  $70^{\circ}\text{N}$ , with an advective timescale of 2-3 months. Both the North Atlantic Oscillation and the Iceland Lofoten Difference atmospheric patterns influence DSO salinity, with the former exerting a dominant influence between 2010 and 2014, and the latter more important between 2005 and 2009. Finally, it is argued that the reduction in sea ice concentration between 1998 and 2015 in the wind forcing region has reduced the effective wind stress there, thus weakening the DSO freshening events.

## **Access Condition and Agreement**

Each deposit in UEA Digital Repository is protected by copyright and other intellectual property rights, and duplication or sale of all or part of any of the Data Collections is not permitted, except that material may be duplicated by you for your research use or for educational purposes in electronic or print form. You must obtain permission from the copyright holder, usually the author, for any other use. Exceptions only apply where a deposit may be explicitly provided under a stated licence, such as a Creative Commons licence or Open Government licence.

Electronic or print copies may not be offered, whether for sale or otherwise to anyone, unless explicitly stated under a Creative Commons or Open Government license. Unauthorised reproduction, editing or reformatting for resale purposes is explicitly prohibited (except where approved by the copyright holder themselves) and UEA reserves the right to take immediate 'take down' action on behalf of the copyright and/or rights holder if this Access condition of the UEA Digital Repository is breached. Any material in this database has been supplied on the understanding that it is copyright material and that no quotation from the material may be published without proper acknowledgement.



# Table of contents

<b>List of tables</b>	<b>ix</b>
<b>List of figures</b>	<b>xi</b>
<b>1 Introduction</b>	<b>1</b>
1.1 Overview of North Atlantic Ocean circulation . . . . .	1
1.2 The AMOC . . . . .	2
1.2.1 Context . . . . .	2
1.2.2 Upper limb . . . . .	6
1.2.3 Lower limb . . . . .	9
1.2.4 Temporal variability . . . . .	10
1.2.5 Climate impacts . . . . .	13
1.3 Formation of North Atlantic Deep Water . . . . .	15
1.3.1 Densest source waters . . . . .	15
1.3.2 Nordic Seas Overflows . . . . .	22
1.3.3 Entrainment . . . . .	23
1.4 The Denmark Strait Overflow . . . . .	25
1.4.1 Sources and characteristics . . . . .	26
1.4.2 Temporal variability . . . . .	29
1.5 Research questions . . . . .	35
1.6 Thesis outline . . . . .	36
<b>2 Data and methods</b>	<b>37</b>
2.1 The Angmagssalik array . . . . .	39
2.1.1 Background . . . . .	39
2.1.2 MicroCAT conductivity and salinity calibration . . . . .	43
2.1.3 Salinity time series preparation . . . . .	49
2.2 Upstream moorings and CTD stations . . . . .	51
2.2.1 Spill Jet section . . . . .	52
2.2.2 Denmark Strait . . . . .	53

2.2.3	Faxaflói CTD station 9 . . . . .	55
2.2.4	Kögur . . . . .	56
2.3	ERA5 . . . . .	59
<b>3</b>	<b>Intra-annual and seasonal property variability of the DSO</b>	<b>65</b>
3.1	Introduction . . . . .	65
3.2	Temporal variability of DSO properties at ANG . . . . .	67
3.2.1	Multi-annual variability . . . . .	67
3.2.2	Intra-annual variability . . . . .	70
3.2.3	Effect of temperature and salinity on density . . . . .	73
3.3	Sustained intra-annual freshening events . . . . .	75
3.3.1	Temporal variability . . . . .	76
3.3.2	Cross-stream variability . . . . .	76
3.4	Intra-annual variability of DSO properties at the Denmark Strait sill . . . . .	81
3.4.1	Densest water . . . . .	82
3.4.2	Lighter overflow water . . . . .	85
3.5	Upstream origin of salinity variability at DS and ANG . . . . .	90
3.5.1	Advection from KGA to DS . . . . .	91
3.5.2	Advection from KGA to ANG . . . . .	93
3.6	Concluding remarks . . . . .	95
<b>4</b>	<b>The mechanisms driving seasonal freshening of the DSO</b>	<b>99</b>
4.1	Introduction . . . . .	99
4.2	Candidate mechanisms . . . . .	100
4.2.1	Introduction . . . . .	100
4.2.2	Hydrography of DSO source water at KGA . . . . .	101
4.2.3	Mechanism 1: offshore flow during Ekman downwelling . . . . .	106
4.2.4	Mechanism 2: Ekman pumping . . . . .	107
4.2.5	Mechanism 3: Shelfbreak EGC enhancement . . . . .	107
4.2.6	Mechanism 4: freshening of MIW . . . . .	108
4.3	Evidence for Mechanism 1 . . . . .	109
4.3.1	Methodology . . . . .	109
4.3.2	Barrier wind impact on hydrography at KGA . . . . .	110
4.4	Evidence for Mechanism 2 . . . . .	115
4.5	Evidence for Mechanism 3 . . . . .	118
4.5.1	Methodology . . . . .	118
4.5.2	Current transport variability . . . . .	120
4.5.3	Mean water mass transports . . . . .	121

---

4.5.4	Composite water mass transports . . . . .	124
4.5.5	Contribution to freshening of the DSO . . . . .	126
4.6	Evidence for Mechanism 4 . . . . .	128
4.7	Discussion . . . . .	132
4.7.1	Downstream evolution of the DSO sources south of KGA . . .	132
4.7.2	Property seasonality at DS . . . . .	134
4.8	Conclusions . . . . .	136
<b>5</b>	<b>The relationship between atmospheric forcing and DSO salinity</b>	<b>139</b>
5.1	Introduction . . . . .	139
5.2	Atmospheric circulation . . . . .	141
5.2.1	Time-mean circulation . . . . .	141
5.2.2	Leading modes of variability . . . . .	141
5.2.3	Temporal variability . . . . .	145
5.3	Wind field-DSO salinity correlations . . . . .	147
5.3.1	Method . . . . .	147
5.3.2	Spatial variability . . . . .	148
5.3.3	Temporal variability . . . . .	154
5.4	Wind stress forcing of intense DSO freshening . . . . .	157
5.4.1	Intense DSO freshening events . . . . .	157
5.4.2	The role of sea ice concentration . . . . .	161
5.5	Conclusions . . . . .	164
<b>6</b>	<b>Discussion and conclusions</b>	<b>167</b>
6.1	Discussion and future work . . . . .	167
6.1.1	Ocean circulation of DSO source water in the Blosseville Basin	168
6.1.2	Role of dense shelf water in the AMOC . . . . .	172
6.1.3	Evolution of the DSO in the Irminger Basin . . . . .	174
6.1.4	The impacts of future climatic changes . . . . .	179
6.2	Conclusions . . . . .	182
	<b>Abbreviations</b>	<b>184</b>
	<b>References</b>	<b>187</b>



# List of tables

1.1	The formation of dense water masses in the Nordic Seas . . . . .	18
2.1	Overview of the datasets used in this thesis . . . . .	38
2.2	Salinity and conductivity offsets between CTD and MC used to correct the MC time series . . . . .	45
3.1	Salinity correlation between KGA6/KGA11 time series and DS and ANG time series . . . . .	93
4.1	Mean southwestward water mass transports through KGA of all snapshots, and of all snapshots when the Shelfbreak EGC is strong . . . .	123



# List of figures

1.1	Schematics of the global ocean circulation and the key physical processes involved (adapted from Talley (2013)) . . . . .	3
1.2	Oxygen ( $\mu\text{mol/kg}$ ) distribution in the Atlantic Ocean . . . . .	5
1.3	Map of AMOC circulation in the subpolar North Atlantic . . . . .	7
1.4	Schematic of the formation of the AMOC lower limb in the subpolar North Atlantic . . . . .	10
1.5	Schematic map indicating the formation of dense ( $\sigma_\theta > 27.8 \text{ kg m}^{-3}$ ) AMOC water masses . . . . .	16
1.6	Circulation in the Nordic Seas and formation of dense shelf water. . .	21
1.7	Temperature of the DSO as function of distance downstream from DS	25
1.8	The hydrography of DSO source water masses upstream of DS . . . .	27
1.9	Distribution of DSO source water masses at DS . . . . .	28
1.10	Time series of the volume transport of the DSO and Faroe-Bank Channel overflow . . . . .	31
1.11	Map of atmospheric conditions for a barrier wind event composite . .	33
2.1	Vertical CTD section snapshot of temperature and salinity at the Angmagssalik array . . . . .	39
2.2	Vertical section of deployment mean flow speeds of the DSO at Angmagssalik . . . . .	41
2.3	Spatial and temporal distribution of MC instrument deployments at ANG between 1998 and 2015 . . . . .	42
2.4	Comparison of concurrent mooring and CTD salinity measurements between 2000 and 2003 . . . . .	44
2.5	Pressure as a function of time during a CTD calibration upcast in June 2012 . . . . .	46
2.6	Conductivity offsets between MC and CTD at bottle stops during a calibration cast carried out in summer 2012 . . . . .	47

2.7	Salinity anomaly time series, smoothed with a second order band-pass Butterworth filter with variable frequency cutoffs . . . . .	50
2.8	Salinity correlations between near-bottom MC salinities and MP salinities at different moorings of the Spill Jet sections . . . . .	53
2.9	Cross-section of the DS section showing the location of gridded CTD and mooring data . . . . .	54
2.10	Configuration of KGA moorings between the Greenland shelf and Iceland shelfbreak . . . . .	56
2.11	Observed near-bottom flow speeds on the Greenland shelf at KGA12 between 2011 and 2014 . . . . .	58
2.12	Direct comparison between observed and modelled near-bottom tidal flow speeds on the Greenland shelf . . . . .	59
2.13	Map of 1998-2015 mean of monthly mean wind, sea level pressure and sea ice concentration fields east of Greenland . . . . .	60
2.14	Map of 1998-2015 time-mean distribution of daily sea ice concentration error estimate . . . . .	62
3.1	Smoothed time series between 1998 and 2015 of density, temperature, salinity and salinity anomaly of the DSO at ANG . . . . .	68
3.2	Spectrum of DSO salinity at ANG . . . . .	69
3.3	Intra-annual variability of DSO salinity and temperature anomaly at ANG	71
3.4	Salinity anomaly of the DSO at ANG as a function of calendar month between 1998 and 2015 . . . . .	72
3.5	Salinity time series comparison between mooring observations and a linear regression model with an annual (i.e. 365 day) frequency . . . . .	73
3.6	Comparison of the intra-annual density variability, from the TEOS-10 software, and from a linearised decomposition at ANG . . . . .	74
3.7	Time series of freshening intensity across the DSO at ANG . . . . .	78
3.8	Salinity at mooring UK1 minus salinity at mooring UK2 composite as a function of day of year . . . . .	79
3.9	Time series of salinity anomaly of the near-bottom water across the slope at the Spill Jet section (Figure 1.8), in 2007-08 . . . . .	80
3.10	time-mean vertical salinity section at DS, between the Greenland and Iceland shelfbreaks . . . . .	82
3.11	Property time series in the core of the DSO at DS 2, between 2005 and 2015 . . . . .	83
3.12	Intra-annual variability of salinity anomaly of the DSO in the DS trough	84

3.13	$\theta$ -S distribution in each season composite and the median profiles in AMJ and OND at DS . . . . .	86
3.14	$\theta$ -S distribution and salinity cross-section in four synoptic snapshots between Nov 2003 and Nov 2004 at DS . . . . .	89
3.15	Time series of salinity in 2011-12 at KGA, and in 2011-13 at DS 2 and ANG . . . . .	92
4.1	Schematic of the time-mean hydrography on the Greenland shelf and slope and ocean circulation north of DS . . . . .	100
4.2	Schematics of the ocean circulation associated with the four proposed freshening mechanisms . . . . .	102
4.3	Cross sections of average along-stream velocity, temperature, and salinity at KGA . . . . .	104
4.4	$\theta$ -S profiles of DSO source water at KGA . . . . .	105
4.5	Local wind speeds at KGA between 2011 and 2014 with barrier wind events indicated . . . . .	110
4.6	Composite response of the near-bottom ocean properties on the Greenland shelf and slope to barrier wind events . . . . .	112
4.7	Composite response of the ocean velocity (in $\text{m s}^{-1}$ ) profile at KGA12 to barrier wind events . . . . .	113
4.8	Barrier wind composites of wind stress curl and Ekman pumping . . . . .	117
4.9	Snapshots of along stream velocity, salinity and temperature on 1 Sep 2011 . . . . .	119
4.10	Volume transport variability of DSO source water passing through KGA in 2011 via the three different current branches . . . . .	121
4.11	time-mean volume transport through KGA as a function of temperature and salinity for the three different current branches . . . . .	122
4.12	Volume transport as a function of temperature and salinity for all three current branches, for the intensified Shelfbreak EGC composite . . . . .	125
4.13	Time series of the volume transport weighted salinity of DSO source water passing through KGA . . . . .	127
4.14	Time series of isopycnal depth and salinity within density classes at FX9129	
4.15	Salinity anomaly at FX9 as a function of calendar month . . . . .	131
4.16	Time-mean $\theta$ -S profiles of the DSO at DS . . . . .	133
4.17	The $\theta$ -S distribution in April-May-June and October-November-December at DS . . . . .	135

5.1	1998-2015 mean of monthly mean wind speed, wind vectors and sea level pressure . . . . .	142
5.2	The two leading Empirical Orthogonal Function modes of sea level pressure east of Greenland and the NAO index and ILD index time series between 1998 and 2015 . . . . .	143
5.3	Composite wind speed, wind vectors and sea level pressure during strong positive NAO index months . . . . .	144
5.4	Composite wind speed, wind vectors and sea level pressure during strong negative ILD index months . . . . .	145
5.5	The intra-annual variability of the NAO index and ILD index, between 1998 and 2015 . . . . .	146
5.6	Complex lagged correlation coefficients between the non-deseasonalised ERA5 wind and the DSO salinity at ANG between 1998 and 2015 . . . . .	149
5.7	Complex lagged correlation coefficients between the deseasonalised time series of ERA5 wind and DSO salinity at ANG between 1998 and 2015 . . . . .	151
5.8	Map showing the integral timescale of the deseasonalised wind speed east of Greenland . . . . .	152
5.9	Approximate transit times of salinity anomalies along the east Greenland shelfbreak, north of DS, to ANG, for dense water . . . . .	154
5.10	The time series of correlation coefficient between the wind at two locations: r2 and r3, and the DSO salinity at ANG . . . . .	155
5.11	Lagged correlation maps between the wind field and the DSO salinity at ANG during subsets of the 1998-2015 time series . . . . .	156
5.12	1998-2015 time series of monthly averaged DSO salinity at ANG, wind speed, sea ice concentration and effective wind stress at r2 and r3, and a map showing the location of the time series . . . . .	159
5.13	Correlation between the wind at r2 and r3 in $\text{m s}^{-1}$ and the rate of change of salinity ( $\text{dS}/\text{dt}$ ) in $\text{months}^{-1}$ at ANG . . . . .	160
5.14	October-March mean sea ice concentration contours between 1998 and 2015 . . . . .	162
5.15	The variability of the drag coefficient as a function of sea ice concentration in the Marginal Ice Zone, derived from a parameterisation model . . . . .	164
6.1	Schematic sketch of the proposed seasonality of ocean circulation in the Blosseville Basin . . . . .	170

---

6.2	Time-mean salinity cross section at DS between 1990 and 2019, showing the presence of the dense shelf water . . . . .	173
6.3	Velocity spectra at mooring arrays in the pathway of the deep boundary current in the subpolar North Atlantic from observations and a model. . . . .	176
6.4	Advection of dense water masses and salinity anomalies in the pathway of NADW source water in the subpolar North Atlantic . . . . .	178
6.5	Time series of modelled and observed sea ice extent in the Arctic in March and in September from 1900 to 2100 . . . . .	181



## **Acknowledgements**

I could not have written this thesis without the help of a number of people. Firstly, thanks to Alex Brearley for being a fantastic supervisor. I am so grateful for all his patience and dedication to the development of this project. Thanks to Stephen Dye for all the time and kind support he has given me over the years. Thanks also to Ian Renfrew and Mike Meredith for all their invaluable input to this project. I am indebted to Bob Pickart and WHOI for hosting me for a wonderful, and inspiring, few months in Massachusetts. I am also grateful to BAS for having me, and for the friendly and sociable student community there. I also say thanks to Lianne, Rachael, David, Leo, the Ryans and Matt for all their support. Thanks to mum, dad, Martha, Ella and the rest of the family for their constant love and support.



# Chapter 1

## Introduction

### 1.1 Overview of North Atlantic Ocean circulation

For centuries, warm waters of the Gulf Stream have been encountered flowing polewards in the North Atlantic; they were even observed as far north as the Arctic Ocean by Nansen (1902). Originating in the Gulf of Mexico, the warm and saline Gulf Stream separates from the coast at Cape Hatteras, in North Carolina, and evolves into the North Atlantic Current, which flows northeastward towards western Europe and the Arctic Ocean. The Gulf Stream itself derives from northward flowing warm water currents in the South Atlantic, including the North Brazil Current, which drive a heat transport of 0.5 PW ( $10^{15}$  W) from the Southern Hemisphere to the Northern Hemisphere (Buckley and Marshall, 2016). This heat transport plays an important role in global climate variability on multi-decadal to multi-millennial timescales (Broecker et al., 1990; Jackson et al., 2015; Vellinga and Wood, 2002).

Once it reaches the Arctic Ocean, the only possible through-flow pathway is the narrow Bering Strait. However, since the mean flow here is also polewards (Roach et al., 1995), the warm polewards flow must be balanced by an equal equatorwards return flow, to satisfy volume conservation. Most of the return flow occurs in the deep ocean. The deep flow propagates southward through the Atlantic beneath, and in the opposite direction to, the northward near-surface flow of warm water. This circulation system of northward surface flow and southward deep flow in the Atlantic is known as the Atlantic Meridional Overturning Circulation (AMOC).

Since the second half of the 20th century, a detailed picture of the deep return flow has developed. Vigorous plumes of cold, dense water, formed through buoyancy loss and deep convection in the Nordic Seas, cascade from the Greenland Scotland Ridge and rapidly descend into the subpolar North Atlantic. The dense cascading 'overflow' currents increase their volume by entraining lighter water, including Labrador Sea

Water (LSW), and form North Atlantic Deep Water (NADW) (Dickson and Brown, 1994). The NADW propagates southward throughout the Atlantic, via the Deep Western Boundary Current. Climate models predict a weakening of the AMOC in the next one or two centuries (Cheng et al., 2013), due to global warming reducing the production of NADW (Weaver et al., 2007), potentially resulting in dramatic changes to global climate, comparable to previous events in the past 100,000-200,000 years, as detected in paleo-climate records (Broecker et al., 1990).

The densest water mass component of NADW is the Denmark Strait Overflow (DSO), which contributes approximately one third of the total transport of the NADW (Dickson and Brown, 1994). Previous work has demonstrated that the DSO is fed by dense water mass sources formed in the Nordic Seas and the Arctic Ocean (Mauritzen, 1996; Rudels et al., 2002; Våge et al., 2013). It has been previously argued that the variability in the contribution of the different sources causes DSO property (salinity, temperature and density) anomalies (Holfort and Albrecht, 2007; Jochumsen et al., 2015), and the anomalies are advected along the east Greenland slope and into the Labrador Sea by the DSO (Yashayaev and Dickson, 2008). The purpose of this thesis is to investigate the characteristics and origins of DSO property variability on advective timescales.

The three main objectives of this chapter are: 1) to summarise current knowledge of the ocean circulation in the Atlantic, 2) to explain the importance of the ocean circulation in the Atlantic, and 3) to identify the research questions that this thesis aims to investigate. Therefore, the outline for the chapter is as follows. In the first part of this chapter (Section 1.2), the AMOC is described in more detail. In Section (1.3), the formation of North Atlantic Deep Water (NADW), at high latitudes in the Northern Hemisphere, is described. Here the locations and processes of dense water mass formation, the Nordic Seas Overflows and entrainment are all covered. Section 1.4 is about the Denmark Strait Overflow (DSO), the densest and one of the most important sources of NADW and the subject of this thesis. And finally, six relevant research questions are asked in Section 1.5, and, in Section 1.6, the thesis outline is described.

## **1.2 The AMOC**

### **1.2.1 Context**

The global Meridional Overturning Circulation (MOC) is characterised by dense water formation and overturning at high latitudes, balanced by upwelling of deep water in specific regions (e.g. the Southern Ocean) and meridional (north-south) transports of

water, heat and carbon. Dense water is formed in the subpolar North Atlantic and the polar gyres of the Weddell (Vernet et al., 2019) and Ross (Jacobs et al., 1970) Seas, whilst lighter water masses are formed in the Indian, Pacific, South Atlantic and Southern Oceans (Talley, 2013). The Atlantic MOC is just one component of an inter-connected global ocean circulation, which has profound implications for climate.

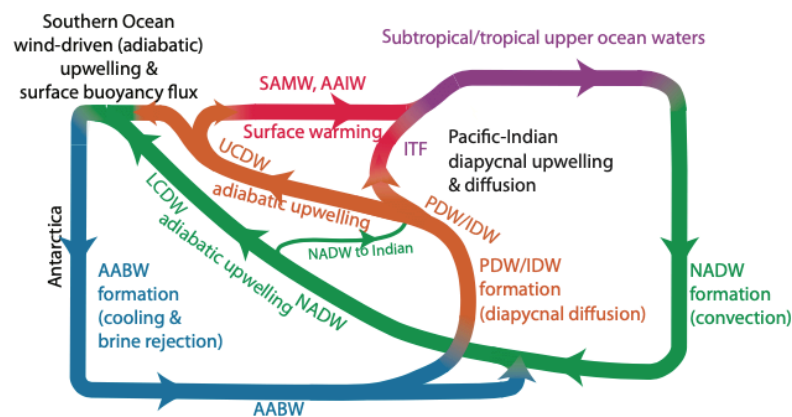
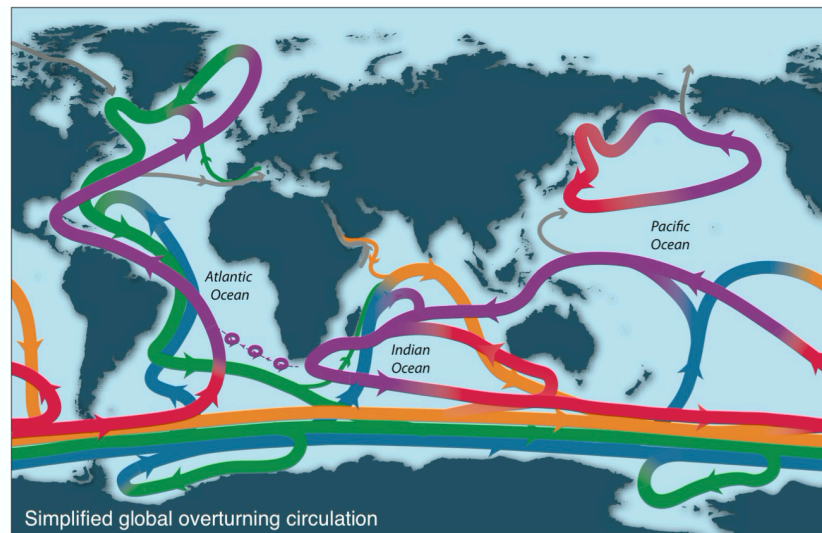


Fig. 1.1 Schematics of the global ocean circulation and the key physical processes involved. In the bottom panel, the Northern Hemisphere is on the right of the schematic and the Southern Hemisphere on the left. The colour scheme for the MOC components are purple (upper ocean/thermocline), red (denser thermocline and intermediate water), orange (Indian Ocean Deep Water (IDW) and Pacific Deep Water (PDW)), green (NADW), blue (Antarctic bottom water (AABW)). The other acronyms are Sub-Antarctic Mode Water (SAMW), Antarctic Intermediate Water (AAIW) and Lower Circumpolar Deep Water (LCDW). The two main regions of buoyancy loss and dense water formation are the Southern Ocean and the North Atlantic. Note that the AMOC upper limb has two source water pathways: one is upwelling PDW/IDW, and the other is northward flowing SAMW/AAIW. Figure from Talley (2013); their Figures 1 and 5a

The NADW and Pacific Deep Water/Indian Deep Water upwell in the Southern Ocean, feeding lower and upper Circumpolar Deep Water respectively (Figure 1.1) (Garabato et al., 2014). The lower Circumpolar Deep Waters are transported to the south of the Antarctic Circumpolar Current and mix with surface water and coastal water in the cyclonic gyres to form Antarctic Bottom Water (Garabato et al., 2014). Conversely, the upper Circumpolar Deep Waters are entrained into the mixed layer of the ACC where they form Sub-Antarctic Mode Water and Antarctic Intermediate Water, which flow northwards (Garabato et al., 2014). Antarctic Bottom Water is exported from the Southern Ocean into the Pacific, Atlantic and Indian Oceans. Branches of Indian and Pacific Deep Water, formed through upwelling of Antarctic Bottom Water (Talley, 2013), enter the South Atlantic via the Agulhus Current and Drake Passage respectively, propagate northwards and ascend to thermocline depths, feeding the upper limb of the AMOC (Ruhs et al., 2019). These water masses are identified in the low latitudes of the Atlantic by their characteristic low oxygen concentrations (Figure 1.2), consistent with the advanced age of the water masses (Talley, 2013). The other two sources of the AMOC upper limb are Sub-Antarctic Mode Water and Antarctic Intermediate Water, fed by Indian/Pacific Deep Water upwelling north of the Antarctic Circumpolar Current. Ultimately the AMOC upper limb supplies the surface water from which NADW is formed. Antarctic Bottom Water also contributes to the NADW downstream of the dense water formation locations in the subpolar North Atlantic, after upwelling and diapycnal diffusion of the former (Talley, 2013).

Figure 1.1 shows the broad-scale pathway of the MOC components and the key density modification processes. Dense water formation is driven by surface processes which remove buoyancy from the near surface waters, including brine rejection during sea ice formation and/or atmospheric cooling. On the other hand, water mass warming (buoyancy increase) and upwelling are driven by diapycnal mixing (mixing between water of different densities) at depth and surface warming at low latitudes, with much of the upwelling occurring in the Southern Ocean (Talley, 2013). In general the upwelling of the densest water mass in the global oceans (Antarctic Bottom Water), which fills the deep ocean, is achieved by upwelling at basin edges (i.e. continental margins and ridges) driven by shear-driven mixing by internal waves and other types of flow topography interaction (Ferrari et al., 2016).

The global MOC has profound implications for the global climate. The MOC is responsible for sequestering heat, carbon and oxygen from the atmosphere, and it is stored in the ocean. Johnson (2008) estimated that the average residence time of Antarctic Bottom Water (NADW) is 870 years (500 years). Improved understanding of the rate and mechanisms of heat and carbon uptake and vertical export by the ocean is

essential for coupled climate models to accurately forecast future climate conditions (Buckley and Marshall, 2016). The MOC also transports heat from low to high latitudes. The relative contribution of polewards ocean heat transport to the total polewards heat transport (atmosphere + ocean) varies by latitude, but, in general, atmospheric transports are greater than the ocean (Trenberth and Caron, 2001). The contribution of the ocean to the total polewards heat transport is higher in the Northern Hemisphere, since the ocean heat transport is polewards in both the North Atlantic and North Pacific (Trenberth and Caron, 2001), and the maximum ocean heat transport (estimated at between 1 PW and 1.5 PW) occurs at around 20°N (Buckley and Marshall, 2016). Conversely, the heat transport is equatorwards in the South Atlantic (due to the AMOC), which reduces the contribution of ocean transport to the total polewards heat transport (Trenberth and Caron, 2001). Thus, it is due to the AMOC that polewards heat transports are greater in the Northern Hemisphere than in the Southern Hemisphere.

Additionally, the sinking MOC branches have high concentrations of dissolved oxygen and therefore ventilate the interior oceans. The oxygen distribution in the Atlantic is shown in Figure 1.2, where the elevated concentrations of oxygen ( $> 220 \mu\text{mol/kg}$ ) in the deep ocean ( $> 2000 \text{ m}$ ) are indicative of NADW and Antarctic Bottom Water. The deep ocean oxygen concentrations are lower in the North Pacific than the North Atlantic, because deep water formation occurs in the North Atlantic, but not the North Pacific (Talley, 2011). For example, the oxygen concentration at 2000 m, at 47°N,

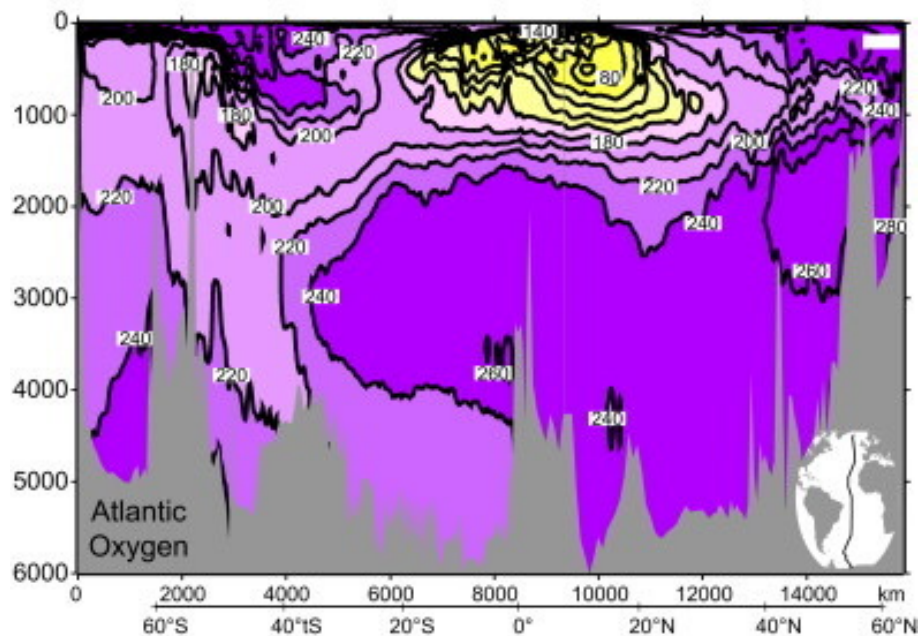


Fig. 1.2 Oxygen ( $\mu\text{mol/kg}$ ) distribution in the Atlantic Ocean, from a World Ocean Circulation Experiment transect. The inset map shows the location of the transect. This figure is from Talley (2011): their Figure 4.11d.

in the North Pacific is around  $100 \mu\text{mol/kg}$ , compared with  $250 \mu\text{mol/kg}$  in the North Atlantic (Talley, 2011).

It follows that the MOC provides the oxygen required for important biogeochemical cycles (e.g. the carbon and nitrogen cycles) and prevents the expansion of oxygen minimum zones, which are located at mid-depths in multiple areas of the global oceans, for example between  $20^\circ\text{S}$  and  $40^\circ\text{N}$  (Figure 1.2). Should the supply of oxygen decrease (as is expected) due to increased upper-ocean stratification (associated with reduced formation of intermediate and deep water masses, and thus increased  $\text{O}_2$  outgassing), changes to biogeochemical cycling will occur. For example the production of Nitrous Oxide ( $\text{N}_2\text{O}$ ), which is produced during nitrification in oxic conditions and during denitrification in anoxic conditions, will increase with lower oxygen concentrations (Keeling et al., 2010).  $\text{N}_2\text{O}$  is a strong greenhouse gas, which accelerates global warming. This highlights the importance of the MOC in the carbon cycle.

### 1.2.2 Upper limb

One component of the MOC, described above, is the AMOC. In the near surface layer of the Atlantic (upper 1000 m), the AMOC drives a northward volume and heat transport, which has important consequences for global climate. The Benguela Current flows northward along the southwest coast of Africa feeding the northwestward flowing South Equatorial Current, which turns northward near the South American coast around  $18^\circ\text{S}$  forming the North Brazil Current (Garzoli and Matano, 2011). The North Brazil Current comprises water masses that form during upwelling of deep water in the Pacific and Indian Ocean and enter the South Atlantic via the Drake Passage and Agulhus Current respectively (Talley, 2013). These water masses are then made lighter during upwelling in the South Atlantic (Ruhs et al., 2019). The mean northward volume transport of the North Brazil Current is approximately 26 Sv (Hummels et al., 2015).

The North Brazil Current crosses the Equator and feeds the Gulf Stream, which flows along the east coast of North America. One of the main pathways between the North Brazil Current and the Gulf Stream are North Brazil Current rings, which are anti-cyclonic rings with a length scale of around 100 km, that propagate northward to the east of Barbados (Goni and Johns, 2001), before feeding the Gulf Stream. The North Brazil Current rings form when Rossby waves radiate from the North Equatorial Counter Current, which reflect at the Brazilian coast, and form anti-cyclones that travel northwards and evolve into the rings (Jochum and Malanotte-Rizzoli, 2003). The North Brazil Current rings contribute approximately 40% of the total transport of the upper limb at this location; the two other mechanisms are coastal currents on the South American continental shelf and Northward Ekman transport (Garraffo et al., 2003).

Note that Ekman transport is the net water transport arising from the wind stress and the influence of the coriolis effect which results in transport  $90^\circ$  to the right of the wind in the Northern Hemisphere and  $90^\circ$  to the left of the wind in the Southern Hemisphere. Using submarine cables, the northward volume transport of the Gulf Stream through the Florida Straits was estimated at 32 Sv (DiNezio et al., 2009).

After separating from the coast at Cape Hatteras (North Carolina), the Gulf Stream transport rapidly increases to 150 Sv by the Grand Banks (Hogg, 1992), off the coast of Newfoundland, due to inflowing water from the south and north, but primarily from the north (Johns et al., 1995). The Gulf Stream splits into multiple different branches, with one branch - the North Atlantic Current (NAC) - transporting 40 Sv northwards, another branch recirculates to the southwest, and another branching feeding an eastward drift which evolves into the Azores Current (Rossby, 1996). The NAC crosses the Mid-Atlantic Ridge, at which point its transport is reduced to around 20 Sv (Rossby, 1996), thereafter it splits into several branches (Hansen and Østerhus, 2000) (Figure 1.3).

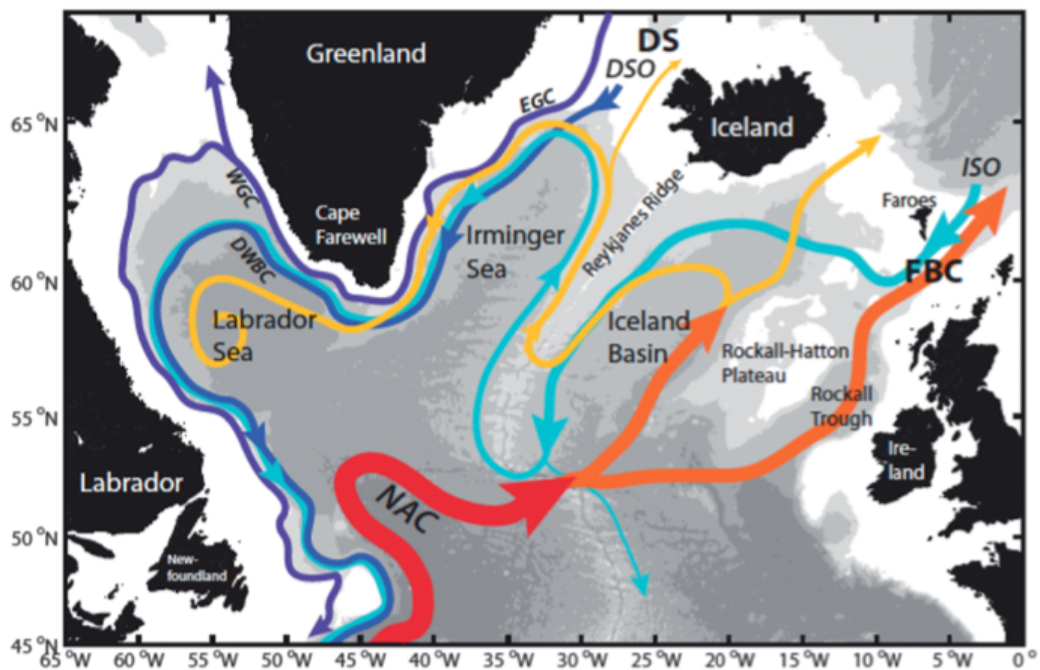


Fig. 1.3 Map of AMOC circulation in the subpolar North Atlantic. The yellow, orange and red colours are warm near surface branches whilst the blue colours are cold currents. The acronyms are as follows: North Atlantic Current (NAC), Iceland Scotland Overflow (ISO), Denmark Strait Overflow (DSO), East Greenland Current (EGC), West Greenland Current (WGC) and Deep Western Boundary Current (DWBC), Faroe-Bank Channel (FBC) and Denmark Strait (DS). Note that the overflows east and west of Iceland merge off the southeast Greenland coast. Figure from Lozier et al. (2017): their Figure 1.

One branch feeds the cyclonic subpolar gyre (the Irminger Current) and two branches enter the Nordic Seas (Iceland, Greenland and Norwegian Seas) east of Iceland. The total volume transport of the Nordic Seas inflow is around 8 Sv (Hansen and Østerhus, 2000).

Two NAC derived current branches enter the Nordic Seas east of Iceland (one enters between Iceland and the Faroe Islands, the other through the Faroe-Shetland Channel along the Shetland slope) (Hansen and Østerhus, 2000). Most of the Atlantic inflow occurs between Iceland and the Faroes, where the average volume transport is 3.5 Sv (Hansen et al., 2010), while the transport through the Faroe Shetland Channel is 2.7 Sv (Berx et al., 2013). Another NAC derived branch enters the Nordic Seas at Denmark Strait via the North Icelandic Irminger Current, which transports 0.9 Sv (Jónsson and Valdimarsson, 2012).

Another NAC derived branch feeds the the Irminger Current, which bifurcates around Denmark Strait. The branch that does not enter the Nordic Seas retroflects at Denmark Strait, flows along the East Greenland coast and around Cape Farewell, entering the Labrador Sea along the West Greenland coast via the East Greenland Current and West Greenland Current as part of the subpolar gyre. The Irminger Current inflow to the Labrador Sea is around 4 Sv (Myers et al., 2007).

Whilst the main source of the Nordic Seas Atlantic inflow is the Gulf Stream, which feeds the NAC, there is also a contribution from the West European Continental Slope Current (Hansen and Østerhus, 2000), distinguished by its high salinity ( $S > 35.4$ ) (Turrell et al., 1992). This current probably derives from Mediterranean outflow or transformation of the water near the west European coast by a combination of strong evaporation in summer and cooling and deepening of saline water in winter (Hansen and Østerhus, 2000). It transports approximately 1 Sv polewards at the location of the Celtic slope (Pingree and Le Cann, 1989), though part of this transport may be attributable to an eastern branch of the NAC. The West European Continental Slope Current contributes to the Atlantic inflow through the Faroe-Shetland Channel (Hansen and Østerhus, 2000).

This northward near-surface flow in the Atlantic results in northward heat transports in the South Atlantic and North Atlantic. Northward heat transports increase from around 0.6 PW at 35°S (Garzoli and Matano, 2011) towards a maximum at around 20°N (Buckley and Marshall, 2016). Using observations across the entire subtropical Atlantic at around 26.5°N, McCarthy et al. (2015) estimated a heat transport of 1.25 PW. Heat transports reduce to 0.45 PW at around 60°N according to a recent study using observations across the entire subpolar North Atlantic at around 60°N (Lozier

et al., 2019). This reduction in northward heat transport indicates that heat is lost to the atmosphere via upwards heat fluxes at the ocean-atmosphere interface.

### 1.2.3 Lower limb

The upper limb of the AMOC must be compensated by the lower limb, which is described below. The lower limb of the AMOC is driven by dense water formation, due to cooling and deep convection principally in the Nordic Seas and Labrador Sea. The dense water exits through overflows across the Greenland-Scotland Ridge (Figure 1.3), which are rapidly entraining gravity currents that descend into the subpolar North Atlantic. There are three major overflows, that collectively transport 6 Sv (Hansen and Østerhus, 2000), before entrainment doubles the net volume transport by the southern tip of Greenland (Dickson and Brown, 1994). The DSO, between Greenland and Iceland, is associated with the largest transports (3.2 Sv (Jochumsen et al., 2017)) and forms the densest part of NADW (Dickson and Brown, 1994). The two overflows east of Iceland (the Iceland-Faroe Ridge overflow and the Faroe-Bank Channel overflow) transport around 3 Sv (Hansen and Østerhus, 2000) and form the layer immediately above the DSO in the NADW (Dickson et al., 2008). The upper limit of the overflows are traditionally identified in the North Atlantic by the  $27.8 \text{ kg m}^{-3}$  isopycnal, after Dickson and Brown (1994).

Downstream of DS, the DSO entrains warmer water and is fed by dense shelf water, which cascades off the shelfbreak off the East Greenland shelf (Brearley et al., 2012; Falina et al., 2012; Rudels et al., 2002), causing around a two fold increase in volume transports (Dickson and Brown, 1994). These processes are explained in more detail below.

NADW is principally advected southward through the Atlantic by the Deep Western Boundary Current, first proposed by Stommel (1958), and since confirmed by observations; for example (Bryden et al., 2005; Lozier et al., 2019). Southward volume transports of NADW at the subpolar Overturning in the subpolar North Atlantic Programme (OSNAP) array were 15 Sv between 2014 and 2016, concentrated on the western boundary (Lozier et al., 2019). Further south at the subtropical RAPID array (the RAPID array is a cross-basin array deployed between 2004 and the present day at  $26.5^\circ\text{N}$  in the North Atlantic), time-average (2004-2017) transports are roughly 17 Sv (Smeed et al., 2018). In the South Atlantic (at  $34.5^\circ\text{S}$ ), time-mean NADW transports (15 Sv) are also dominated by the Deep Western Boundary Current (Meinen et al., 2017). Passing through the low latitudes, the NADW is warmed through diapycnal mixing, acquiring lower densities (Talley, 2013) and then upwells along steeply sloping isopycnals in the Southern Ocean, due to wind forced Ekman upwelling (Marshall and

Speer, 2012). The upwelling NADW contributes to the formation of Circumpolar Deep Water and Antarctic Bottom Water (Marshall and Speer, 2012).

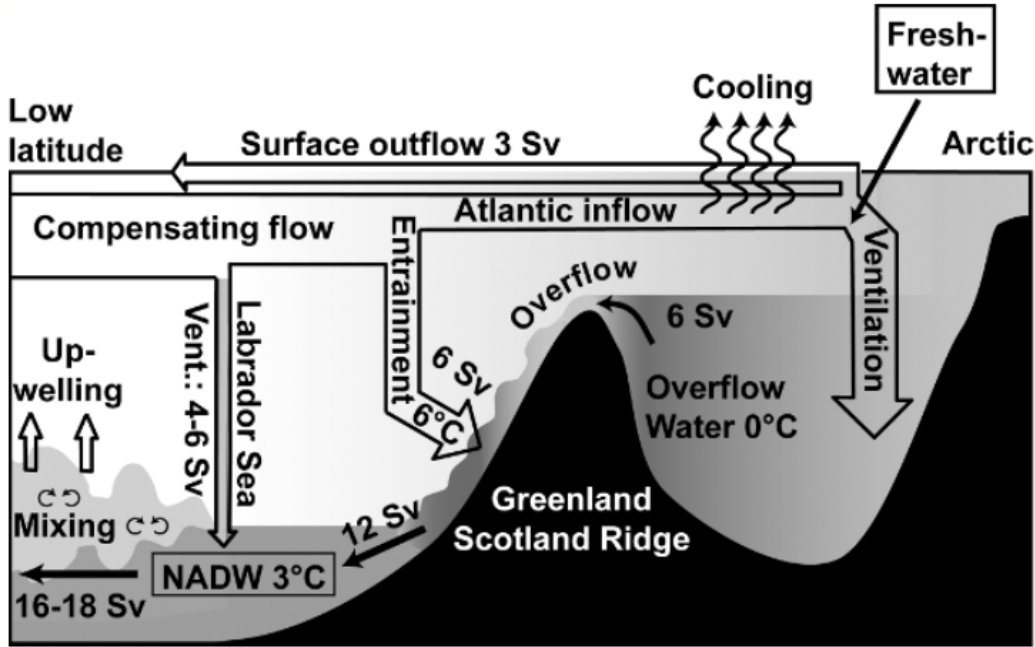


Fig. 1.4 Schematic of the formation of the AMOC lower limb in the subpolar North Atlantic. The cooling and dense water formation occurs north of the Greenland Scotland Ridge, exiting southward with overflows which entrain warmer water and form North Atlantic Deep Water (NADW). Figure from Quadfasel and Käse (2007); their Figure 1.

## 1.2.4 Temporal variability

In addition to the time-mean circulation summarised above, the time-variant component of the AMOC may make an important contribution to the total volume transport of the AMOC (Kanzow et al., 2010). The AMOC strength is generally defined as the maximum of the stream function, and the two key components of the AMOC stream function are the Ekman component ( $\Psi_{ek}$ ) and the thermal wind component ( $\Psi_{tw}$ ) (Buckley and Marshall, 2016), which are defined as follows:

$$\Psi_{tw}(z) = \int_z^\eta \frac{1}{f} \int_{-H}^z (b(X_e) - b(X_w)) dz dz, \quad (1.1)$$

$$\Psi_{ek}(z) = \int_z^\eta \int_{X_w}^{X_e} \frac{\tau^x}{\rho_0 f D_{ek}} dx dz, \quad (1.2)$$

where  $\tau^x$  is the zonal wind stress,  $D_{ek}$  is the Ekman depth,  $f$  is the coriolis parameter,  $\rho_0$  is the reference density,  $\eta$  is the height of the free surface,  $H$  is the water depth,  $b(X_e)$  is the buoyancy on the eastern boundary and  $b(X_w)$  is the buoyancy on the western boundary,  $x$  is the zonal coordinate and  $z$  is the vertical coordinate (Buckley and Marshall, 2016).

On short timescales (intraseasonal), local wind driven Ekman transport is the dominant driver of AMOC variability. At any latitude, the magnitude of high frequency variability is high and can be similar to the mean (Buckley and Marshall, 2016). As the strength of the AMOC is determined by the local wind forcing on short timescales, the meridional coherence of the AMOC reflects the meridional coherence of the wind forcing (Buckley and Marshall, 2016). Conversely, on longer timescales, the thermal wind component plays a more important role than the Ekman component in AMOC variability, as detailed below.

On seasonal timescales, Kanzow et al. (2010) report maximum AMOC strength (or, equivalently, maximum upper ocean transports) in autumn and minimum in spring (at  $26.5^\circ\text{N}$ ), with the thermal wind component dominating the Ekman component on this timescale. Anticyclonic wind stress curl in summer causes downwelling of density surfaces in autumn on the eastern boundary of the North Atlantic around  $26.5^\circ\text{N}$  (Kanzow et al., 2010). This increases the east-west horizontal density gradient, thereby enhancing the thermal wind component of the AMOC by around 7 Sv compared with spring, when the volume transports are weakest (Kanzow et al., 2010). Conversely, Zhao and Johns (2014) highlight the role of Ekman transport in driving seasonality, especially at tropical latitudes. Mielke et al. (2013) use evidence from a numerical ocean model and observations to argue that, in the North Atlantic, the non-Ekman component of AMOC is covariable at subtropical and mid-latitudes on seasonal and interannual timescales, i.e. the variability at  $41^\circ\text{N}$  could be inferred from the observed variability at  $26^\circ\text{N}$ .

Furthermore, the multi-annual to multi-decadal variability of the AMOC is also thought to be associated with variability of horizontal density gradients and attendant changes to the thermal wind component (Buckley and Marshall, 2016). A number of studies have highlighted the importance of density anomalies, in the upper 1000 m, around the boundary between the subpolar and Sub-Tropical gyres in the northwest Atlantic (Buckley and Marshall, 2016; Tulloch and Marshall, 2012). The anomalies change the horizontal density gradients which drive the geostrophic component of AMOC and cause meridionally coherent variability (Buckley and Marshall, 2016). Conversely, a recent weakening of the AMOC by around 3 Sv (between 2004-08 and 2008-17) was attributed to reduced southward flow of the densest component of AMOC,

i.e. the densest (found below 3000 m) component of NADW fed by the DSO (Smeed et al., 2018).

Similarly, the variability of NADW production is linked with AMOC variability on multi-centennial to multi-millennial timescales. On these timescales, the AMOC is thought to switch rapidly between two stable states: the 'on' and the 'off' state (Broecker et al., 1990). During the 'off' or 'glacial' state, the dense water formation and NADW is shifted south of Iceland and shoals, whereas in the 'on' or 'modern' state (e.g. present day), the dense water formation is primarily north of Iceland and the NADW penetrates deeper, and AMOC warms high latitudes in the Northern Hemisphere (Alley and Clark, 1999). Evidence from deep ocean sediment cores and numerical models suggest that the variability is likely driven by the changing rate of ice sheet calving in the Northern Hemisphere (Menviel et al., 2014). When ice-sheet calving is increased, fresh water input to the NADW formation regions also increases, resulting in a more stable water column and therefore reduced formation of NADW through deep convection and thus, a weakened AMOC, and when ice sheet calving is decreased the opposite chain of events occurs (Sarnthein et al., 2001). In the last glaciation, periods of weakened AMOC coincided with stadial (cold) phases of the Dansgaard-Oeschger climate cycle in the Northern Hemisphere, prompting some to highlight the role of the AMOC in causing abrupt global climate change (Henry et al., 2016).

Sea Surface Temperature (SST) observations in the North Atlantic imply that the AMOC may have weakened in the 20th century. Specifically, whilst SSTs have largely been increasing in the 20th century, there is an area of cooling in the subpolar North Atlantic just south of Greenland (Rahmstorf et al., 2015). Accompanying this is an elevated warming of the western subtropical Atlantic around the Gulf Stream (Caesar et al., 2018). Both results are consistent with a reduction in the polewards heat transport of the AMOC. Caesar et al. (2018) used an observational based SST index to reconstruct AMOC from 1950 to the present day, and estimated a 3 Sv reduction over that period.

Continued weakening of the AMOC is predicted in the next century, with coupled climate models forecasting a 5 to 60% reduction by 2100 (Cheng et al., 2013). Although there is a spread in the predicted weakening between models, all agree that weakening will occur. Generally speaking, coupled climate models are subject to three main sources of uncertainty: the uncertainty of future greenhouse gas emissions, the uncertainty of AMOC internal variability (i.e. the non-radiatively forced variability) and the uncertainty of model response to radiative forcing (Hawkins and Sutton, 2009). For the AMOC, model uncertainty is likely the largest source of uncertainty (Reintges et al., 2017), exceeding greenhouse gas emission scenario uncertainty even at the longest lead times. Specifically, model uncertainty in the projections of the salinity distribution in

the subpolar North Atlantic and Arctic Ocean arises from uncertainties in projecting the freshwater fluxes and the subpolar gyre circulation (Reintges et al., 2017).

The cause of the present AMOC weakening might be reduced formation of NADW. There are three key trends which may drive the reduction of dense water formation and all are related to anthropogenic global warming. Firstly, ocean temperatures warm and less heat is lost to the atmosphere, which also warms (i.e. air-sea heat fluxes are reduced), leading to a reduction in buoyancy extraction (Gregory et al., 2005). Secondly, warming atmospheric temperatures cause increased melting of the Greenland ice sheet (Bakker et al., 2016), thus increasing the freshwater input to the ocean. Both factors increase the buoyancy of the near surface waters and therefore reduce dense water formation. The latter process (increased freshwater input) is a key source of uncertainty to model projections of the AMOC (Reintges et al., 2017). Comparing the effects of increased freshwater flux and reduced air-sea fluxes, Gregory et al. (2005) proposed that the reduced air-sea fluxes was the leading cause of AMOC weakening. Additionally, receding sea ice extent, caused by rapidly warming Arctic air temperatures, may reduce the strength of atmospheric cooling and deep convection in key dense water formation locations (Moore et al., 2015). Conversely, the receding of the sea ice in the Iceland Sea has exposed areas of the ocean to the atmosphere that were previously ice covered, which has led to increased heat fluxes out of the ocean and deep convection occurring over the Greenland slope (Våge et al., 2018).

### 1.2.5 Climate impacts

The northward heat transport in the Atlantic associated with the AMOC influences global climate. For instance, AMOC influences global air temperatures, particularly in the Northern Hemisphere (Vellinga and Wood, 2002) and the sea ice distribution in the Arctic (Mahajan et al., 2011). The ocean heat transport associated with the AMOC is the dominant cause of the higher average annual temperatures in the Northern Hemisphere, as compared to the Southern Hemisphere, with the enhanced greenhouse effect of increased water vapour in the Northern Hemisphere a positive feedback of the northward ocean heat transports (Kang et al., 2015). The effects of the different land-ocean ratio in the two hemispheres on the temperatures is judged small in comparison to the meridional ocean heat transports by Kang et al. (2015). Data from paleo-climate records and numerical simulations provide insight into how different the global climate might be under different AMOC regimes.

Firstly, investigations based on numerical simulations demonstrated that without the AMOC, SST and surface air temperatures are 5°C lower in the Northern Hemisphere than they are with an active AMOC (Manabe and Stouffer, 1988). Accompanying this

is a reduction in Northern Hemisphere mid-latitude precipitation, which, together with cooling, results in reductions to continental primary productivity of approximately 25% in Europe (Jackson et al., 2015). The results from paleo-climate studies are consistent with the numerical simulations (Timmermann et al., 2003). Numerical models have also investigated the wider climate impacts of a weakened AMOC. As well as confirming the North Atlantic cooling, Kageyama et al. (2009) show that a weak AMOC state drives a weakening of the Asian monsoon and a southward migration of the Inter-Tropical Convergence Zone. This changes precipitation patterns over South America, Africa and Asia. AMOC weakening is also associated with increased ocean temperatures in the high latitude South Atlantic, consistent with weakened northward heat transports here (Alley and Clark, 1999).

On shorter timescales (sub-centennial), studies have shown that AMOC variability may play an important role in climate variability. AMOC variations cause SST anomalies in the North Atlantic (Buckley and Marshall, 2016) and are thought to explain around one third of the SST variability in the North Atlantic on multi-decadal timescales (Muir and Fedorov, 2015). The two other suggested key drivers of SST variability in the North Atlantic are aerosol variability (from anthropogenic and volcanic sources) (Booth et al., 2012) and stochastic atmospheric circulation forcing (Clement et al., 2015).

The Atlantic Multidecadal Variability is an index based on SST in the North Atlantic. The index is typically constructed by calculating the SST, spatially averaged between 0°N and 60°N basin-wide in the North Atlantic, and to create the index time series, the mean and the warming trend is removed from the time series (Sutton and Hodson, 2005). The Atlantic Multidecadal Variability influences global climate, especially in the Northern Hemisphere. Positive phases (positive SST anomalies in the North Atlantic) are associated with increased temperature and precipitation in Europe and increased temperatures and decreased precipitation in the United States, and negative phases are associated with the opposite conditions (Sutton and Hodson, 2005). Furthermore, variability of this index is associated with variability of the Inter-Tropical-Convergence Zone (ITCZ), which controls the amount of rainfall in the Sahel region, in North Africa (Ting et al., 2011). Also, the activity of Atlantic Hurricanes is linked to the Atlantic Multidecadal Variability, with cold phases associated with fewer hurricanes (Zhang and Delworth, 2006). On decadal timescales, the Atlantic Multidecadal Variability is the dominant driver of summertime climate in Europe and North America (Sutton and Hodson, 2005).

Thus, observing and understanding the variability of the AMOC, on different timescales, improves the prospects for climate predictability, which is of great importance to society. Specifically, climate predictability is of the utmost importance for

society to prepare for patterns of weather that may be different to that experienced in the recent past. It is primarily on these grounds that more research, based on further oceanographic observations and numerical modelling of the AMOC, is justified. In 2014, an observational array across the width of the subpolar North Atlantic basin was initiated (the OSNAP array; introduced earlier) and the first results are beginning to emerge (e.g. see Lozier et al. (2019)). Cross-basin arrays have also been deployed in the Atlantic at 26.5°N (RAPID; previously introduced), 16°N (MOVE; Send et al. (2011)) and 34.5°S (SAMBA; Meinen et al. (2017)). Observations from these cross-basin arrays and sustained/repeated observations of individual AMOC components, combined with data from constantly improving numerical models, are essential to our continually evolving understanding of the AMOC.

## **1.3 Formation of North Atlantic Deep Water**

### **1.3.1 Densest source waters**

Some of the density transformation required to drive the formation of the lower limb of the AMOC occurs in the Nordic (Norwegian, Greenland and Iceland) and Labrador Seas and Arctic Ocean. Dense source water is formed both in the deep interior of the basins, away from the strong boundary currents (Brakstad et al., 2019; Lavender et al., 2000; Swift and Aagaard, 1981), and around the basin edges (Mauritzen, 1996). The key processes are rapid atmospheric cooling and brine rejection during sea ice formation in winter. These processes remove buoyancy from the near surface waters, enabling subduction or sinking of dense water and overturning via deep convection.

Deep convection usually occurs in winter during strong atmospheric cooling in the deep centre of the basins, where there is cyclonic ocean circulation. Cyclonic ocean gyre circulation causes the isopycnals to dome upwards, preconditioning the water column for deep convection, as occurs in the Greenland and Iceland Seas (Swift and Aagaard, 1981). Further, the weak background flow in the centre of the basins enables sustained deep convection, uninterrupted by advection driven restratification (Lavender et al., 2000). Deep convection involves the removal of buoyancy from surface waters, which reduces the stability of the water column and drives the deepening of the mixed layer. Dense water is also formed on the basin edges when boundary currents are cooled by the atmosphere (Mauritzen, 1996) and interact with dense plumes formed on the shelves by brine rejection (Rudels et al., 1994). Deep convection occurs in small scale convective chimneys, which have a diameter of approximately 10 km (Wadhams et al., 2002).

## Nordic Seas

Wintertime deep convection forms dense water masses east of Greenland in the Iceland and Greenland Seas (Brakstad et al., 2019; Swift and Aagaard, 1981). This process creates a water mass traditionally called Iceland Sea Arctic Intermediate Water (ISAIW) and Greenland Sea Arctic Intermediate Water (GSAIW) respectively. Both ISAIW and GSAIW are relatively cold ( $\theta < 0^\circ\text{C}$ ) and dense ( $\sigma_\theta > 27.97 \text{ kg m}^{-3}$ ), with GSAIW the denser of the two ( $\sigma_\theta \approx 28.05 \text{ kg m}^{-3}$ , see Table 1.1) because turbulent heat fluxes out of the ocean are greater there (Moore et al., 2015). The approximate formation regions are shown on the map in Figure 1.5.

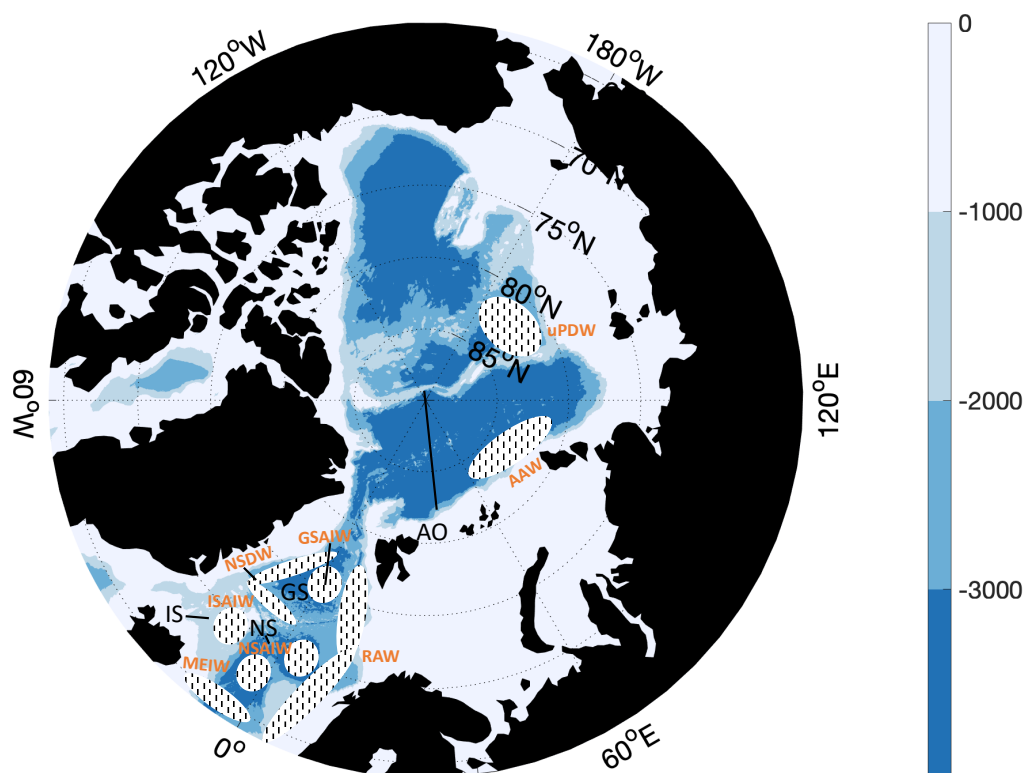


Fig. 1.5 Schematic map indicating the formation of dense ( $\sigma_\theta > 27.8 \text{ kg m}^{-3}$ ) AMOC water masses. The water mass acronyms (in orange) are as follows: Modified East Icelandic Water (MEIW), Norwegian Sea Arctic Intermediate Water (NSAIW), Iceland Sea Arctic Intermediate Water (ISAIW), Greenland Sea Arctic Intermediate Water (GSAIW), Norwegian Sea Deep Water (NSDW), Recirculating Atlantic Water (RAW), Arctic Atlantic Water (AAW) and upper Polar Deep Water (uPDW). The location acronyms (in black) are: Iceland Sea (IS), Greenland Sea (GS), Norwegian Sea (NS) and Arctic Ocean (AO). The bathymetry is from the International Bathymetric Chart of the Arctic Ocean (IBCAO) 30 arc-second product version 3, from the General Bathymetric Chart of the Oceans (GEBCO); the 1000 m, 2000 m and 3000 m isobaths are all shown.

ISAIW formation was first observed in the central Iceland Sea in the 1970s by Swift and Aagaard (1981), where it is likely driven by the inflow of the high salinity North Icelandic Irminger Current water (Våge et al. (2011); see Figure 1.6). Recent observations have revealed that the densest water and the deepest mixed layers are presently observed in the north Iceland Sea near the sea ice edge (Våge et al., 2015). Conversely, the deepest mixed layers in the Greenland Sea are in the deepest, central, part of the sea (Brakstad et al., 2019). Some fraction of GSAIW and ISAIW enter the Lofoten Basin and Norwegian Basin respectively, mix with an Arctic Ocean water mass called upper Polar Deep Water (uPDW) and create another dense water mass - Norwegian Sea Arctic Intermediate Water (NSAIW) (Jeansson et al. (2017), Table 1.1, Figure 1.5). The Lofoten Basin and Norwegian Basin are basins of the Norwegian Sea, separated by the Jan Mayen Fracture Zone and Vøring Plateau, with the former located to the north and the latter located to the south of these bathymetric features. The origins of the uPDW will be explained later.

Estimates of deep convection rates in the Iceland and Greenland Sea and exports of GSAIW and ISAIW have been difficult to calculate; sea-ice and inclement weather make the necessary winter measurements challenging to obtain. Nevertheless, using Conductivity-Temperature-Depth (CTD) measurements from different seasons, Swift and Aagaard (1981) estimated a minimum combined export of ISAIW and GSAIW of 0.84 Sv. More recent studies estimated a 1 Sv export of GSAIW (Brakstad et al., 2019) and a 2 Sv export of ISAIW (Våge et al., 2015). The exported ISAIW and GSAIW exit the Nordic Seas and propagate southward via the Nordic Seas Overflows. These water masses contribute to the Nordic Seas Overflow east of Iceland (Jeansson et al., 2017) and west of Iceland, i.e. the DSO, via the East Greenland Current (EGC) (Rudels et al., 2002) and the North Icelandic Jet (NIJ) (Harden et al., 2016; Jónsson and Valdimarsson, 2004; Semper et al., 2019; Våge et al., 2011). This contribution was estimated as 0.6 Sv by Tanhua et al. (2005), but is likely more than this given that the NIJ, which transports only ISAIW and GSAIW, transports around 1.8 Sv of DSO source water southward (Semper et al., 2019).

Deep convection in the central Greenland Sea also forms the densest water mass in the Nordic Seas - Greenland Sea Deep Water (GSDW) (Hansen and Østerhus, 2000). GSDW is formed by intense deep convection reaching depths of 3500 m (Malmberg, 1983), it is cold ( $\theta < -1^{\circ}\text{C}$ ) and relatively fresh ( $34.88 < S < 34.90$ ) (Aagaard et al., 1985). However, production of the water mass has stopped since the 1970s (Jeansson et al., 2017). It is too dense to exit the Nordic Seas over the sills, but it contributes to the formation of dense source water masses. Specifically, GSDW mixes isopycnally with Eurasian Basin Deep Water entering the Greenland Sea from the north (Swift

Water mass	Formation region	Formation process	Properties	Overflow it feeds	References
<b>MEIW</b>	East of Iceland	Water mass mixing	$34.7 < S < 34.9$ , $\theta < 3^\circ\text{C}$	IFRO	Read and Pol-lard (1992), Hansen and Østerhus (2000)
<b>NSAIW</b>	NS	Water mass mixing	$34.87 < S < 34.9$ , $27.97 < \sigma_\theta < 28.06 \text{ kg m}^{-3}$	IFRO, FBCO	Hansen and Østerhus (2000), Jeansson et al. (2017)
<b>ISAIW</b>	IS	Deep convection	$\theta < 0^\circ\text{C}$ , $27.97 < \sigma_\theta < 28.01 \text{ kg m}^{-3}$	DSO	Swift and Aagaard (1981), Harden et al. (2016), Jeansson et al. (2017)
<b>GSAIW</b>	GS	Deep convection	$\theta < 0^\circ\text{C}$ , $\sigma_\theta \approx 28.05 \text{ kg m}^{-3}$	DSO	Swift and Aagaard (1981), Jeansson et al. (2017)
<b>NSDW</b>	GS	Water mass mixing	$\theta < -0.5^\circ\text{C}$ , $S \approx 34.91$ , $28.06 < \sigma_\theta < 28.08 \text{ kg m}^{-3}$	IFRO, FBCO	Swift and Koltermann (1988), Hansen and Østerhus (2000)
<b>RAW</b>	Eastern boundary of Nordic Seas	Heat loss to atmosphere	$\theta > 0^\circ\text{C}$ , $\sigma_\theta > 27.8 \text{ kg m}^{-3}$	DSO	Mauritzen (1996), Rudels et al. (2002), Håvik et al. (2019)
<b>AAW</b>	AO - North-east of Barents Sea	Heat loss to atmosphere and mixing of Atlantic water branches	$\theta > 0^\circ\text{C}$ , $\sigma_\theta > 27.8 \text{ kg m}^{-3}$	DSO	Mauritzen (1996), Rudels et al. (1994)
<b>uPDW</b>	Canadian Basin in AO	Warming of deep layer by plumes descending off shelf	$-0.5 < \theta < 0^\circ\text{C}$ , $\sigma_\theta > 27.97 \text{ kg m}^{-3}$	DSO	Rudels et al. (1994), Rudels et al. (2002)

Table 1.1 The formation of dense water masses in the Nordic Seas (Greenland, Iceland and Norwegian Seas) and the overflows they feed. The water mass acronyms are as follows: Modified East Icelandic Water (MEIW), Norwegian Sea Arctic Intermediate Water (NSAIW), Iceland Sea Arctic Intermediate Water (ISAIW), Greenland Sea Arctic Intermediate Water (GSAIW), Norwegian Sea Deep Water (NSDW), Recirculating Atlantic Water (RAW), Arctic Atlantic Water (AAW) and upper Polar Deep Water (uPDW). The location acronyms are: Iceland Sea (IS), Greenland Sea (GS), Norwegian Sea (NS) and Arctic Ocean (AO). The Nordic Sea overflow acronyms are: Iceland-Faroe Ridge Overflow (IFRO), Faroe-Bank Channel Overflow (FBCO) and Denmark Strait Overflow (DSO). This table accompanies Figure 1.5

and Koltermann, 1988). The mixing occurs in the western and southern Greenland Sea and the product is Norwegian Sea Deep Water (NSDW), which acquires a higher temperature ( $\theta = -1^\circ\text{C}$ ) and salinity ( $S=34.91$ ) than Greenland Sea Deep Water before filling the deep Lofoten and Norwegian Basins (both in the Norwegian Sea) where it is found beneath the NSAIW (Swift and Koltermann (1988), Figure 1.5). The Faroe-Bank Channel Overflow (FBCO) transports approximately 2.2 Sv over the Greenland Scotland Ridge and into the Atlantic (Hansen et al., 2016), of which 50% derives from NSAIW and 50% from NSDW (Fogelqvist et al., 2003). Since the NSDW is too dense to contribute to the overflow west of the Faeroes, the total export of NSDW is roughly 1 Sv.

In the mid 1990s, Mauritzen (1996) drew attention to a different process of dense water formation; taking place within the Nordic Seas boundary current. The boundary current circulation in the Nordic Seas is cyclonic with inflow east of the Faroes and outflow west of Iceland (Figure 1.6). The 2.7 Sv inflow through the Faroe-Shetland channel (Berx et al., 2013), feeds the Norwegian Atlantic slope current (NwASC in Figure 1.6). This combines with the Norwegian Atlantic Frontal Current (NwAFC in Figure 1.6) and splits into three branches. Two branches enter the Arctic Ocean: one via the Barents Sea and another on the eastern side of Fram Strait. Dense water is formed along these Arctic Atlantic Water (AAW) pathways and will be discussed later in this section. The third branch retroflects at Fram Strait (around  $79^\circ\text{N}$ ), and turns southward with the East Greenland Current (Figure 1.6).

The properties of this Nordic Seas Atlantic inflow branch are modified alongstream. In the southern Norwegian Sea, Atlantic Water is situated in the  $27.4 \text{ kg m}^{-3} < \sigma_\theta < 27.8 \text{ kg m}^{-3}$  density class increasing to  $\sigma_\theta > 27.9 \text{ kg m}^{-3}$  north of the Lofoten Basin (Mauritzen, 1996), see Figure 1.5). The water mass product is known as Recirculating Atlantic Water (RAW) in the literature. This branch loses heat primarily through atmospheric cooling and freshens due to mixing with the Norwegian coastal current and sea ice melt, becoming denser in the process (Mauritzen, 1996). In the Iceland Sea, at the other end of the circulation, Atlantic Water core densities are predominantly found in the  $27.9 \text{ kg m}^{-3} < \sigma_\theta < 28 \text{ kg m}^{-3}$  density interval (Håvik et al., 2017). This constitutes a total density increase of up to  $0.6 \text{ kg m}^{-3}$  with most of the densification occurring in the Norwegian Basin and Lofoten Basin, hence why the formation of RAW is shown to be on the eastern side of the Nordic Seas in Figure 1.5.

This dense water formation scheme was advocated by two studies using CTD sections between Fram Strait and Denmark Strait. First, Rudels et al. (2002) demonstrated that the mixing of water masses associated with the East Greenland Current was primarily isopycnal between the straits. Second, Håvik et al. (2017) showed that there

was relatively little change in density of the RAW and AAW between Fram Strait and Denmark Strait, implying that most of the required density transformation does indeed occur in the Norwegian and Lofoten basins - as argued by Mauritzen (1996). Despite this, Håvik et al. (2017) demonstrated that the RAW and AAW are cooled and freshened between Fram Strait and Denmark Strait by mixing with Polar origin water masses transported by the EGC. This reduces the temperature of the RAW to close to  $0^{\circ}\text{C}$ , however a  $0^{\circ}\text{C}$  lower limit is usually used to define RAW (Table 1.1). Moreover, this mixing forms fresh pycnocline water ( $S < 34.9$ ), which is dense enough to contribute to the DSO, and is further investigated in Chapter 4.

### Arctic Ocean

Formation of some of the dense water takes place within the Arctic Ocean. This occurs when branches of Atlantic inflow are cooled by the atmosphere and interact with surrounding water masses. Atlantic inflows occur through the Barents Sea and through Fram Strait (Rudels et al., 1994) (Figure 1.6). These inflows transport approximately 2 Sv and 1.25 Sv of Atlantic Water polewards, respectively (Jones, 2001). The Barents Sea inflow is colder than the Fram Strait inflow due to the intense cooling by the atmosphere in the Barents Sea (Jones, 2001). These separate branches merge to the northeast of the Barents Sea and mix, decreasing the temperature of the Fram Strait inflow (Rudels et al., 1994).

These processes create AAW (see Figure 1.5), which recirculates in the Eurasian Basin of the Arctic Ocean and re-enters the Nordic Seas via Fram Strait (Mauritzen, 1996; Rudels et al., 1994). As with the RAW, the AAW is generally defined by temperatures greater than  $0^{\circ}\text{C}$ , which is how it is identified (Table 1.1). The RAW and AAW mix between Fram Strait and Denmark Strait and the water masses are usually not separately distinguishable (Håvik et al., 2019, 2017). AAW is transported by the East Greenland Current from Fram Strait to Denmark Strait, where it contributes to the DSO (Rudels et al., 2002). Using a multi-variate analysis, Tanhua et al. (2005) estimated the Atlantic origin contribution to the DSO (RAW + AAW) as 1.1 Sv.

Another water mass; upper Polar Deep Water (uPDW) is formed primarily in the Canadian Basin of the Arctic Ocean (Figure 1.5, Rudels et al. (2000)). This water mass forms when water on the East Siberian Shelf is cooled and made more saline by atmospheric cooling and brine rejection respectively (Rudels et al., 2000). This dense shelf water forms descending shelf plumes, which entrain AAW and thus warm the layer below (Rudels et al., 1994). The uPDW is defined by low temperatures  $-0.5 < \theta < 0^{\circ}\text{C}$ , high densities  $\sigma_{\theta} > 27.97 \text{ kg m}^{-3}$  (Rudels et al., 2002) and a salinity profile that increases with depth, as opposed to the Arctic Intermediate waters formed

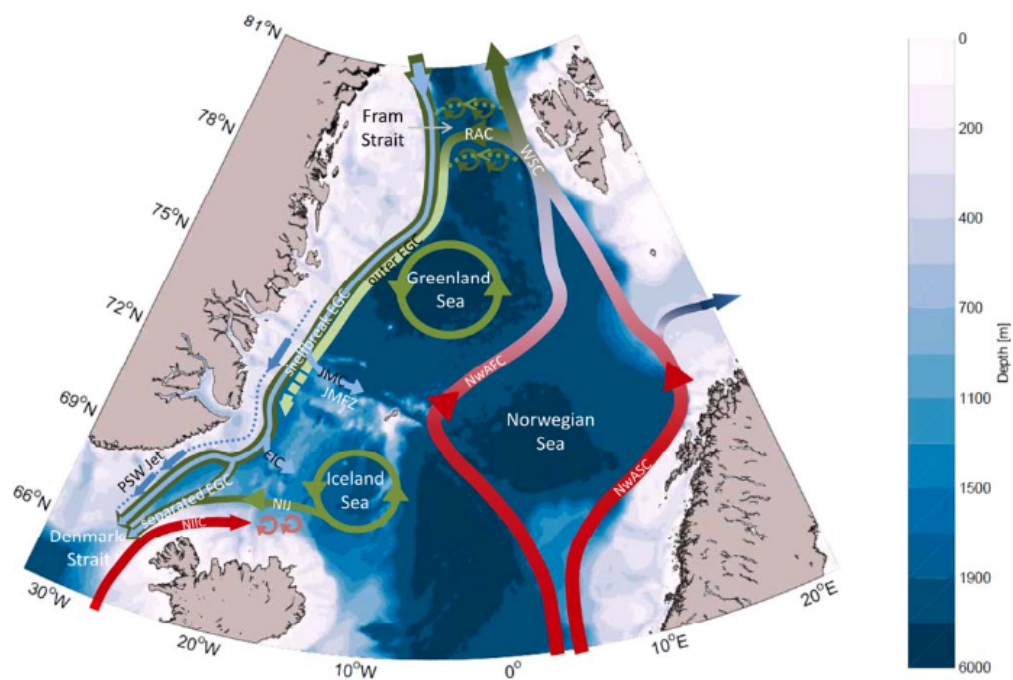


Fig. 1.6 Circulation in the Nordic Seas and formation of dense shelf water. The acronyms are: Polar Surface Water (PSW), East Greenland Current (EGC), North Icelandic Irminger Current (NIIC), North Icelandic Jet (NIJ), Jan Mayen Current (JMC), Jan Mayen Fracture Zone (JMFZ), Returning Atlantic Water (RAW), West Spitsbergen Current (WSC), Norwegian Atlantic Frontal Current (NwAFC) and Norwegian Atlantic Slope Current (NwASC). The red colours represent AMOC upper limb branches whilst green represents lower limb branches and the intermediate colours indicate transition from the upper limb to the lower limb of the AMOC. This Figure is from Håvik et al. (2017) (their Figure 13).

in the Nordic Seas, which have a more homogenous profile (Rudels et al., 1994). The key formation region is on the continental slope around the boundary of the Canadian Basin, east of the Kara Sea, according to Rudels et al. (1994) and Rudels et al. (2000). Once formed, the uPDW circulates around the Canadian basin and flows back in to the Eurasian basin along the North Greenland slope and towards Fram Strait where it enters the Nordic Seas (Rudels et al., 1994). Downstream, the uPDW mixes with GSAIW, enters the Norwegian Sea and makes a dominant contribution to the formation of NSAIW (Jeansson et al., 2017).

Entering the Greenland Sea at Fram Strait above the mid-depth dense water masses is Polar Surface Water (PSW). PSW is formed by the mixing of Atlantic inflow with freshwater (sourced principally from rivers and net precipitation) on the continental shelves and deeper parts of the Arctic Ocean (Rudels, 1989). It is advected from the Fram Strait to Denmark Strait by the EGC (Håvik et al., 2017) and its core is beneath the surface, usually at around 100 m depth (Rudels et al., 2002). The PSW is cold ( $\theta <$

0°C), fresh ( $S < 34.4$ ) and light ( $\sigma_\theta < 27.7 \text{ kg m}^{-3}$ ) and contributes to the overflow west of Iceland only after mixing with denser water masses (Mastropole et al., 2017; Tanhua et al., 2005), therefore it is not included in Table 1.1, which focuses on the dense source water masses of the Nordic Seas overflows.

Polar Intermediate Water (PIW), which apparently originates from the Arctic Ocean thermocline (Rudels et al., 2002), is observed on a mixing line between PSW and RAW/AAW (Tanhua et al., 2005). The PIW is defined by  $\sigma_\theta > 27.7 \text{ kg m}^{-3}$  and  $\theta < 0^\circ\text{C}$  and is situated beneath the PSW within the EGC (Rudels et al., 2002), and is equivalent to the fresh pycnocline water, alluded to above. In the same study, Rudels et al. (2002) argue that PIW forms the fresh lid of the DSO at Denmark Strait (DS) and downstream of DS.

### 1.3.2 Nordic Seas Overflows

The dense water masses formed in the Nordic Seas and Arctic Ocean exit the Nordic Seas via overflows. The Nordic Seas overflows are dense currents that exit the Nordic Seas at depth and enter the northeast Atlantic. The Greenland-Scotland ridge is a bathymetric flow barrier that separates the northeast Atlantic from the Nordic Seas. Deeper channels cut into the ridge are exit points for dense water to overflow the ridge and enter the northeast Atlantic. The three major overflows are: The FBC Overflow, between the Faroe Islands and The Shetland Islands, The Iceland-Faroe Ridge (IFR) Overflow, between Iceland and The Faroe Islands, and the DSO, between Greenland and Iceland (Hansen and Østerhus, 2000). Of the total 6 Sv overflow transport (see Figure 1.4), approximately 2 Sv, 1 Sv and 3 Sv are advected by the FBC Overflow, the IFR Overflow and the DSO respectively (Hansen and Østerhus, 2000). Since the sills, where the overflows exit the Nordic Seas, are located at the summit of the Greenland-Scotland Ridge, the water depth is shallower than the region upstream and downstream. Therefore the overflows are governed by topographic control (Whitehead, 1998). Under topographic control, the volume transport of the overflows is proportional to the height of the dense water interface (head) above sill depth upstream (north) of the sills (Whitehead, 1998).

Traditionally the overflows are distinguished in the North Atlantic by a minimum potential density of  $27.8 \text{ kg m}^{-3}$  (Dickson and Brown, 1994). During their descent, the temperature and volume transport of the overflows increases through entrainment. The FBC overflow is warmed the most, since the entrained water is warmest here (Hansen and Østerhus, 2000). Despite the entrainment of lighter water, the overflows retain their high density signature. The overflows are steered by bathymetry as they descend

deeper into the Atlantic, reaching around 3000 m at the southern tip of Greenland (Cape Farewell) where the different branches converge.

The Denmark Strait Overflow propagates along the southeast Greenland slope, descending from 650 m at the Denmark Strait sill to 3000 m at Cape Farewell. In contrast, the Iceland-Scotland Overflow branches flow westwards to the Rekjanes Ridge and then flow southward along its eastern flank before turning northwards on its western flank (Figure 1.3). Finally it turns westwards to join the Denmark Strait Overflow south of Greenland (Dickson and Brown, 1994). After entrainment the transport of the DSO is 5 Sv, which combines with the Iceland Scotland Overflow Water and Labrador Sea Water resulting in a total transport of 13.3 Sv south of Greenland (Dickson and Brown, 1994).

### 1.3.3 Entrainment

The volume transport of the Nordic Seas overflows increases through entrainment of lighter water. Entrainment is the process whereby lighter ambient water in the pathway of the overflow plumes is incorporated into the dense water plumes. Entrainment is high in specific locations, particularly where the vertical shear of horizontal velocity is high (Koszalka et al., 2017), and where the topography is steeply sloping (Price and Baringer, 1994). Other examples of dense gravity plumes entraining ambient water include the Mediterranean overflow, the Ross Sea overflow and the Weddell Sea overflow (Legg et al., 2009). This section discusses the key entrained water masses and the processes and rates of entrainment that contribute to the formation of NADW.

In the southwest Labrador Sea, hydrographic observations show winter mixed layer depths exceeding 800 m (Lavender et al., 2000). Here, Clarke and Gascard (1983) reported the existence of a recirculating gyre, which traps water and stimulates deep convection. The water mass produced is known as LSW. The formation region is in the southwest Labrador Sea, and not the northwest, northeast or southeast, for two reasons. Firstly, the atmospheric forcing (cold westerlies) is strong (Clarke and Gascard, 1983; Moore et al., 2012) and secondly the preconditioning of the water column is conducive to deep convection (Pickart et al., 2002). On the other hand, deep convection is inhibited in the eastern side of the central basin by a stabilising fresh cap in the surface water column, originating from the West Greenland Current (Pickart et al., 2002) and because the air-sea fluxes are weaker here (Sproson et al., 2008).

LSW is exported away from the Labrador Sea and fills the intermediate depths of the North Atlantic Ocean and is detected by its characteristic low potential vorticity signature (Talley and McCartney, 1982). The potential density of LSW is typically around  $27.7 \text{ kg m}^{-3}$  and therefore it overlies the Nordic Seas overflows which are found

beneath the  $27.8 \text{ kg m}^{-3}$  isopycnal (Dickson and Brown, 1994). When the overflows travel around the northern and western boundary of the North Atlantic they encounter and entrain LSW east of Greenland (McCartney, 1992) and in the Labrador Sea itself (Pickart et al., 2002), thereby increasing NADW transports.

Another important entrained water mass is Middle Irminger Water (MIW). MIW originates from the Iceland basin; it is derived from the Gulf Stream and Africa Water advected northwards along the African and European continental shelves (Van Aken and De Boer, 1995), and is transported westward across the Reykjanes Ridge and into the Irminger Basin before it is entrained into the DSO (Tanhua et al., 2008). In the Irminger Basin, it is typically found at a depth of around 1000 m and is relatively warm  $\theta > 3.5$  °C with a potential density of around  $27.76 \text{ kg m}^{-3}$  (Tanhua et al., 2008). Using an optimum multi-parameter analysis on hydrographic and chemistry data from the DSO, Tanhua et al. (2008) argue that entrainment of MIW dominates the entrainment into the DSO in the initial 400 km downstream of DS, with entrainment of LSW becoming more important beyond this point.

Entrainment is driven by vertical and horizontal mixing processes. For the DSO, lateral stirring by eddies and shear driven vertical turbulent mixing both play a role in driving entrainment (Voet and Quadfasel, 2010). Voet and Quadfasel (2010) argued that the lateral eddy stirring mechanism is dominant beyond 200 km downstream of the DS, but could not account for the rapid rate of warming ( $0.4$  or  $0.5$  °C/100 km) within 200 km of Denmark Strait alone (Figure 1.7). Therefore vertical shear driven turbulent mixing must play a key role between Denmark Strait (DS) and 200 km downstream. The vertical shear is increased by the surface intensified EGC/Irminger current, cyclonic eddies and the bottom intensified DSO, all of which contribute to the vertical turbulent mixing in the water column (Voet and Quadfasel, 2010). Price and Baringer (1994) proposed that entrainment is amplified in locations of steeply sloping topography where the plume speeds are highest, since vertical shear driven turbulent mixing is enhanced. The theory also predicts that entrainment is typically highest close to the point of overflow (the sill point) (Price and Baringer, 1994). This is also supported by observational evidence for the overflows west (Voet and Quadfasel, 2010) and east (Kanzow and Zenk, 2014) of Iceland.

Entrainment increases the volume transport and temperature of the overflows. The initial entrainment into the DSO is up to 2 Sv for the DSO (Dickson and Brown, 1994) and 1 Sv for the Iceland-Scotland Overflow Water (FBCO + IFRO) (Kanzow and Zenk, 2014). This constitutes a 50% increase in the volume transport of the overflows from 6 Sv to 9 Sv. Further entrainment is likely, since the volume transport at the southern tip of Greenland is estimated at 13 Sv by Dickson and Brown (1994).

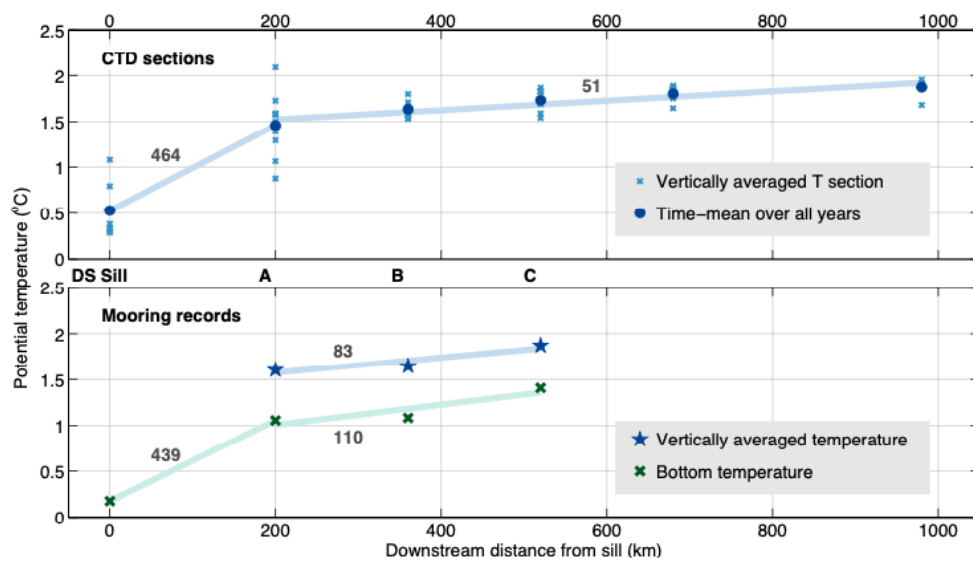


Fig. 1.7 Temperature of the DSO as function of distance downstream from DS. The top panel shows the DSO temperature from CTDs and the bottom panel shows the DSO temperature from moorings. The numbers indicate the warming rate (in mK/100 km). This Figure is from Voet and Quadfasel (2010); their Figure 5.

Furthermore, the entrainment of LSW in the Labrador Sea (Pickart et al., 2002) increases the volume transport of NADW. The total AMOC volume transport is approximately 15 Sv, according to Lozier et al. (2017) using data from the OSNAP array located at approximately 57°N.

## 1.4 The Denmark Strait Overflow

Of all the overflows, the Denmark Strait Overflow (DSO) makes the greatest contribution to the formation of NADW (Dickson and Brown, 1994). It also forms the deepest, densest component of NADW (Dickson et al., 2008). The DSO derives from dense water formed in the Nordic Seas and Arctic Ocean (Table 1.1 and Figure 1.5), and its variability reflects variations in the contributions of the different source water masses. In this section, first the characteristics and second the variability of the DSO are discussed. The particular focus of this section is the seasonal to multi-annual property variability of the DSO; thus the current knowledge of this variability is summarised, leading to the identification of key research questions relevant to this thesis.

### 1.4.1 Sources and characteristics

Investigating Sulfur hexafluoride ( $\text{SF}_6$ ) versus density profiles, Dickson et al. (2008) showed an increase for water denser than  $27.85 \text{ kg m}^{-3}$  indicative of the more recently ventilated DSO (compared with the overflows east of Iceland). Therefore Dickson et al. (2008) used this isopycnal as a clearer indication of the component of the DSO that had originated from DS. Nevertheless, the  $27.8 \text{ kg m}^{-3}$  isopycnal is used to define DSO in this thesis, for consistency with the literature (e.g. Harden et al. (2016)). The DSO is also the coldest  $\theta < 2.5^\circ\text{C}$  (Voet and Quadfasel, 2010) and deepest component of NADW. It is slightly fresher ( $S \approx 34.89$ ) than the overlying Iceland Scotland Overflow Water (ISOW), likely due to the addition of fresh Greenland shelf water, originating from the Arctic Ocean, cascading off the shelfbreak and joining the DSO and due to reduced entrainment compared with the overflows east of Iceland (Dickson et al., 2008).

Dense water is delivered to Denmark Strait (DS) from the north via currents along the Greenland and Iceland continental slopes. This is illustrated in Figure 1.8a, which shows the 2011-12 mean velocities across the Kögur array (KGA), a set of moorings deployed 200 km upstream of DS (Harden et al., 2016). The EGC forms around Fram Strait (at  $80^\circ\text{N}$ ) and flows southward along the East Greenland shelfbreak splitting into two branches: the Shelfbreak EGC and the Separated EGC at  $69^\circ\text{N}$ , which both flow towards DS (Våge et al. (2013), Figure 1.8b).

The NIJ emerges northeast of Iceland and flows westward towards DS along the Iceland continental slope and its volume transport increases en-route through entrainment (Semper et al., 2019). The mean volume transports between 2011-12 were 2.5 Sv for the EGC and 1 Sv for the NIJ (Harden et al., 2016), but CTD snapshots between 2004 and 2018 suggest NIJ transports may be higher at other times (Semper et al., 2019).

The densest DSO source water is Arctic Intermediate Water (AIW) ( $\sigma_\theta > 28 \text{ kg m}^{-3}$ ), which is derived from GSAIW and ISAIW formed in the Greenland and Iceland seas respectively (Table 1.1 and Figure 1.5), and advected towards DS primarily by the NIJ (Våge et al., 2011). This water mass dominates the trough at DS, which is the deepest part of the DS (Figure 1.9), according to a study using an end-member analysis of repeat CTD sections at DS (Mastropole et al., 2017). Dense ( $\sigma_\theta > 27.8 \text{ kg m}^{-3}$ ) Returning Atlantic Water (RAW) (derived from AAW and RAW: see Table 1.1 and Figure 1.5) is transported by the EGC from Fram Strait to DS (Håvik et al., 2017; Rudels et al., 2002). This water mass is found in near-bottom regions of DS on the Greenland side of the section, above the above the dense AIW in the trough Figure 1.9. These two water masses (AIW and RAW) are the two most important sources of the DSO at DS (Mastropole et al., 2017).

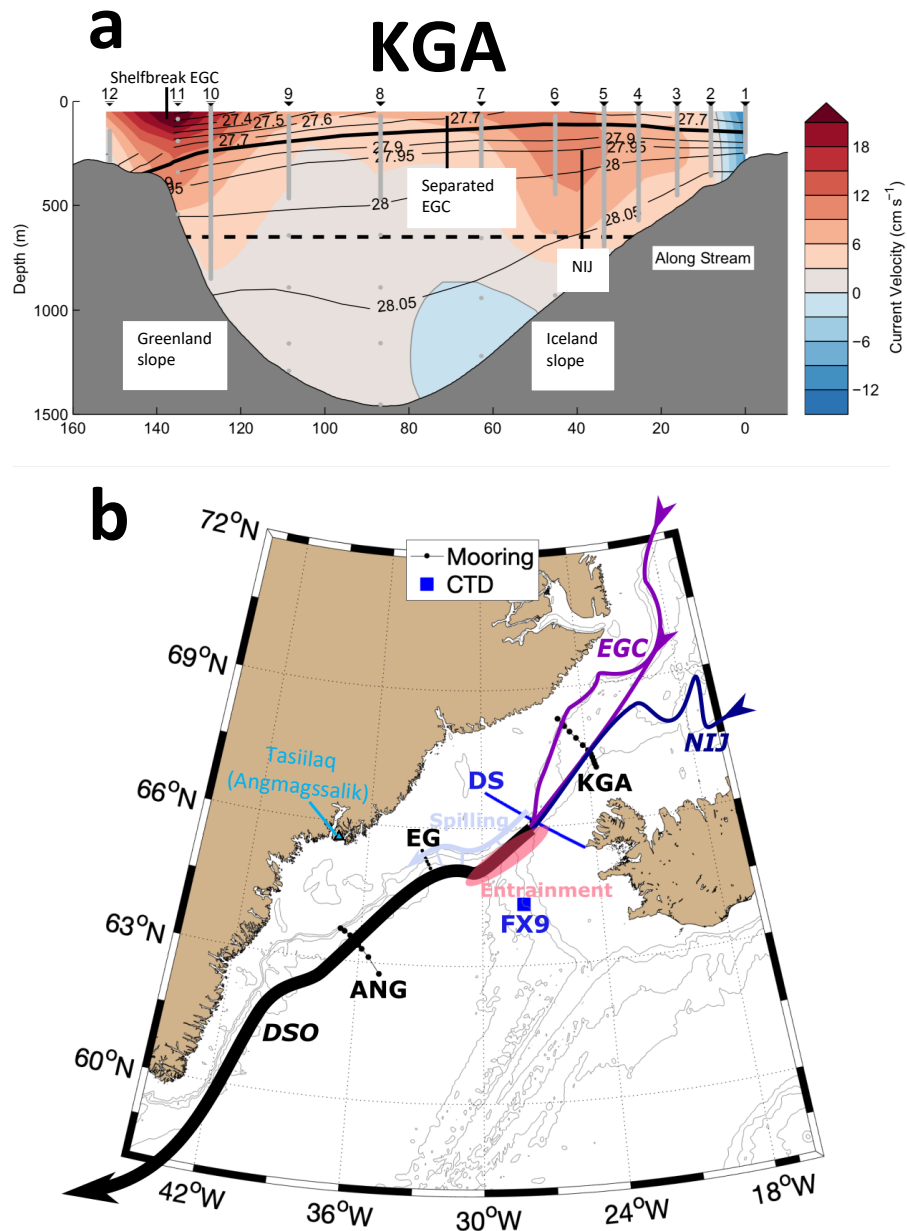


Fig. 1.8 a) The mean along-stream velocity at the Kögur array (KGA) in 2011-12. Note that while positive=northward is the convention, in this case positive=southward. The numbers at the top and the lines and dots beneath indicate the position of the moorings and the black lines are potential density contours (thick line is  $27.8 \text{ kg m}^{-3}$  isopycnal). b) Map of the ocean circulation of the sources of DSO and the pathway of the DSO. The current acronyms (in italics) are as follows: East Greenland Current (EGC), North Icelandic Jet (NIJ) and Denmark Strait Overflow (DSO). The other acronyms are Denmark Strait (DS), East Greenland Spill Jet section (EG), Faxaflói station 9 (FX9) and Angmagssalik array (ANG). The blue squares denote CTD stations (i.e. hydrographic stations) and the black circles denote mooring stations. The thin grey lines are 500 m, 1000 m, 1500 m and 2000 m isobaths, from the GEBCO\_2014 grid (Arndt et al., 2013). Panel a) is adapted from Harden et al. (2016); their Figure 5a.

Additionally, Mastropole et al. (2017) demonstrated a contribution from lighter source waters, found in the upper layers of the DSO at DS (Figure 1.9). Higher concentrations of the Irminger Current Water are found over the Greenland shelf and Iceland slope (Figure 1.9). This supports the findings of a study which used numerical particle tracking simulation to argue that around 16% of the DSO at DS is composed of Irminger Current Water which gets entrained into the DSO. Tanhua et al. (2008) argued that it is the denser Irminger current water - MIW - which contributes to the DSO.

The dense water found on the Greenland shelf is an admixture of these two water masses (Figure 1.9). This water contributes to the DSO downstream of DS after spilling off the shelfbreak (Brearley et al., 2012; Falina et al., 2012; Koszalka et al., 2013). Low salinity water in the stratified upper layers of the DSO was documented by Rudels et al. (2002), who termed this feature the 'fresh lid' of the overflow, and demonstrated that this feature descends the Greenland slope with the DSO plume, and is observed

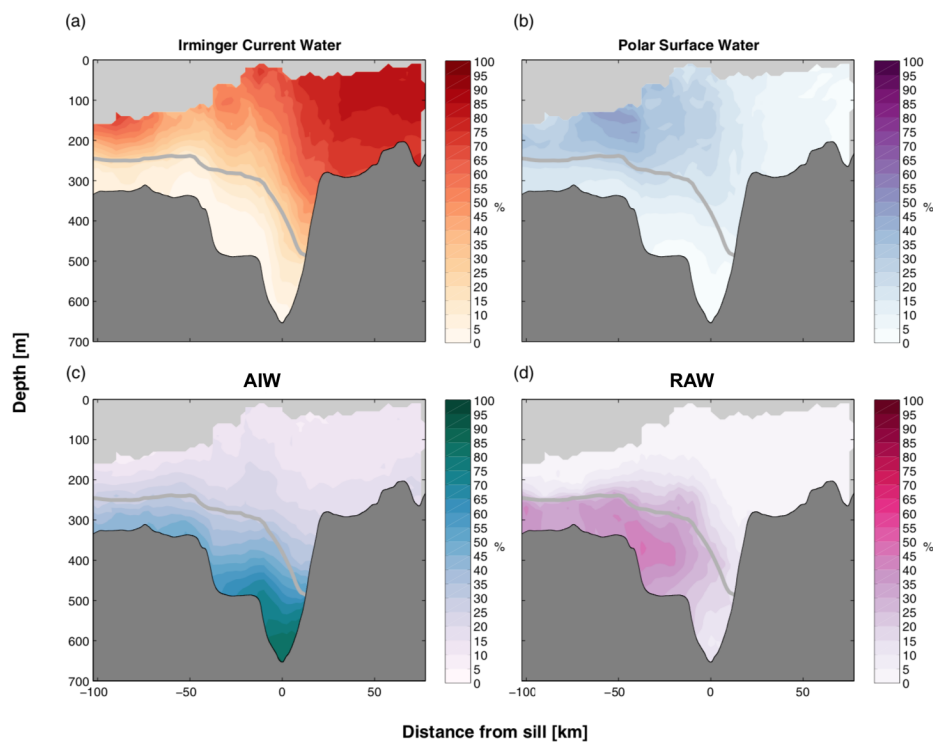


Fig. 1.9 Distribution of DSO source water masses at DS (for location of section, see Figure 1.8b), from an end member analysis of repeat CTD sections. The thick grey line indicates the depth of the  $27.8 \text{ kg m}^{-3}$  isopycnal, which is traditionally used as the upper boundary of the DSO. The water mass end-members are a) Irminger Current Water ( $\theta = 6.97^\circ\text{C}$ ,  $S = 35.07$ ) b) Polar Surface Water ( $\theta = -1.42^\circ\text{C}$ ,  $S = 34.07$ ), c) AIW ( $\theta = -0.63^\circ\text{C}$ ,  $S = 34.92$ ), d) RAW ( $\theta = 2.50^\circ\text{C}$ ,  $S = 34.98$ ). For derivation of the end-members, see Mastropole et al. (2017), from which this figure is adapted (their figure 8).

downstream of DS on the Greenland slope in the Irminger Basin. The PSW and RAW are the two main water masses transported by the EGC from Fram Strait to DS (Håvik et al., 2017). The contribution of this fresher water, found in the stratified lighter layers of the DSO, to the DSO is a particular focus of this thesis.

The time-mean DSO volume transport through the DS section between 1995 and 2015 was 3.2 Sv (Jochumsen et al., 2017), consistent with the earlier estimate by Dickson and Brown (1994) of 2.9 Sv. Downstream, DSO transports increase rapidly to 5 Sv at Dohrn Bank, 160 km south of DS, due to entrainment (Dickson and Brown, 1994). Once the ISOW merges with the DSO near the southern tip of Greenland, there is isopycnal mixing between the overflows, causing the lighter classes of DSO to warm and salinify (Dickson et al., 2008) upstream of Cape Farewell where the OSNAP array is deployed. The total southward transport of NADW around the southern tip of Greenland is 13 Sv (Dickson and Brown, 1994). However, the DSO varies on multiple different timescales, and this variability is described below.

## 1.4.2 Temporal variability

### Intra-seasonal timescales

Firstly, on short timescales (daily-weekly), Harvey (1961) identified exceptionally thick lenses of very cold and dense water at the Denmark Strait sill. More recently, von Appen et al. (2017) demonstrated the existence of two distinct types of high frequency variability at the Denmark Strait sill. One was consistent with previous observations of a thickening of the cold and dense layer (a bolus). The other type of variability involved a thinning of the cold and dense near bottom layer and flow acceleration (a pulse). Both boluses and pulses increase the DSO transport by around 30-40% (von Appen et al., 2017). Note that pulses increase the volume transport through higher southward velocities of the current.

The formation and downstream propagation of the deep boluses and pulses is in phase with intermediate depth cyclonic eddies (von Appen, 2013). Cyclonic eddies were shown to increase the entrainment of warmer lighter water into the DSO (Figure 1.8b) by increasing the vertical shear of horizontal velocity, and through horizontal stirring (Koszalka et al., 2017; Voet and Quadfasel, 2010).

The formation of the cyclonic eddies is governed by water column stretching of intermediate layers when the overflow descends over the sill into deeper water (Spall and Price, 1998; von Appen, 2013). This process imparts cyclonic relative vorticity to the intermediate water column to conserve angular momentum, thus creating the cyclones (von Appen, 2013). Another forcing mechanism at play here is baroclinic instability.

Baroclinic instability is high around the DSO interface, increasing the potential for perturbations to evolve into eddies (which could be cyclonic or anti-cyclonic) (Jungclauss et al., 2001). However, the fact that the observed mesoscale eddies are always cyclonic (von Appen, 2013) implies that water column stretching is the main mechanism, because baroclinic instability does not preclude the formation of anti-cyclonic eddies. Fischer et al. (2015) investigated the high frequency velocity variability of NADW, from the southeast Greenland slope to the northwestern boundary of the Atlantic around the tail of the Grand Banks. This paper showed the dominant period of variability of 10 days at most of the locations, which was linked to topographic Rossby waves formed due to the mesoscale processes discussed above.

Using measurements of salinity and dissolved oxygen, Falina et al. (2012) identified shelf water in the DSO south of DS in 3 out of 11 CTD sections analysed, and calculated that individual freshening events can contribute up to 25% to DSO transports. The fresh dense shelf water source of DSO is represented schematically in Figure 1.8b (see grey/blue line and arrows). However, the contribution of this water to the volume transport of the DSO varies substantially on synoptic timescales (Brearley et al., 2012; Falina et al., 2012). Furthermore, the contribution of the shelf water to the volume transport of the DSO on different timescales is not well known. Below, the variability of the DSO on longer timescales is discussed.

### **Seasonal to multi-annual timescales**

On seasonal timescales, variability of the DSO volume transport at DS is very weak, according to Jochumsen et al. (2017), who used multiple years of mooring data at DS. This supports Dickson and Brown (1994), who demonstrated the lack of seasonal signal in DSO velocity using moorings downstream of DS. Using the same moorings at DS, Jochumsen et al. (2017) also showed that the DSO volume transport exhibits weak interannual variability; the range in annual mean transport is around 0.4 Sv, but there has been no sustained trend (Figure 1.10). Also shown in Figure 1.10 is the FBC overflow transport time series, which has a time-mean of 2.2 Sv and similarly no long term change (Hansen et al., 2016). Note that between 1996 and 2002 the time series appear anti-correlated, whilst the time series are correlated between 2007 and 2013 (Figure 1.10), however the correlation between the full time series is not statistically significant (Jochumsen et al., 2017).

Conversely, the southward volume transport of the DSO source water branches 200 km north of DS, through KGA (Figure 1.8), exhibited seasonality between 2011-12 (Harden et al., 2016). Specifically, the Shelfbreak EGC was enhanced in the winter and weaker in summer, and the NIJ was weaker in winter and enhanced in summer. The

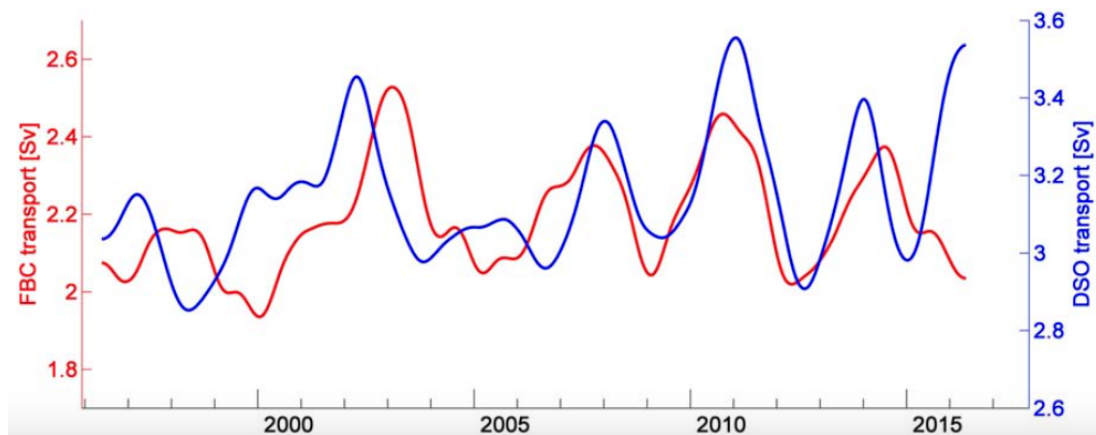


Fig. 1.10 Time series between 1996 and 2015 of the volume transport of the DSO (blue) and Faroe-Bank Channel (FBC) overflow (red) calculated from mooring observations. The time series are smoothed using a fourth order Butterworth Filter with a 2 year low pass frequency cut off. The units are Sv ( $1 \text{ Sv} = 10^6 \text{ m}^3 \text{ s}^{-1}$ ). This is Figure 14 from Jochumsen et al. (2017).

seasonality of the different branches compensated each other, and as a result the net southward volume transport of the source water only exhibited a very weak seasonal cycle, which is consistent with the lack of strong seasonality in the volume transport of the DSO through DS (Jochumsen et al., 2017). It is important to note that the variability of the DSO sources, demonstrated by Harden et al. (2016), was only based on one year of data, which may not be representative of other years.

A number of previous studies have identified property variability of the DSO on seasonal to multi-annual timescales. Looking at the property variability in source waters of the DSO at Angmagssalik (ANG) (see location of array in Figure 1.8b) using an end-member analysis, Jochumsen et al. (2015) found that fresh water derived from the EGC is enhanced in summer; warm and saline entrained water from the Irminger Basin (i.e. MIW) is enhanced in winter and the deep, densest DSO sourced NIJ waters does not exhibit seasonality. This is consistent with the observation made by Dickson et al. (2008), who noted the seasonal dependence of negative salinity anomalies in the DSO at ANG, but did not investigate further. However, the question of whether the DSO exhibits a robust, statistically significant seasonal cycle remains unresolved.

Some studies have identified sustained negative property anomaly events in the DSO at ANG. Firstly, Hall et al. (2011) highlighted anomalously negative salinity anomalies in the DSO at ANG in 1999 and 2004. Yashayaev and Dickson (2008) described the occurrence of negative salinity and temperature anomalies at ANG, which were advected around Cape Farewell, and into the Labrador Sea up to 1 year afterwards. Furthermore, Yashayaev and Dickson (2008) demonstrated that the size of the anomalies

were not reduced downstream, suggesting limited mixing between the DSO and ISOW or LSW. This shows that the advection of property anomalies in the DSO could be used as evidence of the interaction between the dense water masses which form the NADW. However, the origins of the DSO property variability on seasonal to multi-annual timescales has not been established to date.

Many possible mechanisms explaining the seasonal and multi-annual property variability of the DSO have been proposed, however a rigorous assessment of their different contributions to the DSO properties has not been carried out to date. Evidence is required to: a) verify the occurrence of the mechanism and b) quantify the role of the mechanism in causing DSO property variability on these timescales. This thesis is a contribution towards that effort. Nevertheless, previous investigators have proposed some candidate mechanisms, which serve as a starting point for this investigation and, therefore, these will be described below.

Some studies emphasise the role of wind forcing in causing DSO salinity variability and speculate about the wind-driven ocean processes that connect cause and effect. Both Hall et al. (2011) and Holfort and Albrecht (2007) suggest that strong winds enhance the contribution of fresher DSO source water (via the EGC) to the DSO, causing freshening. Focusing on the northeast Greenland continental margin, around 75°N, Hall et al. (2011) argued that northerly winds drive onshore flow in the surface Ekman layer, which sets up an enhanced onshore Sea Surface Height (SSH) gradient, in turn enhancing the barotropic component of southward flow. Contrastingly, Holfort and Albrecht (2007) emphasise the role of northeasterly winds through DS (66°N) driving freshening. Alternatively, Harden et al. (2016) argue that the sign of the wind stress curl in the Blosseville Basin determines whether the local ocean circulation is cyclonic or anti-cyclonic, and that drives the seasonal volume transport of the DSO source water branches through KGA, described above. This could drive seasonality of the properties of the DSO downstream, because the different source water branches have different properties (Harden et al., 2016).

One meteorological phenomena that impacts on the ocean in the region are northeasterly barrier winds (Figure 1.11). Barrier winds occur because the mountains on the east Greenland coast block the flow of air, causing convergence and enhancing the pressure gradient force perpendicular to the coast, in turn causing acceleration of along coast wind speed around DS (Harden et al., 2011) (Figure 1.11). When the barrier wind events are particularly intense, or frequent, the wind forcing through DS will strengthen, and Holfort and Albrecht (2007) argued that this would result in negative salinity anomalies in the DSO downstream, in the Irminger basin. Also, Harden et al. (2011) showed that

the number of barrier wind events each month is positively correlated ( $r=0.57$ ,  $p<0.01$ ) with the monthly North Atlantic Oscillation (NAO) index.

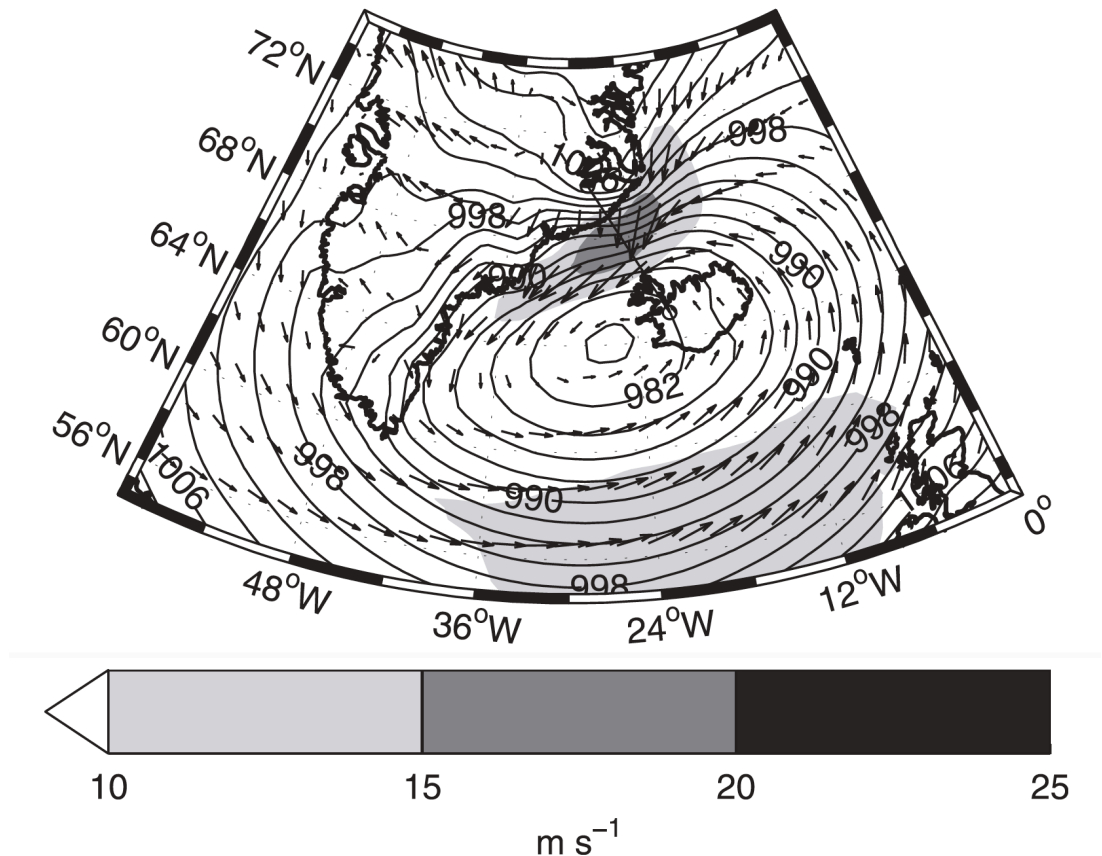


Fig. 1.11 Map of sea level pressure (black contours; in hPa), wind speed (shaded area) and wind direction (both in  $\text{m s}^{-1}$ ) for a barrier wind event composite. The thin black line indicates the location of the maximum wind forcing in the composite. The sea level pressure minimum is the Icelandic low, the centre of action in the region. The data are from ERA-Interim, and the figure is adapted from Harden et al. (2011); their Figure 8.

The NAO index is defined as the normalised sea level pressure difference between Iceland and the Azores (Jones et al., 1997). The variability of the NAO index has also been linked with variable contraction and expansion of the subpolar gyre, which can cause changes to the temperature and salinity of the DSO, and the overflows east of Iceland (Sarfanov, 2009). The two large scale atmospheric patterns investigated in this thesis are the NAO and the Iceland-Lofoten Difference (ILD) pattern, which is defined by the normalised pressure difference between the Lofoten Islands, off the northwest coast of Norway, and Iceland (Jahnke-Bornemann and Brümmer, 2008). It is not currently known what role, if any, these atmospheric patterns have on the property

variability of the DSO. This is one of the research problems which this thesis aims to investigate.

The cold season NAO exhibits multi-decadal variability, for example in the 1950s and 1960s the NAO was consistently in a negative phase whereas in the 1980s and early 1990s the NAO was in a sustained positive phase (Hurrell, 1995). After a period of generally weak NAO index winters between 1999 and 2008, there were strongly negative NAO winters in 2009-10, 2010-11 and 2012-13, and strongly positive NAO winters in 2011-12, 2013-14 and 2014-15 (González-Pola et al., 2019) (see also Figure 5.2e). Accordingly, winter wind speeds are autocorrelated on multi-annual timescales, e.g. winters with strong winds tend to occur successively. One of the key drivers of variability on interannual to multi-decadal timescales is the meridional shifting of the storm tracks, which is influenced by atmospheric blocking systems (Woollings et al., 2015). During a positive NAO phase, atmospheric blocking (typically anticyclonic circulation) is weakened over Greenland and strengthened in the lower latitude North Atlantic (e.g. the Azores) displacing the storm track northwards (Woollings et al., 2015).

Alternatively, it is possible that other mechanisms, unrelated to wind forcing, are the most important mechanisms for determining the temperature and salinity of the DSO. Jochumsen et al. (2015) attribute the seasonality of DSO properties to the variability of the warm inflow of the Irminger Current at DS. This supports a previous hypothesis, suggested by Rudels et al. (2002). It is also possible that the seasonal variability of the DSO properties are driven by seasonality of MIW properties, because this water mass also makes an important contribution to the DSO (Tanhua et al., 2008). Specifically, MIW is one of the key water masses which is entrained into the DSO in the Irminger basin (Tanhua et al., 2008), and any property variability of this water mass will likely imprint on the DSO.

### **Multi-decadal timescales**

As previously stated, climate models predict that reduced NADW formation will cause AMOC to weaken in the next one or two centuries (Cheng et al., 2013; Weaver et al., 2007). Some studies propose that multi-decadal AMOC weakening has already taken place (Caesar et al., 2018). One possible cause of AMOC weakening is DSO weakening. However, the volume transport of the DSO shows no signs of weakening between 1996 and 2015 (Figure 1.10), according to volume transport estimates based on ADCP observations (Jochumsen et al., 2017).

Conversely, the properties of the DSO have exhibited more sustained trends (i.e. on multi-annual timescales), for example freshening between the 1960s and 2000 which amounted to a salinity reduction of around 0.04 (Dickson et al., 2002). The sustained

freshening of the DSO, which was also observed in the FBC overflow, was linked to freshening in the upper 1500 m of the Nordic Seas, believed to be caused by changing components of the Nordic Seas freshwater balance (Dickson et al., 2002). For example, increased input of sea ice from the Arctic Ocean and increased precipitation along the Norwegian Atlantic current were both proposed as potential causes (Dickson et al., 2002). This trend was followed by almost a decade of increasing salinity (Dickson et al., 2008). Reflecting this latter trend, there was a warming and salinification of the ISOW and intermediate water masses of the Irminger and Iceland Seas between the late 1990s and mid 2000s (Sarafanov et al., 2007). Therefore, sustained property changes of the DSO may reflect large scale changes in the ocean circulation in the subpolar North Atlantic.

In summary, the DSO is a key contributor to NADW, which is fed by dense water from the north via the EGC and NIJ. The main dense water masses are AIW and RAW, but there is also a contribution from lighter and fresher overlying water. The lighter water overlying the EGC, which is considered dense enough to contribute to the DSO, is particularly fresh, and is likely an admixture of PSW and RAW. The temperature and salinity of the DSO has been shown to vary from year-to-year by multiple previous studies. However, the nature and origins of seasonal property variability are unknown. To address this uncertainty is the central focus of this thesis. The thesis is oriented around some key research questions, which are outlined below.

## 1.5 Research questions

The research questions regarding the DSO that this thesis aims to address are as follows:

1. What is the spatiotemporal variability of its properties on seasonal timescales?
2. What role do salinity and temperature play in controlling its density variability?
3. What processes cause sustained intra-annual freshening, where do they occur, and how?
4. How does the variability of the ocean circulation north of DS affect its salinity?
5. How do large scale atmospheric patterns influence its salinity variability?
6. What is the influence of sea ice concentration variability on its salinity variability?

## 1.6 Thesis outline

In the next chapter (Chapter 2), the observational data used to investigate the research questions posed above, are introduced. Here, deployment of moorings at the DS, north of DS and south of DS, and the atmospheric reanalysis product are all summarised, and the processing and analysis techniques used on the data are detailed. In Chapter 3, the variability of DSO properties on seasonal timescales is characterised in detail. The objective of this chapter is to address questions 1 and 2 above. This involves quantifying the spatial and temporal variability of temperature and salinity, and investigating their competing effects on density variability on timescales beyond the eddy period. The eddy period is 5-10 days, and is identified as the spectral peak in the DSO velocity time series at ANG and DS, and other locations in the Irminger Basin, corresponding to mesoscale eddies which form close to DS and travel southward in conjunction with the DSO (Fischer et al., 2015; Jochumsen et al., 2015).

In Chapter 4, the multiple different candidate oceanographic mechanisms that may cause sustained seasonal freshening of the DSO are examined. Here, data from the Greenland shelf and slope 200 km upstream of DS are used in conjunction with local atmospheric reanalysis data to identify and characterise the freshening mechanisms and their contribution to the seasonal freshening of the DSO, thus investigating questions 3 and 4 above. In Chapter 5, the relationship between remote wind forcing and the variability of DSO salinity is investigated. Here, the influence of large scale atmospheric patterns and sea ice concentration variability on the DSO salinity variability is explored, and thus questions 5 and 6 are investigated. Finally, in Chapter 6, the implications of the new insights presented in this thesis are explored and areas for future research are identified.

# Chapter 2

## Data and methods

In this thesis, data from four different mooring arrays, two CTD sections and one atmospheric reanalysis product are used to investigate the property variability of the DSO. The data cover a large region east of Greenland (Figure 1.8), in locations important to the formation of the DSO and thus to the AMOC. An ambitious synthesis of various different datasets from a large region is carried out in this study, to better understand the formation and variability of the DSO. This is the unique approach of this study. For example, mooring and hydrographic section data from upstream of DS (Figure 1.8) are investigated and linked to the variability 500 km downstream of the DS at the Angmagssalik array (named from the old Danish name marked on GEBCO 1978 charts of the nearby settlement that is now known as Tasiilaq) at  $63.5^{\circ}\text{N}$  to gain insight into the formation and advection of salinity signals in the DSO. Further, insights from these data may help towards the interpretation of AMOC variability observed downstream of the ANG at, for example, the North Atlantic cross basin arrays: the OSNAP at approximately  $60^{\circ}\text{N}$  and the RAPID array at  $26.5^{\circ}\text{N}$ . An overview of the datasets used in this thesis is presented in Table 2.1.

Firstly, the ANG is introduced in Section 2.1. The time series recovered from ANG are unique in their length, since moorings were deployed there between 1986 and 2015. Sixteen years of conductivity and salinity from Sea Bird Electronics (SBE) MicroCAT (MC) instrument deployments, between 1998 and 2015, are calibrated systematically using CTD casts and the procedure is described in this section. In section 2.2, the upstream mooring arrays and CTD sections are introduced and the data used from these locations are described. Finally, in Section 2.3, the ECMWF Reanalysis 5 (ERA5) is introduced.

Name (location)	Time period	Variables	Source/provider	QC and calibration reference	Funding
ANG (63.5°N 36°W)	1998- 2015	Ocean properties and velocity	S. Dye	This thesis	Cefas, UoH, FIMR
DS <sup>2</sup> (66°N 27°W)	2005- 2015	Ocean properties	K. Jochumsen	Jochumsen et al. (2015)	MRI, UoH
ERA5 (northeast Atlantic + Nordic Seas)	1998- 2015	Wind speed and direction (at 10 m), sea level pressure and sea ice concentration	<a href="https://cds.climate.copernicus.eu/">https://cds.climate.copernicus.eu/</a>	Hersbach et al. (2020)	EU
FX9 (64.3°N 28°W)	1989- 2019	Ocean properties	M. Danielsen	M. Danielsen (pers. comms.)	MRI
KGA (67.6°N 24°W)	2011- 2014	Ocean properties and velocity	<a href="http://kogur.whoi.edu">http://kogur.whoi.edu</a>	Harden et al. (2016), L. de Steur: Pers. Comms., this thesis	WHOI, MRI, NIOZ, UiB
Látrabjarg section (66°N 27°W)	1990- 2018	Ocean properties	<a href="http://kogur.whoi.edu">http://kogur.whoi.edu</a>	von Appen et al. (2014), Mastropole et al. (2017), Lin et al. (2020)	MRI
Spill Jet section (65°N 33°W)	2007- 2008	Ocean properties	R. Pickart	von Appen et al. (2014), this thesis	WHOI

Table 2.1 Overview of the datasets used in this thesis. Ocean properties refers to potential temperature, salinity and potential density. The acronyms for the dataset names are given in Figure 1.8. The other acronyms are as follows: Centre for the Environment, Fisheries and Aquaculture Science (Cefas), University of Hamburg (UoH), Finnish Institute of Marine Research (FIMR), Marine Research Institute, Iceland (MRI), European Union (EU), Woods Hole Oceanographic Institute (WHOI), Royal Netherlands Institute for Sea Research (NIOZ), University of Bergen (UiB).

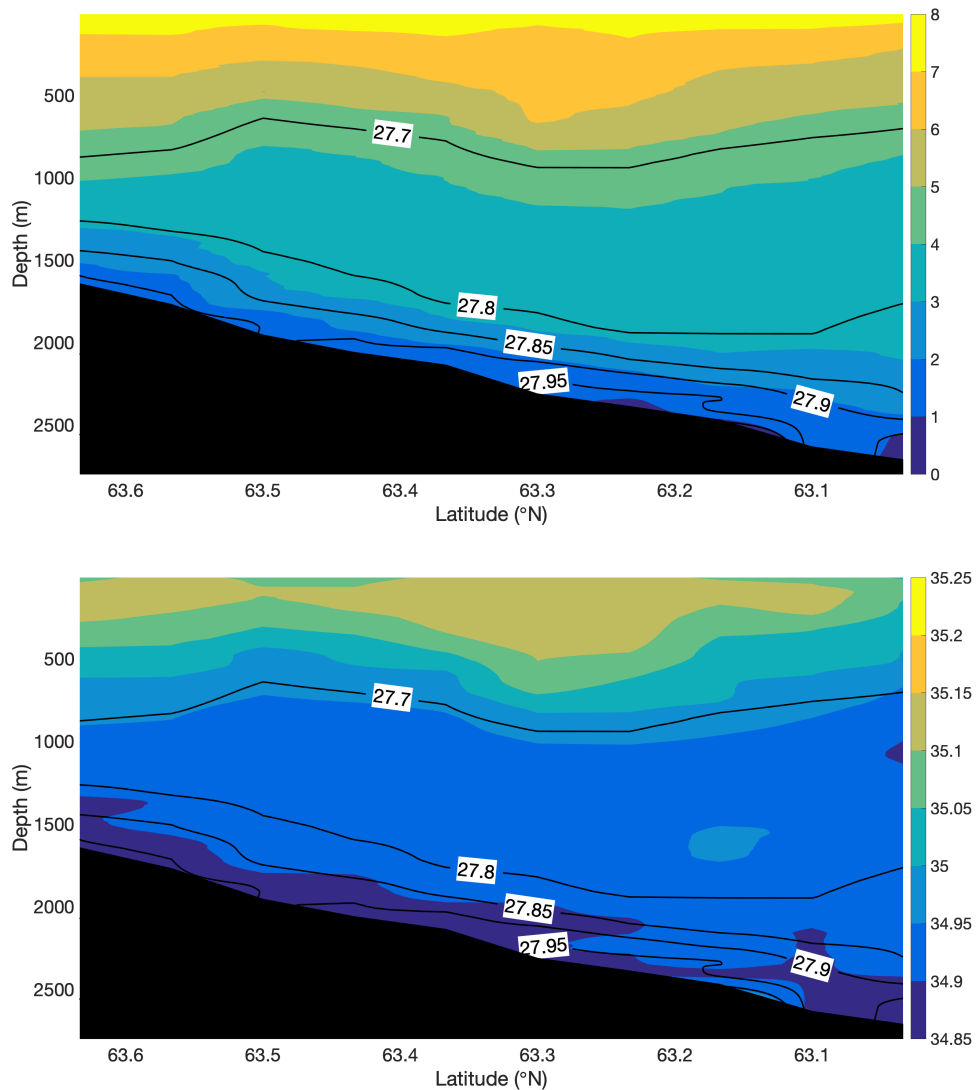


Fig. 2.1 Vertical sections of potential temperature (in  $^{\circ}\text{C}$ ) (top) and salinity (bottom) during a CTD section crossing of ANG in August 2011 (see cruise report: (Karstensen, 2013)). The thick black lines are isopycnals of potential density (in  $\text{kg m}^{-3}$ ). The DSO is the freshest, coldest and densest water at the near-bottom.

## 2.1 The Angmagssalik array

### 2.1.1 Background

In 1986, near-bottom oceanographic moorings were first deployed on the Greenland continental slope at  $63.5^{\circ}\text{N}$  (ANG) (Figure 1.8). The rationale of the mooring deployments was to quantify the volume and heat transport of the deep branch of the AMOC, and to better understand its variability on annual-interannual timescales. Before these

deployments, most of the direct measurements of the deep AMOC were either CTD snapshots or short (< 5 weeks) mooring time series and the variability on longer-time scales was not known (Dickson and Brown, 1994). The densest water observed here is the DSO. The moorings were equipped with (primarily current meter) instruments close to the ocean bottom in order to monitor the near-bottom portion of the water column where the core of the deep AMOC is present. The ANG measurements were sustained continuously from the 1980's until 2015, except for breaks between 1990 and 1995 and in 1996. Most of the funding for the moorings was provided by the Centre for Environment, Fisheries and Aquaculture Science (Cefas), the University of Hamburg and the Finnish Institute of Marine Science (FIMR) (see Table 2.1).

CTD sections of salinity and potential temperature at ANG are shown in Figure 2.1. The property sections are snapshots from a CTD section carried out in August 2011 (Karstensen, 2013). The DSO is the densest ( $\sigma_{\theta} > 27.85 \text{ kg m}^{-3}$ ) water observed near-bottom on the lower Greenland slope, below around 1500 m. During August 2011, the DSO was colder ( $\theta < 2.5^{\circ}\text{C}$ ) and fresher ( $S < 34.90$ ) than the overlying water. This is consistent with CTD crossings of the ANG section at other times, which also show that the DSO is associated with elevated concentrations of the tracer SF<sub>6</sub>, indicating a more recent contact with the atmosphere compared with the overlying water masses (Dickson et al., 2008).

The lighter overlying water masses are warmer and more saline (Figure 2.1), with lower tracer concentrations (Dickson et al., 2008). They are Iceland-Scotland Overflow Water (ISOW) and Labrador Sea Water (LSW). The ISOW is typically found within the  $27.8 \text{ kg m}^{-3} < \sigma_{\theta} < 27.85 \text{ kg m}^{-3}$  potential density class (Dickson et al., 2008) and is associated with a temperature of around  $3^{\circ}\text{C}$ , whilst the LSW is found within the  $27.7 \text{ kg m}^{-3} < \sigma_{\theta} < 27.8 \text{ kg m}^{-3}$  potential density class (Dickson et al., 2008). All three water masses make a contribution to the formation of North Atlantic Deep Water (NADW) (Dickson and Brown, 1994).

The average flow speeds of the DSO, from mooring deployments at the array in 2003-04, are shown in Figure 2.2. The flow speeds are derived from Rotor Current Meters (RCM). Three RCM were typically deployed: one at the near-bottom ( $H=20$  m) and the other two above, separated by 100-150 m. Also deployed, from 1998-2015, were SBE MC instruments (Model SBE-37 SM), which measure the conductivity, temperature and (for some instruments) pressure of the water with high accuracy. The instruments were attached with shackles and rings to Kevlar rope, which connected the anchor on the sea floor with buoyancy spheres around 300-400 m above the bottom. An acoustic release just above the anchor was used to release the mooring line each year

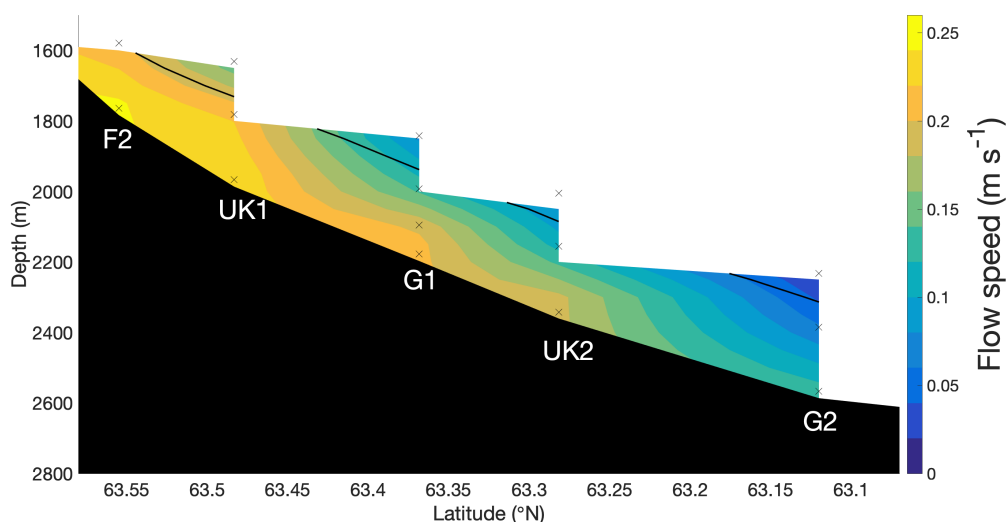


Fig. 2.2 Vertical section of deployment mean flow speeds ( $\text{m s}^{-1}$ ) of the DSO on the Greenland slope at ANG, from moored observations in 2003-04. The flow direction is southwestward. The moorings names are labelled in white font and the black crosses indicate the depth of Rotor Current Meter (RCM) instruments, from which the speeds are derived. The broken black lines indicate the  $2.5^{\circ}\text{C}$  isotherm (from *in-situ* RCM temperature measurements), which approximately indicates the upper limit of the DSO (Voet and Quadfasel, 2010).

for mooring recovery. Further information on the mooring design is available in Jones and Read (1993).

Maxima flow speeds occur over the 1700 m-2000 m isobath, with lower speeds further down the slope (Figure 2.2). The highest speed ( $0.25 \text{ m s}^{-1}$ ) is recorded at mooring F2. The flow is bottom intensified, with maxima speeds at the deepest instruments (typically around 20 m above bottom). To compare with mooring F2, near-bottom flow speeds at UK1, G1, UK2 and G2 are 0.24, 0.21, 0.21 and  $0.13 \text{ m s}^{-1}$  respectively. The mean flow directions range from  $210^{\circ}$  to  $251^{\circ}$  (clockwise from northward) i.e. to the southwest (not shown). The volume transport of the DSO through the ANG section is an estimated 4 Sv (Dickson et al., 2008), in the 2003-04 period when moorings were deployed across the entire width of the overflow. The accuracy of the speeds, derived from RCM instruments is  $\pm 0.01 \text{ m s}^{-1}$  or 4% of the flow speed, which ever is highest. Note that the speed used in Figure 2.2 is the mean of one deployment period (2003-04), which is likely representative of other years, since Dickson and Brown (1994) argued that the mooring speed time series at ANG reach a stable mean after 5 weeks, basing their reasons on 5 years of moored data.

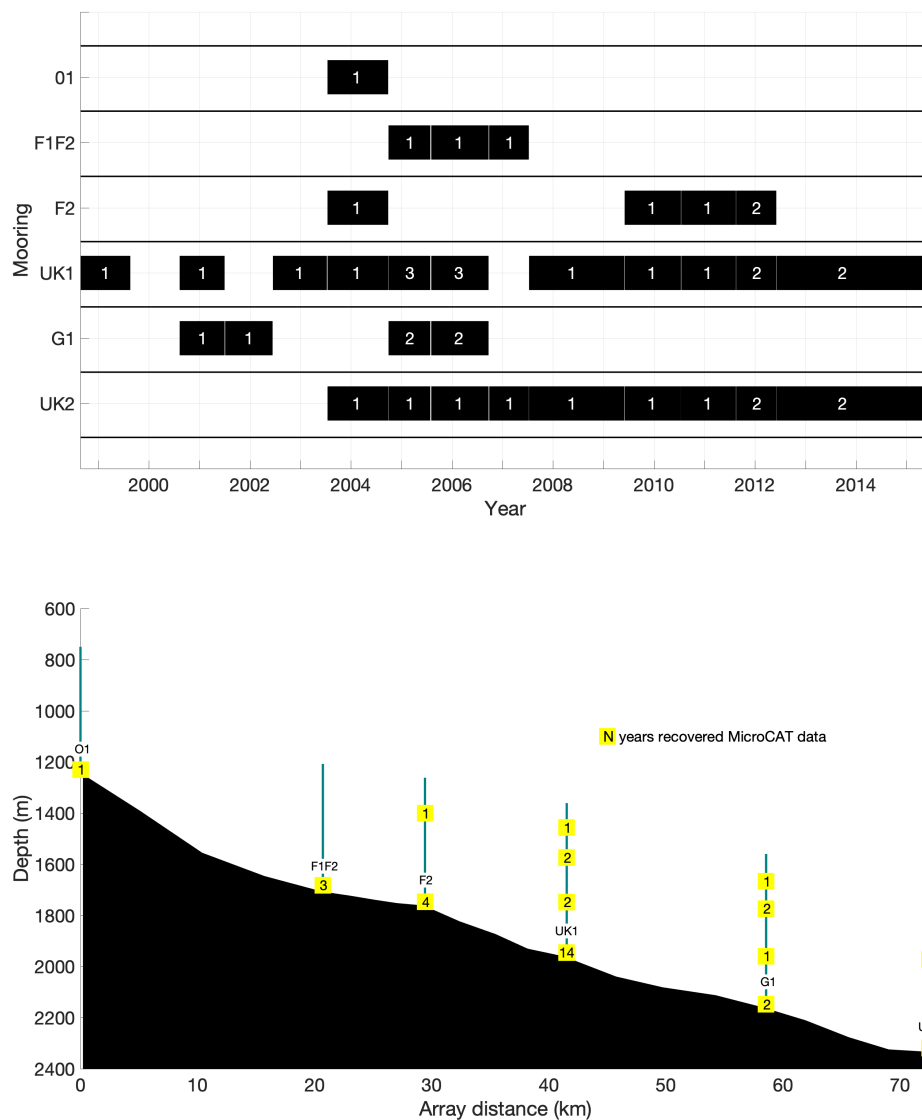


Fig. 2.3 Deployment of MC instruments at ANG between 1998 and 2015. The top panel shows the number of instruments recovered at the different moorings versus year and the bottom panel shows the mooring locations and the total number of successful recoveries at each mooring (numbers in yellow boxes).

The most frequently recovered moorings were UK1 and UK2, which were deployed in most years (Figure 2.3). The F1, F1F2 and F2 moorings were also deployed frequently, though their location on the slope changed from year to year (Figure 2.3). Conversely, only one year of data were recovered from mooring O1, which was deployed in 2003 up the slope from the other moorings and outside the DSO (Figure 2.3). Many moorings that were deployed were unfortunately lost. Nevertheless, data were recovered from at least two moorings consistently between 2003 and 2015 (Figure 2.3). These contemporaneous data from neighbouring moorings are used to characterise the spatiotemporal variability

of sustained freshening events in Chapter 3. Further, in Chapter 3, the property data from this array are synthesised with the DSO property variability at upstream mooring arrays at DS and north of DS, which will be introduced below, in order to investigate the advection of water masses and anomalies from north of the strait to ANG. Furthermore, in Chapter 5, MC data from ANG, are used to investigate the relationship between atmospheric patterns, sea ice, and the salinity variability of the DSO.

### 2.1.2 MicroCAT conductivity and salinity calibration

The conductivity cell on the MC instrument is particularly susceptible to errors caused by biological and chemical fouling, or cell damage. This malfunction results in inaccurate salinity. Salinity can be inaccurate due to a constant error (bias), or an error that drifts with time. CTD casts were carried out on mooring recovery cruises and used as a reference to check for error and to calibrate the MC conductivity/salinity. On the other hand, the MC temperature tends to be reliable, not requiring correction. Typically, ship CTD sensor data are independently calibrated to World Ocean Circulation Experiment (WOCE) standards, that is to an accuracy of  $\pm 0.002$  °C (for temperature) and  $\pm 0.002$  (for salinity) (Joyce, 1988). Once calibrated, Uchida et al. (2008) estimated that the standard deviation of the SBE-37 MC salinity data is 0.0013 and therefore the uncertainty is 0.0026.

Between 2000 and 2002, just two MC instruments were deployed exclusively (MC1538 and MC1541) at moorings UK1 and G1. Both instruments showed a small salinity error in these early years with salinities lower than the reference (CTD) salinities. Figure 2.4 shows the mooring salinity time series each summer between 2000 and 2003 and the near-bottom CTD salinities from stations on the Angmagssalik line taken during recovery/deployment cruises, which are used as a reference. The CTD salinities shown are the median in the bottom 100 m of the cast and there were multiple casts every summer (see the multiple crosses in figure 2.4). The median salinities in the last 24 hours (before recovery), or the first 24 hours (after deployment), of the mooring time series were subtracted from the CTD salinities to compute salinity offsets (Figure 2.4). The mooring data closest in time to the CTD data were used to calculate the offsets. The salinity error of both instruments is found to be systematic between 2000 and 2003, not increasing from one end of deployment to another as would be symptomatic of sensor drift. The median offset for both instruments between 2000 and 2003 varies from around 0.02 to 0.03 (Figure 2.4). Therefore, the error is resolved by applying the median offset each year to the mooring time series (Table 2.2).

From 2004-15, the MC conductivities were calibrated directly, using calibration casts. Calibration casts were carried out immediately after mooring recovery using the uncleaned MC instruments. During a calibration cast, the MCs are fixed to the CTD

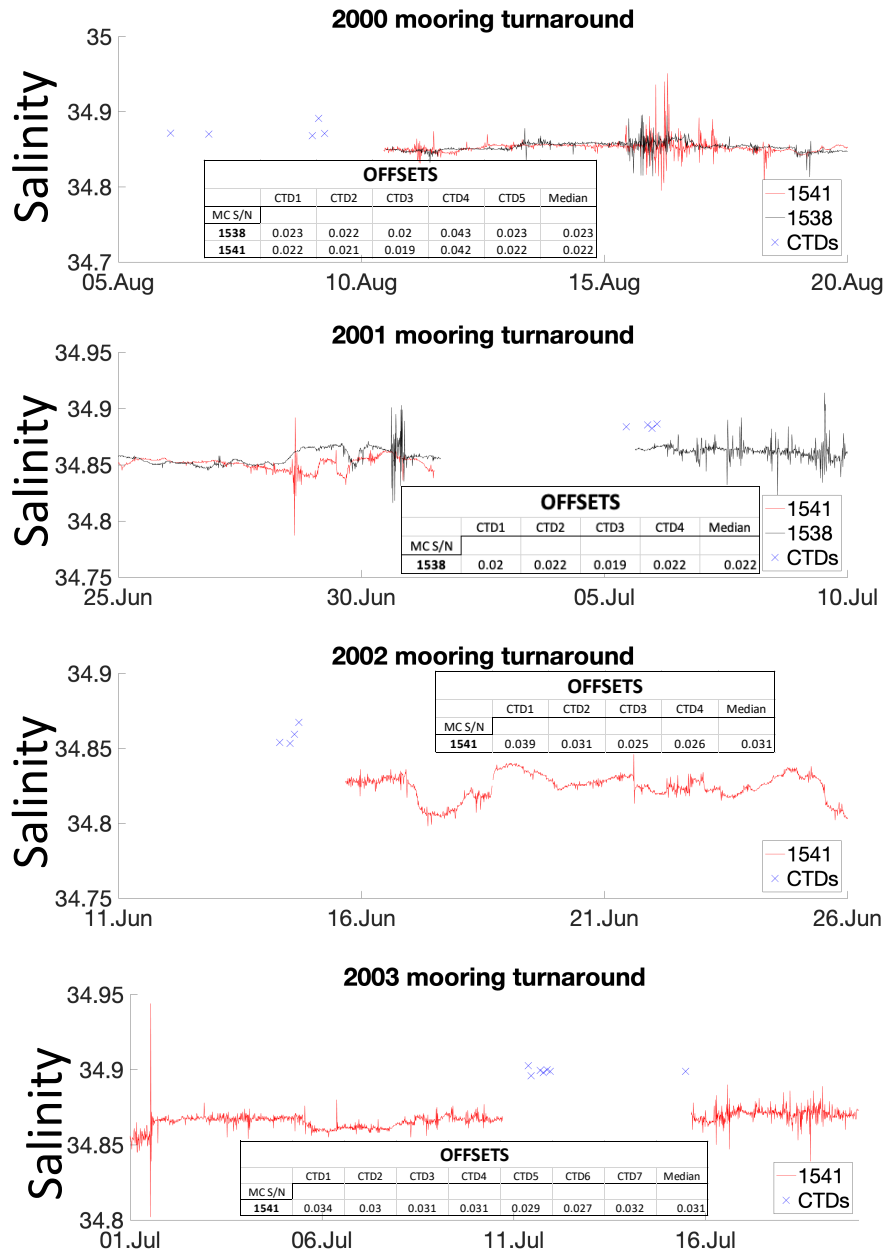


Fig. 2.4 Concurrent mooring (red and black lines) and CTD (blue crosses) salinity, and offsets between them, in summer between 2000 and 2003. The red and black lines correspond to salinity from the different MC instruments (the number is the serial number of the instrument deployed near-bottom at moorings UK1 and G1 on the Angmagssalik array). The CTD salinity is the vertically averaged salinity from the deepest 100 m of CTD casts carried out on the Angmagssalik array in the vicinity of the moorings.

Deployment year		O1	F	UK1			G1			UK2		Cruise code
2000	S/N	-	-	-	1538	-	-	1541	-	-	-	POS263 and M50/3
	S offset	-	-	-	0.023	-	-	0.022	-	-	-	
2001	S/N	-	-	-	-	-	-	1538	-	-	-	M50/3 and POS290
	S offset	-	-	-	-	-	-	0.022	-	-	-	
2002	S/N	-	-	-	1541	-	-	1538	-	-	-	POS290 and M59/1
	S offset	-	-	-	0.031	-	-	N/A	-	-	-	
2003	S/N	2404	2887	-	1541	-	-	1538	-	2885	-	M59/1, CD164/165B
	C offset (S/m)	0.0036	0	-	0.0018	-	-	N/A	-	0	-	
2004	S/N	-	3523	-	1541	2885	3096	3097	3098	3529	-	AF 08/2005
	C offset (S/m)	-	0.001	-	0.0018	0.0007	0	0	0	0.0007	-	
2005	S/N	-	3098	-	2935	3096	3097	1596	2803	1538	-	D311
	C offset (S/m)	-	0.0008	-	0.0009	0	0.001	N/A	N/A	0.0021	-	
2006	S/N	-	3098	-	-	-	-	-	-	2885	-	MSM05/04
	C offset (S/m)	-	0	-	-	-	-	-	-	0	-	
2007	S/N	-	-	-	4253	-	-	-	-	2885	-	MSM12/1
	C offset (S/m)	-	-	-	0.0013	-	-	-	-	0	-	
2009	S/N	-	2885	-	6439	-	-	-	-	6621	-	M82/1
	C offset (S/m)	-	CC*	-	CC*	-	-	-	-	CC*	-	
2010	S/N	-	7575	-	7574	-	-	-	-	7573	-	M85/2
	C offset (S/m)	-	0.0013	-	0.0009	-	-	-	-	0	-	
2011	S/N	-	6439	6621	2885	4253	-	-	-	4219	4337	MSM21/1
	C offset (S/m)	-	0	0.001	0	0	-	-	-	0	0	
2012	S/N	-	-	-	7575	-	-	-	-	7573	7574	POS486
	C offset (S/m)	-	-	-	0.0016	-	-	-	-	0	0.0008	

Table 2.2 Salinity (S) and conductivity (C) offsets between CTD and MC used to correct the MC time series. The serial number (S/N) of each MC and the cruise code of the calibration cast is given. The research vessel initials are as follows: Poseidon (POS), Meteor (M), Arni Freidrickson (AF), Charles Darwin (CD), Maria S. Merian (MSM), Discovery (D). CC\* indicates previously calculated correlations. N/A stands for not applicable, either because the conductivity cell failed or no calibration CTD cast was carried out.

package, alongside the CTD sensors, and set to maximum sampling rate (usually 10 seconds). MC conductivity is compared to CTD conductivity at multiple bottle stop depths, where the CTD package remains stationary for several minutes, usually on the upcast. At these depths, conductivity offsets are calculated.

Unfortunately, calibration casts of the cleaned or new MC instruments were not carried out prior to deployment of the moorings. Only calibration casts of the recovered 'dirty' MC instruments were carried out. Therefore it was not possible to say whether cleaning the instruments removed the source of conductivity error (e.g. biological deposits on the conductivity cell), or whether the the source of error could not be removed by cleaning (e.g. material erosion from the electrode). Thus it was not possible to determine whether the conductivity offsets on recovery indicate a constant error (indicative of material erosion from the electrode) or an error that increases (drifts) with time (indicative of biological deposits). If there was data drift caused, for example, by biological deposits, it was not possible to determine the nature of the drift (i.e. linear or non-linear), and thus it was assumed that the error was constant in all cases.

An example of an upcast, from June 2012, is shown in Figure 2.5, when there were 5 bottle stops between the bottom depth of 2500 dbar and the surface. At the bottle stops, the CTD package remains essentially stationary, allowing the MC sensors to

equilibrate to the conditions of the water column at that depth, so the measurements can stabilise. This is necessary because the MC sensors have a slower response time than the CTD sensors. The equilibration time can exceed 5 minutes (Kanzow et al., 2006). To determine the accuracy of the MC conductivities (and by extension salinities), the difference between CTD and MC, or offset, is calculated. The average offset after 3 minutes is used, to account for equilibration time. Occasionally, the duration of the bottle stops was not as long as the 5 minute equilibration time recommended by Kanzow et al. (2006), hence why the average offset after 3 minutes was used instead.

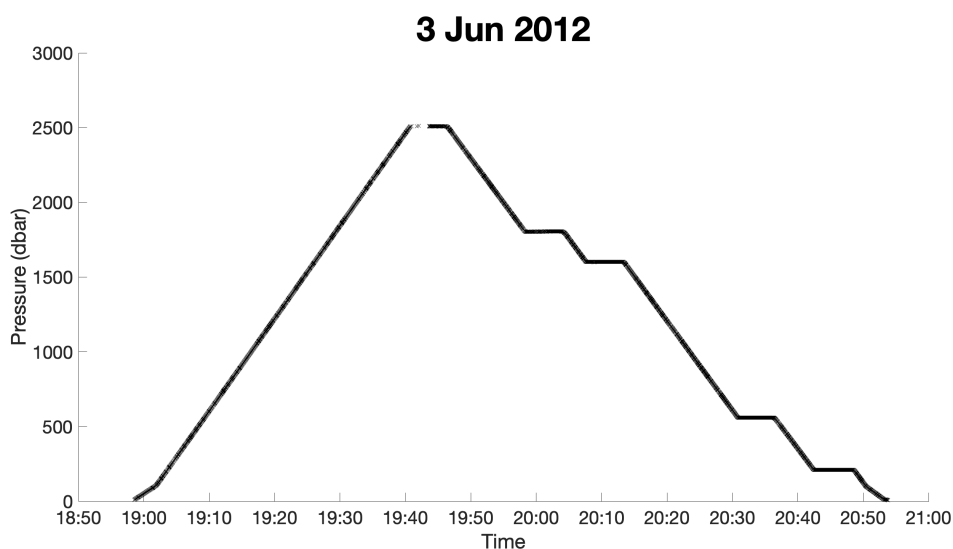


Fig. 2.5 Pressure as a function of time during a CTD calibration upcast in June 2012. The data from CTD stops on the upcast are used to calibrate the MC instruments.

By way of an example, the conductivity offsets in June 2012 for the MC instruments deployed in 2011-12 are shown in Figure 2.6. The conductivity offsets (CTD minus MC) for the six instruments are shown as a function of bottle stop depth and minutes at bottle stop. In general, the offsets stabilise with time and settle on a value (the true offset) after equilibrating. Should this value be within  $\pm 0.0006 \text{ S m}^{-1}$  (Siemens/metre) of zero, no correction to the mooring conductivities is required. This threshold choice is based on the maximum overlap of the error bars associated with the conductivity measurements of both the CTD and MC instruments. The error bars are based on the initial conductivity measurement accuracy, which is  $0.0003 \text{ S m}^{-1}$  for both the CTD and MC instruments.

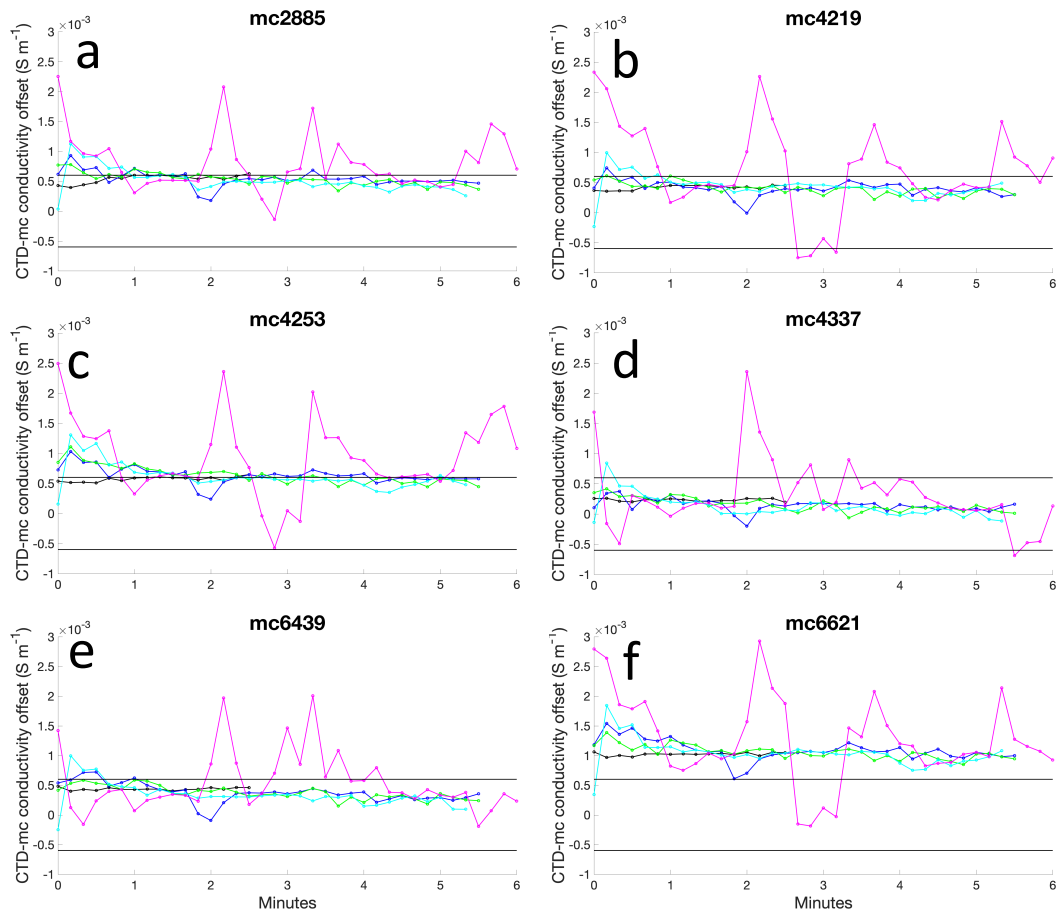


Fig. 2.6 Conductivity offsets (CTD minus MC) as a function of depth (colour) and time (x-axis) at bottle stops during a calibration cast carried out in summer 2012. Each panel shows the offsets for the different MC instruments, which are labelled.

In this example, only one MC instrument records offsets outside of the threshold - MC6621 with an average offset after equilibration of  $+0.001 \text{ S/m}$  (Figure 2.6f). This value is the average offset after three minutes at bottle stops 1-4, stop 5 (pink line) was not used because it appeared to be unstable and the offsets fluctuated (Figure 2.6f). This indicates that the conductivities measured by the MC are too low (too fresh). Therefore the mooring conductivity time series is corrected by applying the offset as a fixed value to the mooring time series. The approach illustrated in Figure 2.6, for the 2011-12 conductivities, were used systematically for all other deployments between 2004 and 2012 (the last deployment was three years - 2012-15). The one exception was the 2009-10 data, which had been calibrated using calibration coefficients previously (Table 2.2).

Some bottle stops were unhelpful (e.g. bottle stop 5 (pink line) in Figure 2.6: all panels) either because the CTD package drifted upwards or downwards or because

of strong vertical hydrographic gradients, which prevent the MC from equilibrating. The latter was the problem for bottle stop 5 in June 2012, this was the bottle stop closest to the surface (Figure 2.5), the bottle stop took place in the halocline (not shown). Therefore, small oscillations of the CTD rosette may cause conductivity (salinity) spikes and the MC instrument requires more time to equilibrate. Useful bottle stops are those where the rosette is completely stationary and in a well-mixed depth of the water column. The quality of the bottle stop was assessed on a case by case basis. In the case of a systematic conductivity offset at all bottle stops, this is a clear sign of MC conductivity error which requires correction. If the offsets are variable at the different bottle stops, the offsets from the most stable bottle stops are used.

Once derived, the conductivity correction offset is applied to the mooring time series and the salinities are recalculated. The conductivity (from 2004 onwards) and salinity (before 2004) offsets used to correct the MC data are shown in Table 2.2. The offsets are invariably positive, indicating that the MC conductivities are systematically too low (fresher salinity) relative to the CTD references, for example the MC6621 instrument deployed in 2011-12 (Figure 2.6). This is typical of MC conductivities and the most likely cause is biological or geochemical fouling of the conductivity cell and/or fouling of the electrode or loss of material from the electrode (Freitag et al., 1999).

The post-calibrated moored salinity time series were also visually inspected. The purpose of this was to determine whether there is any evidence that does not support the choice of correction. Only the salinities from the near-bottom instruments were tested because these instruments occupy the dense DSO, which is the focus of this thesis. To carry out the verification, salinity time series from neighbouring moorings are compared with each other. Previous work has shown that the salinity across the DSO plume at ANG is unchanging (Hall et al., 2011; Jochumsen et al., 2015), i.e. the DSO salinity is well mixed by this point in its descent from the DS sill. For example, the CTD snapshot from August 2011 (Figure 2.1) demonstrates this characteristic. Therefore, if the post-calibrated time series were substantially more fresh or more saline than time series from neighbouring moorings, this would indicate inaccurate salinity. However, all of the calibrated time series appeared good.

Note that the salinity measurements have an uncertainty of  $\pm 0.004$ , based on the initial measurement accuracy of the SBE conductivity sensors ( $0.0003 \text{ S m}^{-1}$ ). MC sensor drift is a source of uncertainty in this study. Since the necessary data to determine whether sensor drift had occurred were not available (as previously mentioned), it is assumed in this thesis that salinity drift did not occur. However, if the salinities did, in fact, drift, it would result in salinity variability which might be identified, spuriously, as ocean variability.

### 2.1.3 Salinity time series preparation

In order to investigate the intra-annual salinity variability of the DSO, multiple years of salinity measurements are required. The more years of salinity, the greater the statistical certainty of the analysis. Therefore, salinity from adjacent moorings are concatenated to form the longest possible time series. The constructed time series was filtered using a Butterworth filter to remove variability on different timescales.

Note that practical salinity (which has no units) is used in thesis, instead of absolute salinity (which has units of  $\text{g kg}^{-1}$ ), for the sake of consistency with previous studies (e.g. Hall et al. (2011), Jochumsen et al. (2015)). Consistently, potential temperature (in  $^{\circ}\text{C}$ ), which is the temperature of water brought adiabatically to the surface, is calculated from in-situ temperature, and is used in this thesis (instead of conservative temperature) for the same reason. Potential density is calculated from the salinity and potential temperature, and the  $27.8 \text{ kg m}^{-3}$  potential density contour (isopycnal), is used to define the upper boundary of the DSO, consistent with the traditional definition (Dickson and Brown, 1994). Potential temperature and potential density are computed using the TEOS-10 toolbox (McDougall and Barker, 2011). Specifically, potential density is computed by converting the practical salinity and potential temperature into absolute salinity and conservative temperature respectively, which are the inputs into the potential density calculation. Potential temperature ( $\theta$ ) and potential density ( $\sigma_{\theta}$ ) are termed temperature and density respectively, hereafter in this thesis, for brevity.

The ANG salinity time series is constructed with near-bottom salinities, predominantly from UK1. However, salinity gaps at UK1, due to instrument failure in 2001-02 and 2006-07, were filled using salinities from moorings G1 and UK2 respectively. This is justified because the salinities at UK1 are correlated with G1 ( $r=0.36$ ,  $p=0.0004$ ) and UK2 ( $r=0.79$ ,  $p<<0.01$ ) in 1 and 10 years of concurrent data respectively. These correlations increase to  $r=0.90$  ( $p<<0.01$ ) and  $r=0.93$  ( $p<<0.01$ ), for the UK1-G1 and UK1-UK2 correlation respectively, when the high frequency variability is removed using a 20 day centred moving average filter. Moreover, the time-mean salinities over the concurrent period are within 0.002 of each other. This supports previous findings (Dickson et al., 2008; Hall et al., 2011; Jochumsen et al., 2015) that the salinity of the DSO is relatively homogeneous, as illustrated in Figure 2.1. Conversely, the temperature decreases down the slope because the DSO is temperature stratified. Therefore only temperature from UK1 is used in the temperature time series. Therefore, the salinity time series is 16 years long (1998-2015 with one gap in 1999-2000) and the temperature time series has a duration of 14 years.

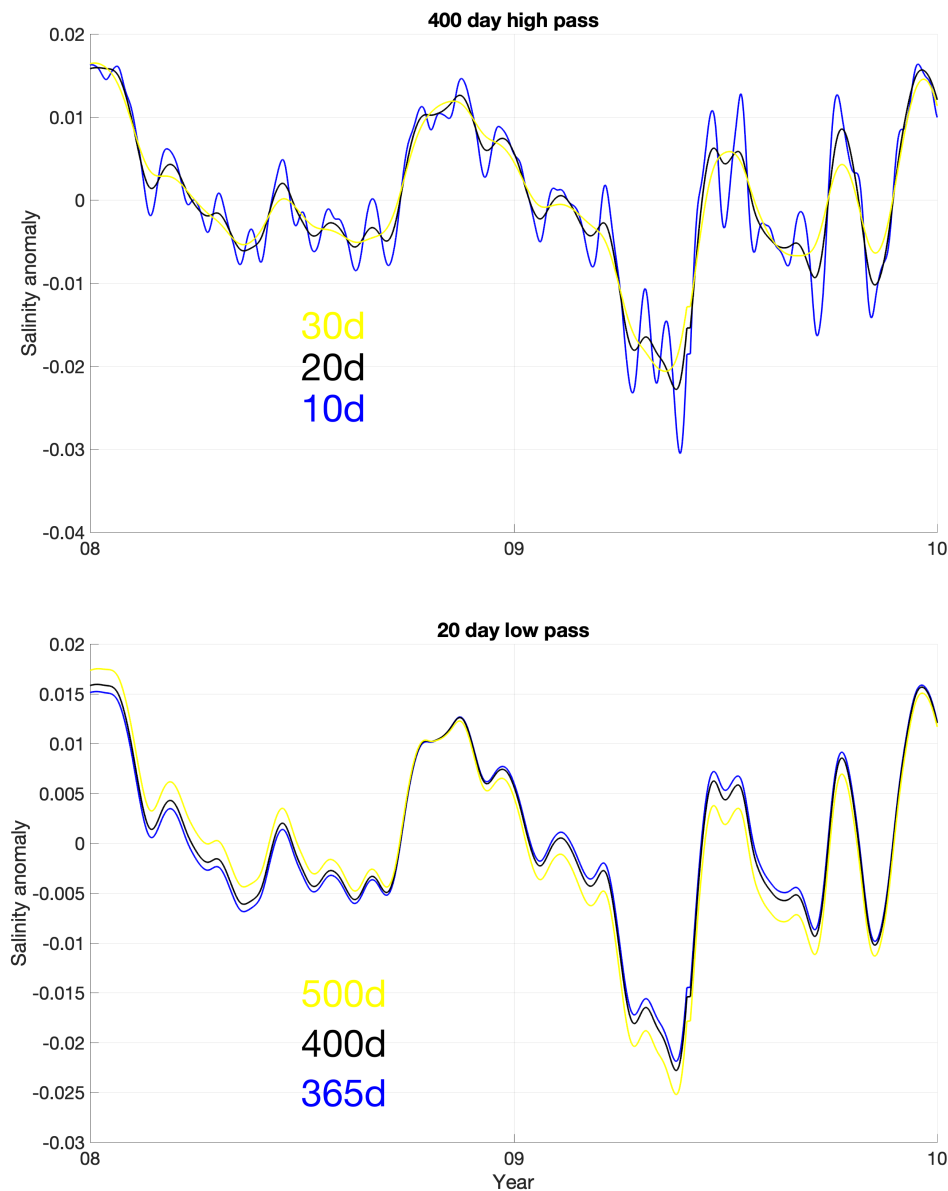


Fig. 2.7 Salinity anomaly (mean removed) time series (between 2008 and 2010), and smoothed with a second order band-pass Butterworth filter with variable frequency cutoffs. In the top panel, the 400 day high pass is held constant and the low pass cutoff is 30 days (yellow), 20 days (black) and 10 days (blue). In the bottom panel, the 20 day low pass is held constant and the high pass cut off is 500 days (yellow), 400 days (black) and 365 days (blue).

A Butterworth filter was designed to filter out signals not relevant to the investigations of this thesis. This thesis is focused on the advective property variability, specifically on seasonal timescales, and not the high frequency variability associated with cyclones, boluses and pulses originating from DS, as described by von Appen

et al. (2014) and von Appen et al. (2017). Therefore, the objective is to remove the multi-annual variability and the variability in the high-frequency end of intra-annual variability. A 2nd order band-pass Butterworth filter, with frequency cut offs of 20 and 400 days was used. The choice of filter order has very little effect on the resulting time series. The choice of frequency cut off does not qualitatively change the results, but does have a quantitative effect. To demonstrate this, Figure 2.7 shows the salinity time series between 2008 and 2010, a representative period of the time series, with variable frequency cut offs.

The effect of the high pass cutoff has only a minor quantitative effect on the salinity time series (Figure 2.7). However, the choice of low pass cutoff (10 day, 20 day or 30 day) has a greater effect on the time series. For example the salinity minimum in spring 2009 is most negative in the 10 day cutoff (-0.03), which is around 0.01 below the other cutoff time series Figure 2.7. Nevertheless, regardless of the choice of frequency cutoff, all time series capture the spring freshening event in 2009. The freshening events are a key focus of this thesis. Ultimately, the 20 day cutoff is used to be consistent with previously published research (Jochumsen et al., 2015). However, it should be noted that the property values quoted in the following chapters are dependent on the filtering procedure.

## 2.2 Upstream moorings and CTD stations

Before the upstream moorings and CTD sections are introduced, a general note about data uncertainty should be made. The downstream temperatures and conductivities used in this thesis (described below) all derive from SBE-37 MC or SeaCAT instruments, and are previously calibrated. The initial temperature and conductivity accuracy of the instruments are  $\pm 0.001^{\circ}\text{C}$  and  $0.0002 \text{ S m}^{-1}$  respectively. Using SBE-37 MC instruments from Pacific Ocean moorings, Uchida et al. (2008) estimate that the accuracy of moored temperature and salinity measurements by MCs is  $0.0006^{\circ}\text{C}$  and  $0.0026$  respectively, after calibration, relative to accurate CTD reference casts. Conversely, the velocities are derived from RCM, Acoustic-Doppler Current Profiler (ADCP) and Acoustic Current Meter (ACM) instruments. The corresponding uncertainties are  $\pm 0.01 \text{ m s}^{-1}$ ,  $\pm 0.005 \text{ m s}^{-1}$  and  $\pm 0.005 \text{ m s}^{-1}$  for RCM, ADCP and ACM instruments respectively. Note also that the various datasets used in this thesis (summarised in Table 2.1), which were acquired in different formats, were converted into '.mat' format and are processed and analysed on MATLAB.

### 2.2.1 Spill Jet section

Seven moorings (two on the Greenland shelf and five on the upper Greenland slope) were deployed in a section called the East Greenland Spill Jet section, situated at approximately 65.25 °N in 2007-08 (von Appen et al., 2014) (SJ in Figure 1.8; see also Table 2.1). Full depth profiles of temperature, salinity and velocity were recovered from ADCP, ACM and Coastal and McLane Moored Profiler (MP) instruments and the moorings were spaced between 6.5 km and 10.5 km apart. SBE MC were also deployed at 100 m and near-bottom on each mooring. These provide higher sampling resolution (hourly) at the same depth than the MP instruments (twice daily), which move up and down the mooring cable. In the below, the MP data are used to validate the MC data.

The motivation for the deployments was to advance understanding of the Spill Jet - a rapid current of dense water deriving from water spilling off the Greenland shelf, previously observed in CTD snapshots (Brearley et al., 2012; Pickart et al., 2005) - and its role in the AMOC. Once the high-frequency activity of the eddies was removed, the Spill Jet was defined as a bottom intensified jet, which transports an average of 3.3 Sv southward (von Appen et al., 2014). It is lighter than the DSO which is found further down the slope at the array; the three most offshore moorings (EG5-EG7) occupy the DSO (mean density  $> 27.8 \text{ kg m}^{-3}$ ) and the upper slope moorings EG3 and EG4 occupy the Spill Jet (von Appen et al., 2014). The Spill Jet advects water in the  $27.6 \text{ kg m}^{-3} < \sigma_{\theta} < 27.8 \text{ kg m}^{-3}$  density class southward and therefore likely contributes to the AMOC in the layers above the Nordic Seas overflows, specifically in the LSW class (von Appen et al., 2014). However, Brearley et al. (2012) and Koszalka et al. (2013) also show that the Spill Jet advects water denser than  $27.8 \text{ kg m}^{-3}$ . Further, Harden et al. (2014) demonstrated that the Spill Jet is supplied, to some extent, by local Ekman Downwelling induced by northeasterly winds and by offshore advection caused by the leading edge of southward propagating cyclonic ocean eddies.

The near-bottom salinities and velocities from the slope moorings (EG3-EG7; see five furthest offshore stations in Figure 1.8) are used in this study (Chapter 3) to investigate sustained freshening events on the Greenland slope in 2007-08. The MC salinities were validated using the MP salinities in the deepest bin (ranging from 1 m to 25 m above the MC) and the results are shown in Figure 2.8. The MP instruments carried out a profile twice daily; once at 00:00 and once at 08:00. Whilst the EG3, EG4, EG5 and EG7 salinities show excellent agreement ( $r > 0.80$ ), unfortunately the salinities from EG6 were unusable due to sensor drift (Figure 2.8). The correlation coefficient between the MC and MP salinities at EG6 is just 0.52 (Figure 2.8). The MP salinities at EG6 are independently verified using the salinities from the 100 m MC at this morning (not shown), indicating that it is the near-bottom MC salinities that are erroneous at this

mooring. The velocities were previously processed by von Appen (2013), where other details of the mooring deployments can be found.

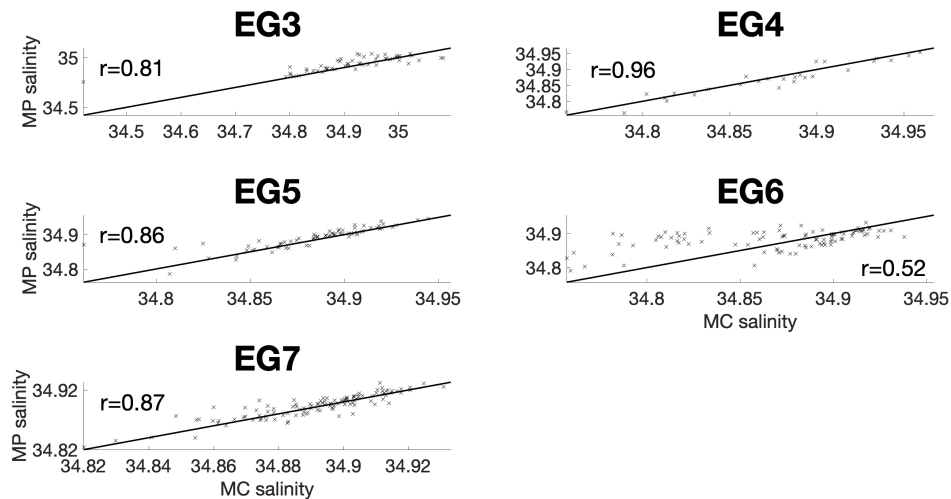


Fig. 2.8 Salinity correlations between near-bottom MC salinities and MP salinities (1 m - 25 m above) at different moorings at the Spill Jet section. The correlation coefficient ( $r$ ) is marked on and the thick black line is the  $y=x$  line.

### 2.2.2 Denmark Strait

Sustained mooring observations have been made at the sill of DS (cross section shown in Figure 2.9) since the late 1990's (Macrander et al., 2005). The reason that moorings have been deployed here is because it is the 'saddle point' where the DSO first enters the Atlantic, rapidly descending the Greenland-Scotland Ridge. These observations have shed light on the dynamics and the properties of the overflow. The mean volume transport of the DSO is 3.2 Sv towards the south (Jochumsen et al., 2017), but it is highly variable on short timescales (von Appen et al., 2017). Specifically, there are boluses, which are thick lenses of weakly stratified overflow water, and pulses, which are associated with DSO thinning and flow acceleration (von Appen et al., 2017). Boluses and pulses occur every 3.4 and 5.4 days respectively and cause an increase in volume transports, compared to the background state, of around 30-40% (von Appen et al., 2017). Further, the transports of the DSO vary from year to year with high transports in 1999-2000, compared with 2002-03, for example (Macrander et al., 2005). The near-bottom properties in the trough are very cold ( $\theta < 0^\circ\text{C}$ ) and dense ( $\sigma_\theta > 28 \text{ kg m}^{-3}$ ) and may originate from Arctic Intermediate Water (AIW), formed in the Greenland and/or Iceland Sea, and fed from the NIJ (Mastropole et al., 2017).

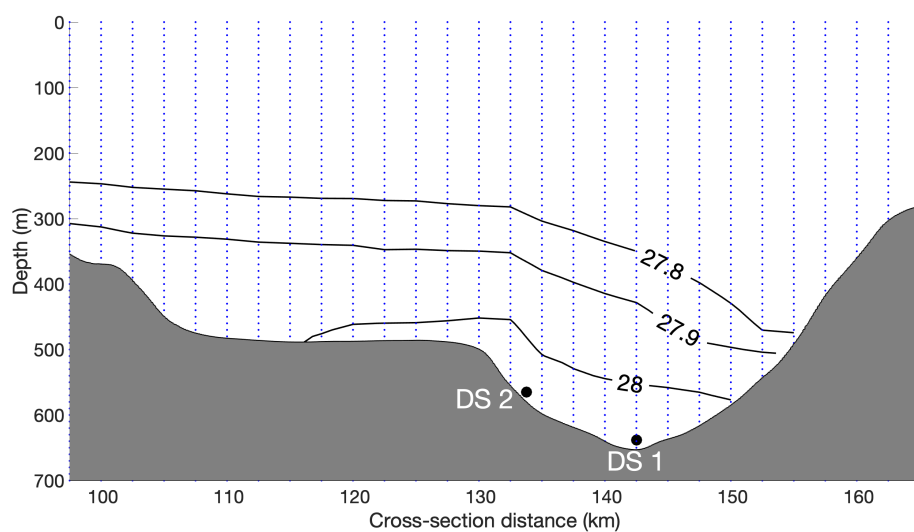


Fig. 2.9 Cross-section of the DS section showing the location of gridded CTD (blue dots) and mooring data (large black dot). The thin black lines show density contours (in  $\text{kg m}^{-3}$ ) from the time-mean CTD section between 1990 and 2012. Note that the DS 2 mooring is deployed in the dense core of the DSO, whilst the CTD data record the dense core and also captures the lighter parts of the DSO.

Two moorings: DS 1, in the deepest part of the trough (650 m) and DS 2, on the Greenland slope side of the trough at a bottom depth of around 570 m, have been deployed since 1996 (Jochumsen et al., 2017). The moorings are typically equipped with an upward facing ADCP and MC, situated near-bottom (typically 6 m above the bottom) (Jochumsen et al., 2012). In this study, the salinities from DS 2 (Figure 2.9) collected between 2005 and 2015 are used (Figure 1.8; Table 2.1). This time period is chosen because it overlaps with the ANG deployments. Each deployment (typically once a year) the MC salinities were calibrated using CTD calibration casts (Jochumsen et al., 2017). Salinities from DS 1 are not used because they were not calibrated between 2010 and 2015. Furthermore, Jochumsen et al. (2015) showed that the DS 2 and DS 1 salinities are correlated ( $r=0.57$ ), though they noted that freshening events that were observed at DS 2 were absent from DS 1 (in the deep trough).

In addition, a repeat CTD section of DS has been occupied since around 1990 and these data are also used (Table 2.1). This section, represented by the black line in Figure 1.8, is called the Látrabjarg section and is typically occupied four times per year - in February, May, August and November (von Appen et al., 2014). The gridded product of 111 CTD sections collected between 1990 and 2012, and presented in Mastropole et al. (2017), is used here. Only the data in the deeper part of the section (i.e. not the continental shelves) are used since this is the only area where the DSO is observed

in all four seasons. Quality checks of the profile data from each CTD station were carried out, with small scale density spikes and inversions removed (Mastropole et al., 2017). The data are interpolated using a Laplacian spline interpolator with tension, onto an evenly spaced grid, with a 10 m vertical spacing and 2.5 km horizontal spacing (Mastropole et al., 2017), as shown in Figure 2.9. Temperature, salinity and density data are available but velocity is not available from this gridded product. Additionally, 10 crossings of the Látrabjarg section were carried out between 2013 and 2018. These data were interpolated on to the grid designed by Mastropole et al. (2017), and are included in this study, courtesy of Peigen Lin (Pers. Comms).

### 2.2.3 Faxaflói CTD station 9

The Faxaflói section is also a repeat CTD section instigated by the Marine Institute of Iceland (Malmberg et al., 2001), which is located off the southwest coast of Iceland (Figure 1.8; see Table 2.1 also). As with the Látrabjarg section, the Faxaflói section is typically occupied four times per year, once in each season. The Faxaflói CTD section is comprised of 9 standard stations, and the most offshore station (FX9), located over the 1000 m isobath on the lower Iceland slope (Figure 1.8), is used in this thesis. Temperatures and salinities from FX9 are derived from SBE-911 plus CTD rosettes (Briem et al., 2000), with SBE 3 temperature and SBE 4 conductivity sensors used (M. Danielsen, pers. comms.). The manufacturers quote that the sensors have high initial conductivity accuracy of  $\pm 0.0003 \text{ S m}^{-1}$  and an initial temperature accuracy of  $\pm 0.002^\circ\text{C}$ . Conductivity samples were taken at the lowest depth at each station, and analysed using an Autosal 8400/8400b, and the salinities were recalculated with the slope correction found by using the procedure recommended by SBE (M. Danielsen, pers. comms.). Data from 116 occupations of the CTD station, with a vertical spacing of 1 dbar, ranging from 1 dbar to 1069 dbar, are used in this thesis.

The FX9 CTD station was previously used, by Malmberg et al. (2001), to document the temperature and salinity variability of water approaching DS with the Irminger Current. This station occupies the deeper part of the Irminger Current, which flows northwards towards DS (Malmberg et al., 2001). A recent study used the backward trajectories of numerical particles to argue that a sizeable fraction (time-mean: 16%) of the DSO at DS derives from the Irminger Current (Saberri et al., 2020). Furthermore, this water is entrained into the DSO south of DS according to other studies (McCartney, 1992; Tanhua et al., 2008). Therefore, the FX9 data are used because they capture possible DSO source water, upstream of DS.

## 2.2.4 Kögur

Fourteen moorings were deployed North of Iceland, at around 68°N between 2011 and 2014 (Figure 2.10). The moorings were in approximately the same location as the Kögur CTD section, which is one of the repeat CTD sections carried out around Iceland (Malmberg et al., 2001), and is thus termed the Kögur mooring array (KGA) (Figure 1.8; Table 2.1). The mooring array extends between the Greenland and Iceland continental shelves, with a maximum water depth of around 1500 m in the centre of the array (Figure 2.10). Between 2011-12, twelve moorings were in the water ranging from KGA1 around the Iceland shelfbreak and KGA12 on the outer Greenland shelf. Between 2012-14 three moorings were deployed on the Greenland shelf (KGA12 and two inshore moorings KGA13 and KGA14).

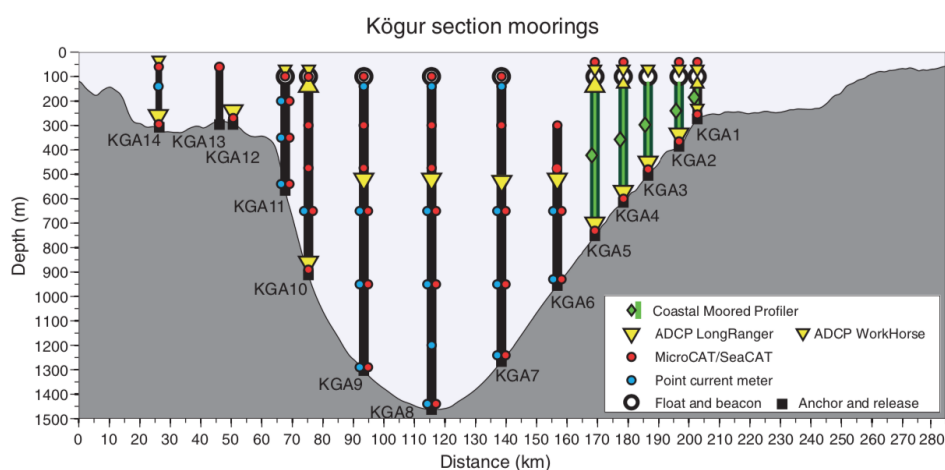


Fig. 2.10 Configuration of KGA moorings between the Greenland shelf and Iceland shelfbreak. The types of instrument deployed are shown in the legend. The salinity from MicroCAT/SeaCAT instruments at 550 m at KGA11 and KGA6 are used in Chapter 3. Figure from de Steur et al. (2017): their Figure 2.

The purpose of deploying this array is to better understand the northern sources of the DSO. Using these data, Harden et al. (2016) demonstrated that the average southward volume transport of DSO source water is 3.54 Sv between 2011-12. Furthermore, 2.54 Sv derives from the EGC, with the other 1 Sv deriving from the NIJ. In this thesis, the hydrographic variability of the DSO source water is investigated (in Chapter 4), and related to the intra-annual salinity variability of the DSO downstream, at ANG (characterised in Chapter 3).

Conductivity, temperature and pressure were measured by SBE MC/SeaCAT and moored profiler instruments (Harden et al., 2016) (Figure 2.10). Temperatures and conductivities were calibrated using in-situ CTD calibration casts (Harden et al., 2016)

and post-deployment calibration at Sea-Bird (Harden et al., 2016). Furthermore, temperatures and conductivities were compared with adjacent moorings to identify any instances of sensor drift. The salinities derived from KGA12 at 280 m exhibited a linear drift in all three deployments (not shown). This was corrected using CTD casts at the location of the mooring at the start and end of the deployment (L. de Steur: Pers. Comms).

Velocity data were collected by current meters (Nortek Aquadopps and Aanderaa RCMs), and profiling instruments (ADCPs and Aanderaa Recording Doppler Current Profilers), see Figure 2.10 (Harden et al., 2016). Some of the flow directions measured by the ADCP instruments showed an offset, caused by an asymmetric distribution of metal around the compass, and these were corrected by Harden et al. (2016). The ADCP compasses were calibrated before and after deployment, and the profiling velocity data were verified using the single point current meters (Harden et al., 2016). The accuracy of the Aquadopps and RCM instruments is  $0.01 \text{ m s}^{-1}$ , whilst the accuracy of the profiling instruments is  $0.005 \text{ m s}^{-1}$ . However, the velocity recorded by the upward facing ADCP deployed at 280 m at KGA12 was inconsistent in the different deployments. Specifically, the speeds were substantially lower in 2011-12 and 2012-13 than in 2013-14 (Figure 2.11). This required further inspection as is detailed below.

In this thesis, velocities and properties from the entire section are used. Firstly, data from between the upper Greenland slope and Iceland shelfbreak, from the 2011-12 KGA gridded product (Harden et al., 2016), are used. The gridded dataset has a temporal resolution of 8 hours, a vertical resolution of 50 m, and a horizontal resolution of 8 km. In Chapter 4, volume transports through the section are computed using the gridded data. Harden et al. (2016) estimated that the average error of the net volume transport at each time step is 0.45 Sv, and the error of their time-mean volume transport is 0.16 Sv. Secondly, velocity and property data derived from moorings deployed on the shelf (KGA12 and KGA14) are used (Figure 2.10).

### **Testing ADCP velocity from KGA12**

The near-bottom flow speeds at KGA12 between 2011 and 2014 are shown in Figure 2.11. Mean flow speeds at KGA12 in 2013-14 are  $0.15 \text{ m s}^{-1}$ , compared with  $0.04 \text{ m s}^{-1}$  in 2011-12 and 2012-13 (Figure 2.11). The fact that the speed increases at the exact point of mooring re-deployment in 2013 and the new higher speeds are maintained for the entire deployment (Figure 2.11) is too coincidental to be explained by a physical change in ocean dynamics. Instead, the discrepancy must be due to sensor error. The ADCP instrument used at the mooring was the same for all three years, however there were differences in the instrument settings in the different deployments. Specifically,

in the 2011-12 and 2012-13 deployments, the instrument was set to record in earth coordinates, whereas in the 2013-14 deployment the instrument was set to record in beam coordinates. The hypothesis is that the velocity in 2011-12 and 2012-13 is erroneous and the 2013-14 velocity is accurate.

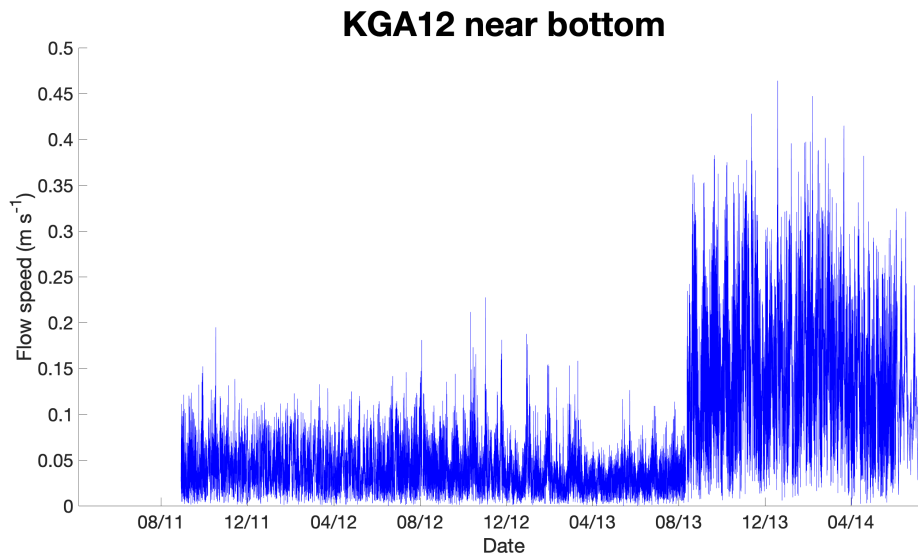


Fig. 2.11 Observed near-bottom flow speeds on the Greenland shelf at KGA12 between 2011 and 2014. Note the very low flow speeds between 2011-13, compared with the higher flow speeds between 2013-14.

A harmonic analysis of the velocity time series at KGA12 and the nearby mooring KGA14 (25 km inshore of KGA12 - see Figure 2.10) was carried out using the UTide package (Codiga, 2011) and compared to each other and output from a barotropic tidal model - AOTIM-5 (Padman and Erofeeva, 2004). The 59 leading tidal constituents in the region were extracted from the velocity records. The major tidal component velocities should not change notably over 25 km, or from year to year. The tidal flow speeds at KGA14 and KGA12, derived from the UTide analyses, are plotted against AOTIM-5 in Figure 2.12.

The UTide tidal flow speed distribution at KGA12 in 2013-14 agrees more closely with AOTIM output (Figure 2.12). Furthermore, the tidal flow speeds at KGA12 in 2013-14 agree well with the tidal flow speeds at the adjacent mooring - KGA14. Specifically, the mean flow speed at KGA14 is  $0.11 \text{ m s}^{-1}$  and the maximum flow speed is  $0.29 \text{ m s}^{-1}$  compared with a mean speed of  $0.11 \text{ m s}^{-1}$  and a maximum speed of  $0.27 \text{ m s}^{-1}$  at KGA12 in 2013-14 (compare panel a with panel d in Figure 2.12). Furthermore, the flow speeds from these deployments is in much closer agreement with the AOTIM flow speeds (Figure 2.12).

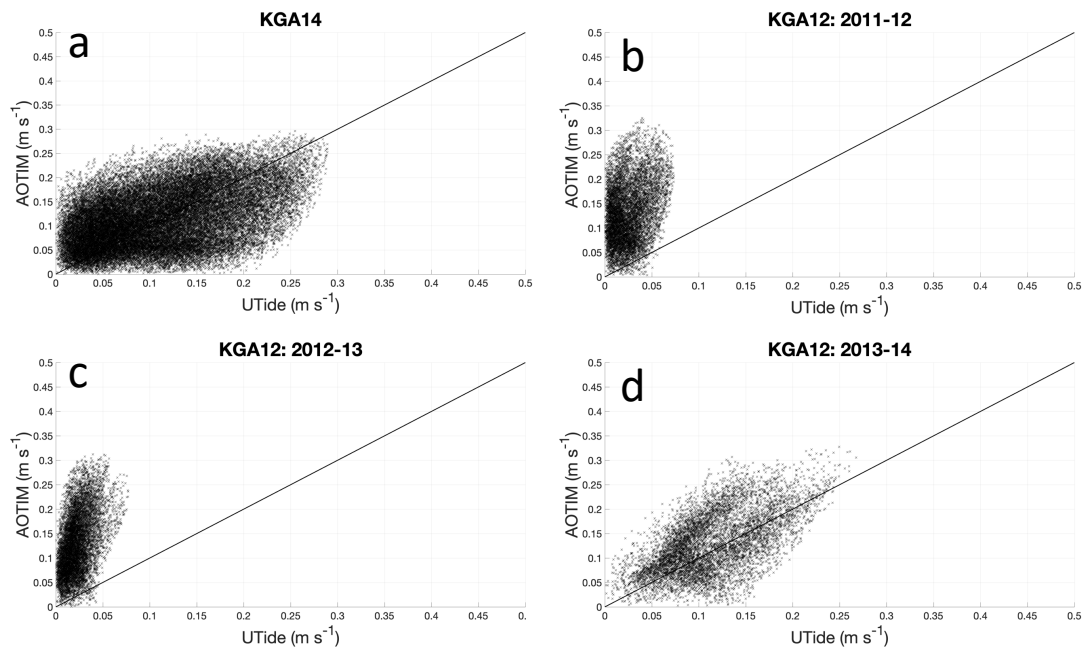


Fig. 2.12 Direct comparison between observed and modelled near-bottom tidal flow speeds on the Greenland shelf for a) KGA14 velocities between 2012-14, b-d) KGA12 velocities from individual deployments. The temporal resolution of all time series is one hour. The observed tidal flow speeds are derived from UTide analyses (Codiga, 2011) of ADCP velocity, from moorings deployed on the shelf (Figure 2.10), whilst the model speeds are from the AOTIM model. Note the very low flow speeds between 2011-13, compared with the higher flow speeds between 2013-14.

Conversely, flow speeds from the KGA12 2011-12 and 2012-13 deployments are much weaker than AOTIM flow speeds (Figure 2.12b-c). Therefore, either the ADCP velocities at KGA14 between 2012-14 and the velocities at KGA12 between 2013-14 and the AOTIM output are all erroneous, or the velocities at KGA12 between 2011-13 are erroneous. The latter case is more likely since the tidal speeds derived from the 2011-13 deployment do not match the modelled speeds. The error in the first two deployments may have derived from a set up error; the ADCP was programmed to record in earth coordinate mode, however the heading of the ADCP frame was not recorded, and this may regrettably have resulted in unsalvageable velocities (L. de Steur, pers. comms.).

## 2.3 ERA5

The fifth generation atmospheric reanalysis product from ECMWF (ERA5) is used in this study (Table 2.1). An atmospheric reanalysis is a numerical description of

atmospheric conditions, which incorporates historical atmospheric observations from a range of sources using modelling and data assimilation systems. Compared with ERA-Interim (the previous generation product), ERA5 uses a more advanced model, which builds on the previous model, and has a higher spatial (31 km) and temporal (1 hour) resolution (Hersbach et al., 2020). The data are accompanied by an uncertainty estimate, which is another new feature not available from ERA-Interim (Hersbach et al., 2020).

Data from the subpolar North Atlantic and Nordic Seas, east of Greenland are used in this study (Figure 2.13). Output from the previous generation of reanalysis product - ERA-Interim - was compared with shipboard observations around Denmark Strait, by Harden et al. (2011). They found excellent agreement for wind speeds, with strong wind events just  $1 \text{ m s}^{-1}$  weaker in ERA-Interim than in observations (Harden et al., 2011). Sea level pressure was also in excellent agreement.

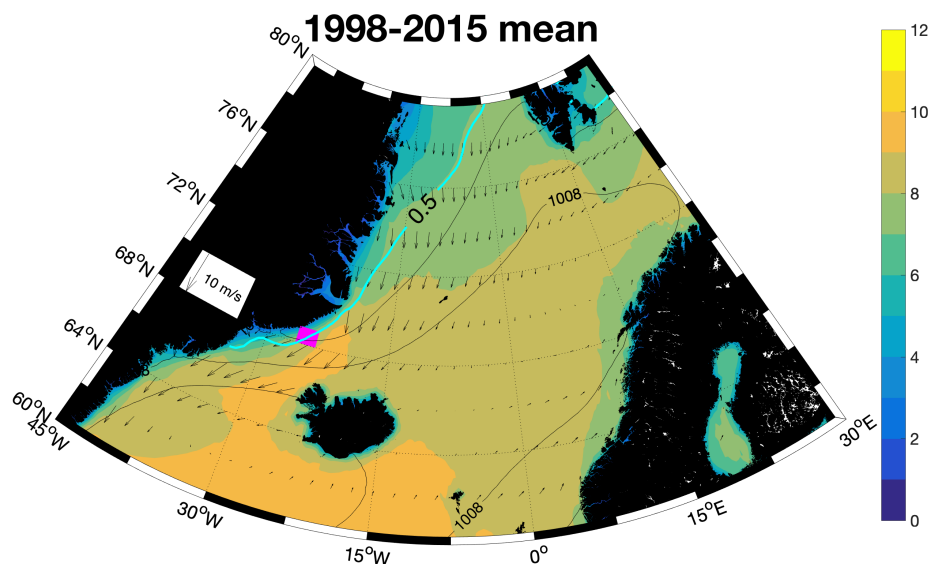


Fig. 2.13 Map of 1998-2015 mean of monthly mean wind, sea level pressure and sea ice concentration fields east of Greenland. The colours are wind speed, the quivers are wind vectors (both in  $\text{m s}^{-1}$ ), the black lines are sea level pressure contours (in hPa), and the thick blue line is the 0.5 sea ice fraction isoline. The  $10 \text{ m s}^{-1}$  wind velocity reference quiver is shown to the left of the map. The small pink area indicates the location of the hourly 2011-14 dataset used to investigate the impact of wind forcing on hydrographic variability of DSO source water north of DS.

Two separate datasets were downloaded and prepared for analysis in this thesis. Firstly, monthly averaged data from a large region covering the northeast Atlantic and the Nordic Seas are used (Figure 2.13). The wind data downloaded includes the zonal

(u) component, the meridional (v) component at 10 m above the ocean surface (in  $\text{m s}^{-1}$ ). In addition, sea level pressure (in mbar) and sea ice concentration data are used. The time period chosen (1998-2015) was selected because it coincides with the MC deployments at ANG (Figure 2.3).

The purpose of using this datasets is to investigate the role of atmospheric forcing in driving oceanographic processes which result in property anomalies in the DSO. Atmospheric data over the Greenland shelf and upper slope (Figure 2.13) at DS, and to the north, are investigated because previous research has shown that the action of the wind on the ocean here may have an effect on the salinity of the DSO (Hall et al., 2011; Håvik and Våge, 2018; Holfort and Albrecht, 2007). The 17 year period of concurrent atmosphere/ocean data is more than twice as long as previous research which has investigated the atmospheric forcing of DSO salinity (Hall et al., 2011; Holfort and Albrecht, 2007). Also, atmospheric data over the whole Nordic Seas and the subpolar northeast Atlantic are incorporated in order to investigate how the larger scale atmospheric patterns may be affecting the variability of DSO salinity in Chapter 5. Furthermore, in this thesis, three years of concurrent data are used, extending the analysis of Håvik and Våge (2018), who focussed on one year. The sea ice concentrations are used in Chapter 5 to investigate the influence of sea ice concentration on wind driven DSO salinity variability, since previous research has shown that the presence of sea ice modulates the momentum exchange across the atmosphere-ocean/sea ice boundary (Elvidge et al., 2016).

Secondly, a dataset with a high temporal resolution in the vicinity of the Greenland shelf at KGA is downloaded (see purple area in Figure 2.13). This dataset includes the absolute wind speed, and the wind speed in the zonal (u), and meridional (v) direction at 10 m above the ocean surface. The time series of the estimated error shows that it is not constant and some time steps are associated with higher error. This is an important caveat of using the higher resolution data. Wind variables from the period of the KGA mooring deployments (between 2011 and 2014) are used, in order to identify and characterise the impact of wind forcing on the ocean circulation to the north of DS, which may give rise to sustained property changes (on timescales beyond the eddy period) in the DSO downstream, at ANG, as will be presented in Chapter 4.

The ERA5 sea ice concentration data product is based on Ocean and Sea Ice Satellite Application Facility (OSI SAF) data, which processes different sources of microwave detecting satellite data in its algorithm (Eastwood et al., 2014). Sea ice is observed over the east Greenland continental margin (Figure 2.13), with highest concentrations occurring further inshore and to the north in months of the cold season.

The ERA5 uncertainty estimate is derived from the Ensemble of Data Assimilation (EDA) system. The EDA system estimates uncertainty in the observations, model parameterisations of physical processes, and the assimilation system (Hersbach et al., 2020). This system is used to estimate the errors of the sea ice concentration and wind used in this thesis. This thesis focuses on the atmospheric and sea ice conditions over the east Greenland continental margin, which have been previously proposed as regions where wind forcing can influence the salinity of the DSO (Hall et al., 2011; Holfort and Albrecht, 2007). Therefore, in the following error analysis, ERA5 uncertainty data from the region between 63.5°N 40°W (location of ANG) in the southwest and 80°N 0°W (Fram Strait) in the northeast, are used. The daily error estimate (at 12:00) of wind and sea ice concentration between 1998 and 2015 at each grid point of this region is used to construct the error estimate time series.

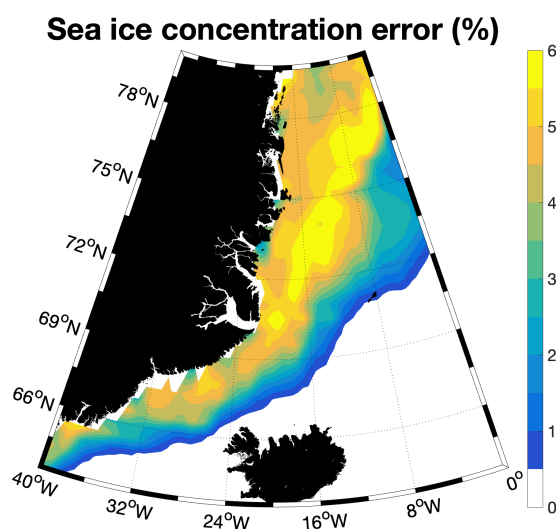


Fig. 2.14 Map of 1998-2015 time-mean distribution of daily sea ice concentration error estimate, derived from ERA5.

The time-mean error of the sea ice concentration estimate in this region peaks at  $>5\%$  on the Greenland shelf north of  $70^\circ\text{N}$  (Figure 2.14), although the error in some months can be higher. The error estimate at DS, and to the south of DS, is slightly lower, and largely  $<5\%$  (Figure 2.14). The size of the error also exhibits seasonality, with lower values in autumn, and higher values in the other seasons. The time-mean wind speed error in the region is  $0.44\text{ m s}^{-1}$ , whilst the individual errors associated with the zonal and meridional component are  $0.30\text{ m s}^{-1}$  for both (not shown). The error of the wind estimate is highest in the north Irminger Sea and Denmark Strait, where the wind speed error exceeds  $0.6\text{ m s}^{-1}$ . The size of both wind and sea ice concentration errors

decreased slightly with time between 1998 and 2015. The relatively small error of the ERA5 wind and sea ice concentration output gives confidence to the investigation of the relationship between remote winds and sea ice concentration and the salinity of the DSO presented in Chapter 5.

In the following chapter, the ANG dataset is used to characterise the intra-annual property variability of the DSO downstream of DS. These data are synthesised with upstream mooring data, from DS and KGA, to investigate the advection of property signals in the DSO on this timescale.



# Chapter 3

## Intra-annual and seasonal property variability of the Denmark Strait Overflow

### 3.1 Introduction

Unlike the volume transports, which are remarkably constant on timescales beyond the eddy period, the properties of the DSO exhibit variability on seasonal to multi-annual timescales (Dickson et al., 2008; Jochumsen et al., 2015). Property variability is important, because it reflects changes in the properties and/or contributions of source water masses. Furthermore, salinity and temperature anomalies may cause density anomalies, which will affect the evolution of the DSO; specifically its interaction with other water masses forming the lower limb of the AMOC. The salinity seasonality of DSO properties has been noted previously, on small ( $< 10$  years) subsets of the DSO time series (e.g. by Hall et al. (2011) and Jochumsen et al. (2015)), however the nature and origin of this seasonality are not well understood. Additionally, the competing effects of temperature and salinity on density variability of the DSO are not known.

To characterise any seasonal signal robustly, multiple years of sustained observations are required. In this chapter, multiple years of mooring data, recovered from the core of the DSO, at two locations east of Greenland (DS and ANG), are used and the KGA mooring observations, 200 km north of DS, are also used (Figure 1.8). Insights from the mooring observations are supplemented by hydrographic sections at DS to capture other sources of the DSO. These datasets are described in Chapter 2; see Table 2.1 in particular.

In this thesis, the terms intra-annual, seasonal, inter-annual and multi-annual variability are all used to discuss variability on different timescales. Intra-annual variability

occurs on timescales less than a year and could also be expressed as month-to-month variability. Seasonal variability means changes from season to season (i.e. meteorological seasons). Inter-annual variability means differences between two or more years, or the change in one year relative to another. Multi-annual variability means changes that occur over a two year period, or longer (e.g. a trend of increasing temperature over a five year period).

There is general consensus in previous literature that changing contributions of different source water masses to the DSO causes sustained salinity anomalies on intra-annual timescales (Hall et al., 2011; Holfort and Albrecht, 2007; Jochumsen et al., 2015; Rudels et al., 2002). Specifically, an increased contribution of PSW (see Chapter 1 for definition) to the DSO is associated with freshening. However, there is disagreement about how the salinity anomalies are advected from north of DS to the south of DS, where they have been observed by Hall et al. (2011) and Jochumsen et al. (2015). Whilst some studies claim that salinity anomalies originate from DS (Holfort and Albrecht, 2007; Jochumsen et al., 2015) - see Figure 1.8, others propose that salinity anomalies in fact originate from the region off the northeast Greenland coast, between Fram Strait and DS (Hall et al., 2011). Additionally, whilst some studies emphasise the role of atmospheric forcing (Hall et al., 2011; Holfort and Albrecht, 2007), others do not view wind forcing as important (Jochumsen et al., 2015; Rudels et al., 2002).

To shed light on the drivers of property variability, it is first necessary to understand the nature of the DSO property variability and its origin. The aim of this chapter is to characterise the seasonal property variability of the DSO and to investigate the advection of DSO source water masses and property anomalies from north to south, across the sill. The deployment of MC instruments at DS have hitherto been concentrated in the deep trough, and have thus not captured the variability of lighter DSO source water masses which make an important contribution to the property variability of the DSO downstream.

The four questions that this chapter seeks to answer are:

1. How does the salinity of the DSO vary seasonally?
2. Which property is the principal control on the density of the DSO, salinity or temperature?
3. How and why do the DSO freshening events vary in space and time?
4. Is the salinity seasonality of the DSO locally driven or derived from upstream variability?

The structure of this chapter is as follows. Firstly, in Section 3.2, the property variability of the DSO on low-frequency intra-annual timescales is investigated using 16

years of salinity, temperature and density measurements from ANG, a longer mooring time series than ever previously used. Furthermore, in this section, the role of temperature and salinity in density variability is examined. Following that, the sustained freshening phase of the seasonal cycle is characterised by analysing the year-to-year and the cross-stream variability (Section 3.3). Thirdly, in Section 3.4 the property variability of the DSO at DS is analysed, and compared with the variability at ANG, 500 km downstream. Fourthly, in Section 3.5 the KGA salinities from 2011-12 are combined with concurrent salinities from DS and ANG to investigate the advection of property anomalies from the DSO source water observed at KGA, and the DSO at DS and ANG. Conclusions are drawn in Section 3.6.

## 3.2 Temporal variability of DSO properties at ANG

Property time series at ANG from 1998 to 2015 are shown in Figure 3.1. The data are from mooring UK1, which is deployed on the lower Greenland slope at 2000 m in the core of the overflow and the processing steps for this salinity time series are described in Chapter 2. The focus of this section is on the intra-annual property variability, and therefore the salinity time series was filtered with a 2nd order band-pass Butterworth filter, with cut off frequencies of 20 days and 400 days (Chapter 2), and the salinity spectrum is shown in Figure 3.2. However, some observations about the multi-annual variability precedes the investigation of the intra-annual variability.

### 3.2.1 Multi-annual variability

The DSO warms and salinifies between 1998-99 and 2012 (Figure 3.1b and c). Salinity increases from a deployment mean of 34.86 in 1998-99 to 34.90 in 2012 and temperature increases from 1.5 °C to 1.8 °C over the same period. To quantify these trends, and test their statistical significance, a linear model was fitted to the time series. The integral timescale of the time series is greater than 1 month, and therefore the annual average time series (Figure 3.1) are used to quantify the trends, since each data point in these time series are statistically independent from each other. The rate of salinity increase is  $0.0026 \text{ year}^{-1}$  and the rate of temperature increase is  $0.023^\circ\text{C year}^{-1}$ , the regression coefficient ( $R^2$ ) is 0.50 for salinity and 0.54 for temperature and both trends are statistically significant at the 95% level. As a result of the salinification, the density increases slightly from  $27.90 \text{ kg m}^{-3}$  to  $27.91 \text{ kg m}^{-3}$  between 1998 and 2012 (Figure 3.1a) (this trend is not statistically significant at the 95% level). This shows that the salinity trend has a greater effect on density than the temperature trend, thus salinity is controlling the density variability on this timescale.

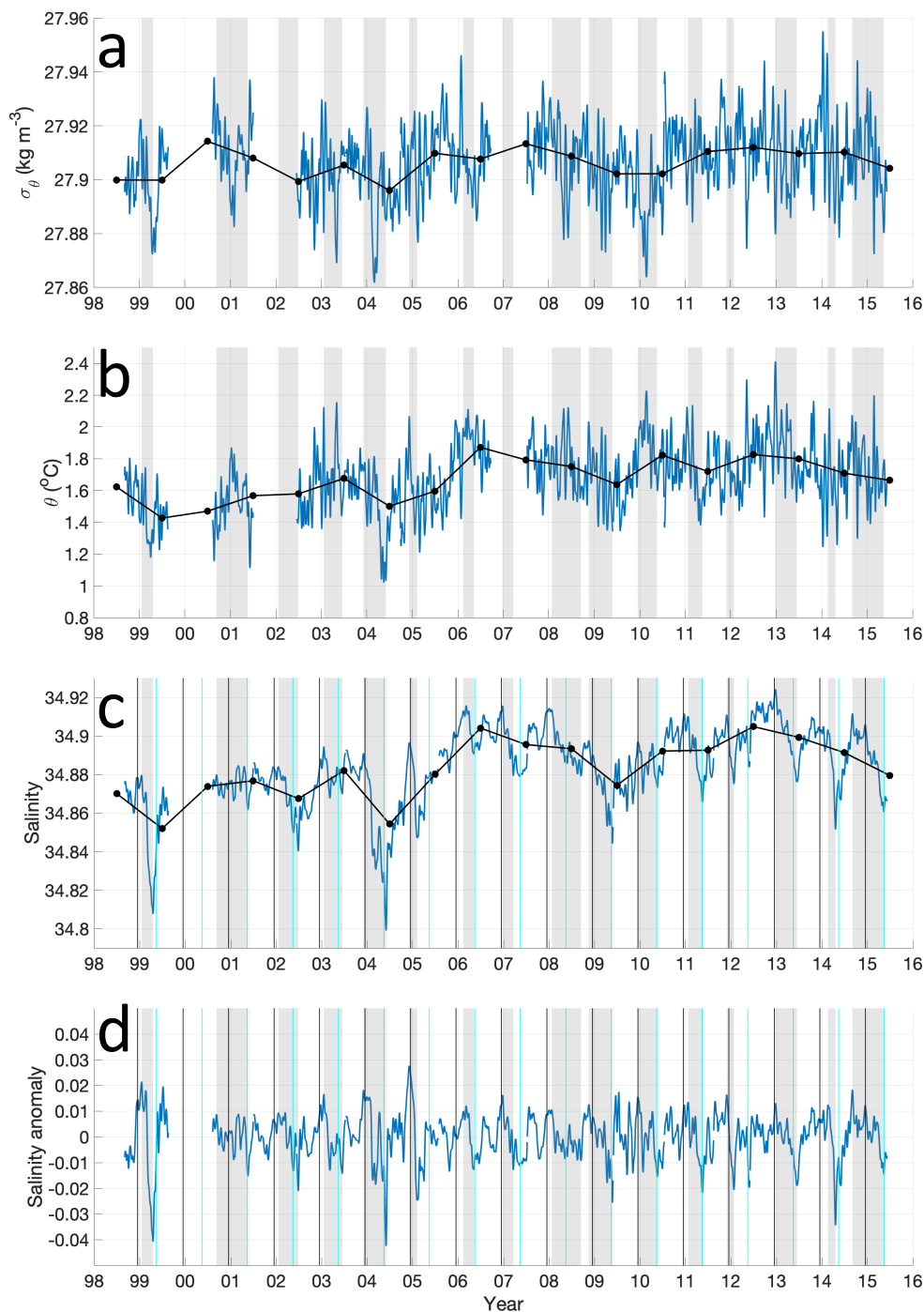


Fig. 3.1 Smoothed time series between 1998 and 2015 of density (a), temperature (b), salinity (c) and salinity anomaly (d) of the DSO from mooring UK1 at ANG (see location of mooring in Figure's 1.8b and 2.2). Time series a-c are filtered with a 2nd order low-pass Butterworth filter, with a frequency cut off of 20 days, whilst the salinity anomaly time series (d) is the anomaly from the time-mean after being smoothed with a 2nd order band-pass Butterworth filter, with frequency cut offs of 20 days and 400 days. Small gaps during mooring turnover are filled using linear interpolation. The grey shaded areas indicate the sustained freshening periods, defined as the period between the cold-season maximum and annual minimum in the salinity anomaly time series (d). The joined black dots in panels a-c are the annual mean properties. The black and cyan vertical lines in panels c and d mark 15 December and 15 May respectively, to emphasise the salinity seasonality.

Before 2000, in the second half of the 20th century there was sustained multidecadal freshening of 0.04 between the 1960s and 1990s (Dickson et al., 2002). The freshening was linked to freshening of the DSO source waters in the upper layers of the Nordic Seas (Dickson et al., 2002). While beyond the scope of this thesis, the cause of the reversal of this freshening trend since 1998 (Figure 3.1) may be decreasing precipitation since 1998.

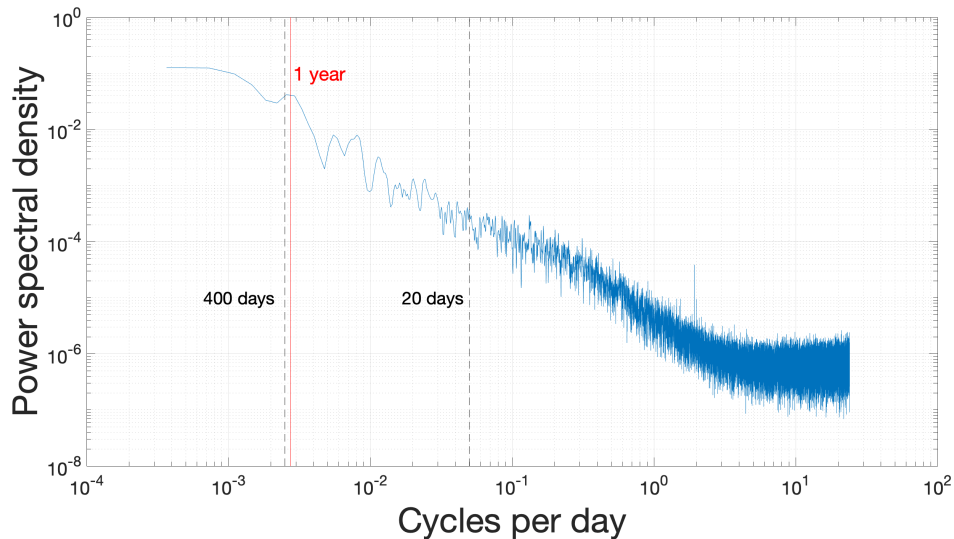


Fig. 3.2 Spectrum of DSO salinity at ANG. The salinity time series derive from the UK1 mooring between 2000 and 2015. This was created using the Welch periodogram method with a Hanning window of 4 years and 50% overlap between segments. The gaps associated with mooring turnaround were filled using linear interpolation. The cut off frequencies, used for the band-pass Butterworth filter, are indicated by the dashed black lines and the 1 year peak is marked by the red line.

Alternatively, the increasing salinity trend might be a result of the increasing salinity (and temperature) of the Atlantic inflow into the Nordic Seas between the mid 1990s and mid 2000s (Holliday et al., 2008). These inflow waters were shown to feed the overflows after circulating around the Nordic Seas or Arctic Ocean, where they are cooled by the atmosphere and acquire higher densities as a result (Mauritzen, 1996) (for background, see descriptions of Recirculating Atlantic Water (RAW) and Arctic Atlantic Water (AAW) in Chapter 1). However, the testing of the proposed mechanisms of long term property changes is left to future work because the focus of this work is on shorter timescales.

Superimposed on the long term trend, there are shorter timescale (multi-annual) phases of cooling and freshening (Figure 3.1b and c). Firstly, the temperature cools from 1.9 °C in 2006 to 1.6 °C in 2009 and the salinity decreases from 34.9 to 34.87

and the density decreases from  $27.91 \text{ kg m}^{-3}$  to  $27.90 \text{ kg m}^{-3}$  over the same period. Secondly between 2012 and 2015, the DSO freshens from 34.90 to 34.88 and cools from  $1.8 \text{ }^\circ\text{C}$  to  $1.6 \text{ }^\circ\text{C}$ , and becomes slightly lighter. The response of density demonstrates that salinity is also controlling density variability on multi-annual timescales. What are the causes of this shorter timescale multi-annual variability? One possibility is that the variability is also advected from the Atlantic inflow to the Nordic Seas, as proposed for the longer term property changes. Alternatively, atmospheric forcing at DS has been linked with overflow property variability on these timescales (Holfort and Albrecht, 2007). However, the focus of this thesis is on DSO property variability on seasonal timescales.

### 3.2.2 Intra-annual variability

The property variability on intra-annual timescales exceeds the longer term variability, which is discussed above. Sustained periods of freshening are detected in the band-passed salinity time series and are indicated by the grey shading in Figure 3.1. Each year, the maximum is usually in winter and the minimum usually in the following spring, with the freshening period in between. The period between the September-February maximum and the minimum in the following year (or the same year if the maximum is in January/February), in the band-passed time series (Figure 3.1d) is shaded grey in all panels of Figure 3.1. The freshening period is almost always in winter and spring, usually beginning in December. The apparent seasonality of the freshening events raises the question: do DSO properties exhibit a robust seasonal cycle?

To investigate the question, composites of property anomalies for each day of the year were calculated and the intra-annual variability is shown in Figure 3.3. Here, the median and inter-quartile range of the temperature and salinity anomaly is shown as a function of day of the year. The median is used to minimise the impact of outliers, which have a greater influence on the mean than the median, since each day of the year is composed of just 16 data points.

Salinity exhibits a clear seasonal cycle (Figure 3.3a). Positive salinity anomalies are observed in winter with a maximum in mid-December of  $+0.010$ . This is followed by a period of sustained freshening for five months until mid-May when the salinity anomaly is at a minimum of  $-0.010$ . This freshening pattern is reflected in the inter-quartile range too, with the upper quartile falling below  $-0.005$  in May and the lower quartile rising above  $0.005$  in December. They are also detectable in the range. This period reflects the sustained freshening periods highlighted in Figure 3.1d.

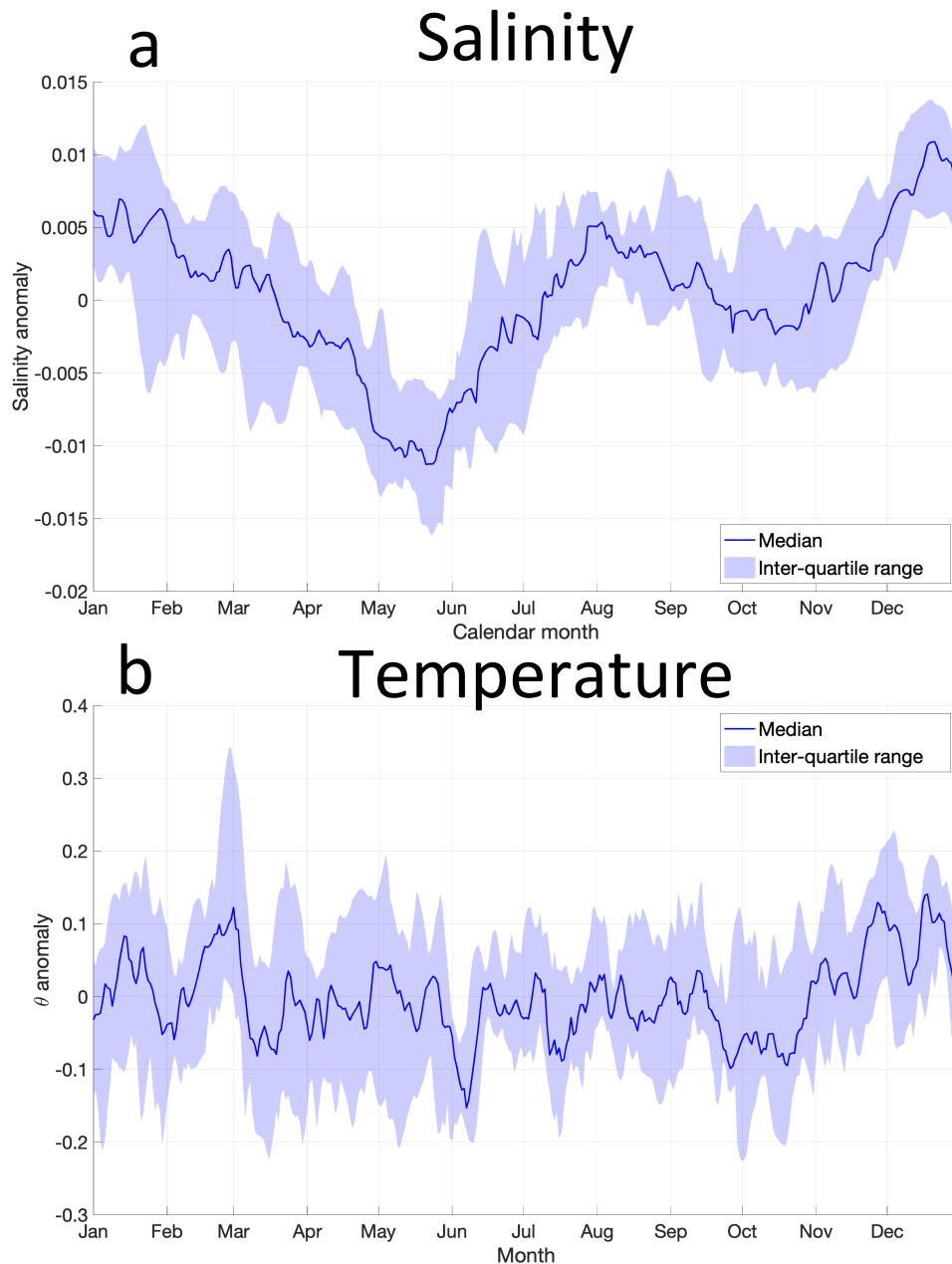


Fig. 3.3 Intra-annual (i.e. month-to-month) variability of DSO salinity (a) and temperature (b) anomaly at ANG. The sampling frequency of the time series is 1 day, since a composite is created for all years for each day of the year. These are the anomalies from the long-term means and the data are filtered using a 2nd order band-passed Butterworth filter with timescale cut-offs of 20 days and 400 days to focus on the lower frequency component of the intra-annual variability. The thick blue line is the median and the blue shaded area is the inter-quartile range. Note the salinity minimum is in May and maximum in Dec (see cyan and black lines in Figure 3.1c and d), the interquartile range in May does not overlap with the interquartile range in the other seasons.

In addition, salinity increases towards a maximum of 0.005 in July before a freshening period between July and October when a salinity minimum of -0.004 is reached before rapidly increasing towards the December maximum (Figure 3.3a). This secondary freshening event is around half the size of the freshening event in the first half of the year. Note that this freshening pattern is not so clearly manifest in the interquartile range, compared with the winter-spring freshening. The timing of the secondary minimum (autumn) implies that it may result from increased meltwater concentrations due to the melting of sea ice and the Greenland ice sheet in summer, which causes the DSO sources, located near the surface north of DS (Harden et al., 2016), to freshen. However, the focus of this work is on the first minimum in May.

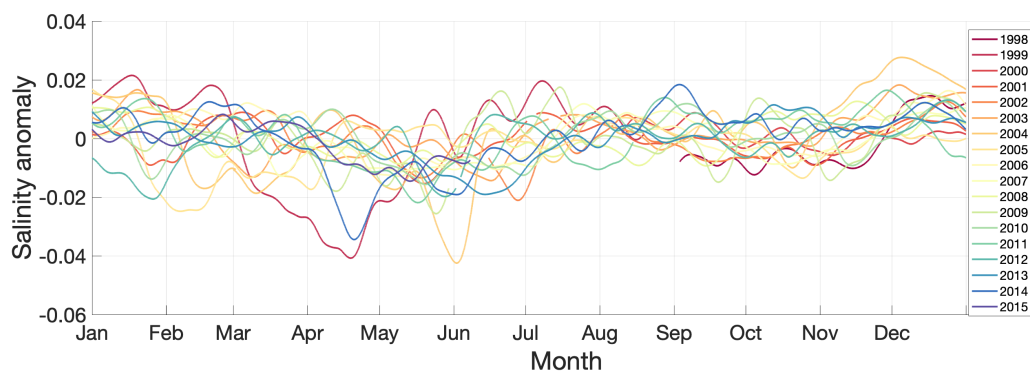


Fig. 3.4 Salinity variability of the DSO at ANG as a function of calendar month between 1998 and 2015. Each colour represents a different year and the salinity anomaly is defined as the anomaly from the long term mean of the bandpass filtered time series (i.e. Figure 3.1d).

Figure 3.3b shows the annual variability of temperature at the ANG array. Two separate temperature minima are evident in the median and interquartile range. The temperature minimum in June is  $-0.18^{\circ}\text{C}$ , whilst the minimum is  $-0.1^{\circ}\text{C}$  in October. On the other hand temperature anomaly maxima ( $0.10^{\circ}\text{C}$ ) occur in December and late February/early March. The intra-month variability of temperature exceeds that of salinity and the year-to-year variance of temperature is also high (Figure 3.3b). As a result, there is no statistically significant annual cycle of temperature. For instance, the minimum in June is transient compared with the sustained salinity minimum in May (Figure 3.3).

For completeness, the salinity anomaly time series in different years are shown as a function of calendar month in Figure 3.4. This demonstrates the year to year differences in the salinity variability, whilst highlighting particularly low salinities in 1999, 2004 and 2014, which may also be observed in Figure 3.1d. Nevertheless, the sense of the salinity seasonality remains clear in Figure 3.4.

Moreover, a linear regression model with a frequency of one cycle per year was fitted to the observations. This frequency is associated with a high amount of variance, as shown by the peak in the spectrum (see red line in Figure 3.2). The observations are shown against the linear regression model in Figure 3.5. The model appears to represent the salinity seasonality reasonably well. The peak to trough amplitude of the model is 0.02 (Figure 3.5), which is in agreement with the intra-annual variability demonstrated in Figure 3.3, with the maximum in November and the minimum in May. The seasonal signal represented by the linear regression model explains approximately 37% of the variance of the monthly averaged salinity time series (Figure 3.5). This demonstrates that the seasonal signal is an important component of the total variability.

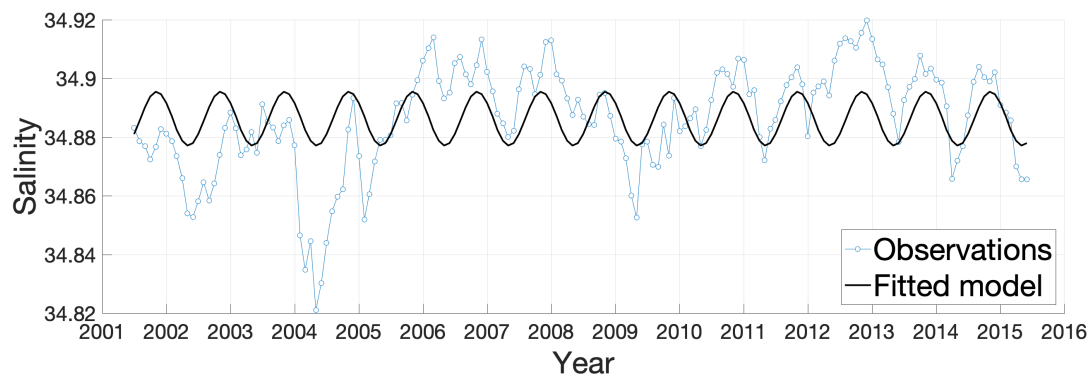


Fig. 3.5 Salinity time series comparison between mooring observations and a linear regression model with an annual (i.e. 365 day) frequency. The observations are the monthly averaged salinity at mooring UK1 at ANG. The fitted model is created from a spectral analysis of the monthly averaged time series using Fourier transformation.

### 3.2.3 Effect of temperature and salinity on density

The intra-annual variability of salinity and temperature (Figure 3.3) both impact the intra-annual density variability, which is investigated below. Comparing the annual salinity variability with the temperature and density variability, shows that the winter/spring freshening causes a negative density anomaly, despite the coincident cooling compensation (Figure 3.6a). On the other hand the secondary freshening event is associated with comparable cooling, which compensates and causes a positive density anomaly. The density minimum is in May (median:  $-0.006 \text{ kg m}^{-3}$ ) and in October the density anomaly is at a maximum ( $+0.005 \text{ kg m}^{-3}$ ). The two strongest freshening events on record - 1998-99 and 2003-04 caused strong negative density anomalies of  $-0.02$  and  $-0.03 \text{ kg m}^{-3}$  respectively (not shown). This raises the question: which property is the principal control on density?

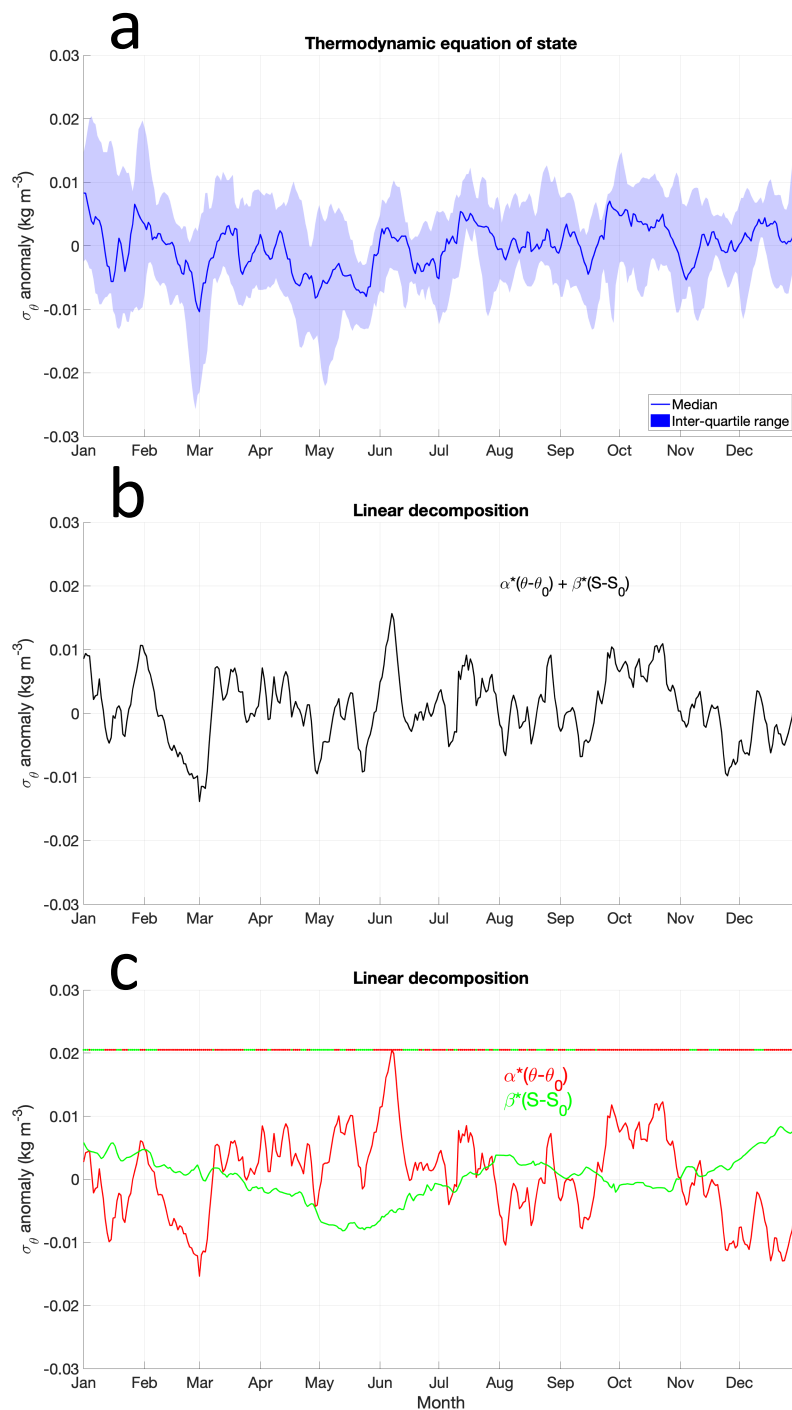


Fig. 3.6 Comparison of the intra-annual density variability, from the TEOS-10 software (a), and a linearised decomposition (b and c) at ANG. Whilst (b) shows the sum of the linearised decomposition of the equation of state, (c) shows the temperature (red) and salinity (green) terms in the linearised decomposition of the equation of state. The coloured dots in the bottom panel indicates which term is dominating the density variability (green=salinity, red=temperature). The band-passed time series (with time-mean removed) of temperature, salinity and density are used for the anomalies ( $T - T_0$ ,  $S - S_0$  and  $\rho - \rho_0$  respectively) - see Figure 3.3. Note that both temperature and salinity terms play a role in density variability, with salinity dominating in May and causing a negative density anomaly.

Figure 3.6c shows the contributions from the salinity term and the temperature term in the linearised equation of state. The equation used is adapted from Talley (2011):  $\rho - \rho_0 = \alpha(T-T_0) + \beta(S-S_0)$ , where  $\rho - \rho_0$  is the density anomaly,  $\alpha$  and  $\beta$  are the thermal expansion and haline contraction coefficients respectively and  $(T-T_0)$  and  $(S-S_0)$  are the temperature and salinity anomaly respectively (see Figure 3.3). This equation decomposes the density anomaly ( $\rho - \rho_0$ ) into the salinity term ( $\beta(S-S_0)$ ) and temperature term ( $\alpha(T-T_0)$ ). The thermal expansion ( $\alpha$ ) and haline contraction ( $\beta$ ) terms were calculated using the TEOS10 Gibbs Sea Water toolbox (McDougall and Barker, 2011). The agreement between the (non-linear) density anomaly, and the density derived from the linearised equation of state, is excellent (compare Figure 3.6a and b).

It is determined that temperature controls density for two thirds of the year and salinity is dominant in the other third (Figure 3.6c). For 249 days the temperature term dominates, especially for long periods in late summer and autumn. For the other 116 days, the salinity term controls the density variability, notably in January and May, when the negative salinity anomaly results in a negative density anomaly of  $-0.005 \text{ kg m}^{-3}$  Figure 3.6a. This means that the salinity dominates density in the May freshening event, causing a negative density anomaly. Examples of negative density anomalies during freshening events can be seen in Figure 3.1, for example in 1999 and 2004, when density minima of  $27.875 \text{ kg m}^{-3}$  and  $27.865 \text{ kg m}^{-3}$  respectively occur during spring freshening.

The importance of both temperature and salinity terms in the density variability of the DSO highlights its sensitivity to future changes in either property. At present, the temperature variability controls density variability for most of the year, but salinity can also play an important role. Should the ocean temperatures in the subpolar North Atlantic increase in the coming decades, as predicted by climate models forced by different greenhouse gas (GHG) emission pathways (Collins et al., 2013), the role of temperature variability may become more dominant, because the  $\alpha$  term becomes larger at higher temperatures. However, the fluctuations in temperature ( $T-T_0$ ) and salinity ( $S-S_0$ ) also affect the density. It is not clear whether the magnitude of temperature/salinity fluctuations will increase or decrease, or stay the same, in the coming decades.

### 3.3 Sustained intra-annual freshening events

The intense freshening events in 1999 and 2004, highlighted above, that cause negative density anomalies are just two examples of sustained freshening events, which occur in most years in the DSO at ANG (Figure 3.1). These events are defined by the time

between the salinity maximum and minimum in the following year (or the same year if the maximum is in January/February), in the band-passed time series (Figure 3.1d). The freshening intensity is defined as the peak to trough salinity difference of the low-passed time series, and the freshening duration is time taken between maximum and minimum. The variability of the freshening events in space and time has not been adequately investigated to date, and thus a thorough investigation is the objective of this section. By answering the question of how the freshening events vary, one might find explanations for an important follow up question, i.e.: why do the freshening events vary?

### 3.3.1 Temporal variability

Particularly strong freshening (i.e. change in salinity:  $\Delta S < -0.05$ ) is observed in 1998-99, 2003-04, 2004-05, 2008-09, 2013-14 and 2014-15. Of these the strongest individual freshening events were in 1998-99 and 2003-04 when freshening intensity was -0.07 and -0.09 respectively, causing a sustained salinity minimum of around 34.8. This greatly exceeds the intensity of multi-decadal freshening in the latter half of the 20th century, which was approximately -0.04 (Dickson et al., 2002), or the interannual freshening trend between 2006-09 and 2012-15, which was -0.03 and -0.02 respectively.

As well as magnitude, the duration and phase of the freshening events is different from year to year too. Typically the duration of the freshening events is around 4 months, however there are some exceptions. For instance, longer than average freshening ( $> 6$  months) occurs in 2008 (freshening between January and September with the salinity minimum in September that year). Additionally, in 2008-09 the freshening event lasted 6 months, starting in November 2008 and ending in May 2009. On the other hand the freshening is more transient in 2004-05 when freshening occurs between December and February with salinity minimum in February. Other examples of brief freshening are between March and May 2006 and a succession of transient events in 2009-10 cause multiple salinity minima, but no single minimum.

### 3.3.2 Cross-stream variability

As has been shown above, the salinity of the DSO exhibits multi-month variability with freshening in winter-spring. However, this analysis has primarily been based on a single mooring - UK1 at ANG. It remains to be seen whether this variability is consistent across the width of the DSO. By using observations from neighbouring moorings, relevant questions can be answered: do salinity anomalies occur at different points across the width of the DSO and if so how do the anomalies vary cross-stream? Are the

anomalies comparable in phase and magnitude, or do they differ? By answering these questions, an investigation into the likely origins of the freshening events can begin.

Here, near-bottom MC salinities from moorings UK2 and F1F2/F2 are incorporated (See Chapter 2). Whilst UK2 is located downslope from UK1, at a bottom depth of around 2350 m, F1F2 and F2 are both located upslope, close to the 1700 m isobath and are separated by just 8.5 km (Figure 2.3 in Chapter 2). Mooring F2 was deployed in 2003-04 and 2009-12 and F1F2 was deployed in 2004-07. Thus, for simplicity, salinities at F1F2 and F2 are combined and referred to as salinity at a single mooring 'F' hereafter. The calibrated (see Chapter 2) time-mean density is  $27.88 \text{ kg m}^{-3}$  at F,  $27.91 \text{ kg m}^{-3}$  at UK1 and  $27.94 \text{ kg m}^{-3}$  at UK2. Therefore, all three moorings occupy the dense DSO.

The sustained freshening is generally amplified up the slope, at the shallower F and UK1 moorings, compared with the deeper UK2 mooring. This is illustrated in Figure 3.7, which shows the freshening intensity ( $\Delta S$ ) across the ANG array between 2004 and 2015, when two or three moorings occupied the water every year. Freshening is more intense at F (bottom depth: 1700 m) and/or UK1 (bottom depth: 2000 m) than UK2 (bottom depth: 2350 m) in 11/12 of all years. The median intensity at UK1 and F is -0.05, compared with -0.03 at UK2. The only year where the freshening was most intense at UK2 was in 2005-06, when the freshening at UK2 was -0.029, compared with -0.027 at UK1 and -0.023 at F (Figure 3.7).

The freshening events cause fresher water to be observed upslope, at UK1, compared with downslope, at UK2, in spring. In the other seasons (summer through to winter) the water down the slope, at UK2, is more fresh than the water found up the slope, at UK1. This is demonstrated in Figure 3.8, which shows the salinity at UK1 minus UK2 for the ten simultaneous deployment years. The salinity difference maximum is in September (+0.006) and the minimum is in May (-0.003). This shows that the winter/spring freshening signal exhibited in Figure 3.3, is clearly concentrated upslope and attenuates downslope in the denser classes of DSO. This indicates an onshore origin of the freshening events. The strong freshening in spring causes a negative density anomaly at that time, as shown in Figure 3.6. However, a similar density anomaly occurs at UK2 (not shown) and therefore the signal does not cause a change in the cross-stream density gradient.

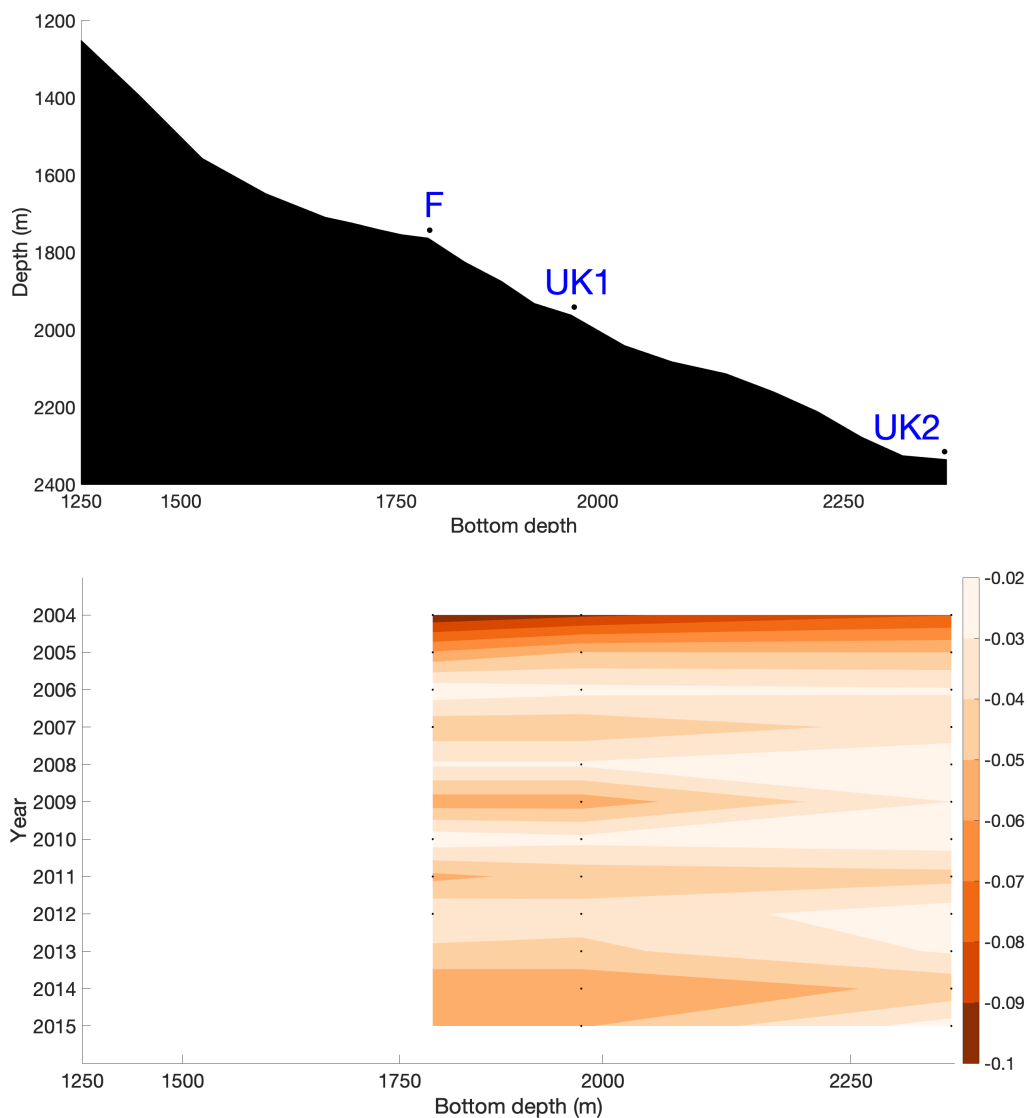


Fig. 3.7 Time series of freshening intensity across the DSO at ANG. The top panel shows the location of the ANG moorings on the Greenland slope and bottom panel shows the freshening intensity over the years at the different mooring locations. The dots indicate the mooring locations. Time series gaps at F are set to the value at UK1 and vice versa. Freshening is consistently greater at shallower isobaths (lighter DSO) between 1750 m and 2000 m (F and UK1) than further down the slope at 2300 m (UK2).

There is also some indication of a phase lag (upslope leading downslope) in the 11 years of concurrent salinities from UK1 and UK2. This result is interpreted as a more general result for the DSO salinity variability, rather than being specific to the freshening events. In fact, salinity correlation between the adjacent moorings (on advective timescales) is maximised ( $r=0.93$ ,  $p<0.05$ ,  $R^2=0.60$ ) when the UK1 time series leads UK2 by 3 days (not shown). The correlation was calculated using 11 years

of concurrent data between 2003 and 2015. Time series were smoothed prior to the calculation, using a 20 day centred moving mean filter, after which each time series had 30 degrees of freedom, and this reduced number of degrees of freedom was accounted for in the calculation of statistical significance of the correlation.

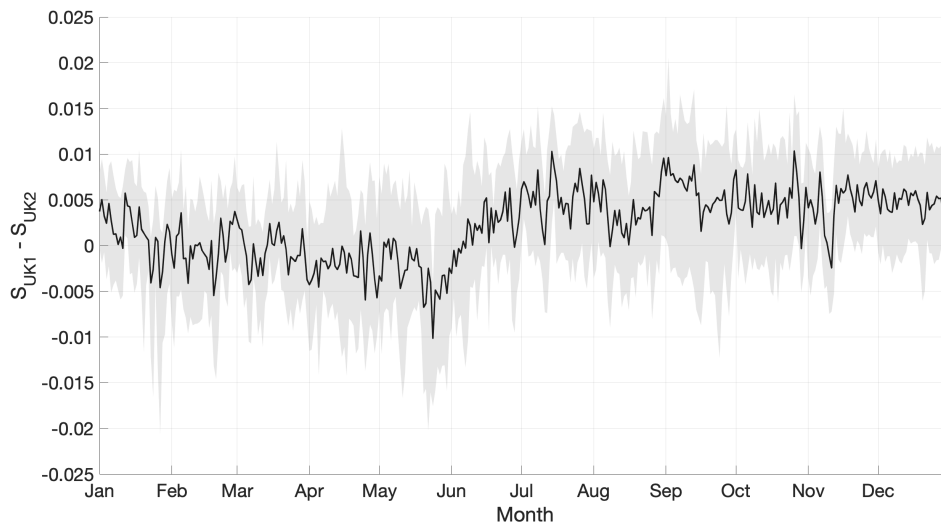


Fig. 3.8 Salinity at mooring UK1 minus salinity at mooring UK2 composite as a function of day of year. This composite was constructed using 11 years of simultaneous data between 2003 and 2015. Contrast the period of negative values in spring (UK1 fresher than UK2) with the positive values during the rest of the year (UK2 fresher than UK1). This is a signature of the sustained freshening period.

The lagged correlation is likely a result of variable DSO plume speeds; higher velocities are observed at UK1 (and F) than at UK2 (see Figure 2.2 in Chapter 2) enabling the faster advection of signals to UK1 than UK2. The median speeds at F and UK1 are  $0.25$  and  $0.24$   $\text{m s}^{-1}$  respectively, compared with  $0.22$   $\text{m s}^{-1}$  at UK2. This is consistent with the velocity observations in 2007-08 at the Spill Jet section, 250 km upstream of ANG, where maxima DSO velocities ( $0.24$   $\text{m s}^{-1}$ ) are observed upslope in lighter classes of the current (not shown). DSO flow speeds vary on short timescales, but on timescales beyond 5 weeks, the flow speeds are constant (Dickson and Brown, 1994). The advection time from DS to ANG (a distance of 500 km) is 23, 24 and 26 days for advection speeds of  $0.25$ ,  $0.24$  and  $0.22$   $\text{m s}^{-1}$  respectively. Therefore, the 3 day lag of the salinity correlation between moorings is possibly a result of variable advection speeds across the DSO. In reality, transit times between DS and ANG are shorter since DSO advection speeds are higher upstream of ANG (Dickson and Brown, 1994; Jochumsen et al., 2015). Nevertheless, the slower advection speeds at the deeper UK2 mooring, demonstrated here, and at the deeper moorings at the Spill Jet section,

show how signals may appear here after they manifest at the shallower moorings where advection speeds are greater.

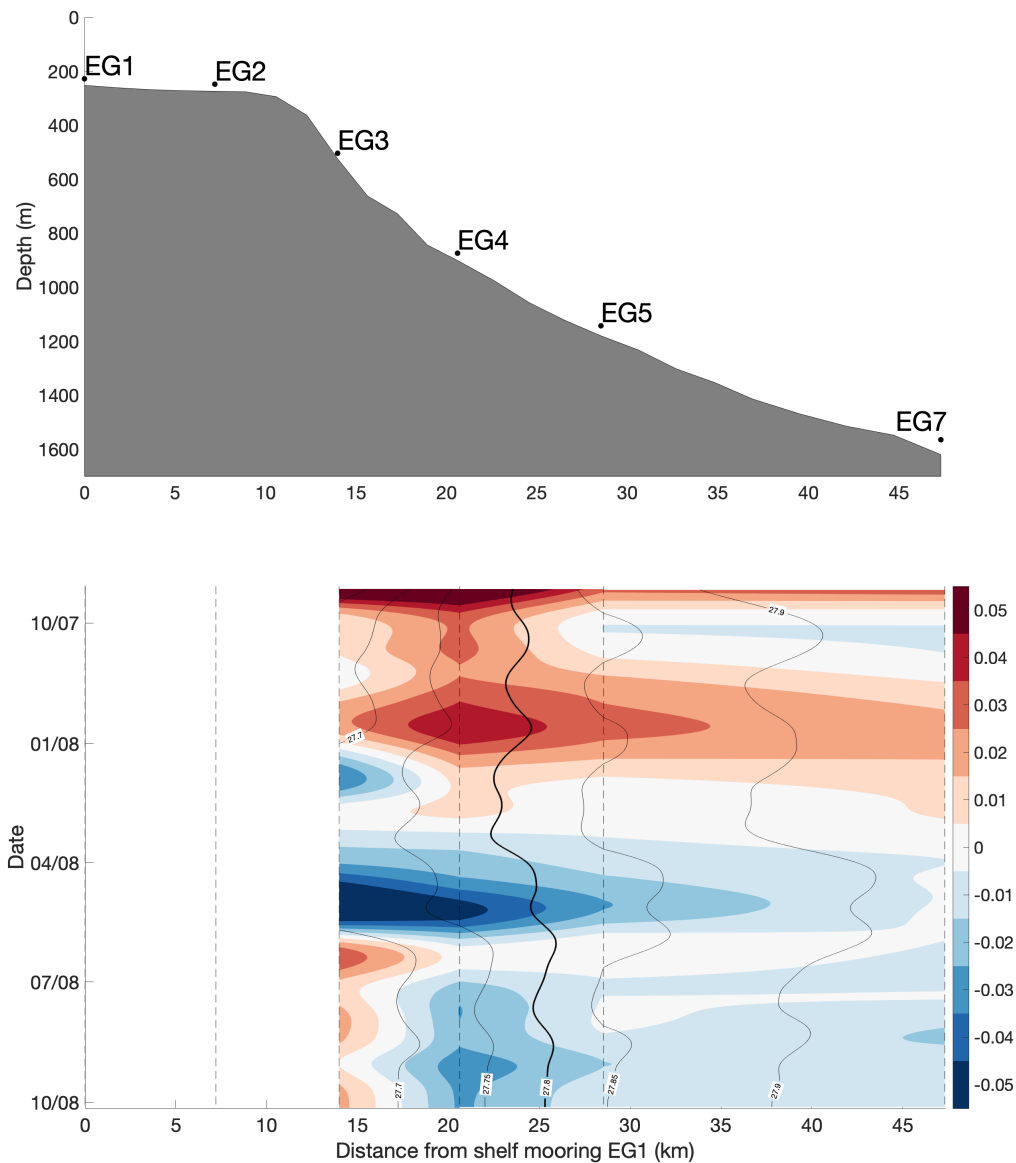


Fig. 3.9 Time series of salinity anomaly (deployment mean subtracted from each mooring) of the near-bottom water across the slope at the Spill Jet section (Figure 1.8), in 2007-08. The top panel shows the locations of the near-bottom MCs deployed with each mooring on the Greenland slope, which are used to create the time series in the bottom panel. The bottom panel has colours representing the salinity anomaly and the black lines are isopycnals; the thick black line is the  $27.8 \text{ kg m}^{-3}$  isopycnal, which is traditionally used as the upper boundary of the DSO. Note that freshening of the DSO water ( $\sigma_{\theta} > 27.8 \text{ kg m}^{-3}$ ) at the offshore mooring is concurrent with freshening up the slope, where the anomalies are more extreme.

The increased freshening intensity of the DSO up the slope raises the possibility that the freshening events originate from the upper Greenland slope, or even the Greenland shelf. To investigate, salinities from MC instruments deployed further up the slope from the DSO, in lighter water masses, were used. Specifically, two moorings were deployed between the 500 m and 900 m isobaths at the Spill Jet section in water lighter than  $27.8 \text{ kg m}^{-3}$  (Figure 3.9), located 250 km upstream of ANG (Figure 1.8). Note that the upper boundary of the DSO (i.e. the  $27.8 \text{ kg m}^{-3}$  isopycnal) is found between the EG4 and EG5 moorings (Figure 3.9).

The DSO freshening at the Spill Jet section coincides with freshening up the slope in lighter water classes ( $27.7 \text{ kg m}^{-3} < \sigma_\theta < 27.8 \text{ kg m}^{-3}$ ) at mooring EG4 (Figure 3.9). The freshening is intensified in the lighter water, for example in April 2008 the salinity anomaly at EG4 is around -0.05, compared with -0.01 at EG7, and in summer the salinity minimum at EG4 is -0.03, compared to -0.02 at EG7. The salinity of the core of the DSO (represented by the time series from mooring EG7;  $\sigma_\theta > 27.9 \text{ kg m}^{-3}$ ) is at its minimum in August 2008 (Figure 3.9). This is unusually late on in the year for the salinity minimum to occur, however it is consistent with the DSO salinity time series at ANG, where the minimum occurs up to 1 month after in August/September 2008 (see Figure 3.1). The evidence of DSO freshening coinciding with freshening up the slope from the DSO in lighter water at the Spill Jet section provides further evidence that the freshening may have an onshore origin.

### 3.4 Intra-annual variability of DSO properties at the Denmark Strait sill

In order to determine the origin of the freshening events, the logical first step is to investigate the variability of DSO source water masses upstream of ANG, at DS. Both moorings and CTD sections occupying DS (Figure 1.8) are used in this study. A near-bottom MC instrument was deployed on mooring DS 2 (situated in the deep trough over the 580 m isobath (Figure 3.10)) in most years between 2005 and 2015. This mooring occupies the densest  $\sigma_\theta > 28 \text{ kg m}^{-3}$  and fastest moving ( $v = 0.5 \text{ m s}^{-1}$ ) water of the DSO, which is generally viewed as the overflow core (Jochumsen et al., 2015, 2017). The location of the DS mooring time series, investigated below, is shown in Figure 3.10.

Conversely, the gridded CTD sections measures a greater cross-sectional area of the DSO, but are limited to synoptic snapshots each season (Mastropole et al., 2017). The CTD data used are the gridded product of CTD occupations of the DS section between 1990 and 2012, created by Mastropole et al. (2017), supplemented with additional snapshots since 2012 (see Chapter 2). Only the CTD data within the DSO, according to

the traditional definition ( $\sigma_\theta > 27.8 \text{ kg m}^{-3}$  (Dickson and Brown, 1994)) and between the Greenland shelf and Iceland shelfbreak, are used in this chapter (Figure 3.10). Whilst dense water is also observed on the Greenland shelf (von Appen et al., 2014), data are not available here in all the seasons and therefore these data were not included in this analysis of the property seasonality of the DSO.

### 3.4.1 Densest water

Property time series at DS 2 are shown in Figure 3.11. Salinity has increased steadily here from 34.88 in 2004-05 to 34.92 in 2014-15, while the temperature oscillates around a time-mean of  $0.2 \text{ }^\circ\text{C}$  but does not exhibit a clear trend (Figure 3.11b and c). As with the ANG time series, a linear model was also fitted to the annual average DS time series to quantify the trend and test the statistical significance (see Section 3.2 for justification). The rate of salinity, temperature and density change is  $0.0037 \text{ year}^{-1}$  ( $p < 0.05$ ),  $-0.0008 \text{ }^\circ\text{C year}^{-1}$  ( $p > 0.05$ ) and  $0.003 \text{ kg m}^{-3} \text{ year}^{-1}$  ( $p < 0.05$ ) respectively. The regression ( $R^2$ ) of salinity, temperature and density is 0.89, 0.0006 and 0.60 respectively.

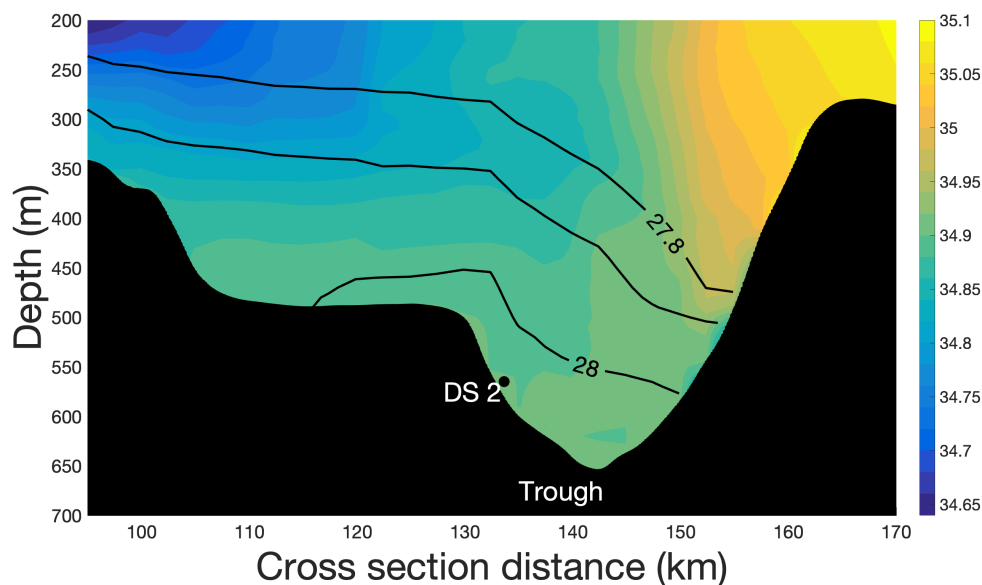


Fig. 3.10 time-mean vertical salinity section at DS, between the Greenland and Iceland shelfbreaks, showing the location of the DS 2 mooring data. The thin black lines show density contours (in  $\text{kg m}^{-3}$ ) from the time-mean CTD section. Note that the DS 2 mooring is deployed in the dense core of the DSO, whilst the CTD sections record the dense core and also captures the lighter parts of the DSO.

Similarly, the salinity of the DSO at ANG increases from 34.88 in 2005 to 34.90 in 2012, which is part of a salinification trend that began at ANG around 2000 (Figure

3.1c). However, the salinity trend ceases at DS between 2012 and 2015 (Figure 3.11c) and similarly, at ANG, the salinity decreases to 34.88 at ANG in that period (Figure 3.1c). The most likely origin of this trend is the salinification of the Atlantic inflow to the Nordic Seas between the mid-1990s and mid-2000s (Holliday et al., 2008). The salinification causes the density to increase from  $28.00 \text{ kg m}^{-3}$  to  $28.03 \text{ kg m}^{-3}$  over this period (Figure 3.11a). The multi-annual freshening and cooling periods recorded between 2006-09 and 2013-15 at ANG (Figure 3.1b and c) are not observed at DS (Figure 3.11b and c).

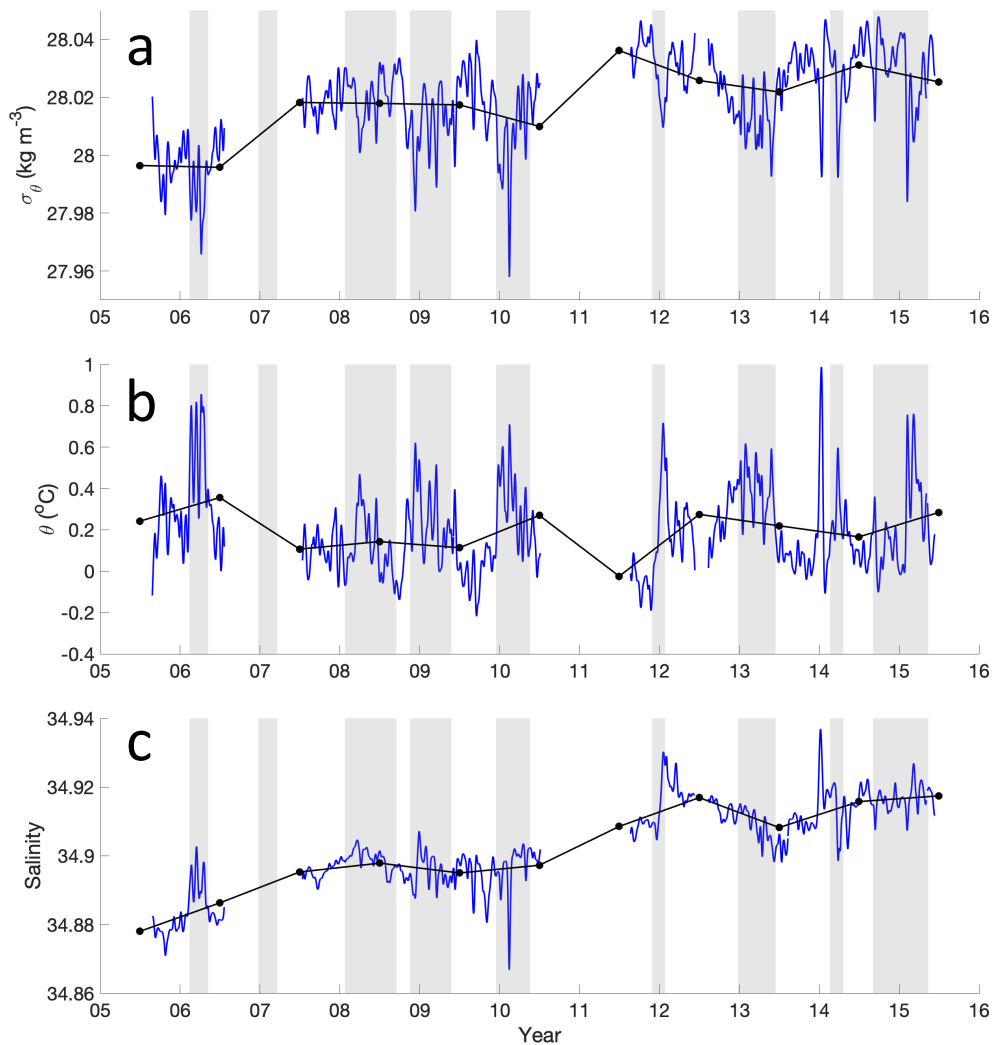


Fig. 3.11 Property time series in the core of the DSO at DS 2, between 2005 and 2015. The blue lines are smoothed time series (using a 2nd order Butterworth Filter with a low-pass cutoff of 20 days). The joined black circles are the annual mean properties. Shaded areas indicate the timing of freshening periods downstream at ANG - see Figure 3.1d. Note the trend of increasing salinity and density between 2005-15, consistent with that observed at ANG (Figure 3.1).

The times of freshening recorded at ANG are indicated by shading on Figure 3.11. Note, advection times between the two locations are between approximately 10 and 20 days according to mooring observations (Jochumsen et al., 2015) and a Lagrangian numerical model (Koszalka et al., 2013). Therefore, if the freshening at ANG derives from DS 2, the freshening is expected to be 10-20 days out of phase.

Although there is sometimes coincident freshening here (e.g. in 2013-14), the freshening is usually relatively weak or entirely absent at this location. For instance, the freshening event in 2008-09 freshened the overflow by 0.06 at ANG, compared with 0.01 here (compare Figure 3.11 with Figure 3.1). Likewise, the event in 2012-13 caused a salinity reduction of 0.05 at ANG, whilst freshening at DS 2 was around 0.015.

The annual salinity variability at DS 2 is shown in Figure 3.12. The maximum (0.005) occurs in early March, whilst the minimum (0.004) occurs in late October (Figure 3.12). This is different to the intra-annual variability observed at ANG, where the maximum occurs in December, followed by freshening and the minimum in May (Figure 3.3). Although there is some freshening at DS 2 in spring (Figure 3.12), it is much weaker ( $\Delta=-0.007$ ) than observed at ANG ( $\Delta=-0.013$ ) over the same period (March-May). Furthermore, in general the intra-annual variability is weaker at DS 2, compared with ANG and there is also no clear seasonal signal at DS 2.

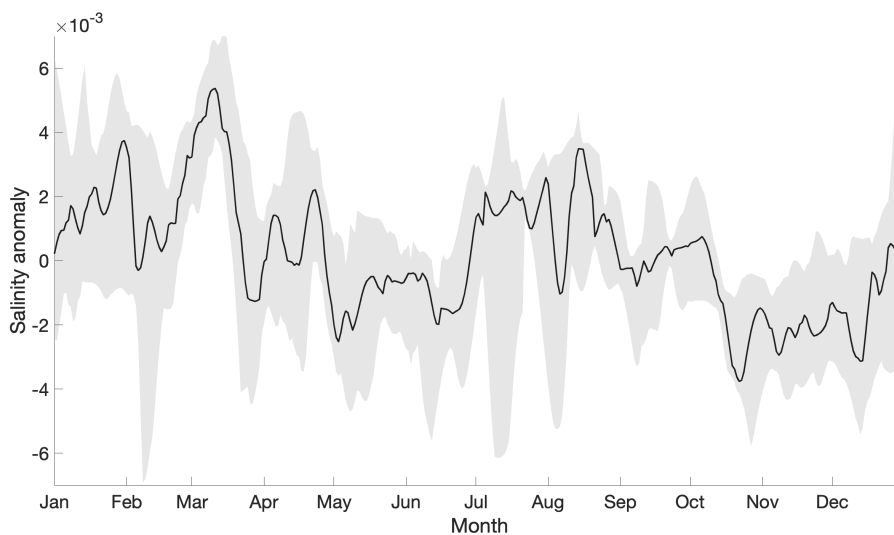


Fig. 3.12 Intra-annual variability of salinity anomaly of the DSO in the DS trough (mooring: DS 2). The anomalies are the day of the year average of the 2nd order band-pass Butterworth filtered salinity time series (Figure 3.11) with low and high pass cutoffs of 20 days and 400 days, and the mean removed. The black line is the median, and the grey shaded area is the inter-quartile range. The salinity minimum is late autumn, which is not consistent with the variability downstream at ANG (see Figure 3.3).

Whilst it has been previously shown that the salinity variability at ANG exceeds the variability at DS (Jochumsen et al., 2015), this is the first time the annual salinity variability has been robustly quantified at DS and shown to be substantially weaker than downstream. In addition, Jochumsen et al. (2015) also observed that the salinity at these two locations are not correlated on timescales beyond the eddy period. Conversely, temperature is correlated (Jochumsen et al., 2015). This might be due to the mixing in of another water mass with comparable temperature, but different salinity, in the intervening distance. Since the water passing through DS 2 is the densest overflow water, the proposed water mass must be fresher. The leading candidate is Polar Surface Water (PSW), which is found over the Greenland shelf at DS and thought to contribute to the DSO (Mastropole et al., 2017; Tanhua et al., 2005). In the following section, the seasonal variability of lighter classes of DSO (which may include PSW) are investigated using the DS CTD data.

### 3.4.2 Lighter overflow water

The DSO freshening events are intensified in lighter density classes at ANG (Figure 3.7). Moreover, there is limited evidence of freshening in the densest source water mass of DSO (Figure 3.11). Therefore, it is hypothesised that the seasonal salinity variability of the DSO at ANG derives from lighter water masses feeding the DSO. To investigate, a gridded dataset derived from repeat CTD crossings of DS (the Latrabjarg section), which is described in detail in Chapter 2, is used. This section was typically occupied once in each season, usually in February, May, August and November, between 1990 and 2012. However, the section was sometimes occupied in the month before, or after, those months, therefore the seasons are defined in this study as January-February-March (JFM), April-May-June (AMJ), June-July-August (JAS) and October-November-December (OND). In the following, seasonal composites are constructed from the gridded dataset to analyse the seasonal property variability of DSO source water masses.

Seasonal composites were constructed by calculating the time-mean of all the gridded temperature and salinity sections for each season. The number of sections forming the composite was 24, 24, 49 and 22 in JFM, AMJ, JAS and OND respectively. To visualise the data, the temperature and salinity composites were binned into discrete classes for each composite. The procedure is as follows. For each season, the data from all sections are binned into the property classes. The bin width is  $0.2^{\circ}\text{C}$  and 0.02 for temperature and salinity respectively. The total number of observations falling into each bin is calculated. Then this number is divided by the total number of observations to

get the percentages of observations that fall into each bin. Other bin widths were also used, to test the sensitivity of the results, but the results are qualitatively unchanged.

The % of total cross-sectional area within each  $\theta$ -S bin in each season is shown in Figure 3.13a-d. The highest percentages ( $> 4\%$ ) are invariably found in the densest classes of water ( $\sigma_\theta > 27.98 \text{ kg m}^{-3}$ ). This shows that the stratification in the denser

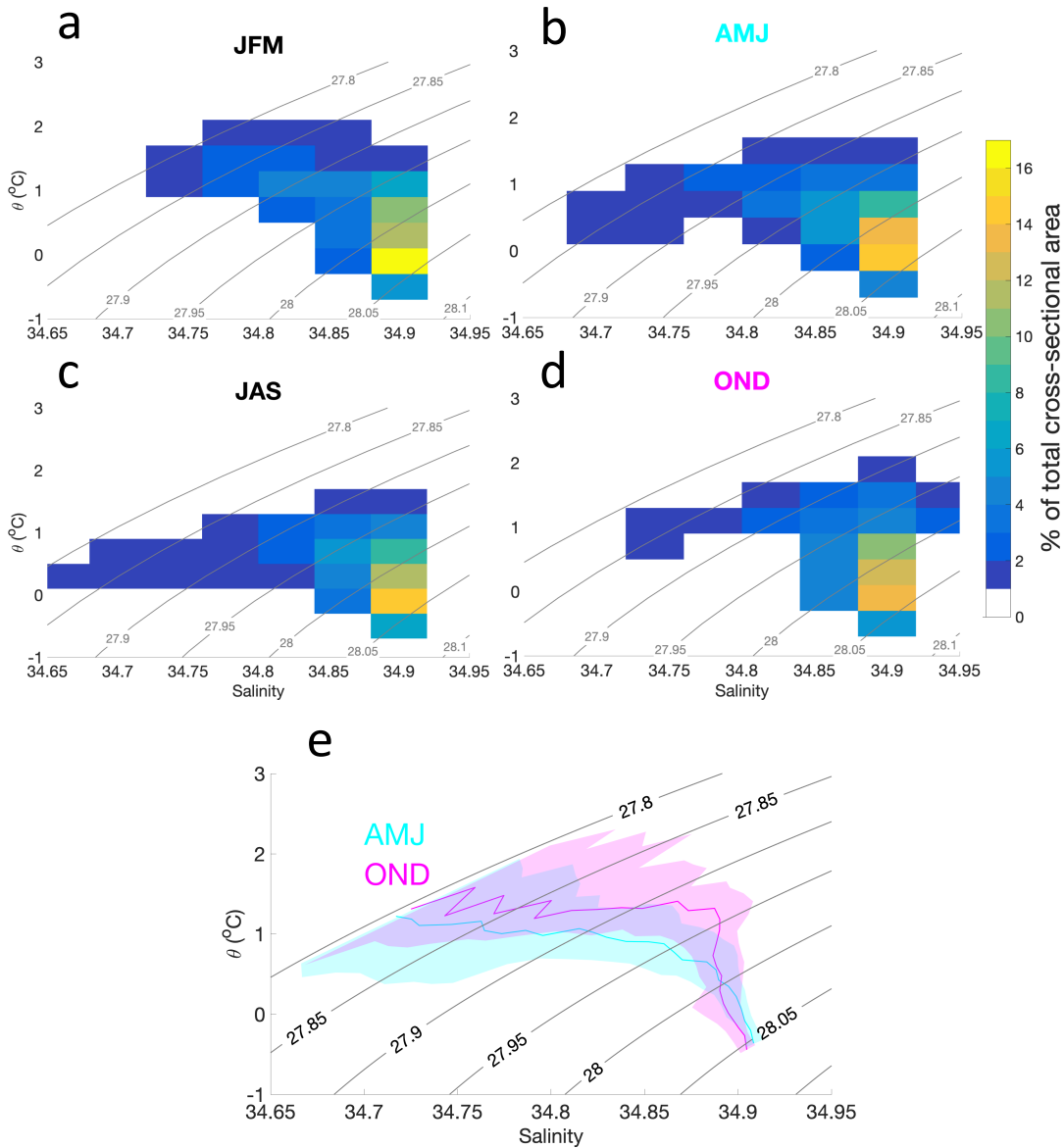


Fig. 3.13  $\theta$ -S distribution in each season composite (a-d) and the median profiles in AMJ and OND (e) at DS. The contours are the % of total cross-sectional area of DSO ( $\sigma_\theta > 27.8 \text{ kg m}^{-3}$ ) contained within each  $\theta$ -S bin. JFM is Jan-Feb-Mar, AMJ is Apr-May-Jun, JAS is Jul-Aug-Sep and OND is Oct-Nov-Dec. The grey lines are the density contours (in  $\text{kg m}^{-3}$ ). In panel (e), the thick lines are the median and the shaded area is the inter-quartile range for AMJ (light blue) and OND (magenta) at different densities.

classes of DSO ( $\sigma_\theta > 27.98 \text{ kg m}^{-3}$ ) is weaker than in the lighter classes of DSO ( $\sigma_\theta > 27.95 \text{ kg m}^{-3}$ ). The  $\theta$ -S profile is more vertical in OND, compared with the other seasons, indicating that the DSO salinity variability is small and is stratified by temperature rather than salinity. This is caused by the generally higher salinities ( $S > 34.85$ ) observed in OND. Contrastingly, a large lens of fresher ( $S < 34.85$ ) water is observed in AMJ, with a temperature of around  $0.5^\circ\text{C}$ . More fresh water is also observed in the other two seasons (JFM and JAS) compared with OND. Note that the freshest component of DSO at DS, which occupies the Greenland shelf (von Appen et al., 2014), is missing from these calculations since there are only summer observations of this water. The seasonality may be greater if these shelf water were included in the calculations.

A direct comparison of the AMJ and OND profiles is also shown in Figure 3.13e. These profiles were made by calculating the median and interquartile range of temperature and salinity in discrete density intervals with a width of  $0.01 \text{ kg m}^{-3}$ . The profiles diverge at around the  $27.98 \text{ kg m}^{-3}$  isopycnal: in lighter DSO classes the water is clearly cooler and fresher in AMJ than in OND. This shows that, above the densest water, there are indications of property seasonality within the DSO, which is missed by the near-bottom observations at DS 2. Moreover, the spring is the fresher season, which is consistent with the observations at ANG (Figure 3.3). Conversely, in denser classes ( $\sigma_\theta > 27.98 \text{ kg m}^{-3}$ ) the water is marginally cooler and fresher in OND than AMJ. This is consistent with, and verified by, the intra-annual variability at DS 2 (Figure 3.12), where the salinity minimum is in October. This autumn salinity minimum in the densest DSO component might be the cause of the autumn negative salinity and temperature anomaly in the DSO at ANG (Figure 3.3). Unfortunately no moored temperatures and salinities from the lighter classes of the DSO are available at DS.

At ANG, the DSO is stratified by temperature rather than salinity (Dickson and Brown, 1994). In fact, the salinity across the DSO plume at ANG is actually fairly unchanging (Jochumsen et al., 2015). Therefore, it is conjectured that internal mixing within the DSO occurs between DS and ANG, resulting in unchanging salinity across the DSO plume. To estimate the salinity of the DSO at ANG in each season, based on the DS CTD section data, the spatially averaged salinity of all waters greater than  $27.8 \text{ kg m}^{-3}$  was calculated for each season. The seasonal mean salinities are 34.86 in JFM, 34.85 in AMJ, 34.86 in JAS and 34.87 in OND. In comparison, the observed salinity of the DSO at ANG varies from 34.86 in 1998-99, to 34.90 in 2012 (Figure 3.1c), which is close, but slightly more saline than the estimated salinity. However, this is expected since the DS CTD data, from which the estimates derive, are from a different time period (1990-2019) to the observed time series at ANG (1998-2015), when the DSO was fresher (Dickson et al., 2002).

There is a 0.02 estimated salinity difference between AMJ and OND at DS, which is comparable to the salinity difference observed at ANG (Figure 3.3). Since the mean is calculated from a relatively small number of sections, the average may be sensitive to the type of averaging method. Therefore the median was also calculated. The median salinity is also at a minimum in AMJ (34.88) and maximum in OND (34.89), though the difference is reduced (0.01).

In, 2004, the DSO underwent its strongest freshening of the whole time series (Figure 3.1c) - when the salinity was reduced from 34.9 to 34.8. Around this time period, the DS CTD section was occupied in November 2003 and February, May, and November 2004. Here, snapshots before (November 2003) during (February and May 2004) and after (November 2004) the freshening period are compared with each other. The  $\theta$ -S distribution and salinity cross sections for all four seasons are shown in Figure 3.14. It is acknowledged that, since these are synoptic snapshots, high frequency mesoscale variability (e.g. boluses and pulses) likely play a key role in the hydrographic variability (von Appen et al., 2017). For example, the overflow interface rises in November 2003 (Figure 3.14b), which is indicative of a bolus (von Appen et al., 2017).

Nevertheless, a clear change in the properties of the DSO is observed between 2003-04 (Figure 3.14), that is not related to high frequency variability. In Feb 2004 and May 2004, vast quantities of fresh water ( $S < 34.85$ ) are observed in the DSO (Figure 3.14c-f). Note that neither sections extend all the way to the Greenland shelfbreak. Despite this, the freshening signal is still evident in the salinity cross-section (core of signal ( $S < 34.70$ ) in the vicinity of the  $27.8 \text{ kg m}^{-3}$  isopycnal) and the  $\theta$ -S distribution. The feature is particularly cold ( $\theta < 0^\circ\text{C}$ ) and fresh ( $S < 34.6$ ) in May 2004 (Figure 3.14e and f). This is around the time of the salinity minimum downstream (Figure 3.1c). Conversely, in Nov 2003 and Nov 2004, there is no fresher water ( $S < 34.85$ ) in the denser classes of overflow ( $\sigma_\theta > 27.9 \text{ kg m}^{-3}$ ) (Figure 3.14a, b, g and h).

Without velocities, one is unable to compute volume transports of the DSO. However, it is possible to compute the cross-sectional area of the DSO from densities alone. The total cross-sectional area of the DSO is  $14.825 \times 10^6 \text{ m}^2$  (in November 2003),  $6.5 \times 10^6 \text{ m}^2$  (in February 2004),  $8 \times 10^6 \text{ m}^2$  (in May 2004) and  $10.05 \times 10^6 \text{ m}^2$  (in November 2004). Supposing the DSO velocity was uniformly  $0.5 \text{ m s}^{-1}$  in each snapshot, as recorded in one snapshot carried out in June 2015 (Jochumsen et al., 2017), the volume transports would be 7.4 Sv (in November 2003), 3.3 Sv (in February 2004), 4 Sv (in May 2004) and 5 Sv (in November 2004). The highest cross-sectional area of the fresher ( $S < 34.85$ ) component of DSO occurs in May 2004 ( $2.875 \times 10^6 \text{ m}^2$ ) and the lowest cross-sectional area of fresh DSO occurs in November 2003 ( $1.525 \times 10^6 \text{ m}^2$ ). This

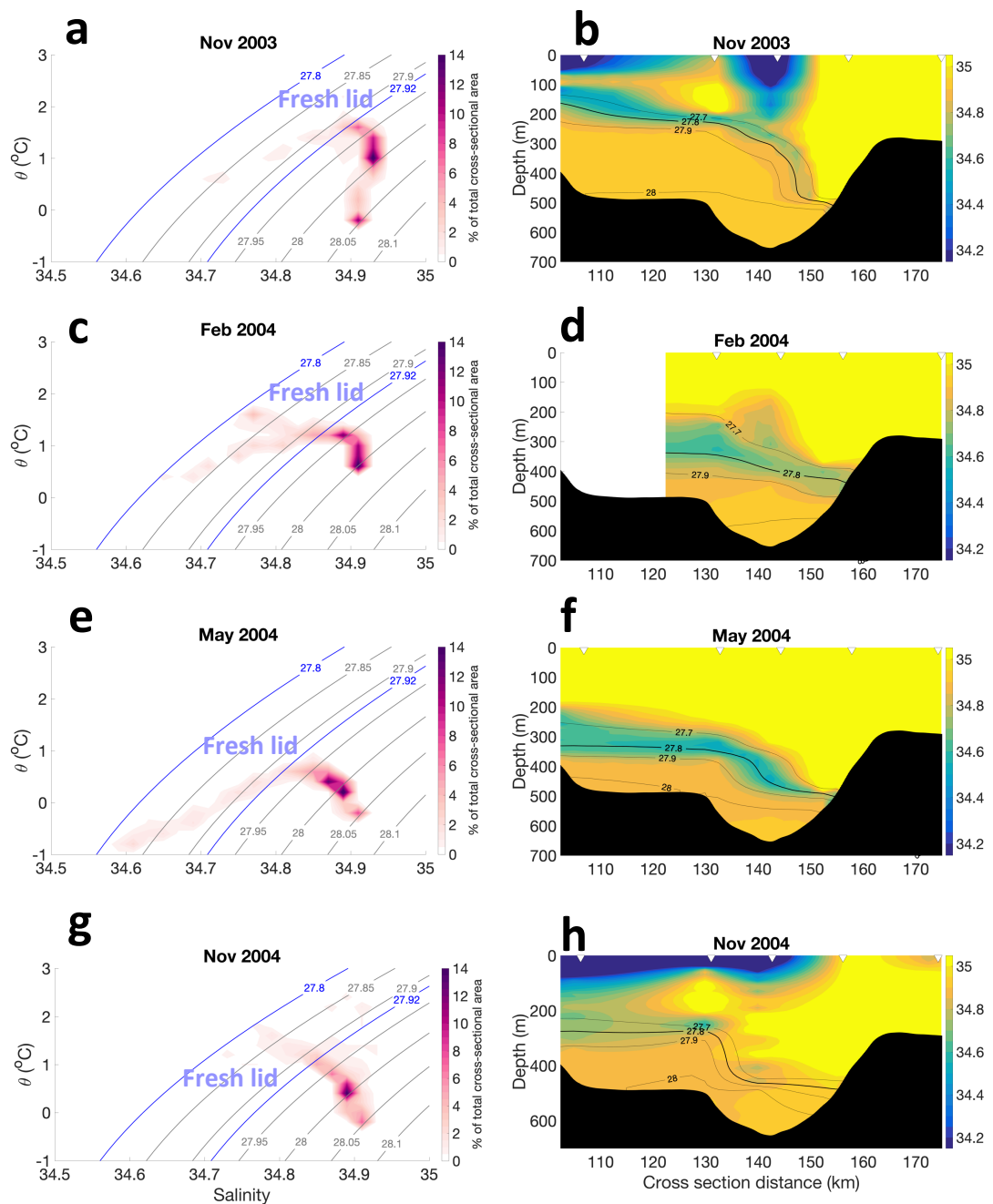


Fig. 3.14  $\theta$ -S distribution (a, c, e and g) and salinity cross-section (b, d, f and h) in four synoptic snapshots between Nov 2003 and Nov 2004 at DS (see Figure 3.10). The  $\theta$ -S distribution gives the % of total cross sectional area of DSO ( $\sigma_{\theta} > 27.8 \text{ kg m}^{-3}$ ) found in each  $\theta$ -S bin. The inverted triangles in the cross sections indicate the location of CTD stations. The grey lines in the first column and black lines in the second column are density contours (in  $\text{kg m}^{-3}$ ). Note the cold, fresh lens in lighter classes of DSO in February and May 2004 during an intense freshening phase of the DSO, as recorded at ANG (Figure 3.1c).

means that there could be approximately double the volume transport of the fresher component of the DSO ( $S < 34.85$ ) in May 2004 than in November 2003.

To estimate the effect of these property changes on the downstream salinity observed at ANG, averages were calculated (see above for justification). The mean salinities are 34.90 in November 2003, 34.86 in February 2004, 34.83 in May 2004 and 34.87 in November 2004. The medians are 34.92 in November 2003, 34.89 in February 2004, 34.87 in May 2004 and 34.89 in November 2004. The difference in means between Nov 2003 and May 2004 ( $\Delta S$ ) is -0.07 and the difference in medians is -0.05, which is comparable with the freshening event observed at ANG (Figure 3.1c) - where the freshening intensity varied from -0.07 to -0.1 depending on position on the Greenland slope (Figure 3.7).

The cold and fresh features observed in Feb 2004 and May 2004 in the lighter classes of overflow are reminiscent of the overflow 'fresh lid' described by Rudels et al. (2002) using CTD snapshots at DS. Conversely, in Nov 2003 and Nov 2004, the upper parts of the overflow are more saline and the fresh lid is absent. The fresh lid was characterised as a fresh lens of water observed around the DSO interface. Their properties were consistent with Polar Intermediate Water, which is defined by  $\theta < 0^\circ\text{C}$  and  $S < 34.68$  (Rudels et al., 2002). The PIW is on a mixing line between PSW and RAW (Tanhua et al., 2005) (Chapter 3.1). Both PSW and RAW are water masses advected by the EGC (Håvik et al., 2017). Holfort and Albrecht (2007) proposed that strong winds enhance the volume transport of the EGC, and the fresher waters of this current may form the fresh lid, which is sufficiently dense ( $\sigma_\theta > 27.8 \text{ kg m}^{-3}$ ) to supply the overflow.

The fresh lid is observed in the spring composite (Figure 3.13b and e) and particularly prominent examples are observed in 2004, coinciding with strong freshening of the DSO. This leads to the proposition that the seasonal presence of the fresh lid on the overflow is causing the salinity seasonality of the DSO, characterised in Section 3.2. However, there is uncertainty whether the fresh lid is formed locally at DS or whether it is advected from upstream. To investigate, data from KGA, located 200 km upstream of DS (Figure 1.8) are used in the next section to ascertain the origin of these lids.

### **3.5 Upstream origin of salinity variability at DS and ANG**

To further examine the upstream source of the DSO salinity variability on advective timescales, salinities from KGA (located a further 200 km upstream of DS) are investigated. The array extends from the Greenland shelf in the North to the Iceland shelf in

the south (Figure 1.8). The dense source water of DSO passes through this array and approaches the sill (Harden et al. (2016), Figure 1.8). Salinities from MC instruments deployed on the upper Greenland slope (mooring KGA11) and the mid-Iceland slope (KGA6) are used (Figure 2.10), where the bottom depths are around 550 m and 950 m respectively. These moorings are selected because they are situated in the time-mean pathway of the main DSO source water branches - the Shelfbreak EGC (KGA11) and the NIJ (KGA6) (Harden et al., 2016) (see Figure 1.8). Moreover, salinities from instruments at 550 m (for KGA11) and 500 m (for KGA6) are used because the time-mean density is  $27.97 \text{ kg m}^{-3}$  and  $28.01 \text{ kg m}^{-3}$  at KGA11 and KGA6 respectively, and therefore this water is dense enough to feed the DSO.

Salinity time series are used to calculate lagged correlations between KGA and DS and between KGA and ANG. Note that although the KGA moorings were deployed between September 2011 and June 2012, both the downstream time series extend until summer 2015, and therefore correlations at lag times of up to 3 years could be calculated. In the below, the maximum correlation at any lag time is shown. Note that the degrees of freedom of the KGA11 time series is 27 and the degrees of freedom of the KGA6 time series is 44. The degrees of freedom of the DS 2 and ANG time series depends on the time period investigated, with the degrees of freedom at DS 2 varying from 14 to 43 and the degrees of freedom at ANG varying from 9 to 38. The reduced degrees of freedom of the smoothed time series was taken into account in the calculation of statistical significance of the correlation between time series.

The objective of this section is to determine whether the salinity seasonality observed at ANG (Section 3.2) and DS (Section 3.4.2) is locally driven, or derived from upstream variability. Further, if the variability does originate from upstream, from which overflow source: the Shelfbreak EGC or NIJ (Figure 1.8)? The intensification of the signal in lighter classes of DSO (see Figure 3.7 and Figure 3.13) suggest that the signal derives from the Shelfbreak EGC, which advects lighter source water masses than the NIJ, which transports the densest DSO source water (Mastropole et al., 2017). Therefore the hypothesis to be tested is that the salinity seasonality derives from the EGC.

### 3.5.1 Advection from KGA to DS

Figure 3.15 shows the salinity time series at KGA, DS and ANG in 2011-13. On the Iceland slope, the salinity variability is relatively weak compared with the Greenland slope (Figure 3.15a). In fact, the salinity standard deviation over the Greenland slope (0.02) is over four times greater than the standard deviation over the Iceland slope (0.005). On the Iceland slope there is no evidence of sustained freshening, comparable to that observed downstream, at ANG (Figure 3.15c), and the salinity remains at

approximately 34.9 over the entire time series (Figure 3.15a). However, positive correlations (though not significant at the 95% level) occur in salinity between KGA6 and DS 2, in the trough at DS. The maximum correlation ( $r=0.49$ ) occurs at a lag time of 49 days (Table 3.1). This indicates the possible advection of water from the mid-Iceland slope to the trough at DS at transit times of approximately 49 days.

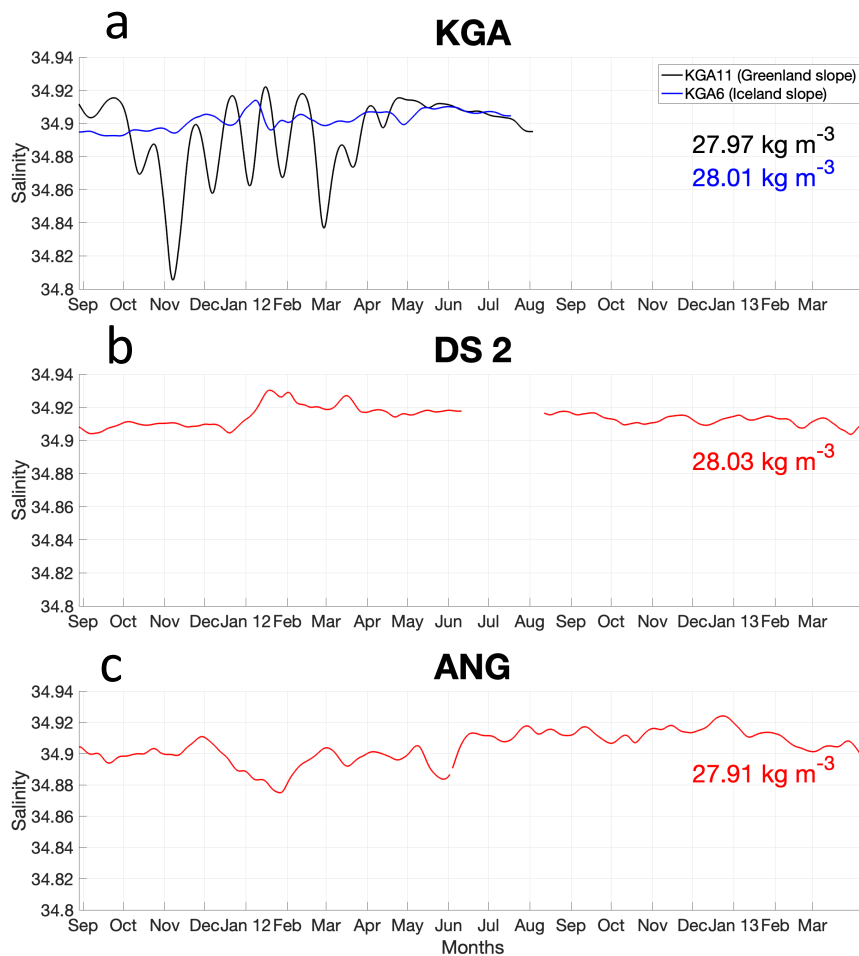


Fig. 3.15 Time series of salinity in 2011-12 at KGA (a), and in 2011-13 at the DS 2 mooring at DS (b) and ANG (c). The KGA salinities are from the MicroCAT at 550 m on KGA11 on the upper Greenland slope (black) and the MicroCAT at 550 m on KGA6 on the mid Iceland slope (blue). All of the salinity time series are filtered with a 2nd order Butterworth Filter with a low-pass frequency cut off of 20 days. The numbers on the right hand side of each panel are the time-mean densities of the time series (in kg m<sup>-3</sup>). Note the freshening events on the Greenland slope in Oct-Nov 2011 and Feb 2012 at KGA11, which are followed by freshening at ANG 2-3 months later.

	DS 2	ANG
KGA6	0.49 (49d)	<b>0.53 (208d)</b>
KGA11	0.24 (142d)	<b>0.73 (78d)</b>

Table 3.1 Salinity correlation between KGA6/KGA11 time series and DS and ANG time series (for mooring locations; see Figure 2.10 and Figure 1.8). The correlation coefficient ( $r$ ) maximum is shown and the lag time that yields the maximum correlation is in parentheses. The correlations in bold are statistically significant at the 95% level.

Conversely, the salinity correlation between the upper Greenland slope (KGA11) and DS 2 is weak (Table 3.1). The KGA11 time series is from the lower part of the EGC on the upper Greenland slope. This supports the idea that the EGC does not directly feed the trough at DS. However, the water masses advected by the EGC (e.g. RAW and PSW) are found in shallower parts of the DS and they make a contribution to the DSO (Harden et al., 2016; Mastropole et al., 2017). Moreover, the time-mean density at DS 2 over the time period of the KGA deployment is  $28.03 \text{ kg m}^{-3}$ , which is close to the time-mean density at KGA6 ( $28.01 \text{ kg m}^{-3}$ ), where the density is greater than at KGA11 ( $27.97 \text{ kg m}^{-3}$ ) (Figure 3.15a and b). The KGA6 time series is situated in the core of the North Icelandic Jet (NIJ) (Harden et al., 2016). The correlations between KGA6 and DS 2 imply that the DS trough is fed by the NIJ. This is consistent with the observations of Mastropole et al. (2017), who claimed that the cold, dense water in the trough is Arctic Intermediate Water (AIW), formed in the Greenland and Iceland Seas and advected towards the trough by the NIJ (Harden et al., 2016). Therefore, the observations at DS 2 - presented in Section 3.4.1 - likely only reflect part of the overflow variability; specifically the NIJ derived variability. However, this conclusion is based on one year of concurrent salinities and a longer time series is required to confirm it.

### 3.5.2 Advection from KGA to ANG

The DSO source water masses, which pass through KGA and feed the DSO at DS, form the DSO which flows southward and passes through ANG. To investigate the advection of different source waters to the south of the sill, the salinity variability at KGA and ANG are compared below.

On the upper Greenland slope, there is high variability from month to month, as shown in Figure 3.15a. Intense freshening is detected in October and November 2011 and February 2012. The peak to trough freshening intensity  $\Delta S$  and duration of freshening is  $-0.1$  and 6 weeks for the 2011 event and  $-0.08$  and 5 weeks for the 2012 event. Both events are reflected between 2-3 months later at ANG (Figure 3.15c). The intensity of downstream freshening is weaker by a factor of around 3. This reflects the

intense entrainment and internal mixing that mixes water masses and likely dampens signals in the intervening distance (Dickson and Brown, 1994; Voet and Quadfasel, 2010). Conversely, these freshening events are only associated with weak freshening, on the order of 0.01, at DS 2 (Figure 3.15b).

Positive lagged salinity correlations occur between KGA11 and ANG (significant at the 95% level; see Table 3.1). The correlations are maximised ( $r=0.73$ ) when the ANG time series lags KGA by 78 days. This implies a 2-3 month transit time of anomalies from KGA11 to ANG, a distance of 700 km. This is equivalent to average advection speeds of  $0.10 \text{ m s}^{-1}$ . Several different current regimes govern the space between KGA and ANG. Initially, advection speeds are slow. The near-bottom advection speeds at KGA11 is  $0.08 \text{ m s}^{-1}$  in the time-mean (Harden et al., 2016). At this speed, it would take a parcel of water 36 days to transit the 250 km from KGA11 to DS. At DS, advection speeds increase to between  $0.2 \text{ m s}^{-1}$  and  $0.5 \text{ m s}^{-1}$  (Jochumsen et al., 2017) reducing to  $0.2 \text{ m s}^{-1}$  at ANG (Dickson and Brown, 1994). Transit times from the sill to ANG are approximately 10-20 days (Jochumsen et al., 2015; Koszalka et al., 2013), but can be longer for water on the Greenland shelf, which may be recirculated (Koszalka et al., 2013). Therefore, the 2-3 month advection time is physically possible, if slightly longer than expected. This advection timescale also supports the idea that increased meltwater input to DSO sources in summer, may cause the gentle Aug-Oct freshening of the DSO at ANG (Figure 3.3).

In addition, significant positive lagged correlations are observed between the time series at KGA6 (Iceland slope) and ANG (Figure 3.15). However, maximum correlations ( $r=0.53$ ) occur at lag times of 208 days, which is longer than estimated. Moreover, the magnitude of salinity variability is much smaller at KGA6 than at ANG and the correlation between them is weaker, therefore it is unlikely that the freshening, observed at ANG, originates from the NIJ on the Iceland slope.

The time-mean density of the DSO at ANG is lower ( $27.91 \text{ kg m}^{-3}$ ) than the mean density at the upstream locations, likely due to the entrainment of lighter water into the DSO that takes place in the intervening distance. One possibility is that the ANG instrument (UK1) resides in a density class that is too light and not influenced by the very dense water of the NIJ passing through KGA6. Correlations between the KGA salinities and salinities from UK2 were also computed. UK2 is located down the slope from UK1 (the salinities used to represent the DSO at ANG for the correlations (Table 3.1)) in denser classes of DSO where the time-mean density is  $27.95 \text{ kg m}^{-3}$ . The correlation maximum is  $r=0.44$  between KGA6 and UK2 at a lag time of 87 days and the correlation maximum between KGA11 and UK2 is  $r=0.64$  at a lag time of 80 days. Both correlations are statistically significant at the 95% level. The higher correlations

between the salinity at KGA6 and the salinity at UK2 at a more realistic lag time (87 days) suggests that the water of the NIJ (passing through KGA6) may exert more of an influence on the denser part of the DSO at ANG. However the higher correlations between the salinity at KGA11 and UK2, and the weakness of the salinity variability at KGA6 compared with that at the ANG moorings, suggest that the Shelfbreak EGC exerts a dominant influence on the salinity of the DSO at ANG (both UK1 and UK2).

The freshening observed over the Greenland slope in Oct/Nov 2011 and Feb 2012 may be caused by enhanced contribution of the PSW to the DSO (Holfort and Albrecht, 2007). Using the density on the upper Greenland slope as a proxy, Håvik and Våge (2018) studied the Ekman upwelling and downwelling occurring at KGA in 2011-12. They observed that periods of downwelling are preceded by strong northeasterly winds over the Greenland shelfbreak, which are downwelling favourable. This forces the fresh/light shelf water (PSW) offshore, where it is advected in greater volumes by the Shelfbreak EGC, potentially forming the fresh lid of the DSO, observed in Section 3.4.2 and by Rudels et al. (2002) previously. In this scenario, the fresh lids cause the seasonal freshening of the DSO, shown in section 3.2. A different hypothesis is that salinity variability of water masses entrained into the DSO drives the seasonal freshening of the DSO, and the EGC variability is less important. These different mechanisms are investigated in Chapter 4.

### 3.6 Concluding remarks

Here, answers for the four questions posed in the introduction are summarised. The questions are as follows:

1. How does the salinity of the DSO vary seasonally?
2. Which property is the principal control on the density of the DSO, salinity or temperature?
3. How and why do the DSO freshening events vary in space and time?
4. Is the salinity seasonality of the DSO locally driven or derived from upstream variability?

#### 1. How does the salinity of the DSO vary seasonally?

For the first time, it has been shown that the DSO exhibits salinity seasonality. This seasonality occurs in the Irminger Basin at ANG, 500 km downstream of DS, and the peak to trough magnitude of the signal is 0.02, with maximum in November/December

and minimum in May. By fitting a linear regression model with an annual frequency to the monthly averaged salinity time series it is estimated that the seasonal signal explains approximately 37% of the salinity variance. Furthermore, the DSO also exhibits salinity seasonality at DS with higher salinity in November and lower salinity in May.

## **2. Which property is the principal control on the density of the DSO, salinity or temperature?**

The freshening of the DSO in winter/spring is not fully temperature compensated and therefore causes a negative density anomaly. Typical anomalies are  $-0.005 \text{ kg m}^{-3}$  but they can be as large as  $-0.02 \text{ kg m}^{-3}$  in some years. By decomposing the density variability into the temperature and salinity terms, the density was shown to be controlled by temperature for two thirds of the year and by salinity for one third of the year. This fine balance highlights the sensitivity of the DSO density to future changes in its mean properties.

## **3. How do the DSO freshening events vary in space and time?**

In most years the DSO freshens in late winter and spring, with particularly strong freshening in 1998-99 and 2003-04 when the change in salinity was  $-0.07$  and  $-0.09$  respectively at ANG. Conversely, the amplitudes of the seasonal cycle are weak in 2002-03 and 2009-10. The freshening intensity varies across the DSO plume, with maximum intensity observed near-bottom inshore (and upslope), in lighter classes of DSO ( $27.88 \text{ kg m}^{-3}$  -  $27.91 \text{ kg m}^{-3}$ ) and weaker freshening down the slope in denser classes ( $\sigma_{\theta} \approx 27.94 \text{ kg m}^{-3}$ ).

The winter-spring freshening is traced back to the lighter classes of DSO source water at DS. This is consistent with the observation that the freshening of the DSO at ANG is intensified on the inshore side of the plume. The repeat DS CTD sections reveal the seasonality in the lighter classes ( $\sigma_{\theta} < 27.98 \text{ kg m}^{-3}$ ) of DSO, located above the deep trough. In spring, the volumetric  $\theta$ -S distributions demonstrate the increased presence of fresh water ( $S < 34.85$ ) in the overflow in lighter classes ( $\sigma_{\theta} < 27.98 \text{ kg m}^{-3}$ ). In February and May 2004, an anomalously cold and fresh lens was observed in the lighter classes of the DSO, coinciding with intense freshening at ANG. The mean DSO salinity in May 2004 was 0.07 less than the mean salinity in Nov 2003 as a result of the fresh lens. The characteristics and location of this signal are consistent with the 'fresh lid', discussed by Rudels et al. (2002), which may originate from the mixing of PSW with RAW within the EGC (Tanhua et al., 2005).

**4. Are the freshening events locally driven or derived from upstream variability?**

The salinity variability of the DSO at ANG in 2011-12 was traced back to moored observations on the upper Greenland slope at KGA11, around 250 km north of DS. Positive salinity correlations between KGA11 and ANG ( $r=0.73$ ,  $p<0.05$ ) were maximised at a lag time of approximately 2.5 months and this lag time appears to be physically realistic. The KGA11 mooring occupies the core of the Shelfbreak EGC, implying that the variability of the Shelfbreak EGC is dominating the salinity variability of the DSO at ANG. However, further years of mooring time series from KGA are required to strengthen this claim. The mooring observations at DS 2 in the deep trough, used to represent the property variability of the DSO at DS in previous studies (e.g. Jochumsen et al. (2015)), likely only reflect part of the overflow variability; specifically the NIJ derived variability (Mastropole et al., 2017).

In the next chapter, the hydrographic variability of the key sources of the DSO (Shelfbreak EGC, Separated EGC, and NIJ) are investigated in more detail to determine exactly what mechanisms may drive sustained freshening of the DSO.



# Chapter 4

## The mechanisms driving seasonal freshening of the Denmark Strait Overflow

### 4.1 Introduction

In the previous chapter, the multi-month to multi-annual salinity variability in the core of the DSO was characterised. At the location of ANG, 500 km downstream of DS, the DSO typically freshens between January and May, and salinifies in the second half of the year towards a salinity maximum in December. The freshening phase of the cycle is weaker in the densest classes ( $\sigma_\theta > 27.95 \text{ kg m}^{-3}$ ) of DSO at ANG and appears to originate from lighter classes of overflow source water at DS. The question is: what causes the sustained (which is defined here as lasting for at least two months), seasonal, freshening of the DSO at ANG? Four freshening mechanisms, which have been highlighted in previous studies, are tested below.

In this chapter, the impact of seasonal variability of different components of DSO source water upstream of DS is connected to salinity variability of the DSO downstream. The source water variability is quantified using oceanographic mooring, ship-board hydrographic observations and an atmospheric reanalysis product. The chapter is structured as follows. Firstly, the candidate freshening mechanisms are described and the connection between these mechanisms and freshening of the DSO at ANG is detailed (Section 4.2). Then, in Sections 4.3 to 4.6, the candidate freshening mechanisms are identified and their contributions to freshening of the DSO quantified using a combination of ocean and atmospheric data. Finally, in Section 4.7 the contributions of the mechanisms to the freshening of the DSO are further discussed and, in Section 4.8, conclusions are drawn.

## 4.2 Candidate mechanisms

### 4.2.1 Introduction

Firstly, the four candidate mechanisms for the sustained seasonal freshening of the DSO are described in the list below. Furthermore, schematics of the ocean circulation without the mechanisms is shown in Figure 4.1 and can be compared with the ocean circulation associated with the schematics in Figure 4.2.

## Time mean hydrography

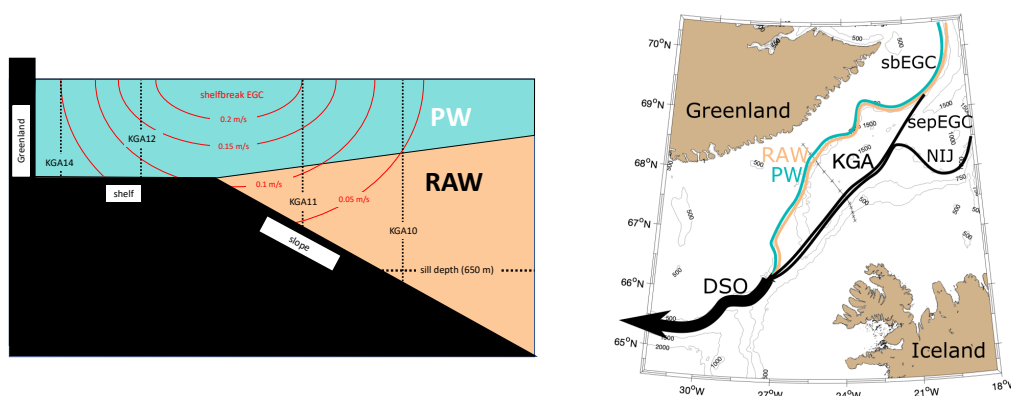


Fig. 4.1 Schematic of the hydrography on the Greenland shelf and slope at KGA (left column) and ocean circulation map (right column) in the time-mean, i.e. without any of the mechanisms highlighted above, north of DS. The time-mean hydrography means the average pathway of currents and water masses, which is based on numerous CTD and velocity section snapshots presented in previous studies including Våge et al. (2013) and Harden et al. (2016). In the left column, the red contours represent the indicative velocity contours of the Shelfbreak EGC (positive=southwestward), the vertical dotted lines are the location of the moorings and the horizontal dotted line indicates the depth of the Denmark Strait sill. The thin grey lines in the circulation map are the bathymetry, showing the location of the 500 m, 750 m, 1000 m, 1500 m and 2000 m isobaths, from the GEBCO\_2014 grid, which has a grid spacing of 30 arc seconds. The acronyms are as follows: the Denmark Strait Overflow (DSO), Returning Atlantic Water (RAW), Polar Water (PW), Shelfbreak EGC (sbEGC), Separated EGC (sepEGC), North Icelandic Jet (NIJ) and the Kögur array (KGA), which are introduced in the text below.

1. Strong northerly/northeasterly winds blow over the Greenland shelf/slope, upstream of DS, and drive onshore Ekman transport in the surface layer, which promotes coastal downwelling and compensating offshore flow at depth, injecting cold, fresh shelf water, originating from the Arctic Ocean, into the core of the

Shelfbreak EGC, thus increasing the freshwater feed of the EGC to the DSO (Figure 4.2a).

2. Ekman pumping over the east Greenland continental slope north of DS forces the saline component of the Shelfbreak EGC to deepen below the depth of the DS sill, which causes this water mass to recirculate, and, in turn, reduces its contribution to the DSO (Figure 4.2b).
3. The volume transport of the Shelfbreak EGC is enhanced, increasing the contribution of fresh, polar origin, water masses transported by the Shelfbreak EGC to the DSO (Figure 4.2c).
4. Middle Irminger Water (MIW), a key contributor to the DSO through entrainment (Tanhua et al., 2008), exhibits time dependent freshening. Sustained freshening of the MIW imprints on the salinity of the DSO (Figure 4.2d).

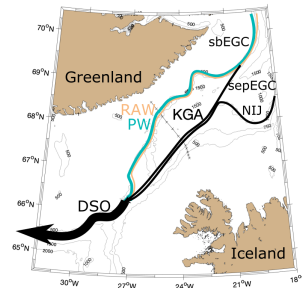
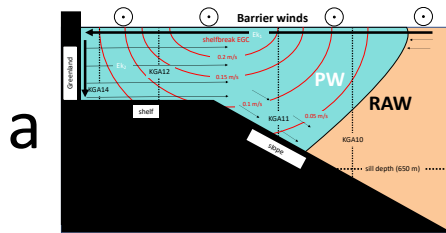
Whilst the hydrography and ocean circulation in the absence of the mechanisms is illustrated in Figure 4.1, the mechanisms 1-3 are illustrated in the schematics in Figures 4.2. Figure 4.2 shows the predicted impact of mechanisms 1-3 on the hydrography at the location of the Kögur array (KGA), situated 200 km to the north of DS, and the ocean circulation in the region. Furthermore, Figure 4.2d shows the change in the regional ocean circulation associated with Mechanism 4.

Whilst mechanisms 1-3 are initiated by strong northerly/northeasterly winds, they are distinct freshening mechanisms, which drive freshening of the DSO in different ways. The role of mechanisms 1 and 3 in driving the salinity variability of the DSO was highlighted before, by Holfort and Albrecht (2007) and Hall et al. (2011), but mechanisms 2 and 4 have not previously been proposed. Furthermore, Håvik and Våge (2018) used ocean densities at KGA to argue that both mechanisms 1 and 3 could be identified locally. But how do these mechanisms, and the other two, result in DSO freshening observed at ANG? The hypothesis associated with each mechanism is detailed below. Firstly, the hydrography of the DSO source water at KGA is described.

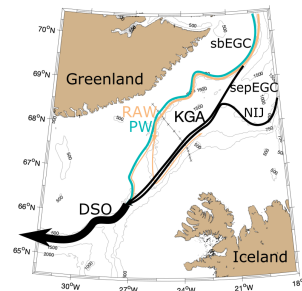
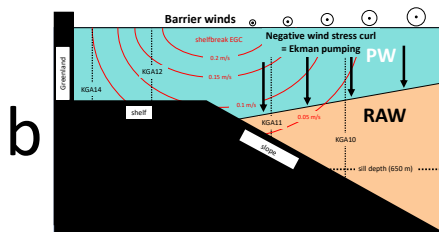
### 4.2.2 Hydrography of DSO source water at KGA

Mechanisms 1-3 involve the variability of the hydrography of DSO source water to the north of DS. Figure 4.3 shows the time-mean KGA vertical section of along-stream velocity, and the time-median vertical sections of temperature, salinity and density. The median of the properties are used on recommendation of Harden et al. (2016).

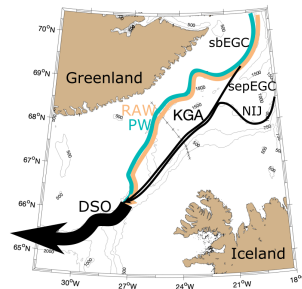
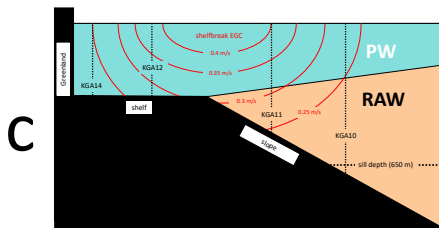
### Mechanism 1: coastal Ekman downwelling



### Mechanism 2: Ekman pumping



### Mechanism 3: shelfbreak EGC enhancement



### Mechanism 4: Freshening of MIW

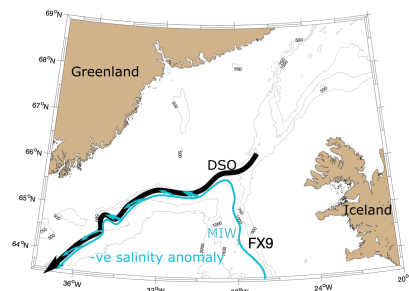
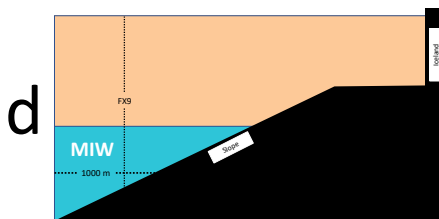


Fig. 4.2 Schematics of the ocean circulation associated with freshening mechanisms 1-4, which are highlighted above. In the left column of panels a-c, the red contours represent the indicative velocity contours of the Shelfbreak EGC (positive=southwestward), the thick black arrows show Ekman transport, the vertical dotted lines are the location of the moorings and the horizontal dotted line indicates the depth of the Denmark Strait sill. In the right column of all panels, the coloured arrows indicate water mass transports. The width of the arrows represents the changing size of the volume transports. Note the recirculation of RAW associated with Mechanism 2. The acronyms are defined in Figure 4.1. The thin grey lines are isobaths, derived from the GEBCO\_2014 grid.

A gridded KGA product, which has a vertical and horizontal resolution of 50 m and 2 km respectively, was created from the property and velocity measurements between 2011 and 2012, using Laplacian spline interpolation (Harden et al., 2016). The gridded data between moorings KGA11 and KGA1 (Harden et al., 2016) are concatenated with data from moorings KGA12 and KGA14 on the Greenland shelf, to create these cross sections. Concatenation was necessary because the gridded shelf salinities and velocities were derived from erroneous data from instruments deployed on mooring KGA12, as explained in Chapter 2. The shelf data derive from mooring deployments between 2011 and 2014. The deployment-average values were interpolated on to a vertical grid, with the same 50 m vertical spacing as the gridded dataset, using cubic piecewise polynomial interpolation, which provides an accurate representation of the water column stratification on the shelf, as observed in CTD occupations at KGA, by Våge et al. (2013).

Figure 4.3a shows the along-stream velocity section at KGA. The EGC flows southward from Fram Strait towards DS, and bifurcates around 69°N, forming the Shelfbreak EGC and Separated EGC (Våge et al., 2013); the latter merges with the NIJ upstream of DS (Harden et al., 2016). The surface intensified Shelfbreak EGC and Separated EGC propagate through the KGA section over the shelfbreak and the lower Iceland slope respectively (Figure 4.3a). The NIJ is a mid-depth intensified current, which emerges over the North Iceland continental slope, and increases its volume transport as it flows towards DS (Semper et al., 2019). All three currents transport water denser than  $27.8 \text{ kg m}^{-3}$ , which is traditionally used as the lighter limit for DSO, after (Dickson and Brown, 1994). Using 10 months of mooring observations, Harden et al. (2016) calculated that the time-mean volume transport of DSO source water is 3.5 Sv, comprising 1.5 Sv from the Shelfbreak EGC branch, 1 Sv from the Separated EGC and 1 Sv from the NIJ.

There are two main DSO source water masses passing through KGA. On the Greenland slope, temperature and salinity increase with depth towards the temperature maximum, which corresponds to the core of Returning Atlantic Water (RAW) (Håvik et al., 2017) (Figure 4.2). The RAW is warm ( $\theta > 0^\circ\text{C}$ ), saline ( $S > 34.9$ ), and is derived from Recirculating Atlantic Water and Arctic Atlantic Water (Harden et al., 2016; Håvik et al., 2017; Rudels et al., 2002), and is advected by the EGC between Fram Strait and Denmark Strait (Mauritzen, 1996). Arctic Intermediate Water (AIW) is situated beneath the RAW on the Greenland slope and extends far up the Iceland slope (Figure 4.3). The  $0^\circ\text{C}$  temperature contour is used as the water mass boundary between RAW and AIW, with AIW defined as the portion of DSO source water colder than  $0^\circ\text{C}$ , after Rudels et al. (2002).

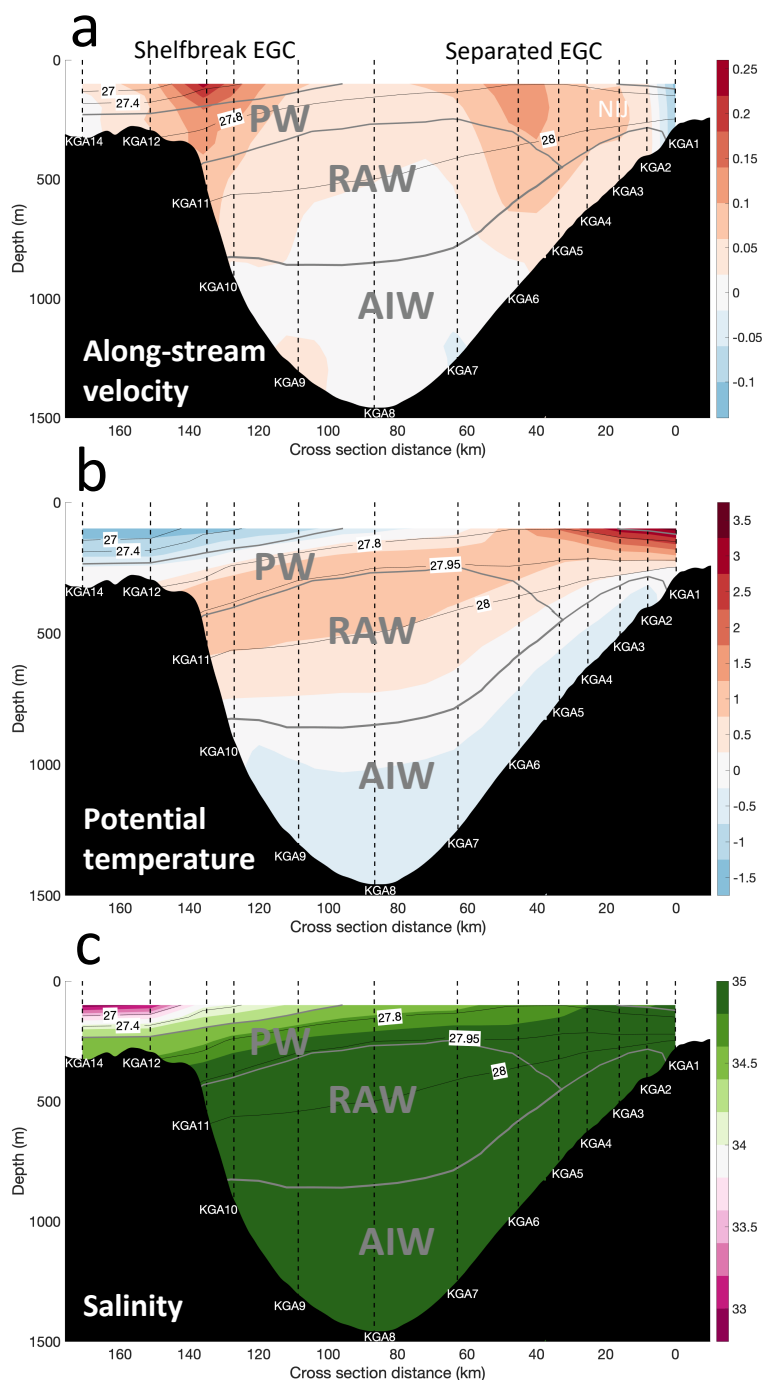


Fig. 4.3 Cross sections of average along-stream velocity (a; in  $\text{m s}^{-1}$ ), temperature (b; in  $^{\circ}\text{C}$ ) and salinity (c) at KGA. The along-stream velocity is the deployment mean, whilst the temperature and salinity are the deployment medians. The thin black lines are density contours (in  $\text{kg m}^{-3}$ ) and the thick grey lines indicate water mass boundaries. The acronyms are Polar Water (PW), Returning Atlantic Water (RAW), Arctic intermediate Water (AIW), EGC (East Greenland Current) and NIJ (North Icelandic Jet). The white labels and dashed black vertical lines indicate the mooring locations. The bathymetry is derived from ship echosounder data.

AIW originates from deep convection in the Greenland (Greenland Sea Arctic Intermediate Water; (Brakstad et al., 2019)) and Iceland (Iceland Sea Arctic Intermediate Water (Swift and Aagaard, 1981)) seas, as explained in detail in Chapter 1. RAW and AIW are the two most important sources of the DSO (Mastropole et al., 2017). However, some of the DSO source water observed at KGA does not fall within the traditional water mass definitions of RAW and AIW, described above. Nevertheless, this water likely makes an important contribution to the volume transport of the DSO, and was included in the calculation of the volume transport of DSO source water through KGA (Harden et al., 2016).

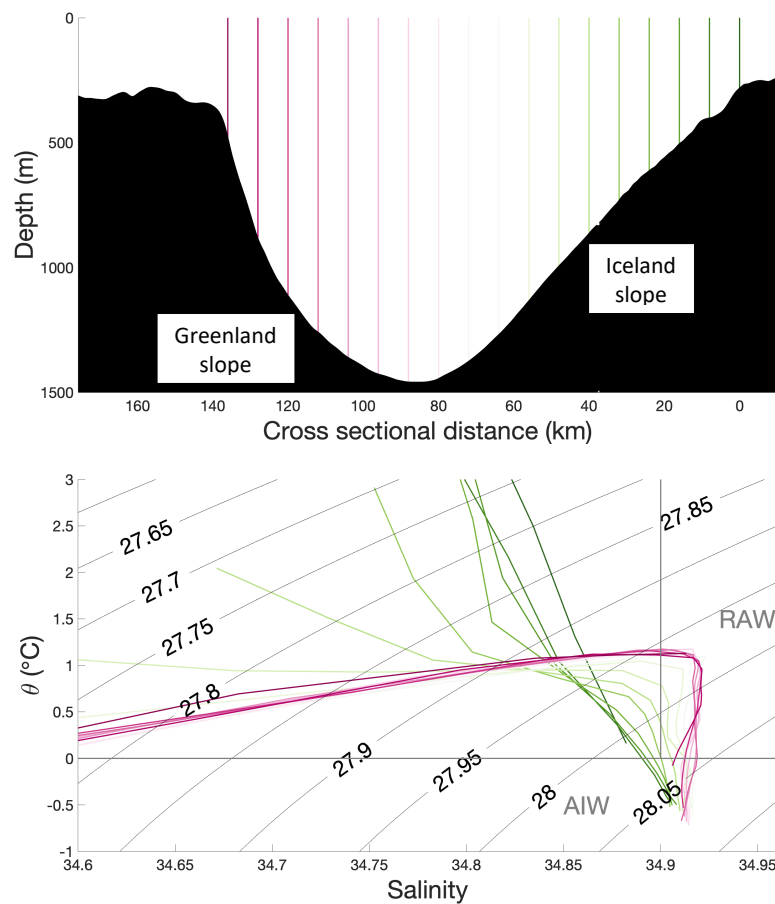


Fig. 4.4  $\theta$ -S profiles of DSO source water at KGA. The bottom panel shows the  $\theta$ -S profiles, whilst the top panel shows the location of the profiles across the array. The profiles are coloured according to a colour grade, which varies from purple (Greenland slope) to green (Iceland slope). The grey boxes indicate the water mass definitions of RAW and AIW, established in the literature. In the bottom panel, the thin black lines are density contours (in  $\text{kg m}^{-3}$ ). The data are from the time-median section (Figure 4.3).

Specifically, the RAW and AIW are overlain by a stratified layer, located between the  $27.8 \text{ kg m}^{-3}$  isopycnal and the upper boundary of RAW/AIW, which ranges from 100 m thick over the Greenland slope to 400 m thick over the mid-Iceland slope in the time-mean (Figure 4.3, Figure 4.4). This includes some very fresh water ( $S < 34.8$ ) observed over the Greenland slope (Figure 4.4). The water overlying the RAW is most likely the product of RAW mixing with polar origin water masses, such as Polar Surface Water (PSW) (for definition and description of PSW, see Chapter 1) between Fram Strait and Denmark Strait, as investigated by Håvik et al. (2017).

Regardless of its origin, this water is clearly the freshest source water of the DSO. Thus, if volume transports of this water increase (e.g. through mechanisms 1 or 3 (Figure 4.2)), the DSO could freshen as a result. Conversely, the water overlying AIW on the mid to upper Iceland slope has a higher temperature and salinity than the water overlying the RAW (Figure 4.4), and may derive from entrainment of lighter water into the NIJ (Semper et al., 2019), and is thus termed NIJ-entrained hereafter. Since this fresher water is dense enough to contribute to the DSO, it is likely important. Therefore, the fresh water overlying the RAW layer within the two EGC branches is thus termed Polar Water (PW) hereafter.

### 4.2.3 Mechanism 1: offshore flow during Ekman downwelling

Firstly, Mechanism 1 is associated with a redistribution of the water masses over the Greenland continental margin. The PW is situated over the Greenland shelf and upper slope (Figure 4.3c). The PW layer is thickest over the Greenland shelf and becomes thinner as it extends offshore, as explained by Våge et al. (2011) and Håvik et al. (2017), and shown in Figure 4.3. Therefore, there is a horizontal salinity gradient from fresh to saline in the offshore direction. During the strong winds, there is onshore flow in the near-surface Ekman layer, which brings the PSW onshore, and offshore flow at depth, which forces the RAW offshore and away from the shelfbreak, whilst the PW migrates offshore from the shelf and into the core of the Shelfbreak EGC (Figure 4.2a). Assuming that the Shelfbreak EGC remains situated over the shelfbreak, this increases the ratio of PW to RAW within the Shelfbreak EGC, ultimately increasing the contribution of PW to the DSO, whilst decreasing the contribution of RAW. During winter, the increased occurrence of strong winds drives this mechanism and results in the salinity seasonality of the DSO. Håvik and Våge (2018) identified negative density anomalies on the upper Greenland slope at KGA, which they argued were driven by this mechanism. However the lag time between the wind forcing and density anomalies was quite long ( $\approx 3$  days) and it was not certain whether density anomalies are caused by local or upstream downwelling. Further, it is not presently known whether this

mechanism actually contributes to the sustained freshening of the DSO, and further investigation is thus necessary, which is carried out in this chapter.

#### **4.2.4 Mechanism 2: Ekman pumping**

Secondly, negative wind stress curl over the Greenland shelf and slope could promote Ekman pumping, resulting in water mass deepening (Mechanism 2). Negative wind stress curl may arise when there is an offshore gradient of wind speed (i.e. wind speeds are higher offshore; Figure 4.2b). Negative wind stress curl is indicative of convergence in the surface Ekman layer, which induces vertical motion below the bottom of the Ekman layer (called Ekman pumping, see Figure 4.2b). Våge et al. (2013) showed that the annual average wind stress curl is negative all along the east Greenland coast, with the most negative values at the location of KGA. Supposing the negative wind stress curl on the Greenland slope intensified, perhaps during barrier wind events (introduced in Chapter 1), Ekman pumping velocities may increase, causing more rapid water mass deepening. This would force the water masses over the Greenland slope, i.e. PW, RAW and AIW, downwards (Figure 4.2). In the time-mean, RAW is found above and below sill depth (650 m) (Figure 4.3). But during strong Ekman pumping, the fraction of RAW that is below sill depth might increase, and as a result more RAW may recirculate in the Blosseville Basin, whilst less RAW may be transported to DS (Figure 4.2).

#### **4.2.5 Mechanism 3: Shelfbreak EGC enhancement**

Thirdly, Mechanism 3 involves enhanced volume transport of the Shelfbreak EGC, and thus enhanced transport of PW within the current (represented by the higher velocity contours in Figure 4.2c). This will increase the feed of PW to DS. As a result, the ratio of PW to more saline water masses (e.g. NIJ-entrained), which are advected by the other DSO source water branches, will increase in their density classes, resulting in freshening of the DSO downstream. Harden et al. (2016) argued that the volume transport of the different current branches through KGA was governed, to some extent, by the wind stress curl in the Blosseville Basin. During positive wind stress curl, the ocean circulation is cyclonic and the Shelfbreak EGC is enhanced, whilst the Separated EGC is weakened.

It is important to note that the mechanisms 1-3 are strongly related, but also independent. All three are likely wind-driven and therefore difficult to separately identify. However, each mechanism has at least one distinguishing feature, which are used to help identify the mechanisms in this chapter. Coastal Ekman downwelling involves a strong cross-shelf flow component with onshore flow at the near-surface and offshore flow at

the near bottom. Ekman pumping is associated with downwards vertical velocity and the Shelfbreak EGC enhancement is associated with increased geostrophic velocities of the Shelfbreak EGC.

#### 4.2.6 Mechanism 4: freshening of MIW

Alternatively, the wind driven mechanisms might not be the most important drivers of DSO salinity. Another possible explanation is that the changing salinity of the overflow waters reflects changes in the properties of the entrained waters, rather than that in the core of the overflow itself. The DSO entrains MIW (Tanhua et al., 2008) and Labrador Sea Water (LSW) (McCartney, 1992; Price and Baringer, 1994), which causes the DSO to warm rapidly and to transport more water in the initial 200 km south of Denmark Strait (Voet and Quadfasel, 2010). Both entrained water masses are warm ( $\theta > 3^{\circ}\text{C}$ ) and saline ( $S > 34.92$ ) (McCartney, 1992). Should the contribution to the DSO, or the salinity, of either water mass decrease at some point in time, a negative salinity anomaly in the DSO might result. This freshening mechanism is clearly independent from mechanisms 1-3.

The time-dependent freshening of MIW (see Mechanism 4 above and in Figure 4.2d) is investigated in this chapter. MIW is derived from the Gulf Stream and water formed on the west African continental shelf (Van Aken and De Boer, 1995), which converge in the Iceland Basin before crossing the Reykjanes Ridge and entering the Irminger Basin. Thus variations in the ratio of the two sources of MIW could result in salinity variability. However, an investigation into the underlying cause of MIW salinity variability is beyond the scope of this study, which is focused on characterising the salinity variability.

Mechanism 4 is evaluated using CTD profile data on the southwest Iceland slope (see FX9 in Figure 4.2d). This station is the furthest offshore station of a CTD section - called the Faxaflói (FX) section - which is a repeat section, typically occupied four times per year between 1990 and 2019 (Chapter 2). Unfortunately, it was not possible to evaluate the contribution of salinity variability within the LSW, because the LSW is typically found in the central Irminger Sea (Talley and McCartney, 1982), or the possibility of changes in the strength of entrainment through time, owing to a lack of appropriate data.

## 4.3 Evidence for Mechanism 1

### 4.3.1 Methodology

Firstly, the wind driven mechanisms 1-3 are investigated. Oceanographic mooring data from the upper Greenland slope (KGA11), and Greenland shelf (KGA12 and KGA14) are used in combination with ERA5 winds to identify and characterise Mechanism 1 - offshore flow during coastal Ekman downwelling. The zonal component ( $u_{10}$ ) and meridional component ( $v_{10}$ ) of wind 10 m above the sea surface were acquired from ECMWF Reanalysis 5 (ERA5) in the vicinity of the Greenland shelf and slope at KGA (see magenta area in Figure 2.13), and are used to identify barrier wind events. The ERA5 dataset, which is described in Chapter 2, has a temporal resolution of 1 hour and a spatial resolution of  $0.25^\circ \times 0.25^\circ$ . Ocean property data are derived from SBE MicroCATs deployed at 80 m and 280 m on the Greenland shelf and 100 m, 200 m, 350 m and 550 m on the upper slope (at KGA11), whereas ocean velocities are derived from Acoustic-Doppler Current Profilers (ADCPs) on the shelf and from Rotor Current Meter's deployed at the same depths as the MicroCATs at KGA11. Data are used from KGA12 between 2011 and 2014, from KGA14 between 2012 and 2014, and from KGA11 between 2011 and 2012.

Strong along-shore winds drive onshore and offshore Ekman transports on the east Greenland continental margin (Håvik and Våge, 2018). The prevailing winds on the East Greenland shelf are northerlies/northeasterlies (see Chapter 5), which drive onshore Ekman transport, causing Mechanism 1 to occur (Figure 4.2). Intense barrier winds occur frequently around DS, especially in winter (Harden et al., 2011). Barrier winds are induced by atmospheric cyclones, which tend to propagate from the Irminger Sea towards the Iceland Sea in the northeast, and are particularly intense and frequent in the cold season, and when the NAO index is positive (see Chapter 5).

Barrier wind events between 2011 and 2014 were identified using the methodology presented in Harden et al. (2011). This involves: (1) Identifying times when the wind direction is between a northerly and an easterly and the wind speed is greater than  $20 \text{ m s}^{-1}$ , (2) Identifying the peaks of the time series (i.e. data points which are greater than its two neighbouring data points) and (3) Ensuring that the peaks are distinct in time, i.e. separated by at least 24 hours from another peak. When peaks are separated by less than 24 hours, only the peak with the highest wind speed is selected and the weaker peak(s) is (are) discarded. The events are identified by red circles in Figure 4.5.

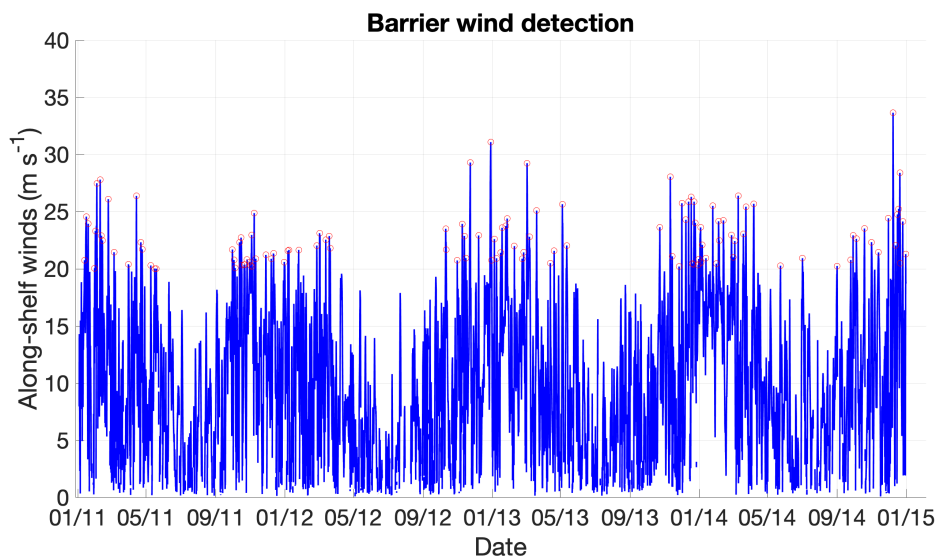


Fig. 4.5 Local wind speeds at KGA between 2011 and 2014 (from ERA5). Winds that are not between a northerly and easterly are removed from this time series. The barrier wind events were identified, using the routine presented in (Harden et al., 2016), and are indicated by the red circles.

Eighty-five barrier wind events, which coincide with the KGA deployments, were identified using this approach, with the vast majority occurring in the cold season (October-March), including 27 events in 2011-12, 26 events in 2012-13 and 29 events in 2013-14. Three events occurred in the other half of the year (all in 2014) (Figure 4.5). The times of the identified events were used to construct a composite of the ocean response to the events, using the Greenland shelf and upper slope mooring data. The composites range from 20 days before the event to 20 days after the event, so as to capture the temporal evolution of the fields and to capture lagged responses. All the ocean time series were smoothed using a second-order 2 day low-passed Butterworth filter prior to the compositing, to remove high frequency variability such as tides.

### 4.3.2 Barrier wind impact on hydrography at KGA

The impact of barrier wind events, introduced in the preceding pages, on the hydrography of DSO source water at KGA is investigated below. Composites are constructed to characterise the typical response of the ocean to the barrier wind events. To construct the composites, the mean of all time steps when a barrier wind event occurred were calculated. This is  $T=0$  in Figure 4.6. The mean of all time steps 20 days before all barrier wind events is calculated ( $T=-20$ ), and then the mean 19 days before is calculated ( $T=-19$ ) and so forth until 20 days after the barrier wind event ( $T=20$ ). Note that many of

the barrier wind events overlap, for example during some barrier wind events a second barrier wind event may occur at  $T=2$  days. The purpose of this section is to describe and quantify the changes to the hydrography driven by barrier wind events.

First it should be noted that the composites are associated with high standard deviation (shaded area in Figure 4.6). Nevertheless, a clear pattern emerges from the mean time series. Barrier winds are associated with negative (near-bottom) density and salinity anomalies on the Greenland shelf and upper slope (Figure 4.6). The ocean response to barrier wind events at KGA14 and KGA12 is similar (Figure 4.6a and b). Here, on the Greenland shelf, the density minimum is associated with temperature and salinity minima. The density begins rapidly decreasing between  $T=0$  and  $T=1$  and continues until the  $T=4-5$  day minimum. The density minimum is sustained between  $T=4$  and  $T=6$  days at KGA14, but begins recovering rapidly after the minimum at KGA12.

The density minimum is associated with salinity minima of 34.45 at KGA14 and 34.42 at KGA12 and temperature minima of  $-0.10^{\circ}\text{C}$  at KGA14 and  $0.11^{\circ}\text{C}$  at KGA12. The anomalies are 0.10 and  $0.35^{\circ}\text{C}$  fresher and cooler than the cold-season mean at KGA12 and 0.05 and  $0.23^{\circ}\text{C}$  below the cold-season mean at KGA14. Despite the temperature minima, density minima occur because salinity is controlling density here. This near-bottom cooling and freshening is consistent with downwelling since both temperature and salinity increase with depth on the shelf (Figure 4.3b and c).

Conversely, offshore, on the upper slope (KGA11) the salinity decreases, but the temperature increases during barrier wind events, reinforcing the density minimum (Figure 4.6c). The temperature maximum is  $1.09^{\circ}\text{C}$  and a salinity minimum (34.86) occur around the same time as the density minimum (i.e. between  $T=4$  and  $T=5$  days). This response is indicative of the core of RAW, defined by the subsurface temperature maximum (Håvik et al., 2017), deepening, as the time-mean position of the core of the RAW is above the near-bottom MC at KGA11 (Figure 4.3b).

This supports the findings of Håvik and Våge (2018), who demonstrated that negative density anomalies on the upper Greenland slope are associated with downwelling favourable winds, and proposed that local coastal Ekman downwelling causes the anomalies. However, the evidence presented to support their argument was not conclusive, for example no velocities were used to show direct evidence of the mechanism. Below, the KGA12 velocities are investigated to examine the evidence for this mechanism.

The velocities from this mooring are used because it is located close to the shelfbreak, and would thus capture any potential cross shelfbreak flows associated with Ekman downwelling. Furthermore, in contrast to the KGA11 and KGA14 data, velocities from

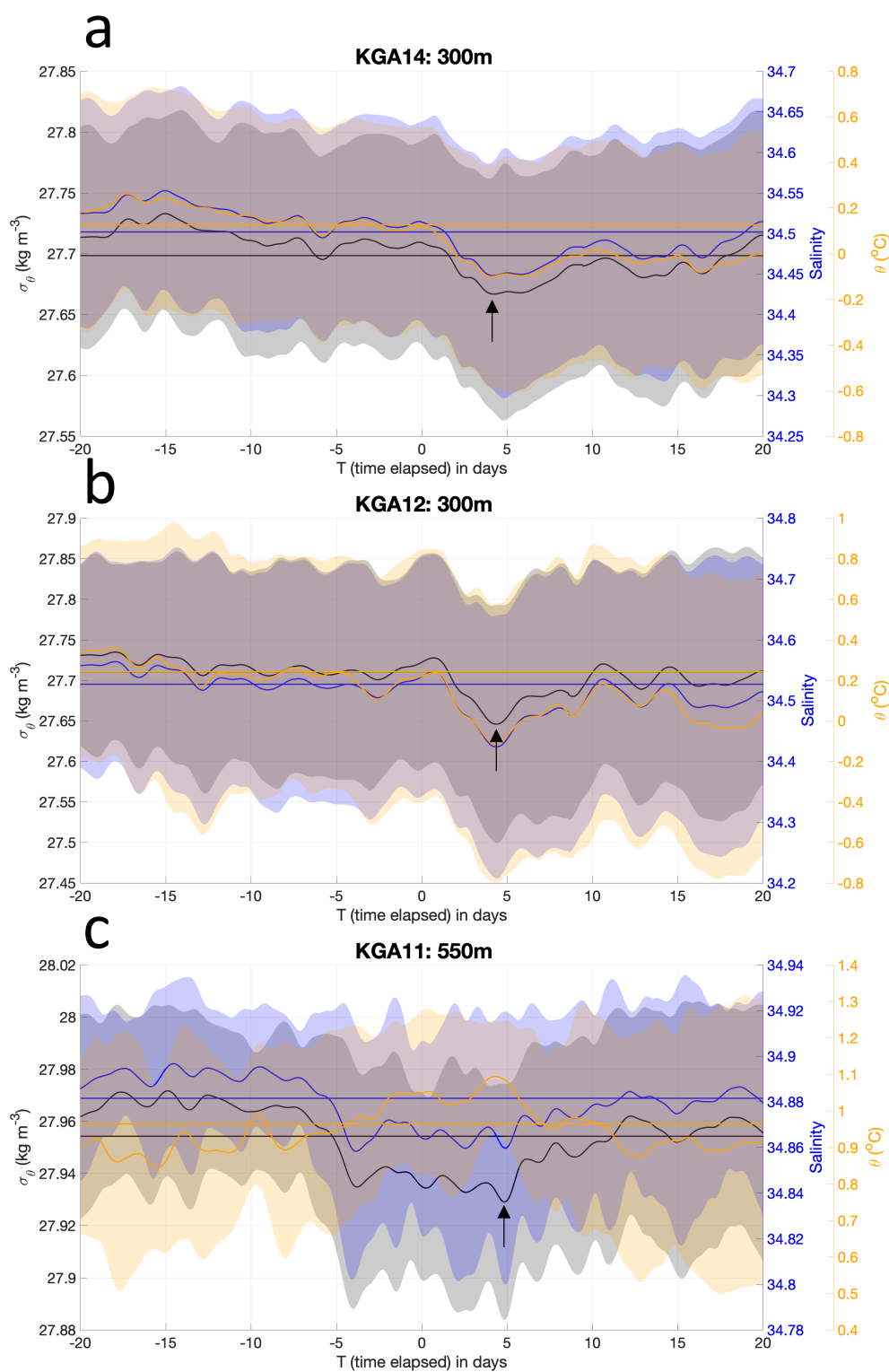


Fig. 4.6 Composite response of the near-bottom ocean properties to barrier wind events at KGA14 (a), KGA12 (b) and KGA11 (c). Potential density ( $\sigma_\theta$ ) is in black, temperature ( $\theta$ ) is in yellow and salinity is in blue. The thick lines are the means and the shaded area is the mean  $\pm 1$  standard deviation. The composites comprised 58 events at KGA14 and KGA12 (between 2012 and 2014) and 27 events at KGA11 (between 2011 and 2012). The black arrows identify the density minimum.

the entire water column (from 30 m to the bottom), recorded by an upwards facing near-bottom ADCP, are available.

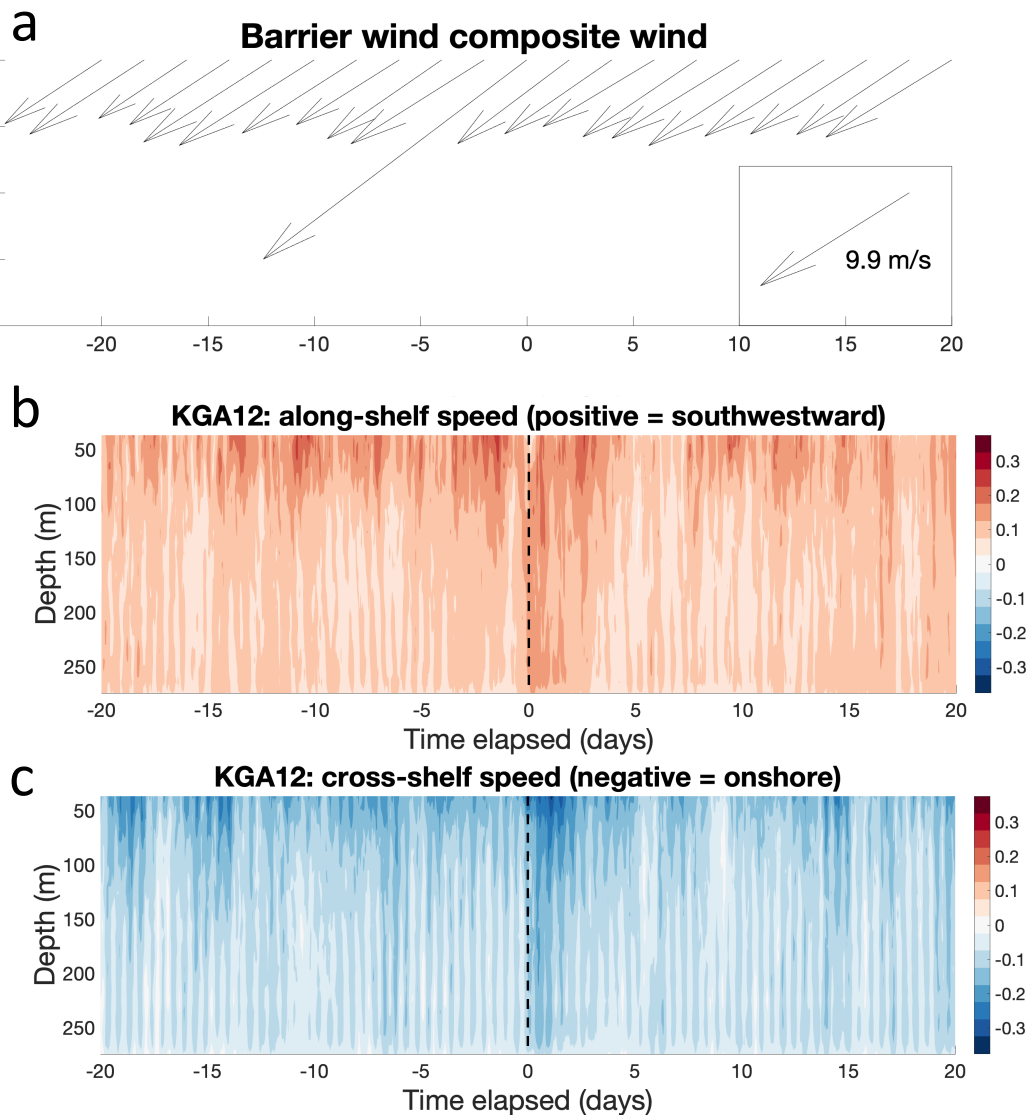


Fig. 4.7 Composite response of the ocean velocity (in  $\text{m s}^{-1}$ ) profile at KGA12 to barrier wind events. Panel a: the wind vectors at the ERA5 grid point nearest the mooring. The legend in this panel shows the reference quiver for the wind quivers. Panels b and c: the along shelf (positive = southwestward) and cross shelf (negative = onshore) ocean velocity profiles at KGA12 respectively. Along shelf is defined as the direction parallel to the barrier wind (i.e.  $220^\circ$  clockwise from northwards), which is also parallel to the shelfbreak, and cross shelf is perpendicular to the barrier wind (i.e.  $130$  degrees clockwise from northwards). The dashed black vertical line in panels b and c indicate  $T=0$  (i.e. the occurrence of the barrier wind event).

The ocean speed in an along shelf and cross shelf direction at KGA12 is estimated. The along shelf direction is defined as positive towards the southwest (specifically

220° clockwise from northward), whilst the cross shelf direction is defined as positive offshore (in the direction perpendicular to the along shore direction). The along shore direction aligns with the orientation of the shelfbreak at KGA (Figure 1.8b). Moreover, the along shore direction aligns with barrier winds (Figure 4.7).

During barrier wind events (between  $T=0$  and  $T=2$  days), there is a clear signal of onshore Ekman velocity, which is intensified at the near-surface where speeds of around  $-0.3 \text{ m s}^{-1}$  occur (negative = onshore; Figure 4.7a). This is consistent with the velocity response at the inshore shelf mooring (KGA14) and the mooring on the upper slope (KGA11) to barrier wind events (not shown). Meanwhile, in the near-bottom layers there is no indication of a compensating offshore transport (illustrated in Figure 4.2). In fact, anomalously high onshore speeds occur throughout the water column (Figure 4.7a). The 'near-bottom' observations at KGA12 are from a height of around 20-40 m and it is possible that this is above the bottom Ekman layer where offshore flow may occur. However, Harden et al. (2014) observed offshore flow in a bottom Ekman layer at this height at a similar latitude, so this is unlikely to be the reason.

Barrier winds also induce anomalously high ocean speeds in the along shelf direction between 100 m and 280 m (Figure 4.7b). The along shelf speed is greater than  $0.1 \text{ m s}^{-1}$  for around 2 days between  $T=0$  and  $T=2$  days between 200 m and 280 m. There is a similar response on the other side of the shelfbreak on the upper slope, at KGA11 (not shown). Conversely, the along shelf speed at the near-surface  $< 100$  m is anomalously weak (Figure 4.7b), because the flow is strongly onshore at those depths. The northeasterly barrier winds cause onshore Ekman transport resulting in an onshore Sea Surface Height (SSH) gradient which increases the pressure gradient force in the offshore direction and drives the geostrophic enhancement of the current. The increased SSH on the shelf was inferred from bottom pressure measurements at KGA12 previously, by Håvik and Våge (2018), who also demonstrated the enhancement of the Shelfbreak EGC in response to strong northeasterly winds. The enhancement of the Shelfbreak EGC is a potentially important freshening mechanism, independent from coastal Ekman downwelling, and investigated below.

The property anomalies, described above, may indicate that offshore flow at depth has displaced the water masses offshore (i.e. Mechanism 1: offshore flow during Ekman downwelling, see Figure 4.2a), however there is no direct evidence (i.e. from the velocity data) of offshore flow at depth during barrier wind events (Figure 4.7). The lag time between barrier wind event and density minimum is perhaps too long (4-5 days) to be explained by a local offshore flow at depth in response to barrier wind events. In fact, in a previous study, Harden et al. (2014) showed that the lag time between wind forcing and offshore flow at depth was 0-0.5 days at a mooring array 250 km downstream of

DS. Therefore, it is possible that the necessary wind-driven offshore flow at depth to cause the negative property anomalies occurs upstream of KGA and causes the property anomalies at KGA via advection.

One location which may be conducive to wind-driven offshore flow at depth is situated around 100 km to the north of KGA at around 69°N (see Figure 1.8b). Here the shelf is very narrow and therefore greater volumes of shelf water may be exported off the shelf and transported by the Shelfbreak EGC. To evaluate the hypothesis that offshore flow at depth occurs here and the signal is advected to KGA, the transit time between these two locations was estimated. To estimate the transit distance, the distance along the 550 m isobath (situated on the upper Greenland slope) from 69°N to KGA11 was integrated, and the distance amounts to 126 km. For a four day advection time along this distance, advection speeds of 0.37 m s<sup>-1</sup> at the near-bottom are required. However, the maximum advection speeds at 550 m on the upper Greenland slope (KGA11) during barrier wind events is 0.15 m s<sup>-1</sup> (not shown). Assuming the observed speed of the Shelfbreak EGC at KGA11 is representative of upstream locations, it is not likely that the density minima in the composites are driven by upstream downwelling at 69°N where the shelf is very thin (Figure 1.8b). It is more likely that the wind driven offshore flow at depth (mechanism 1) occurs between 69° and KGA11.

## 4.4 Evidence for Mechanism 2

An alternative explanation for the property anomalies observed following barrier wind events is Ekman pumping, which is introduced in Section 4.2 as Mechanism 2 (see Figure 4.2b). Ekman pumping induces heaving of the isopycnals, which would bring fresher and lighter water deeper in the water column, causing anomalously fresh and cold water to be detected at the (fixed depth) moored instruments (Figure 4.2). To investigate, Ekman pumping velocities were computed from the  $u_{10}$  and  $v_{10}$  fields at ERA5. The Ekman pumping velocity ( $W_{ek}$ ) is derived from the following equations, based on Gill (1982):

$$\tau_x = \rho_{at} C_d (\sqrt{u_{10}^2 + v_{10}^2}) u_{10} \quad (4.1)$$

$$\tau_y = \rho_{at} C_d (\sqrt{u_{10}^2 + v_{10}^2}) v_{10} \quad (4.2)$$

$$curl(\tau) = \frac{\partial \tau_y}{\partial x} - \frac{\partial \tau_x}{\partial y} \quad (4.3)$$

$$W_{ek} = \frac{1}{\rho_{oc} f} curl(\tau) \quad (4.4)$$

where  $\rho_{at}$  is the reference density of air ( $1.225 \text{ kg m}^{-3}$ ),  $\rho_{oc}$  is the reference density of the ocean ( $1025 \text{ kg m}^{-3}$ ),  $C_d$  is the drag coefficient ( $1.25 \times 10^{-3}$ )  $f$  is the coriolis parameter ( $1.35 \times 10^{-4}$  at KGA) and  $W_{ek}$  is the vertical Ekman velocity, which is proportional to the wind stress curl.

Negative vertical Ekman velocities indicate Ekman pumping. Barrier winds are associated with strongly negative wind stress curl over the Greenland shelf and slope (Figure 4.8a), which is conducive to Ekman pumping. Conversely, the wind stress curl is positive further offshore to the east. This pattern is an intensification of the annual mean wind stress curl distribution described by Våge et al. (2013). During barrier wind events the negative wind stress curl over the Greenland shelf and slope is an order of magnitude ( $1 \times 10^{-5} \text{ N m}^{-3}$ ) more intense than the annual mean presented by Våge et al. (2013). Therefore, barrier wind events may be conducive to increased Ekman pumping velocities over the Greenland shelf and slope.

In the barrier wind composite, the maximum Ekman pumping velocity is around  $2 \text{ m day}^{-1}$ , which occurs between  $T=0$  and  $T=1$  day (Figure 4.8b). The time-mean vertical salinity gradient near-bottom on the upper Greenland slope is  $0.0008 \text{ m}^{-1}$ . Therefore, the Ekman pumping velocity is not sufficiently high to explain the salinity anomalies on the timescale of the barrier wind composite (Figure 4.8b). Furthermore, the salinity minimum occurs around 5 days after the maximum Ekman pumping velocity (compare Figure 4.6 with Figure 4.8b), suggesting that it is unlikely that Ekman pumping is the most important process.

Nevertheless, accumulated over a period of multiple weeks/months, Ekman pumping may have an important effect on the hydrography. For example, de Steur et al. (2017) demonstrate that the wind stress curl is extremely negative, for over a month in October/November 2011 (their Fig. 10), which may explain the negative salinity anomaly on the upper Greenland slope in that period. Therefore, Ekman pumping (Mechanism 2) cannot be completely ruled out as an important mechanism driving sustained freshening of the DSO. The implications of this mechanism on the hydrographic variability of DSO source water north of DS are discussed further in Chapter 6.

To summarise, barrier wind events precede negative salinity and density anomalies on the Greenland shelf and slope, at near-bottom depths, by 4-5 days. Barrier wind events are associated with negative wind stress curl here, which promotes Ekman pumping and isopycnal heaving (Mechanism 2), which may partly explain the property anomalies. However, the rapid change in properties in the barrier wind composites cannot be explained by Ekman pumping alone, because the velocities are too low. Therefore it is likely that offshore flow during Ekman downwelling (i.e. Mechanism 1) plays a role in causing the property anomalies. No direct evidence of this mechanism

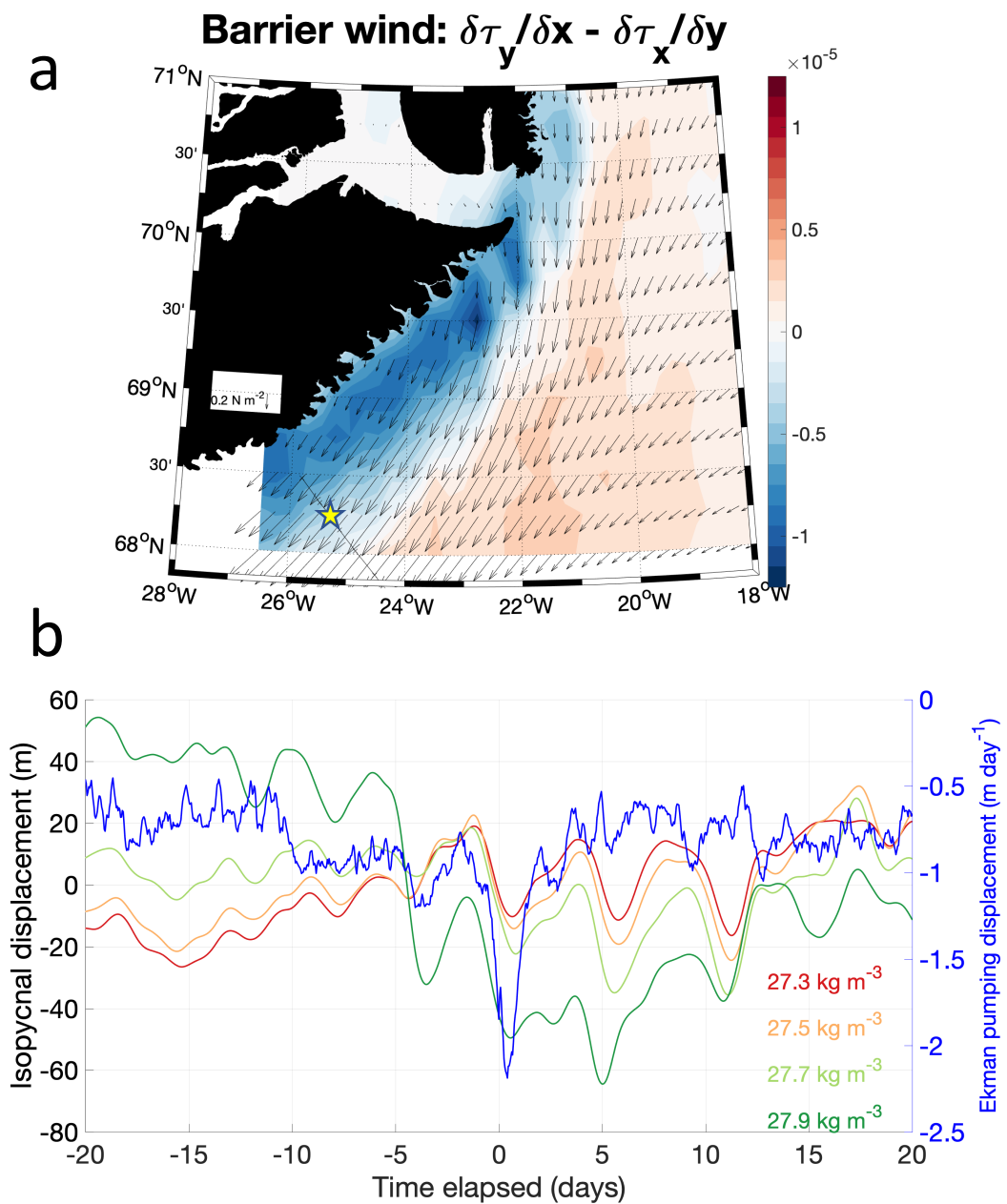


Fig. 4.8 Barrier wind composites of wind stress curl and Ekman pumping. (a): map of wind stress (quivers; in  $\text{N m}^{-2}$ ) and wind stress curl (colours; in  $\text{N m}^{-3}$ ) during barrier wind event ( $T=0$ ). (b): evolution of vertical Ekman velocity (blue)/vertical isopycnal displacement (multicoloured) at mooring KGA11. The location of KGA11 is marked by the yellow star in the map, whilst the other moorings are indicated by the black crosses. The vertical isopycnal displacement is relative to the mean isopycnal depth over the 40 day composite period.

taking place was detected in the velocities, however the 4-5 day lag time between barrier wind event and property anomaly suggests that the downwelling may take place upstream of the mooring observations.

## 4.5 Evidence for Mechanism 3

### 4.5.1 Methodology

In order to identify and characterise the enhancement of the Shelfbreak EGC (Mechanism 3), the volume transport of DSO source water through KGA is quantified, and analysed. The gridded data are used for the calculation of volume transport, except the gridded data from the Greenland shelf which are inaccurate (see Chapter 2). The omission of the shelf data results in slightly lower transports, compared with Harden et al. (2016) who used all of the gridded data. The method described below is repeated at each time step. First, the water above the depth of the  $27.8 \text{ kg m}^{-3}$  isopycnal is removed, since this is traditionally used as the upper boundary for the DSO (Dickson and Brown, 1994). Second, the horizontal boundaries of the different currents are determined, according to the method used by Harden et al. (2016). The horizontal boundaries of the Separated EGC and NIJ are found by comparing the temperature and salinity of profiles between end-member profiles, situated over the lower Iceland slope (Separated EGC), and over the upper Iceland slope (NIJ) in the  $27.97 \text{ kg m}^{-3} < \sigma_\theta < 28.03 \text{ kg m}^{-3}$  interval. The boundary between the Shelfbreak EGC and the Separated EGC is fixed at a cross sectional distance of around 88 km, which is the deepest profile of the section, located at the base of the Greenland and Iceland slopes (Figure 4.9). Third, the volume transport (VT) of each branch is computed by solving the following equation:

$$VT = \int_{H=0}^{H=\eta} \int_{x=x1}^{x=x2} vr \, dx dz, \quad (4.5)$$

where H is height above the deepest data point,  $\eta$  is the height above bottom of the DSO interface,  $x1$  and  $x2$  are horizontal boundaries of the current branches and  $vr$  is the along-stream velocity through the KGA section (positive to the southwest). Equation 4.5 is solved using the Trapezoidal method, for each current branch.

Descriptively, the process of calculating the volume transport using the Trapezoidal rule is as follows. Multiple boxes are derived from the gridded data, and the average velocity through each box is calculated from the mean of the four corners of the box (Figure 4.9a), and multiplied by the cross-sectional area of each box, which is  $400,000 \text{ m}^2$ , to obtain the volume transports (in  $\text{m}^3 \text{ s}^{-1}$ ). For cases near the boundary of the gridded data, the volume transport through the triangles was estimated by multiplying the average velocity of the three sides of the triangle by the area of the half box (triangle). The volume transport of each current branch is then calculated by summing the box/triangle transports between the horizontal current boundaries.

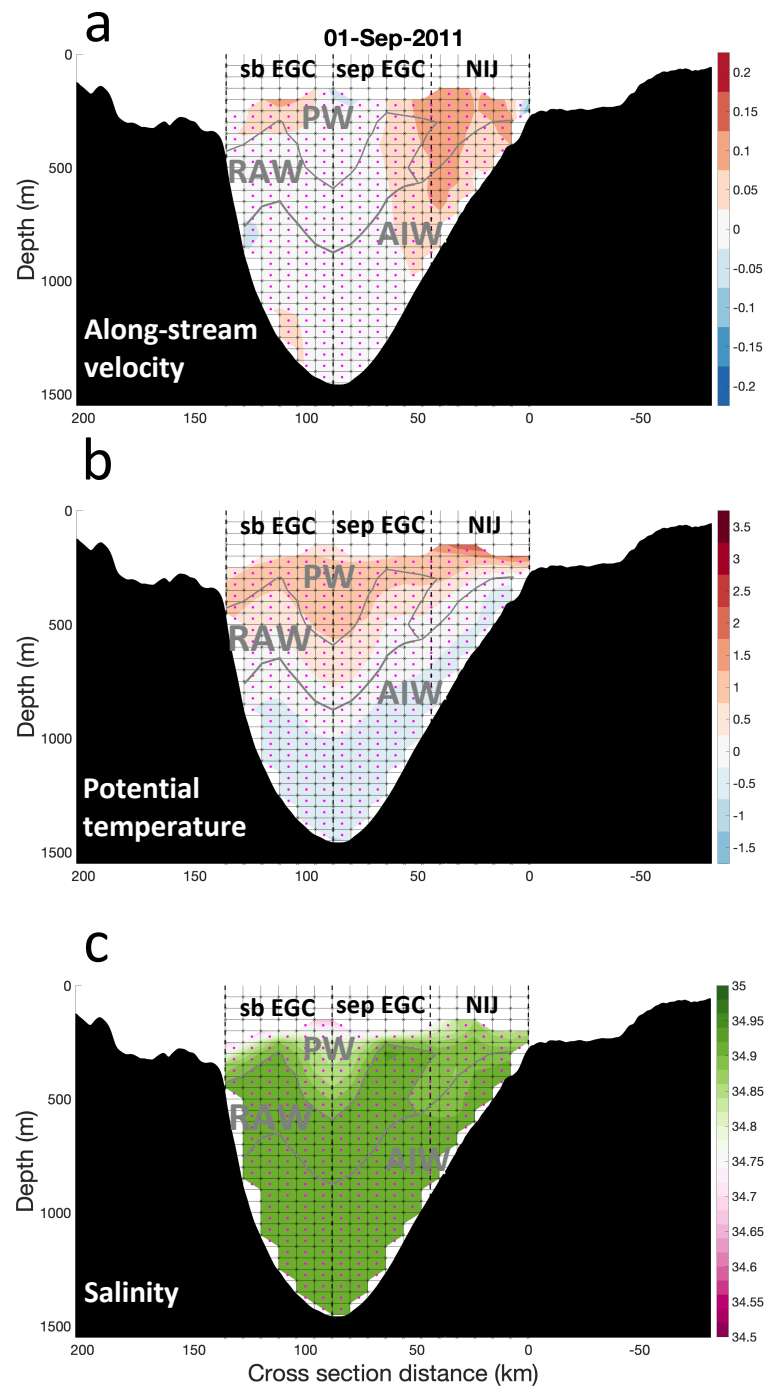


Fig. 4.9 Snapshots of along stream velocity (top), salinity (middle) and temperature (bottom) on 1 Sep 2011. The thin black lines indicate the locations of the gridded data, and the thick dashed lines are the horizontal boundaries of the different current branches, determined from the algorithm created by Harden et al. (2016). The currents labelled are the Shelfbreak EGC (sb EGC), Separated EGC (sep EGC) and North Icelandic Jet (NIJ). The magenta dots are the mid points of the grid boxes/triangles, the value of which is approximated from the mean of the 3 or 4 corners of the shape.

When the boundary between the Separated EGC and the NIJ is found through the middle of a grid box (e.g. in the example snapshot: Figure 4.9), half of the volume transport is assigned to the Separated EGC and the other half is assigned to the NIJ.

The volume transport is analysed in terms of temperature/salinity coordinates to compute water mass transports. This involves sorting each box/triangle into  $\theta$ -S bins and summing the volume transport of the bins. The bins have a salinity width of 0.02, and a temperature width of 0.2°C. The size of the bins used changes the volume transport in each bin, does not change the overall water mass transports. The temperature and salinity of each box/triangle mid-point is determined in the same way as the velocity, by calculating the mean value of the edges of the box/triangle (Figure 4.9b and c). Volumetric  $\theta$ -S decompositions were performed for the sum of all branches, and for the different current branches individually.

#### 4.5.2 Current transport variability

Using the methodology described above, the volume transport time series of the individual branches, and the sum of all branches, is computed, and displayed in Figure 4.10. As demonstrated previously, by Harden et al. (2016), the currents exhibit seasonal variability, with the Shelfbreak EGC at maximum strength in winter months, with transports exceeding 3 Sv in December 2011 and March 2012, and minimum in the summer months. Conversely, the NIJ is at its weakest in the winter months. The Separated EGC is also at its weakest in the cold season, with weakly negative volume transports in December 2011 and March 2012, and at its strongest in April 2012. As a result of this seasonality, the volume transport of the Shelfbreak EGC is approximately equal to the net transport around the turn of the year. The net volume transport has a weak seasonal cycle, and the phase reflects the seasonality of the Shelfbreak EGC.

Furthermore, the anti-correlation between the Shelfbreak EGC and Separated EGC is apparent in Figure 4.10. Harden et al. (2016) argued that this anti-correlation was a result of the ocean circulation in the Blosseville Basin switching from cyclonic, to anti-cyclonic due to negative and positive wind stress curl in the basin respectively. When the circulation is cyclonic, the Shelfbreak EGC is enhanced and the Separated EGC is weakened, and vice versa. Atmospheric reanalysis from 1979-2012 were used to argue that the change in the ocean circulation is seasonal, since the wind stress curl typically changes from negative in the winter to positive in the summer (Harden et al., 2016), and therefore 2011-12 might be representative of other years.

Since the DSO source water branches have different temperature and salinity structure, this raises the possibility that the seasonality of the volume transport of the currents drives the salinity seasonality of the DSO downstream, at ANG. In order to characterise

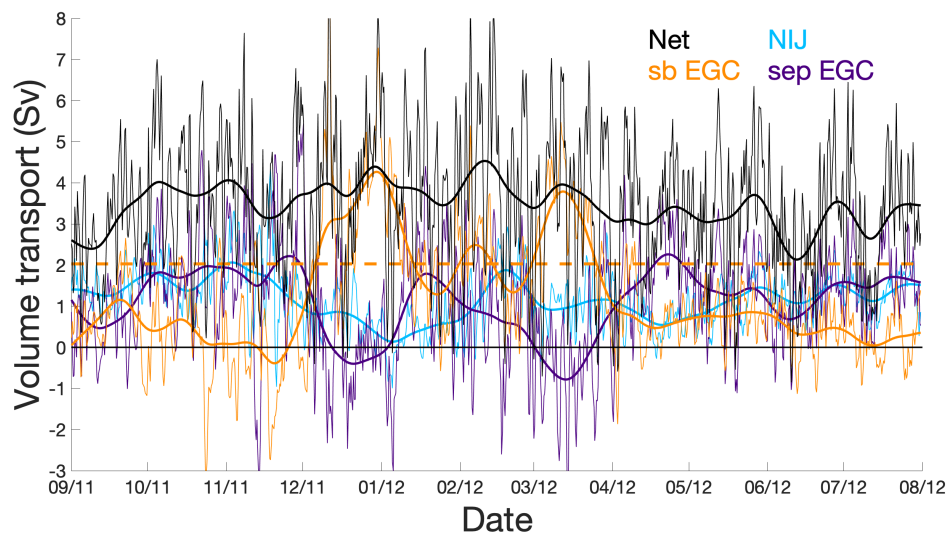


Fig. 4.10 Volume transport (Sv) variability of DSO source water passing through KGA in 2011-12, via the Shelfbreak EGC (sb EGC; orange), Separated EGC (sep EGC; purple), NIJ (light blue), and the net transport (black). The thin lines are the 8 hourly unfiltered data whereas the thick lines are the time series smoothed with a second order Butterworth filter, with a 30 day low passed frequency cut off. The dashed orange line is the upper quartile of the unfiltered Shelfbreak EGC time series.

Mechanism 3, the volume transport of different water masses by the DSO source water branches is quantified below.

### 4.5.3 Mean water mass transports

The time-mean volumetric  $\theta$ -S distribution of the Shelfbreak EGC, Separated EGC, NIJ, and the sum of all three is shown in Figure 4.11. The structure of the three branches is similar, with the weakly stratified densest layers ( $\sigma_{\theta} > 27.95 \text{ kg m}^{-3}$ ) associated with the highest volume transports, and an overlying pycnocline associated with smaller volume transports (Figure 4.11). Whilst the pycnocline of the Shelfbreak EGC has stable salinity stratification and unstable temperature stratification, the Separated EGC pycnocline has stable salinity stratification and neutral temperature stratification, and the NIJ pycnocline has stable salinity and temperature stratification. The net transport is 3.01 Sv (positive = southwestward), which is lower than the estimate of Harden et al. (2016) (3.5 Sv), due to the omission of the inaccurate gridded data.

To quantify the volume transport of the different water masses, the temperature/salinity definitions of AIW and RAW from the literature are adopted, as labelled in Figure 4.4 and Figure 4.11. Note that although the volume transports are quoted to two decimal places, uncertainty of these transports arises primarily from instrument

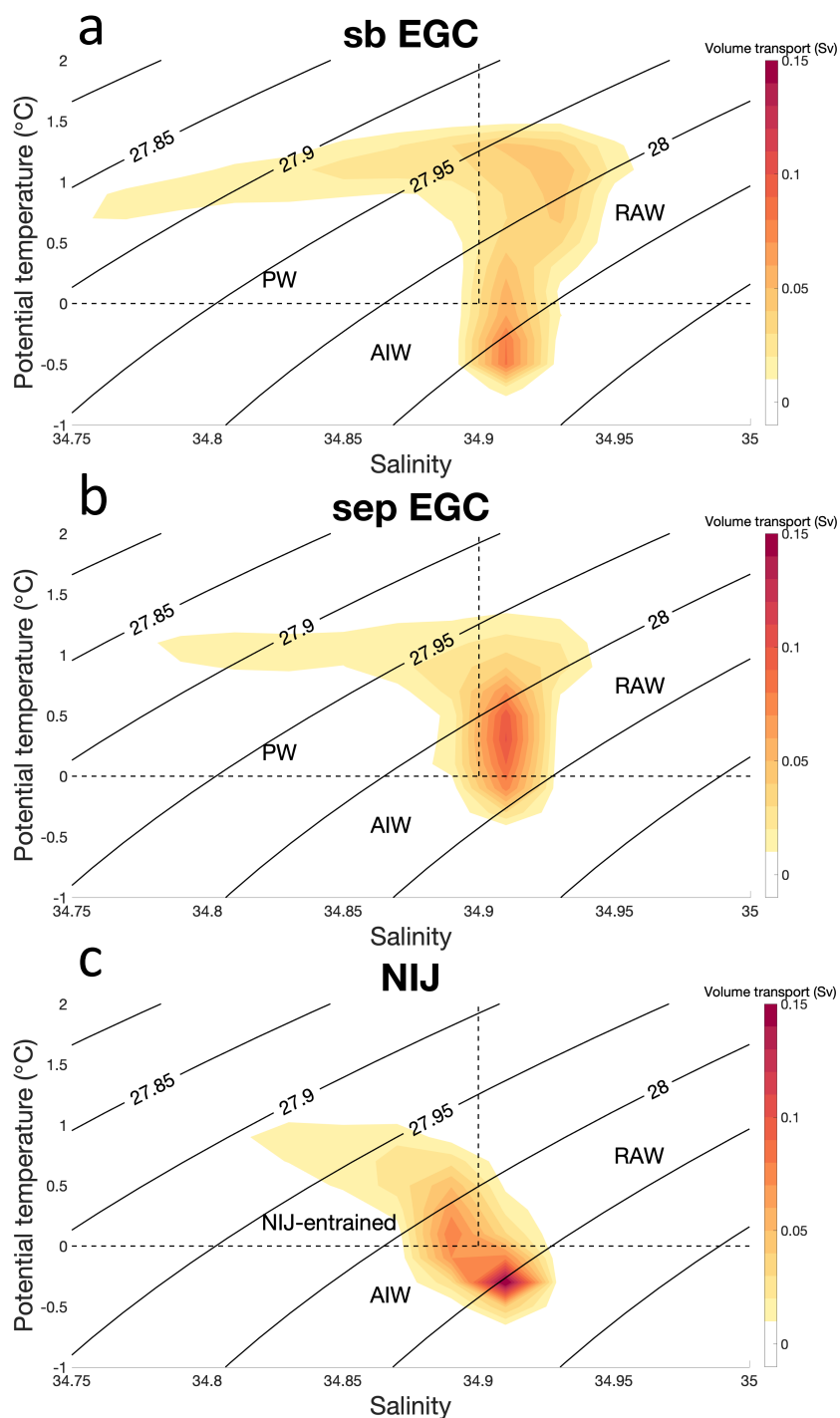


Fig. 4.11 time-mean volume transport (positive=southwestward) through KGA as a function of temperature and salinity for the three different current branches of DSO source water: (a) Shelfbreak EGC (sb EGC), (b) Separated EGC (sep. EGC) and (c) North Icelandic Jet (NIJ). The black dashed lines indicate the AIW and RAW boundaries, as established in the literature. The PW is the water that falls outside of the water mass boundaries, found within the pycnocline in the EGC branches, and the NIJ-entrained is the water found above the AIW, and assumed to be entrained into the NIJ.

Water mass	All snapshots	Strong sb EGC
AIW	$0.72 \pm 0.73$	$0.93 \pm 0.76$
RAW	$1.12 \pm 0.74$	$1.65 \pm 0.78$
PW	$0.7 \pm 0.46$	$1.14 \pm 0.51$
NIJ-entrained	$0.47 \pm 0.36$	$0.33 \pm 0.39$
Total	3.01	4.05

Table 4.1 Mean southwestward water mass transports (mean  $\pm$  standard deviation) through KGA of all snapshots and of all snapshots when the Shelfbreak EGC is strong (i.e. its volume transport is greater than the upper quartile in Figure 4.10). The PW is the water overlying RAW in the EGC, whilst NIJ-entrained is the water overlying the AIW in the NIJ

measurement errors and errors resulting from the fact that the moorings in the central part of the array were too widely spaced apart to fully resolve the horizontal scales of the synoptic field (Harden et al., 2016). The average error of the net volume transport at each time step is 0.45 Sv (Harden et al. (2016); see Chapter 2).

The NIJ transports the highest fraction of AIW (0.37 Sv of a total of 0.72 Sv). The Separated EGC transports 0.1 Sv of AIW, whilst the Shelfbreak EGC transports 0.25 Sv of AIW. This shows that, in the time-mean, the EGC branches contribute roughly half of the AIW volume transport, whilst the NIJ contributes the other half. Conversely, almost all of the RAW is transported by the EGC branches. The Shelfbreak EGC transports the highest fraction of RAW (0.55 Sv of a total of 1.12 Sv), the second highest RAW volume transport is associated with the Separated EGC (0.51 Sv), whilst the NIJ only transports a small fraction (0.06 Sv).

A sizeable fraction of the net volume transport in the time-mean cannot be attributed to either of these water masses, within the traditional water mass  $\theta$ -S boundaries from the literature Figure 4.11a and b. The lighter water within the EGC branches is PW, which is likely formed as the product of PSW mixing with RAW in the EGC between Fram Strait and KGA, as reasoned above, in Section 4.2. Conversely, the the water overlying the AIW in the NIJ has a higher temperature and salinity than the PW of the EGC (Figure 4.11c), and may derive from entrainment of lighter water into the NIJ (Semper et al., 2019), and it is thus termed NIJ-entrained hereafter. The mean volume transport of the NIJ-entrained is 0.47 Sv, whilst the mean volume transport of the PW is 0.7 Sv with equal contributions (0.35 Sv) from the two EGC branches. The volume transport of water masses are presented in Table 4.1.

#### 4.5.4 Composite water mass transports

To investigate the hydrographic changes associated with Mechanism 3 (an intensified Shelfbreak EGC), a volumetric  $\theta$ -S composite was constructed. The composite was created by averaging together all the snapshots when the Shelfbreak EGC volume transport was greater than the upper quartile threshold (see dashed horizontal line in Figure 4.10). The composite was composed of 251 CTD snapshots. Note that 82 of these snapshots (33% of all 251) occurred within 3 days after a barrier wind event, indicating that barrier wind events drive enhancement of the Shelfbreak EGC, but there are other mechanisms that also play a role. As expected, when the Shelfbreak EGC is enhanced, the volume transport of RAW and the PW component of the Shelfbreak EGC increases (Figure 4.12a). The volume transport of RAW in the composite is 1.65 Sv (positive = southwestward) and the volume transport of the PW component of the EGC is 1.14 Sv.

The volume transport of the RAW in the composite is 47% higher than the mean, whilst the volume transport of the PW water is 63% higher in the composite than the time-mean. Conversely, the transport of AIW increases by a smaller amount (29%), from 0.72 Sv in the time-mean to 0.93 Sv in the composite. The southwestward volume transport of the AIW increases by a smaller amount because of the northward (negative) volume transport of this water mass by the Separated EGC (Figure 4.12b).

The increased volume transport of the PW water, which is largely fresh ( $S < 34.9$ ) pycnocline water, may drive sustained freshening of the DSO downstream. At the same time, the volume transport of the saline RAW increases, and this could have the opposite effect on the salinity of the DSO. However, the salinity of the RAW (34.93) is only slightly higher than the salinity of the AIW (34.91) (Figure 4.12), therefore the effect of the changing ratio of the RAW to AIW likely only has a small effect on the salinity of the DSO downstream.

To summarise, the two key source water masses of DSO are RAW and AIW, which are advected through KGA via the Shelfbreak EGC, Separated EGC and NIJ. The time-mean transport of the AIW is 0.72 Sv and the time mean transport of the RAW is 1.12 Sv. There is also an important volume transport of PW, a fresh component of DSO source water, which does not fall within traditional water mass boundaries, via the two EGC branches, totalling 0.7 Sv in the time-mean. The PW water is largely pycnocline water overlying the source water masses, and they are likely a product of mixing between the RAW and polar origin water masses.

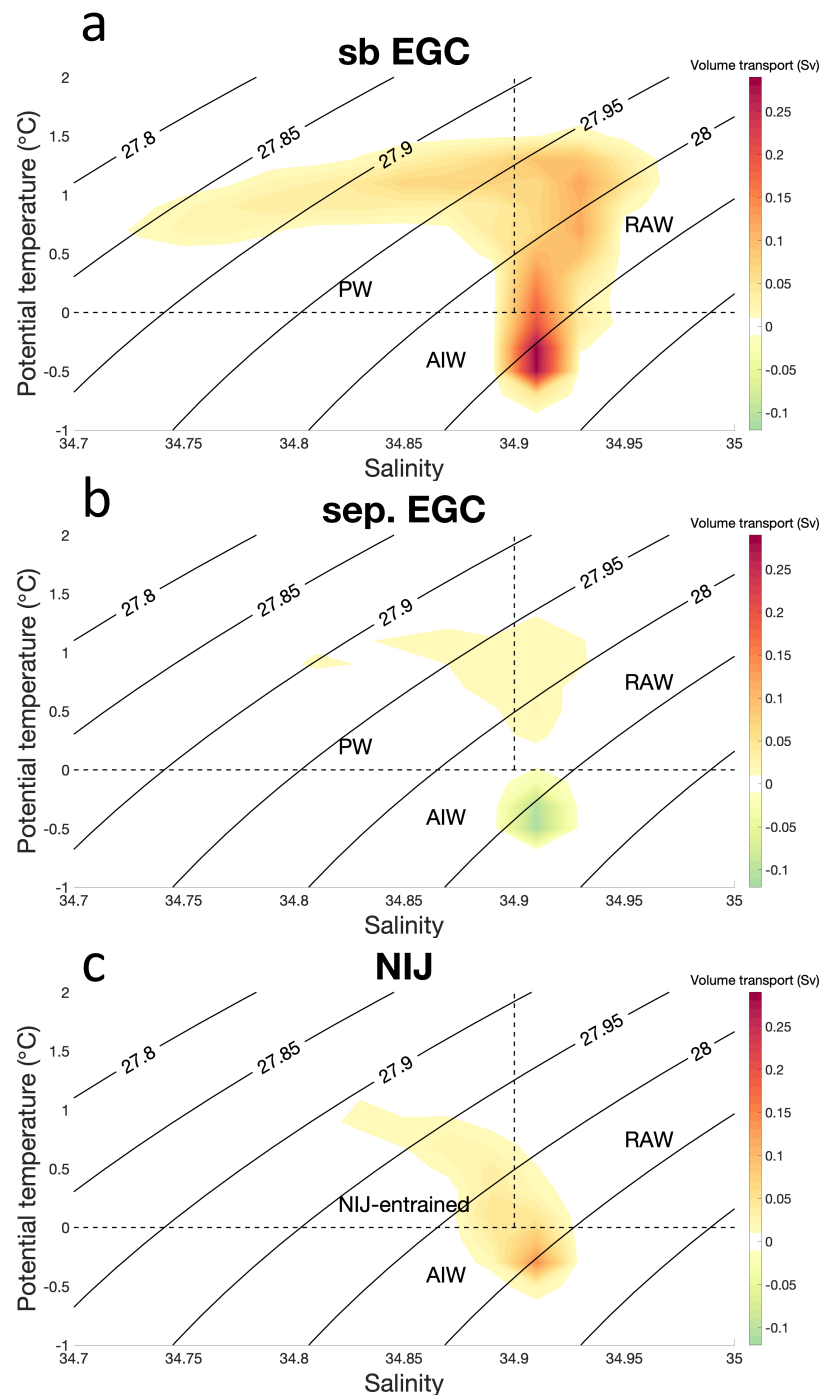


Fig. 4.12 Composite volume transport (positive=southwestward) through KGA as a function of temperature and salinity for the three different current branches of DSO source water: (a) Shelfbreak EGC (sb EGC), (b) Separated EGC (sep. EGC) and (c) North Icelandic Jet (NIJ). The composite is the mean of all snapshots where the volume transport of the sb EGC exceeds the upper quartile transport (see orange horizontal line in Figure 4.10). The black dashed lines indicate water mass boundaries, as established in the literature. The PW is the water that falls outside of the water mass boundaries, found within the pycnocline in the EGC branches, and the NIJ-entrained is the water found above the AIW, and assumed to be entrained into the NIJ. Note the colour scheme is different to that used in Figure 4.11.

It has also been shown that when the Shelfbreak EGC is intensified, the volume transport of the PW water increases by 63%. It is proposed that the increase in the fresh PW source water results in sustained freshening of the DSO. In the following section, the contribution of the enhanced Shelfbreak EGC to the sustained freshening of the DSO is estimated using the concept of transport weighted salinity.

#### 4.5.5 Contribution to freshening of the DSO

The salinity across the DSO at ANG is unchanging (i.e. there is no salinity gradient across the plume) (see Chapter 3), which stands in contrast to the salinity across the different source of DSO at KGA. Therefore, it is likely that the different source water masses of the DSO mix together within the DSO in the approximately 700 km between KGA and ANG. This assumption of mixing between the DSO source water masses is used to estimate the effect of the changing volume transport of water masses through KGA on the salinity of the DSO downstream, using the concept of volume transport weighted salinity.

The concept of volume transport weighted salinity has been used previously, by Szuts and Meinen (2017) to investigate the salinity variability of water masses observed at Florida Straits, and also by Baringer and Price (1997), to investigate the salinity transformation of the Mediterranean Outflow. In this study, the transport weighted salinity equation of Baringer and Price (1997) and equation 4.5 are adapted into the following:

$$\bar{S} = \frac{\int_{H=0}^{H=\eta} \int_{x=x1}^{x=x2} S.vr \, dx dz}{\int_{H=0}^{H=\eta} \int_{x=x1}^{x=x2} vr \, dx dz}, \quad (4.6)$$

where  $\bar{S}$  is the volume transport weighted salinity,  $S$  is the salinity, and the other terms are as they are in equation 4.5. This quantity approximates the resulting salinity of the DSO after the different sources of DSO have mixed with each other downstream of KGA.

The time series of  $\bar{S}$  is shown in Figure 4.13. The salinity fluctuates on short timescales around a time-mean of 34.88. On timescales beyond a month there is variability too, and the standard deviation of the smoothed time series is 0.01. The salinity also varies on a seasonal basis too, with comparatively fresh values in winter (December-January-February mean salinity of 34.867), and more saline values in summer and autumn (mean June-November salinity of 34.882).

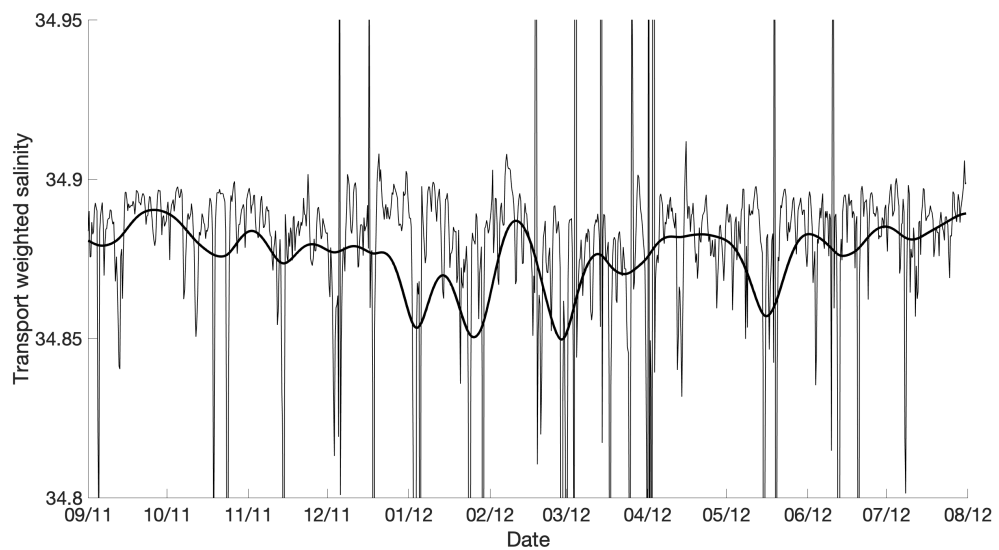


Fig. 4.13 Time series of the volume transport weighted salinity (computed from equation 4.6) of DSO source water passing through KGA to the southwest in 2011-12. The thin lines are from the 8-hourly gridded data, whilst the thick line is the 30-day smoothed time series.

The freshening of  $\bar{S}$  in winter (Figure 4.13) coincides with an enhanced Shelfbreak EGC and weakened NIJ (Figure 4.10). This demonstrates that it is the enhanced volume transport of the fresh PW water in the Shelfbreak EGC which drives the freshening of  $\bar{S}$ . By contrast, when the Shelfbreak EGC is weakened (volume transports  $< 1$  Sv) in summer and autumn months (Figure 4.10),  $\bar{S}$  is 0.015 more than in the winter months, when the Shelfbreak EGC is enhanced.

In their paper, Harden et al. (2016) argued that the seasonality of the volume transport of the Shelfbreak EGC, observed between 2011 and 2012, is representative of other years and driven by the changing sign of the wind stress curl in the Blosseville Basin. Therefore, it could be the seasonality of the Shelfbreak EGC drives seasonality in  $\bar{S}$ , which causes the salinity seasonality of the DSO at ANG.

By comparison, the magnitude of the salinity seasonality of the DSO at ANG is 0.02, which is a similar magnitude to the seasonality of  $\bar{S}$ . However, the DSO source water masses passing through KGA are not the only water masses contributing to the DSO at ANG. The total volume transport of the DSO at ANG is around 5 Sv, with approximately 2 Sv of lighter water (LSW and MIW) entrained between DS and ANG (Dickson and Brown, 1994). Therefore, assuming that the source water passing through KGA contributes a 60% fraction of the total volume transport of the southward volume transport of DSO through ANG, the expected salinity seasonality of the DSO from the salinity seasonality of  $\bar{S}$  is  $0.015 \times 0.6$ , which is 0.009. This is approximately half

the magnitude of the salinity seasonality of the DSO observed at ANG. Furthermore, the phase of the seasonality of  $\bar{S}$  precedes the seasonality at ANG (where the salinity minimum is in spring) by around three months, which is consistent with estimated transit times from KGA to ANG (Chapter 3).

In summary, this evidence suggests that the seasonal freshening of the DSO downstream is partly driven by variation in volume transport of the Shelfbreak EGC to the north of the DS due to wind forcing, but there may also be a role for barrier wind driven Ekman downwelling and Ekman pumping too. It is estimated that the seasonality of the Shelfbreak EGC volume transport may explain around 50% of the salinity seasonality of the DSO. However, this calculation is based on only one year of mooring data from KGA, and it is therefore not clear how representative this result is of other years. Therefore, in Section 4.7, nearly thirty years of data from a seasonally repeated CTD section at DS (see blue squares in Figure 1.8b) are used to discuss the relative contribution of the freshening mechanisms (1-3) discussed above. Preceding this discussion, the evidence for Mechanism 4 is evaluated next.

## 4.6 Evidence for Mechanism 4

While the sources of DSO originating from north of DS dominate DSO transports, there is some contribution to the overflow from water originating from south of DS (Saber et al., 2020; Tanhua et al., 2005). The hypothesis that the sustained intra-annual freshening of the DSO observed at ANG is caused by salinity seasonality of MIW (introduced in Section 4.2), which is Mechanism 4, illustrated in Figure 4.2d, is tested in this section.

Property data from the repeat CTD station - FX9 of the Faxaflói section, are used to test the hypothesis. FX9 is situated on the southwest Iceland slope around the 1000 m isobath (Figure 1.8b), in the pathway of the Irminger Current which advects the MIW northward towards DS (Malmberg et al., 2001). This station also captures the MIW pathway proposed by Saber et al. (2020), based on numerical particle trajectories. This station was occupied four times a year between 1989 and 2019, typically in February, May, August and November (see Chapter 2) and can thus be used to investigate the property seasonality.

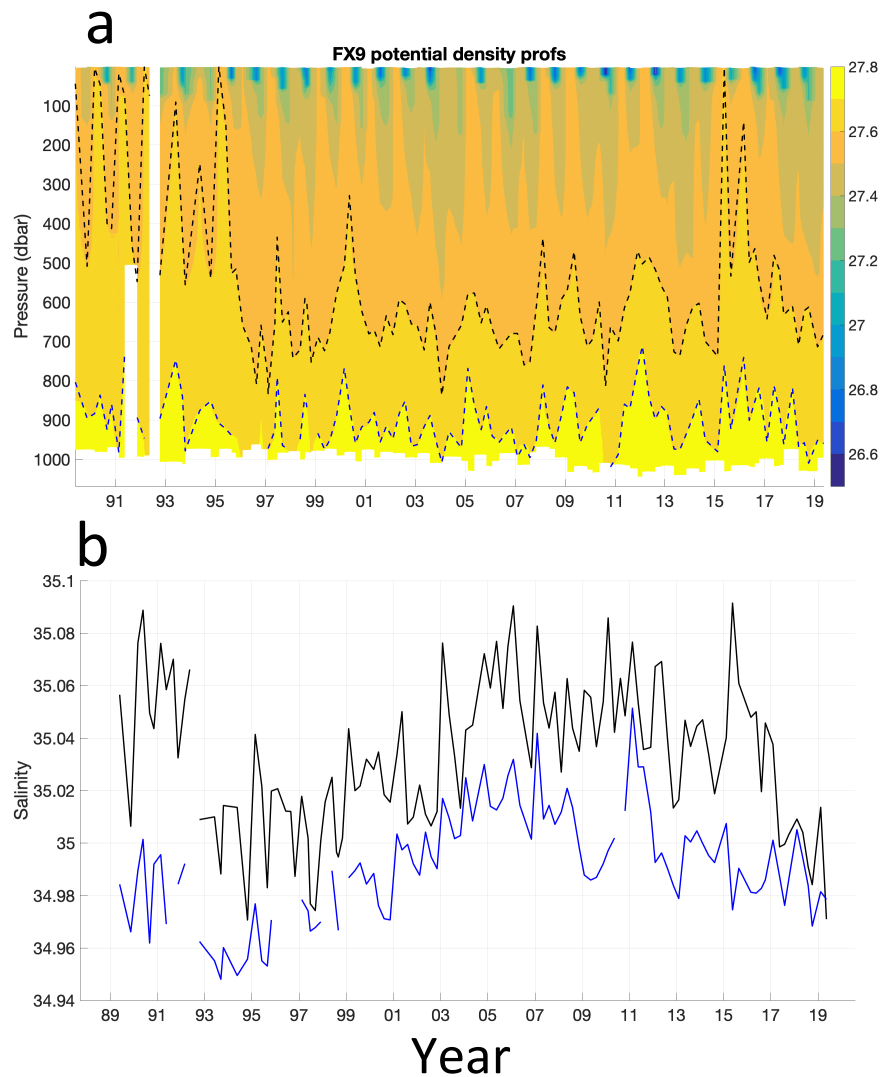


Fig. 4.14 Time series of isopycnal depth (a) and salinity within density classes (b) at FX9. In more detail, (a) is a Hovmöller plot of density ( $\text{kg m}^{-3}$ ) versus pressure and year between 1989 and 2019 at CTD station FX9 on the southwest Iceland slope (for station location, see Figure 1.8b). The dashed black and blue lines are the  $27.6 \text{ kg m}^{-3}$  and  $27.7 \text{ kg m}^{-3}$  isopycnals respectively. The salinity time series are the average salinity within the  $27.6 \text{ kg m}^{-3} < \sigma_\theta < 27.7 \text{ kg m}^{-3}$  layer (black) and the layer between the  $27.7 \text{ kg m}^{-3}$  isopycnal (blue) and the bottom (b).

A Hovmöller plot of density as a function of pressure and time is displayed in Figure 4.14a. In the upper part of the water column, the mixed layer deepens in the cold season and restratifies in the warm season. The deeper, denser water passing through this location is the most likely candidate to feed the DSO because the shallower, lighter water requires substantial modification to become dense enough to contribute to the DSO. Tanhua et al. (2008) defined MIW as having properties of  $\theta \approx 3.86^\circ\text{C}$ ,  $S \approx 34.95$ ,

$\sigma_\theta \approx 27.76 \text{ kg m}^{-3}$ . Therefore, the seasonal salinity variability in the layer between the  $27.6 \text{ kg m}^{-3}$  isopycnal (black dashed line) and the  $\sigma_\theta < 27.7 \text{ kg m}^{-3}$  isopycnal (blue dashed line) and the layer between the  $27.7 \text{ kg m}^{-3}$  isopycnal (blue dashed line) and the bottom (Figure 4.14b) are investigated.

The salinity and temperature (not shown) increased from the mid 1990s to around 2011 before both properties decreased between 2011 and 2019 (Figure 4.14b). The former trends are part of the wider trend of the warming and salinification of the Atlantic inflow into the Nordic Seas, investigated elsewhere (Holliday et al., 2008). To isolate the seasonal signal, the multi-annual variability of salinity was removed. This was achieved by removing the annual average from each data point. The depth of the  $27.6 \text{ kg m}^{-3}$  isopycnal shows some multi-annual variability also; it is found at the near-surface in the first 6 years of the time series, descends to around 650 dbar between 1996 and 2015, rising back up to the near-surface between 2015 and 2017 and descending again from 2017-19. Conversely, the  $27.7 \text{ kg m}^{-3}$  isopycnal mostly stays below the 800 dbar level.

The salinity seasonality is illustrated in Figure 4.15. In both density bins, the salinity maximum is in February with the minimum in the second half of the year (August or November), albeit with large variance. The difference between the means in February and November is 0.02 and 0.01 in the  $27.6 \text{ kg m}^{-3} < \sigma_\theta < 27.7 \text{ kg m}^{-3}$  and  $27.7 \text{ kg m}^{-3} < \sigma_\theta < 27.8 \text{ kg m}^{-3}$  density bins respectively. The salinity increases sharply in winter, possibly because surface driven deep convection forces highly saline near-surface waters downwards. The water column then freshens throughout the year as the surface forcing relaxes and advection removes the signal.

The DSO salinity minimum is in May and the maximum is in December at ANG, compared with the MIW salinity minimum in late summer/autumn and salinity maximum in February at FX9. Supposing the DSO freshening derives from the freshening advecting through FX9, the transit time would therefore be 6-9 months. However, using a numerical particle tracking model, Saberi et al. (2020) argued that the transit times from around the southwest Iceland slope to DS were up to 3 months, and the transit time from DS to ANG is around 10-20 days (Jochumsen et al., 2015; Koszalka et al., 2013). Thus, it appears unlikely that the freshening observed at FX9 is related to that seen at ANG. The magnitude of salinity seasonality is comparable to that observed in the DSO at ANG (as shown in Chapter 3: Figure 3.3). However, the seasonal property anomalies of the MIW are dampened by the other sources of DSO. To estimate the ratio of MIW to other water masses in the DSO, an estimate of the relative contribution of different water masses to the DSO is required.

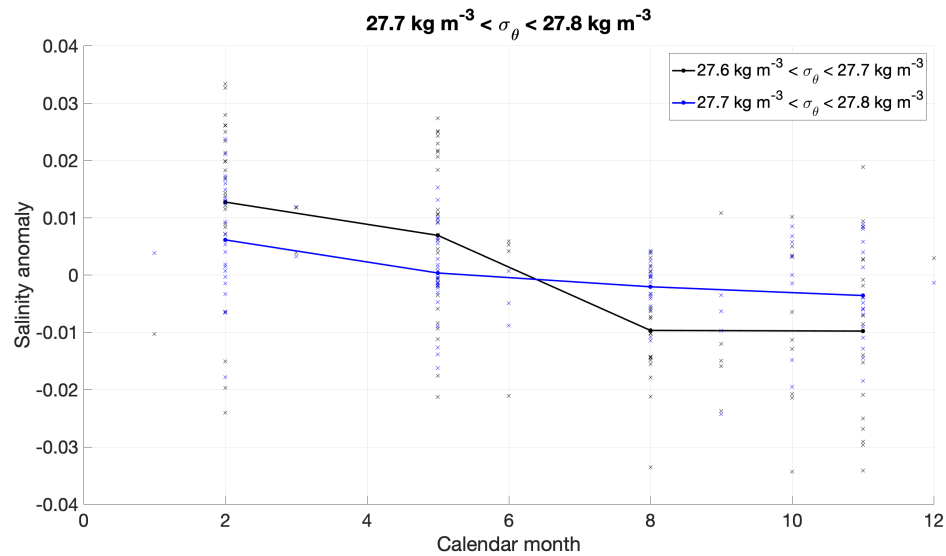


Fig. 4.15 Salinity anomaly (multi-annual variability removed) at FX9 as a function of calendar month in the  $27.6 \text{ kg m}^{-3} < \sigma_{\theta} < 27.7 \text{ kg m}^{-3}$  interval (black) and the  $27.7 \text{ kg m}^{-3} < \sigma_{\theta} < 27.8 \text{ kg m}^{-3}$  intervals. The crosses show the distribution of all data points and the thick lines join the mean values in February, May, August and November.

The volume transport of the DSO increases by approximately 2 Sv within 200 km of Denmark Strait (Dickson and Brown, 1994). Using moored temperature measurements, Voet and Quadfasel (2010) deduced that entrainment is most intense around 175 km downstream of DS. However, dense water on the Greenland shelf cascades off the shelfbreak and merges with the DSO at this location (Brearley et al., 2012; Falina et al., 2012; Koszalka et al., 2013), which also contributes to the transport of the DSO. The relative contribution of entrainment and shelf water to the DSO is not presently known. However, some studies estimate that dense shelf water accounts for approximately 25% of the DSO at ANG, 500 km downstream of DSO (Falina et al., 2012; Koszalka et al., 2013). Assuming the DSO transport here is 5 Sv (Dickson and Brown, 1994), this amounts to 1.25 Sv dense shelf water within the DSO. This leaves a 0.75 Sv contribution from entrainment to the DSO. However, a recent study used results from a numerical particle tracking model to claim that MIW also contributes to the DSO at DS (Saberli et al., 2020), i.e. it is not entrained to the south of DS but likely mixes with lighter overflow water at DS. Therefore, the contribution of MIW and LSW to the DSO might be greater than 0.75 Sv.

Assuming the MIW contribution to the DSO is 0.75 Sv, a negative salinity anomaly of 0.02 in the MIW would result in a salinity anomaly of 0.003  $((0.75 \text{ Sv} / 5 \text{ Sv}) \times 0.02)$  in the DSO at ANG. This is almost an order of magnitude weaker than the observed freshening of the DSO at ANG, which is 0.02 (Chapter 3). Even if the MIW contribution

to the DSO is actually as high as 2 Sv, the mixing of the MIW with the other sources of the DSO would result in an anomaly less than half the magnitude of the observed anomaly.

Moreover, it is also noted that there is no sign of extreme freshening of MIW at FX9 within 6-9 months of the 1999 and 2004 events, when the DSO experienced very strong freshening (compare Figure 4.14b with Figure 3.1 in Chapter 3). Further, the years of weaker freshening in the overflow (e.g. 2000-01 and 2010-11) are not associated with weaker freshening at FX9 (Figure 4.14b). Moreover, in Chapter 3, it was shown that the sustained freshening of the DSO is intensified on the inshore part of the plume, indicating an onshore origin of the freshening, and inconsistent with MIW driven freshening. Therefore, despite evidence of salinity seasonality of the southern sources of DSO, it is unlikely that the seasonal sustained freshening of the DSO derives from this source, though it may play a small part in the eventual admixture of light classes of the DSO. Moored instrumentation would be required to conclusively rule out MIW as a significant freshening source.

## 4.7 Discussion

In the previous sections of this chapter, DSO freshening mechanisms associated with hydrographic variability of DSO source water branches to the north of DS (mechanisms 1-3; illustrated in Figure 4.2) were identified and characterised, using data from oceanographic moorings at KGA and atmospheric reanalysis. However, the investigation was based on only one year of mooring observations. In a previous chapter of this thesis (Chapter 3), the seasonality of the temperature and salinity of the DSO at DS was investigated using data collected between 1990 and 2019 from a seasonally repeated CTD section at DS (introduced in Chapter 2). In this section, this work is extended to test whether there is evidence to support the proposed mechanisms. By characterising the modification of DSO source water between KGA, located 200 km to the north of DS, and DS, the impact of hydrographic variability of DSO source water on the temperature and salinity seasonality of the DSO at DS is estimated.

### 4.7.1 Downstream evolution of the DSO sources south of KGA

Downstream of KGA, the distance between the Greenland and Iceland shelfbreak decreases, and the source water masses converge at DS, and feed the DSO (Figure 4.2). When the water masses converge they come within closer proximity to each other and this will likely increase the mixing between them, via, for example, eddy stirring.

Furthermore, the water depth decreases between KGA and DS, and most of the water below the depth of the Denmark Strait sill (650 m) is recirculated in the Blosseville Basin, though some of it aspirates into the DSO source water above (Harden et al., 2016). Using AIW, RAW, PSW and IW as end-members, Mastropole et al. (2017) argued that the distinct water masses have mixed together in many locations at DS, though not in the deep trough, where the coldest, densest water mass - AIW - dominates. By directly comparing the property distribution of the DSO sources at KGA (Figure 4.4) and DS (Figure 4.16), the mixing that takes place between these two arrays may be better understood.

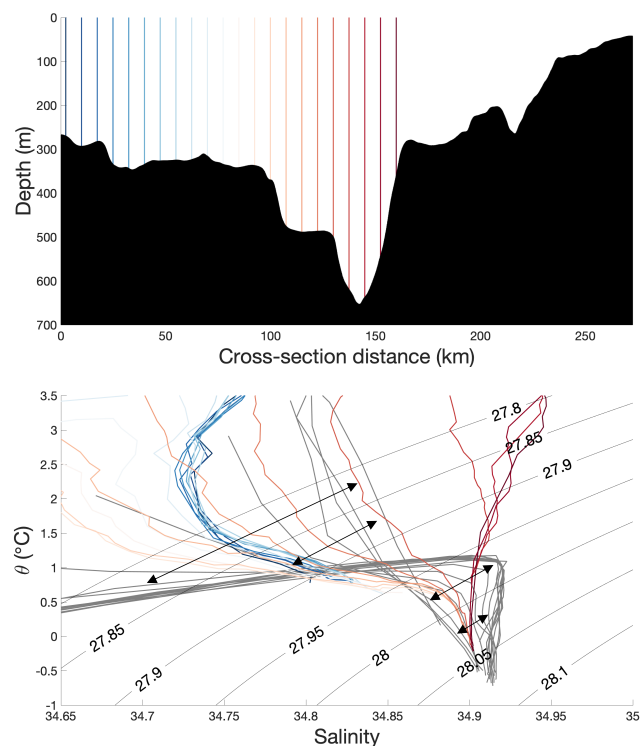


Fig. 4.16 Time-mean  $\theta$ -S profiles of the DSO at DS (coloured profiles) superimposed on the  $\theta$ -S profiles at KGA (grey). The bottom panel shows the  $\theta$ -S profiles, whilst the top panel shows the location of the coloured profiles across the DS array. The profiles are coloured according to a colour grade, which varies from blue (Greenland shelf) to red (Iceland shelfbreak). For the location of the KGA profiles, see Figure 4.4. In the bottom panel, the thin black lines are density contours (in  $\text{kg m}^{-3}$ ), and the black arrows indicate the suggested transformation of the water masses passing through KGA, which takes place between KGA and DS.

The temperature-salinity distribution at the two arrays is shown in Figure 4.16, where it is clear that the DSO source water passing through KGA has been modified

in the intervening distance. Specifically, the temperature and salinity maxima, which indicate the core of RAW at KGA (Figure 4.11a) cool and freshen between KGA and DS (Figure 4.16). This points to isopycnal mixing of the RAW with the fresher and colder water advected by the NIJ in the denser classes of the DSO ( $\sigma_\theta > 27.97 \text{ kg m}^{-3}$ ) over the Iceland slope (Figure 4.4).

Additionally, the cold and fresh polar origin water advected by the Shelfbreak EGC over the Greenland continental margin (Figure 4.4) is made warmer and more saline, likely as a result of isopycnal mixing with Irminger Water, advected by the North Icelandic Irminger Current. For example, the water found over the Greenland slope on the  $27.85 \text{ kg m}^{-3}$  isopycnal surface at KGA has a temperature of  $0.6^\circ\text{C}$  and salinity of 34.73, which increases to  $1.2^\circ\text{C}$  and 34.78 at DS. The idea that Irminger Water modifies the water masses transported by the Shelfbreak EGC is supported by two previous studies. Firstly, Mastropole et al. (2017) used an end-member analysis of the repeat DS CTD sections to show that Irminger Water makes a contribution to the DSO at DS. Secondly, Saberi et al. (2020) used numerical particle back tracking to argue that the Irminger Water contributes around 16% of the volume transport of the DSO at DS.

#### 4.7.2 Property seasonality at DS

To investigate the seasonality of the DSO at DS, seasonal composites of the hydrography at DS (Figure 1.8b) are constructed, as described in Chapter 3.4.2. Unfortunately, this does not include velocities from the section, and thus it was not possible to calculate water mass transports. Nevertheless, the variability of the  $\theta$ -S distribution can shed light on the seasonal changes in the hydrography of the DSO, which will reflect upstream mechanisms that affect the salinity of the DSO. The sections were typically carried out in February, May, August and November each year, though in some years in the sections were carried out in other months. Therefore, seasonal composites were constructed using all sections from three month blocks: April-May-June (AMJ), to represent the DSO salinity minimum phase, and October-November-December (OND), to represent the DSO salinity maximum phase. The purpose of this section is to investigate the spatial differences, in the two seasons, of DSO properties, and to relate these changes to the hydrographic variability of DSO source water originating from the north, which was characterised in the previous sections of this chapter.

The  $\theta$ -S distribution in the two seasonal composites are displayed in Figure 4.17, where there is a clear contrast in the properties of the lighter water in AMJ and OND. Specifically, the DSO above the  $27.9 \text{ kg m}^{-3}$  isopycnal on the Greenland side of the section (see blue profiles in Figure 4.17a and c) has a higher temperature and salinity in OND, than in AMJ. For example, the salinity at the  $27.85 \text{ kg m}^{-3}$  isopycnal surface

around the Greenland shelfbreak is 34.80 and the temperature at the same point is 1.5°C in OND, and the salinity decreases to 34.75 and the temperature decreases to 1°C in AMJ. Conversely, on the Iceland side of the section, and in denser classes of DSO, there exists no such distinct change in properties. This seasonality was also investigated in Chapter 3.4.2 in terms of the cross sectional area of different  $\theta$ -S bins. There it was shown that the section mean salinity is approximately 0.02 lower in AMJ than in OND, which is consistent with the seasonal salinity difference of the DSO downstream, at ANG, in those seasons.

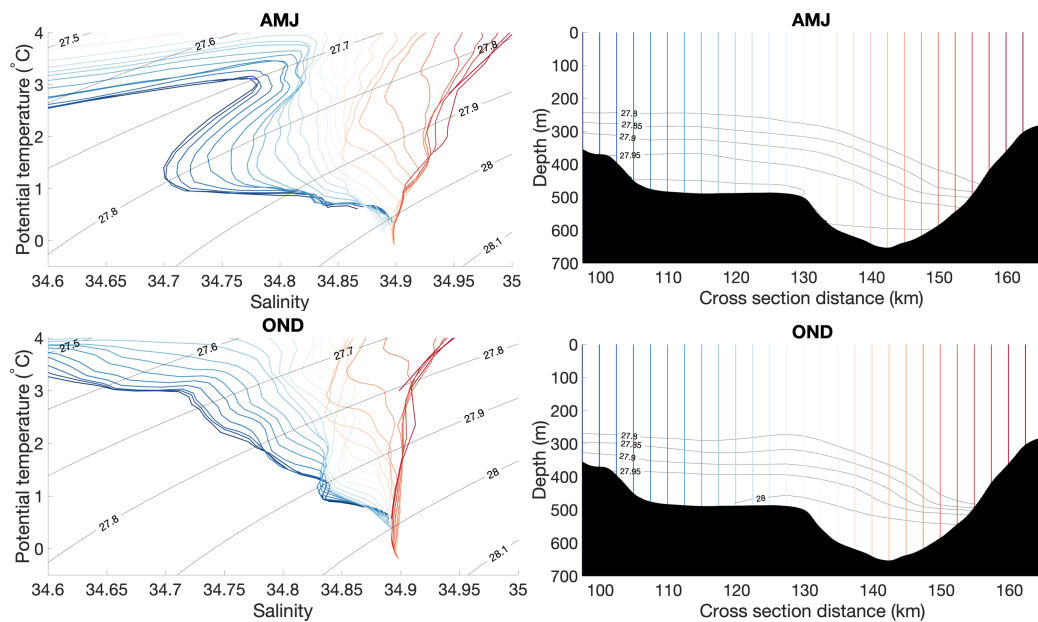


Fig. 4.17 The  $\theta$ -S distribution in April-May-June (a and b) and October-November-December (c and d) at DS. Panels (a) and (c) show the  $\theta$ -S curves, colour coded according to their position along the section (panels (b) and (d)). The thin black lines are isopycnals (lines of constant density).

The spring distribution of  $\theta$ -S indicates a freshening or enhancement of the Shelfbreak EGC, and is thus consistent with mechanisms 1 and 3. As argued above, the DSO source water masses passing through KGA are modified between KGA and DS (Figure 4.16), probably through isopycnal mixing. When the Shelfbreak EGC freshens (Mechanism 1), the mixing product of the Shelfbreak EGC water masses with other water masses along the same isopycnals (e.g. NIJ-entrained) is colder and fresher. When the Shelfbreak EGC is enhanced (Mechanism 3), the volume transport of water masses advected by the Shelfbreak EGC, specifically RAW and PW, and a higher fraction of these water masses will mix with the NIJ-entrained water, resulting in these water

masses dominating their density classes. In the lighter classes of DSO, this results in fresher and colder water.

In summary, there is a clear temperature and salinity difference in the upper, stratified part of the DSO over the Greenland shelfbreak and slope at DS between spring and autumn. Whilst the upper part of the DSO is stratified by salinity in spring, it is stratified by temperature in autumn. The DSO structure in spring is consistent with a weakly stratified overflow underlying a 'fresh lid' of the DSO, which was observed by Rudels et al. (2002) at DS and downstream of DS. However, the fresh lid is not observed in autumn. This implies that it is a seasonal phenomenon, which is possibly formed when the Shelfbreak EGC freshens or is enhanced. Here, it is claimed that the fresh lid originates from fresh pycnocline water, which is likely a product of PSW mixing with RAW within the EGC to the north of DS. It is also argued that it is only present when the Shelfbreak EGC is enhanced, or when coastal Ekman downwelling forces the PW offshore and into the core of the Shelfbreak EGC.

## 4.8 Conclusions

Four oceanographic mechanisms were investigated as candidate mechanisms of the sustained seasonal freshening of the DSO at ANG, 500 km downstream of DS. The first three mechanisms considered are changes to the hydrography of DSO source water to the north of Denmark Strait, and they are illustrated in Figure 4.2a-c. The fourth process is seasonal freshening of MIW, observed passing through the lower southwest Iceland slope before entraining into the DSO (illustrated in Figure 4.2d). The case for each mechanism is summarised below.

### **Mechanism 1: offshore flow during Ekman downwelling**

Firstly, barrier wind events were shown to precede negative salinity and density anomalies in the near-bottom layers of the Greenland shelf and slope by 4-5 days, at KGA. However, the velocity data show no evidence of offshore flow below the surface Ekman layer, to compensate the onshore Ekman transport in the surface layer. Therefore, it is argued that offshore flow during Ekman downwelling occurs upstream of KGA, causing freshening of the Shelfbreak EGC which is advected to KGA and may then drive sustained freshening of the DSO downstream.

**Mechanism 2: Ekman pumping**

It was also demonstrated that barrier winds are associated with anomalously strong negative wind stress curl over the Greenland shelf and slope, which drives Ekman pumping and downwelling of water masses, bringing fresher water to near-bottom layers. This is an alternative cause of the negative salinity and density anomalies associated with barrier winds. However, vertical velocities due to the Ekman pumping associated with negative wind stress curl during barrier wind events are too low to explain the rate of change of salinity/density and, moreover, the property anomalies occur around 4 days after the maximum Ekman pumping velocity.

**Mechanism 3: Shelfbreak EGC enhancement**

To investigate Mechanism 3, the water mass transport via different DSO source water current branches was investigated. The two main sources of DSO are RAW and AIW. In addition, PW water, which falls outside of the traditional water mass definitions, contributes to the DSO. The PW is found within the two EGC branches, and is fresh ( $S < 34.9$ ), largely pycnocline water, probably formed of an admixture of water masses originating from the Arctic Ocean, and RAW. When the Shelfbreak EGC is enhanced in winter, the transport of the PW water is  $1.14 \pm 0.51$  Sv ( $\pm$  standard deviation), 63%, higher than the time-mean of  $0.7 \pm 0.46$  Sv. To estimate the effect of this increase in volume transport of the fresher water, the transport weighted salinity ( $\bar{S}$ ) of the DSO source water is calculated, invoking the assumption that the distinct source water masses mix together to form an unchanging salinity value across the DSO at ANG. The  $\bar{S}$  is 0.015 fresher in winter than in summer in 2011-12, which may explain why the DSO salinity minimum at ANG occurs in spring, because the transit time between KGA and ANG is around 2-3 months (see Chapter 3). However, an investigation of further years of data from KGA is required to confirm whether this year is representative of the seasonal cycle. The magnitude of the seasonality of  $\bar{S}$  is around half the magnitude of the salinity seasonality of the DSO at ANG (between 1998 and 2015), once entrainment of lighter water into the DSO in the Irminger basin is accounted for.

**Mechanism 4: freshening of MIW**

The variability of the deeper, denser, water on the southwest Iceland slope was investigated to evaluate the contribution of the salinity variability of MIW (Mechanism 4) to the freshening of the DSO. There is a seasonal salinity cycle observed in the MIW, however the seasonality was found to be an order of magnitude too small to explain the salinity seasonality of the DSO at ANG. Furthermore, the fact that the freshening of the

DSO is intensified on the inshore part of the plume (Chapter 3) is not consistent with MIW driven freshening. Therefore, Mechanism 4 is rejected.

It is finally concluded that the enhancement of the southward volume transport of the Shelfbreak EGC (Mechanism 3) is the main driver of sustained DSO freshening, however the coastal Ekman downwelling and Ekman pumping mechanisms likely also play an important role. This emphasises the importance of hydrographic variability north of DS, around the location of KGA, to the salinity variability of the DSO downstream, at ANG. The hydrographic variability is likely strongly wind forced, as argued in this chapter and in previous publications (Harden et al., 2016; Köhl et al., 2007). Therefore, in the next chapter, the relationship between atmospheric forcing and DSO salinity is investigated.

# Chapter 5

## The relationship between atmospheric forcing and Denmark Strait Overflow salinity

### 5.1 Introduction

In the previous two chapters, sustained (i.e. lasting for at least two months) freshening in winter and spring in the core of the DSO was characterised and the proposed drivers were evaluated. The anomalies typically occur in spring and are intensified in the lighter classes ( $\sigma_\theta < 27.95 \text{ kg m}^{-3}$ ) of overflow. It was argued in Chapter 4 that winter wind forcing drives anomalously intense freshening and intensification of the Shelfbreak EGC to the north of DS, forming the fresh lid of the overflow, which advects downstream, causing freshening. In this chapter, the hypothesis that wind forcing controls the DSO salinity on seasonal to multi-annual timescales is evaluated, and the wind direction, forcing locations and time lag associated with DSO freshening are established.

The connection between wind forcing and overflow salinity has been the subject of previous research by Holfort and Albrecht (2007) and Hall et al. (2011). However, these two studies disagree over the location of the key forcing region, and the time lags between wind forcing and downstream salinity response. While Holfort and Albrecht (2007) argue that the wind forcing at the DS sill controls the DSO salinity with a 2 month lag, Hall et al. (2011) maintain that the wind forcing at around  $75^\circ\text{N}$  near the east Greenland coast controls the DSO salinity with a 4 month lag. It is notable that Holfort and Albrecht (2007) used data mainly from the 1990s, whereas Hall et al. (2011) used observational data from the 2000s, and an ocean model forced by atmospheric reanalysis.

In addition to the magnitude and direction of the wind, the concentration and type of sea ice can also modulate the effect of the wind on the ocean surface. For instance, Schulze and Pickart (2012) showed that during partial sea ice concentration when the sea ice is free moving, the momentum transfer from the atmosphere to the ocean may be amplified, with maximum amplification depending on the characteristics of the sea ice (Lu et al., 2011). This is because the surface roughness of the sea ice is greater than the open ocean and therefore the drag is greater, which results in a greater momentum transfer from the atmosphere to the ocean (Elvidge et al., 2016). The wind forcing locations proposed in the previous studies are places where there is seasonal sea ice cover, and the variability of the sea ice cover will be investigated later in this chapter. Despite this, neither Holfort and Albrecht (2007), nor Hall et al. (2011) investigated the role of sea ice in the relationship between wind forcing and DSO salinity.

This chapter is structured around four research questions:

1. Is wind forcing a controlling factor on the DSO salinity on seasonal to multi-annual timescales?
2. How sensitive is the DSO salinity to wind forcing in particular regions?
3. What is the role of sea ice concentration in the wind-DSO salinity relationship?
4. How does the large scale variability of atmospheric circulation in the North Atlantic influence the salinity of the DSO?

In this chapter, it is argued that the salinity of the DSO is influenced by large scale atmospheric patterns, which vary on multi-annual timescales. Further, the role of sea ice concentration variability in driving variability of wind driven freshening of the DSO is highlighted.

The structure of the chapter is as follows. Firstly, in section 5.2, the time-mean and variability of the key atmospheric patterns in the study region - east of Greenland - are analysed. In section 5.3, the underlying atmospheric patterns that control the DSO salinity are investigated by using correlation maps (between wind and DSO salinity) to identify important locations and correlation time series to determine how the connections vary in time. The impacts of variability of the most important large scale atmospheric patterns in the region on the wind forcing of the DSO salinity are also investigated here. The purpose of section 5.4 is to address the role of sea ice concentration on the Greenland shelf, which might modulate the influence of the wind on the DSO salinity. Finally, Section 5.5 summarises the key findings of the chapter.

## 5.2 Atmospheric circulation

### 5.2.1 Time-mean circulation

A number of different large scale atmospheric patterns are responsible for the local wind forcing over the ocean on the east Greenland continental margin. The local wind forcing drives oceanographic processes which may result in freshening of the DSO, as investigated in Chapter 4. The atmospheric circulation in the region on timescales of one month and longer is examined here, using monthly averaged fields of sea level pressure, zonal ( $u$ ) and meridional ( $v$ ) components and speed of the wind at 10 m above the ocean surface, from the ERA5 reanalysis product (Hersbach et al., 2020), which is introduced in Chapter 2.

Figure 5.1 shows the 1998-2015 mean of monthly mean atmospheric conditions east of Greenland in the subpolar northeast Atlantic and Nordic Seas. This time span is chosen because it coincides with the deployments of MicroCAT sensors at the ANG array, which make highly accurate salinity measurements. Atmospheric conditions are strongly controlled by the Icelandic low, which is situated west of Iceland. The Iceland low is an important centre of action in the North Atlantic, associated with frequent cyclones (Serreze et al., 1997), which tend to propagate to the northeast, as indicated by the extension of the 1008 hPa contour into the Nordic Seas (Figure 5.1). Wind speeds are high along the east Greenland coast, especially in the vicinity of DS. This amplification is partly due to the occurrence of barrier winds (introduced in Chapter 1). Mean wind speeds exceed  $9 \text{ m s}^{-1}$  here, which is the maximum in the region shown in the map. Barrier winds occur in winter (Harden et al., 2011), which enhances the wind forcing then. The direction of the wind is parallel to the east Greenland coast, with northerlies north of around  $69^\circ\text{N}$  and northeasterlies south of  $69^\circ\text{N}$ , reflecting the changing orientation of the coastline. Conversely, the region near the Norwegian coast is on the opposite side of the cyclone centre of action and the wind is therefore southerly. However, compared with the wind near the Greenland coast, the mean wind speeds are weaker ( $< 8 \text{ m s}^{-1}$ ) and the strength of the mean meridional wind is substantially weaker here.

### 5.2.2 Leading modes of variability

Figure 5.2a-d shows the spatial patterns of the two leading Empirical Orthogonal Functions (EOF) of monthly mean sea level pressure, and their accompanying Principal Component (PC) time series, which together explain 86.3% of the total variance between 1998 and 2015. The process of computing the EOFs and PCs is briefly described below.

The covariance matrix of the sea level pressure field is constructed, and the eigenvalues and eigenvectors of the covariance matrix are found by solving the eigenvalue problem (Hannachi et al., 2007). The EOFs are the eigenvectors, and the PC time series are found by projecting the eigenvectors on the sea level pressure field time series. To estimate the explained variance of each mode, the eigenvalues are multiplied by the trace of the covariance matrix. The purpose of the EOF method is to decompose a space-time field into spatial patterns (EOFs), and associated time series (PCs), which are prominent modes of variability affecting the system (Hannachi et al., 2007).

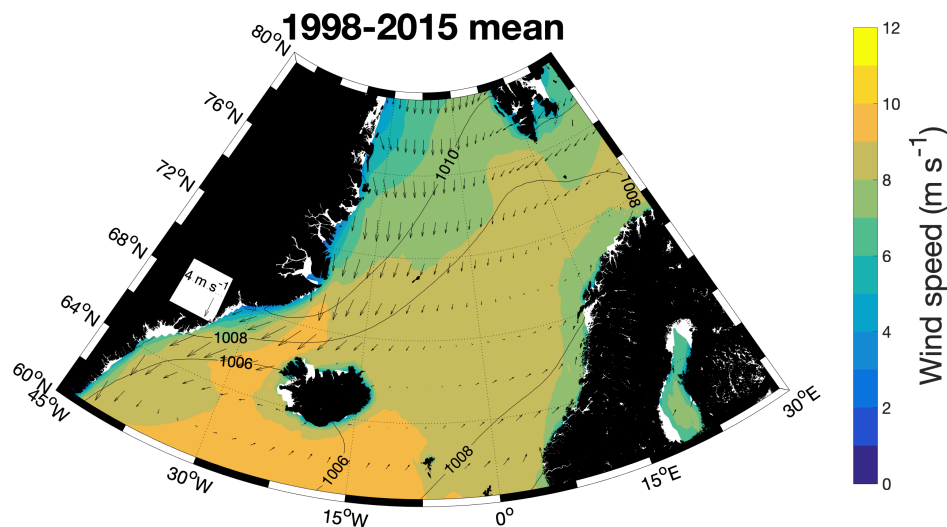


Fig. 5.1 1998-2015 mean of monthly mean wind speed (colours), wind vectors (both in  $\text{m s}^{-1}$ ) and sea level pressure (black contours, hPa). This time period is chosen because it coincides with the mooring deployments at ANG. The atmospheric data are from ERA5.

EOF1 shows a universal positively correlated change in sea level pressure across the whole region, with the greatest changes observed west of Iceland and northeast of Iceland in the central Nordic Seas (Figure 5.2a). This mode represents the NAO (introduced in Chapter 1), with positive phases of the NAO index associated with the negative phase of PC1 and vice versa (compare Figure 5.2c and e). The NAO is defined as the normalised sea level pressure difference between weather stations in Iceland and the Azores (Jones et al., 1997). EOF1 is highly negatively correlated with the monthly NAO index ( $r=-0.68, p<0.01$ ). The atmospheric conditions during strong and weak phases of the NAO are described below.

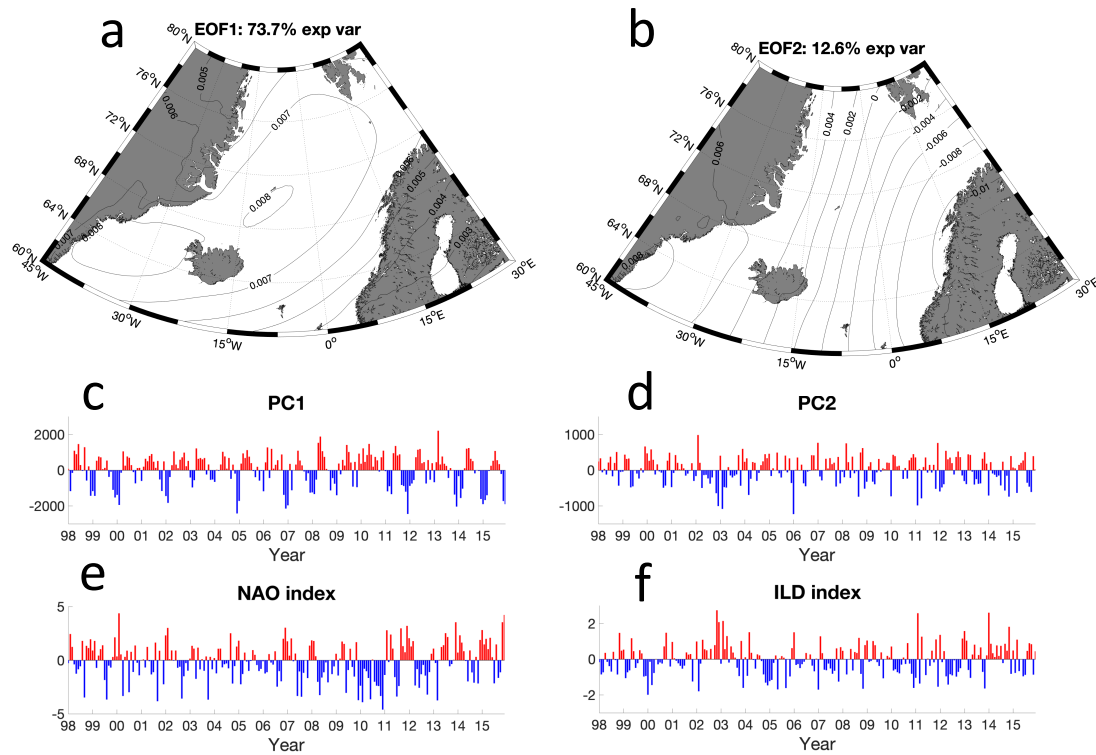


Fig. 5.2 The two leading Empirical Orthogonal Function modes (EOF1 and EOF2) of sea level pressure east of Greenland, and the NAO index and ILD index time series between 1998 and 2015. (a) and (b) display the spatial patterns of EOF1 and EOF2 respectively, with the percentage explained variances shown in the titles, and (c) and (d) show the corresponding temporal variability of PC1 and PC2 respectively, and (e) and (f) display the time series of the NAO and ILD index respectively, as defined in the text.

Conversely, EOF2 shows a pressure anomaly dipole with centres west of Iceland and over the northwest Norwegian coast (Figure 5.2). This EOF pattern is consistent with the Iceland-Lofoten Difference (ILD) pattern, as introduced in Jahnke-Bornemann and Brümmer (2008). The ILD index time series, constructed by subtracting the normalised sea level pressure anomaly at the Iceland centre of action, from the normalised pressure anomaly at the Lofoten centre of action in ERA-40 monthly averaged fields, prepared by Jahnke-Bornemann (2019), is also shown in Figure 5.2f. The PC2 time series is highly negatively correlated with the ILD index time series ( $r=-0.85$ ,  $p<0.01$ ). Conversely, the correlation between PC2 and NAO is weak ( $r=-0.11$ ) and is not statistically significant at the 95% level. In fact, the ILD pattern is independent of the NAO (Jahnke-Bornemann and Brümmer, 2008), and when it is in a strong negative phase it can strengthen the wind forcing over the east Greenland shelfbreak, even when the NAO is not in a positive phase, as described below.

The wind speed and direction and sea level pressure distribution during strong positive phases of the NAO index is shown in Figure 5.3. This was calculated from the mean fields of all the months where the NAO index exceeded 1.5, which is classed as a strong positive NAO month, according to the definition of Pinto et al. (2009). The Icelandic low is much deeper during the positive phase of the NAO compared with the time-mean, with a sea level pressure minimum of 996 hPa centred over the Irminger Sea, and lower pressure everywhere else.

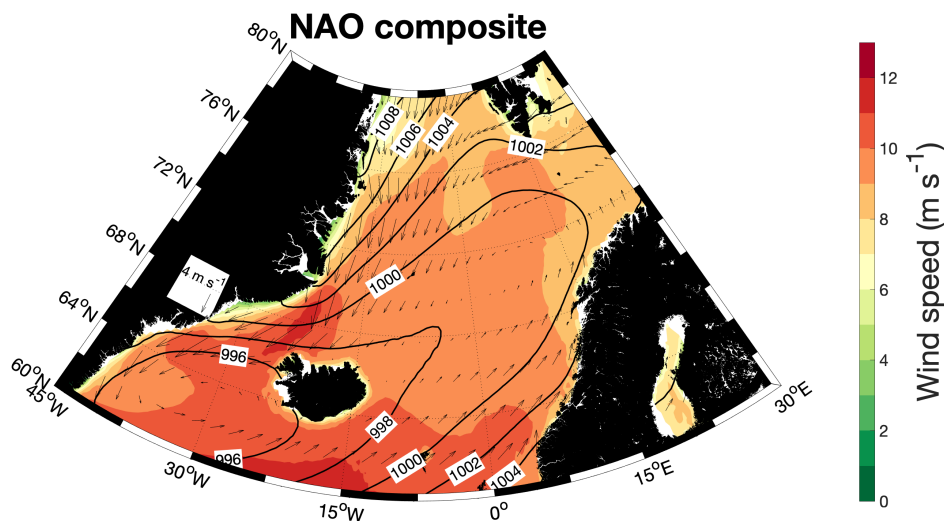


Fig. 5.3 Composite wind speed (colours), wind vectors (both in  $\text{m s}^{-1}$ ) and sea level pressure (thick black lines, in hPa) during strong positive NAO index months. This composite is composed of 37 strong positive NAO index months between 1998 and 2015, according to the definition of Pinto et al. (2009). For scale, a  $4 \text{ m s}^{-1}$  vector is shown on the left side of the map.

Further, wind speeds are enhanced in the whole domain, with northerly/northeasterly wind speeds up to  $3.5 \text{ m s}^{-1}$  faster over the Greenland shelf and slope during strong positive phases, compared to strong negative phases (not shown). When the NAO is positive, Woollings et al. (2015) showed that the North Atlantic storm track shifts northwards, deepening the Icelandic low and accelerating the winds near the southeast Greenland coast. This results in stronger wind stress over the ocean and, potentially, enhancement and freshening of the Shelfbreak EGC, leading to sustained freshening of the DSO as a result.

The wind fields and sea level pressure distribution during strong negative NAO index months is shown in Figure 5.4. The centre of low pressure (998 hPa) in these periods is located off the northwest coast of Norway. This low pressure centre of action is associated with northerlies throughout the Nordic Seas, including over the northeast

Greenland continental margin. Compared with the strong positive NAO phase months, the wind speeds are lower around DS, but greater off the northeast Greenland coast. This implies that there are fewer barrier wind events during strong negative ILD index months, than during strong positive NAO index months. This atmospheric pattern, when dominant - as in the composite in Figure 5.4, may also drive enhancement and freshening of the Shelfbreak EGC, resulting in sustained freshening of the DSO.

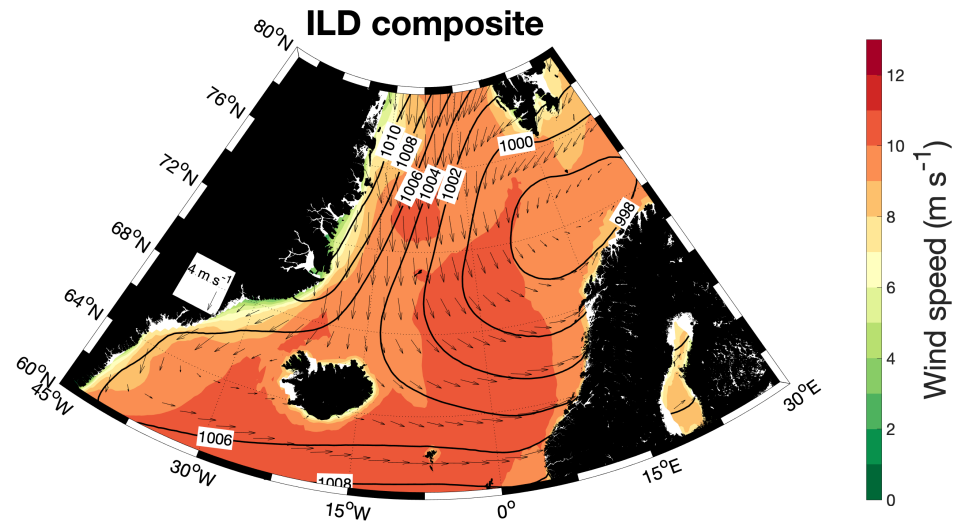


Fig. 5.4 Composite wind speed (colours), wind vectors (both in  $\text{m s}^{-1}$ ) and sea level pressure (thick black lines, in hPa) during strong negative ILD index months. This composite is comprised of 23 strong negative ILD index months between 1998 and 2015, with index values below -1 defined as strong negative. For scale, a  $4 \text{ m s}^{-1}$  vector is shown on the left side of the map.

### 5.2.3 Temporal variability

Atmospheric conditions vary from multi-month to multi-annual timescales. Wind forcing is stronger in the cold season (October-March), when the cyclones are more intense and more frequent (Serreze et al., 1997). This is shown in the intra-annual variability of the NAO and ILD index (Figure 5.5): the NAO index tends to be positive between December and March implying more intense cyclone activity then. There is also some indication of intra-annual variability of the ILD index, with negative phases tending to occur in months of the cold season (November, December and March) (Figure 5.5). Therefore, in winter, the wind driven mechanisms, investigated in Chapter 4, occur more frequently and are more intense, potentially driving freshening of the DSO in late winter and spring (Chapter 3). The fact that the DSO salinity minimum occurs in

May (see Chapter 3), 2 months after the end of the cold season, suggests that remote (rather than local) wind forcing might be controlling the DSO salinity at ANG. This is consistent with Holfort and Albrecht (2007) and Hall et al. (2011).

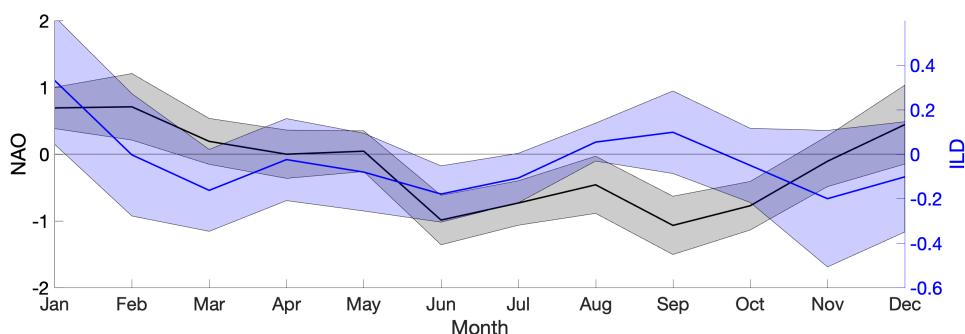


Fig. 5.5 The intra-annual variability of the NAO index and ILD index, between 1998 and 2015 (the full 1998-2015 time series are shown in Figure 5.2e and f). Both the NAO index and ILD index are derived from normalised pressure differences between two centres of action, as described in the text. The thick lines are the means and the shaded area is the standard error for each calendar month.

The EOF-2, which explains 12.6% of the sea level pressure variability, represents the ILD pattern, which is also associated with atmospheric variability. In the time period of this study, the ILD index was in a negative phase between 1998-2001 and 2004-2009, and a positive phase in 2002-2004 and 2014-15 (Figure 5.2f). It is not clear what, if any, effect the ILD index variability has on the occurrence of barrier winds, but it is likely that positive phases are associated with increased barrier wind occurrence. The cold season NAO index also varies from year to year, with weak values between 1999 and 2008 and both extremely positive and extremely negative NAO index winters between 2009 and 2015, as detailed in Chapter 1.

In summary, the prevailing wind all along the east Greenland coast in the cold season is northerly/northeasterly and parallel to the coastline (Figure 5.1), and thus favourable for the DSO freshening mechanisms investigated in Chapter 4. During strong positive phases of the NAO, the prevailing wind forcing intensifies as a result of the deepening of the Icelandic low. In Chapter 4, barrier wind events were linked to freshening and intensification of the Shelfbreak EGC at KGA, thus driving sustained freshening of the DSO. However, the wind forcing of Shelfbreak EGC variability could occur at many different latitudes along the east Greenland coast, in addition to the location of KGA. To investigate the importance of the northerly/northeasterly wind forcing in different locations, correlations between the wind and the salinity of the DSO at ANG are investigated in the next section.

## 5.3 Wind field-DSO salinity correlations

### 5.3.1 Method

To investigate the relationship between the large scale atmospheric patterns, introduced above, and the DSO salinity, lagged correlations between the wind and DSO salinity are computed. This type of analysis has been carried out before on smaller sets of data, first by Holfort and Albrecht (2007) and then by Hall et al. (2011). Holfort and Albrecht (2007) used the sea level pressure difference (data from atmospheric reanalysis) across DS as an index for along strait winds and correlated it with DSO salinity from CTD casts in the southwest Irminger Sea at around  $63^{\circ}\text{N}$ . Hall et al. (2011) correlated northerly winds (also from atmospheric reanalysis) with DSO salinity from ANG moorings in the 2000s. Whilst Holfort and Albrecht (2007) found a negative correlation between northeasterly along strait winds at DS and DSO salinity at a 2 month lag, Hall et al. (2011) observed a negative correlation between the northerlies around  $75^{\circ}\text{N}$  and DSO salinity at a 4 month lag.

There is clearly uncertainty regarding the relationship between the wind and the DSO salinity and this uncertainty is addressed in this study using a longer time series than either previous study. The NAO and ILD patterns are used to help understand the relationship between the wind and DSO salinity. Using calibrated ANG salinity time series between 1998 and 2015 (Chapter 2), the analysis here uses both a longer time period and a much greater number of observations than the previous studies. With the greater degree of statistical confidence possible, the objective is to answer an important research question: how sensitive is the DSO salinity to wind forcing, and what are the specific regions where that forcing occurs?

Lagged, complex/vector correlations of the wind components ( $u$  and  $v$ ) and the DSO salinity are computed, following the method introduced by Kundu (1976). The wind and salinity time series are converted into complex time series. For the wind time series, the  $u$  component is used for the real part and the  $v$  component is used as the imaginary part. For the DSO salinity, the real part is set as the salinity and the imaginary part is set to zero. The vector correlation returns the rotation of the wind which maximises the correlation. The correlation coefficient and  $p$ -value between the wind speed in this direction and the DSO salinity is then calculated. The calculation of the  $p$ -value takes into account the degrees of freedom of the time series, allowing for autocorrelation of both time series. This approach does not rely on an arbitrary choice of key wind direction to determine the correlations. In the following figures, the wind direction shown is the direction of maximum correlation, which is associated with negative salinity anomalies (freshening).

The objective of the correlation analysis is to understand the relationship between the wind and the DSO on two different timescales; seasonal and multi-annual. To recap, the seasonal salinity cycle of the DSO comprises a minimum in May and a maximum in December. The multi-annual variability of DSO salinity is characterised by intense freshening years (1999, 2004 and 2014) and weak freshening years (2001 and 2010).

To investigate both timescales, correlations were calculated with and without removing the seasonality of the time series. The seasonal cycle was removed by subtracting the calendar month mean from each individual month for both the wind and salinity time series. Firstly, correlations of the time series with the seasonal cycle present are discussed. These correlations come with a caveat, that much of the correlation merely reflects the fact that a seasonal cycle exists in the wind and salinity time series, rather than signalling any causal relationship. Therefore, caution should be exercised when interpreting the results. However, since the signal of interest in the DSO is seasonal, it is still instructive to explore the location and lag of these seasonal correlations.

### 5.3.2 Spatial variability

Firstly, the spatial variability of the correlations using the full 1998-2015 time series is investigated. Figure 5.6 shows the correlation for the non-deseasonalised time series. At a 5-6 month lag, the highest correlations ( $r > 0.25$ ) are found north of  $70^\circ\text{N}$  and in some areas close to the southeast Greenland coast. There are medium correlations ( $r > 0.3$ ) at a 4 month lag over a wide area of the Greenland coast from  $60^\circ\text{N}$  to  $74^\circ\text{N}$ . In the 3 month lagged correlations, there are two areas that also have medium correlations ( $r > 0.30$ ); one northeast of DS around  $68^\circ\text{N}$ ,  $26^\circ\text{W}$  and another west of DS around  $66^\circ\text{N}$ ,  $34^\circ\text{W}$ . Significant correlations occur north of  $68^\circ\text{N}$  at a 2 month lag, though the magnitude of the correlations are weaker ( $r < 0.25$ ). At a 1 month lag, there are a few isolated areas of significant, but low ( $r < 0.2$ ) correlations.

At zero lag, the correlations are higher than at 1 month lag but the wind direction associated with freshening is southerly or southwesterly and not consistent with the wind-driven freshening mechanisms proposed in the previous chapter. In general, medium correlations are observed at a 3-6 month lag time and the correlated region moves southward from  $75^\circ\text{N}$  to  $63^\circ\text{N}$  as lag times decrease.

However, when the seasonality of the time series is removed, the wind over the Greenland shelf north of  $70^\circ\text{N}$  is not correlated at a 5-6 month lag (Figure 5.7). In the small isolated areas where there are significant correlations, the correlation is weak ( $r < 0.20$ ) and the wind direction is southerly or southwesterly (i.e. not in the direction consistent with wind forced freshening/intensification of the Shelfbreak EGC). This suggests that the correlations observed at 5-6 month lag in Figure 5.6 are a reflection

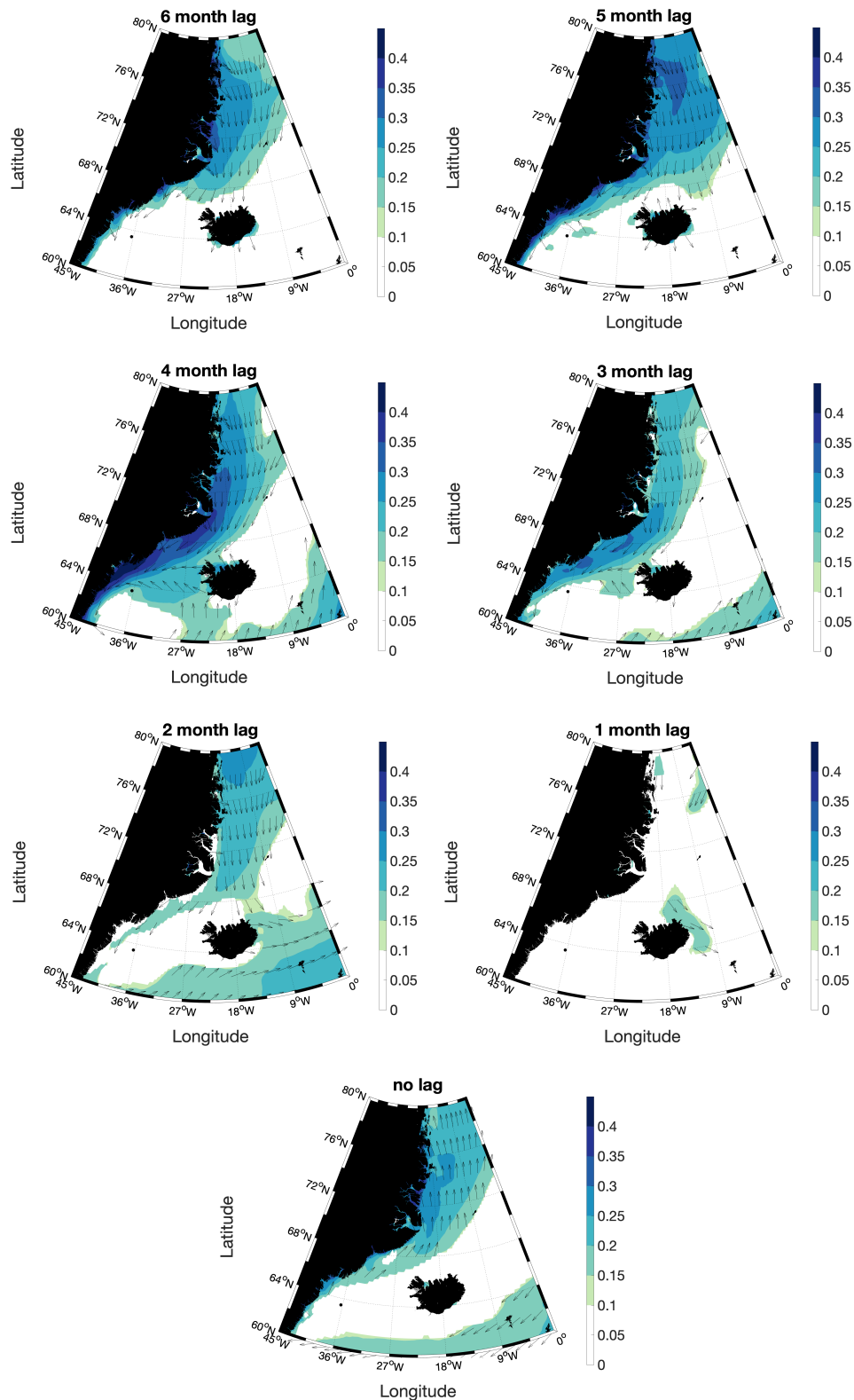


Fig. 5.6 Complex lagged correlation coefficients between the non-deseasonalised ERA5 wind and the DSO salinity at ANG (marked by the black circle) between 1998 and 2015. Whilst the colours show the correlation coefficient value, the quivers are all the same size because they show the direction of wind that results in the highest correlations. The wind direction shown is that associated with negative DSO salinity anomalies.

of the seasonal cycle in the time series pair being correlated (i.e. maximum winds in November/December and salinity minimum in May). This implies there is no causal relationship between the wind and the DSO at lags greater than 4 months.

Conversely, significant correlations do occur at a 2-4 months lag. Maxima ( $r > 0.20$ ) correlations occur between  $65^{\circ}\text{N}$  and  $70^{\circ}\text{N}$  approximately over the Greenland shelfbreak at a 3 month lag time (Figure 5.7). This overlaps with the region of statistically significant correlation when the seasonality is not removed (Figure 5.6).

The maximum correlation ( $r=0.23$ ) at 3 month lag, which is labelled  $r_3$  in Figure 5.7, is located at  $69.5^{\circ}\text{N}$   $20.25^{\circ}\text{W}$ . The maximum correlation ( $r=0.26$ ) at any lag time in the de-seasonalised correlations occurs at  $70^{\circ}\text{N}$   $18.75^{\circ}\text{W}$  ( $r_2$ ) at a 2 month lag. Significant correlations ( $r > 0.20$ ) also occur between  $72^{\circ}\text{N}$  and  $75^{\circ}\text{N}$  at a 1 month lag (Figure 5.7). However, the correlations in this region at a 1 month lag may result from the auto-correlation of the wind time series, which have an integral timescale of between 0.7 and 1.2 months over the Greenland continental margin in this region (Figure 5.8). Therefore, the correlations at a 2 month lag, which, it is argued, indicate a causal relationship, give rise to the correlations at a 1 month lag, due to the autocorrelation of the wind time series here. Furthermore, as reasoned below, a 1 month advective timescale from this region to ANG is not realistic.

At zero lag, there are some medium correlations ( $r > 0.2$ ) around the northeast Greenland continental margin but, as with the non de-seasonalised correlations, southerly winds are associated with freshening. These correlations may arise because the wind time series at zero lag is 180 degrees out of phase with the 2-4 month lagged wind time series (which it is argued cause freshening of the DSO). This may explain why the correlations at zero lag are opposite to those at 2-4 month lag in Figure 5.6 and Figure 5.7.

The two correlation maxima ( $r_2$  and  $r_3$ ) occur in the northern Blosseville Basin, close to where the EGC bifurcates, forming the Shelfbreak EGC and Separated EGC (Våge et al., 2013). Våge et al. (2013) proposed that the bifurcation process is governed primarily by wind forcing and the formation of eddies in the EGC. Specifically, positive (negative) wind stress curl in the Blosseville Basin causes intensification (weakening) of the Shelfbreak EGC, and weakening (intensification) of the Separated EGC (Harden et al., 2016). The fact that the maximum wind-salinity correlation occurs here implies that the wind driven changes to the ocean circulation may have an important effect on the salinity of the DSO at ANG. This is consistent with Chapter 4, where it was argued that variability of the properties and volume transport of the Shelfbreak EGC dominates the intra-annual salinity variability of the DSO downstream, at ANG.

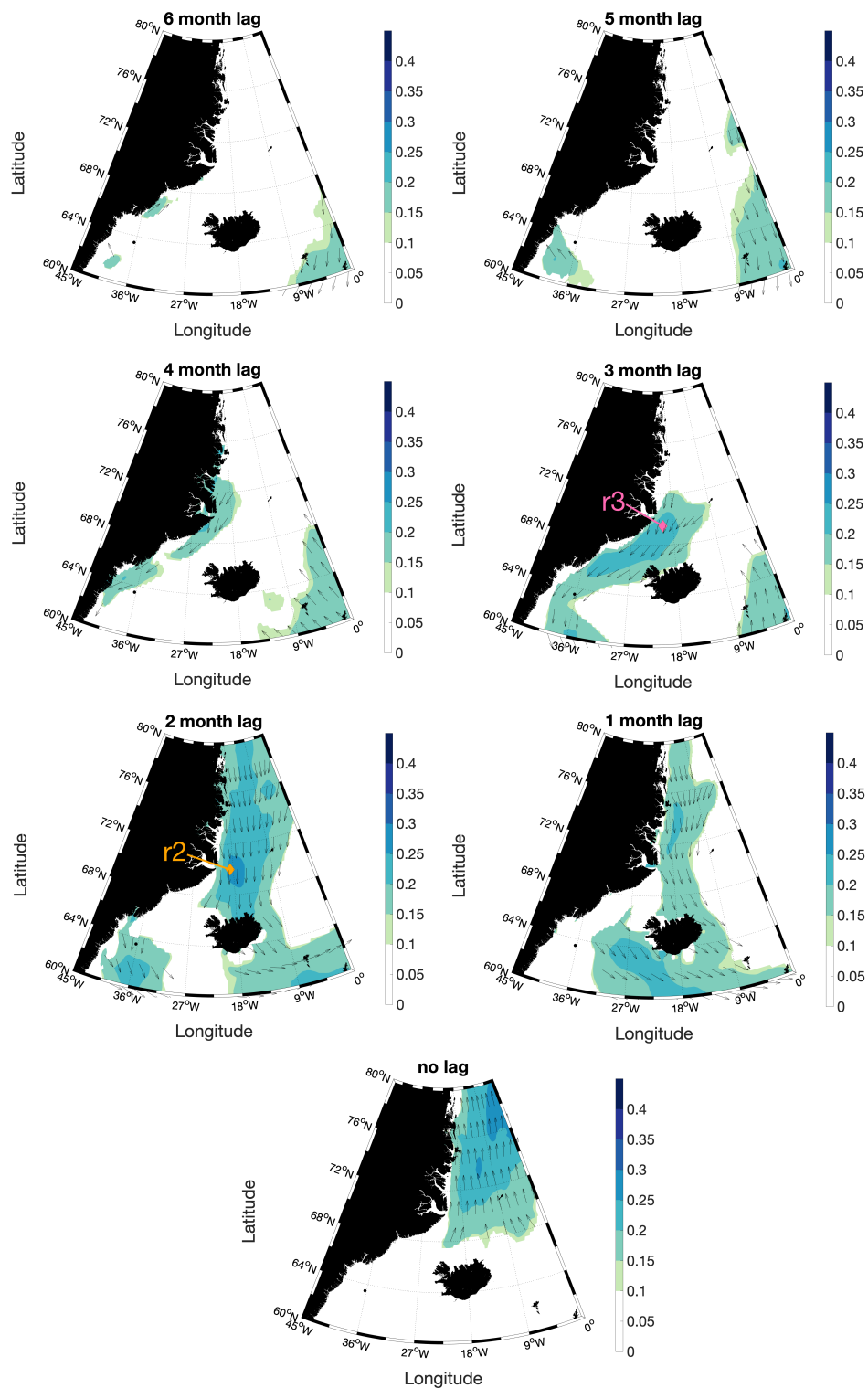


Fig. 5.7 Complex lagged correlation coefficients between the deseasonalised time series of ERA5 wind and DSO salinity at ANG (marked by the black circle) between 1998 and 2015. As with Figure 5.6, this shows the correlation coefficient (colours) and wind direction associated with maximum correlation (quivers), however the difference is that the seasonal cycle is removed from all time series. The pink and orange diamonds indicate the correlation maxima at 3 month lag ( $r_3$ ) and 2 month lag ( $r_2$ ) respectively.

Figure 5.9 shows the estimated transit times of salinity anomalies along the east Greenland slope. The transit time estimates are based on moored velocities from KGA11 on the upper Greenland slope at KGA (See Chapter 2 for description of mooring deployment). It is assumed that the salinity signal is advected by the Shelfbreak EGC, which follows the bathymetry (i.e.  $f$  (Coriolis parameter) /  $H$  (water depth) contours), from Fram Strait to DS and then from DS to ANG by the DSO.

North of DS, it is assumed that the southward pathway of the Shelfbreak EGC follows the 550 m isobath in GEBCO on the upper Greenland continental slope (Figure 5.9). The transit times along this pathway are calculated by dividing the distance by the mean transit speed, which is  $0.08 \text{ m s}^{-1}$ . This speed is the 2011-12 time-mean near-bottom flow speed at KGA11 (Figure 5.9). This is the assumed advection speed of dense water in the EGC from Fram Strait to the DS sill. In the absence of other data, this assumption is considered reasonable, since Håvik et al. (2017) found no evidence that the volume transport of the EGC varied significantly between Fram Strait and DS, although substantial water mass modification occurs between Fram Strait and DS, according to Håvik et al. (2017), and between KGA and DS, as argued in this thesis (see Chapter 4).

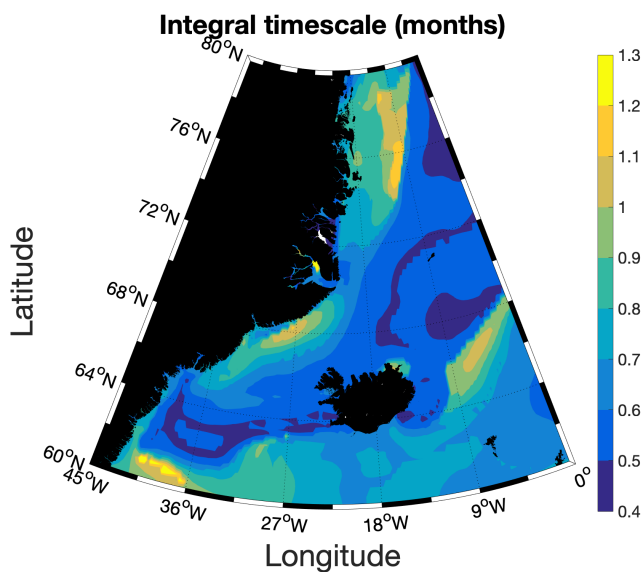


Fig. 5.8 Map showing the integral timescale of the deseasonalised wind speed east of Greenland. The direction of the wind is the direction associated with maximum correlation with the salinity of the DSO at ANG at a 2 month lag (see Figure 5.6). Note that locations around DS and north of  $75^\circ\text{N}$  are associated with integral timescales exceeding 1 month.

Downstream of DS, the advection speed used is  $0.30 \text{ m s}^{-1}$ , which is the time-mean near-bottom speed of the DSO at DS 1, located in the trough at DS. Note that, in Chapter

4, it was argued that the trough at DS is mainly fed by the NIJ. Unfortunately there exists no moored velocities from the around the Greenland shelfbreak at DS, in the likely pathway of the DSO source water within the Shelfbreak EGC, so the DS 1 velocity is used instead. Note that the estimated transit time from DS to ANG is therefore 20 days, which is in line with the transit times from the Greenland shelfbreak at DS to ANG estimated by Koszalka et al. (2013), using output from a particle tracking MITgcm simulation. Furthermore, the correlation between the salinity at 550 m depth at KGA11 and at ANG is maximised at a lag time of 78 days (See Chapter 3; Figure 3.15), which is close to the 2 month transit time from KGA11 to ANG (Figure 5.9).

The estimated transit time from the 72°N to 75°N region to ANG is 5-6 months, which is consistent with the lag time of maximum correlation of Hall et al. (2011). Therefore the one month lag of correlation of the wind in this region with the DSO salinity (Figure 5.7) is too short to be explained by advection. Further, the wind is not correlated with the DSO salinity when the seasonality is included (see 1 month lag in Figure 5.6), implying that the correlation is not robust. As argued above, the maximum correlation occurring at a 2 month lag suggest a causal relationship between the wind and salinity of the DSO at ANG. Moreover, the correlations at a 1 month lag likely result from the auto-correlation of the wind time series, as explained above.

Alternatively, should freshening be caused by a more rapid process, such as Coastal Trapped Waves, this could cause a negative salinity anomaly in the DSO at a shorter lag time. Waves do not transport property anomalies by definition, but they could cause overflow freshening by, for example, causing isohalines to move down the continental slope at the location of ANG. Gelderloos et al. (2021) show that barrier winds trigger Coastal Trapped Waves, which propagate southward rapidly along the east Greenland shelfbreak. Two types of Coastal Trapped Waves were characterised by Gelderloos et al. (2021): waves with a period of 1-3 days and waves with a 5-18 day period. Upstream of DS, the higher frequency waves have a phase speed of  $0.38 \text{ m s}^{-1}$ , whilst the lower frequency waves have a phase speed of  $0.19 \text{ m s}^{-1}$ , and downstream of DS the phase speed of both types of waves is the same ( $0.44 \text{ m s}^{-1}$ ). At these phase speeds, the rate of change of salinity at DSO would likely be greater than observed, as the salinity typically reduces by around 0.04 over a period of around 4 months (Chapter 3). Moreover, the DSO salinity minimum occurs in May at ANG, which is probably too late in the year to be explained by the rapid phase speeds of the waves, given that the wind forcing is strongest in winter. Therefore, it is assumed that the salinity signals are carried by advection, via the Shelfbreak EGC, and then the DSO.

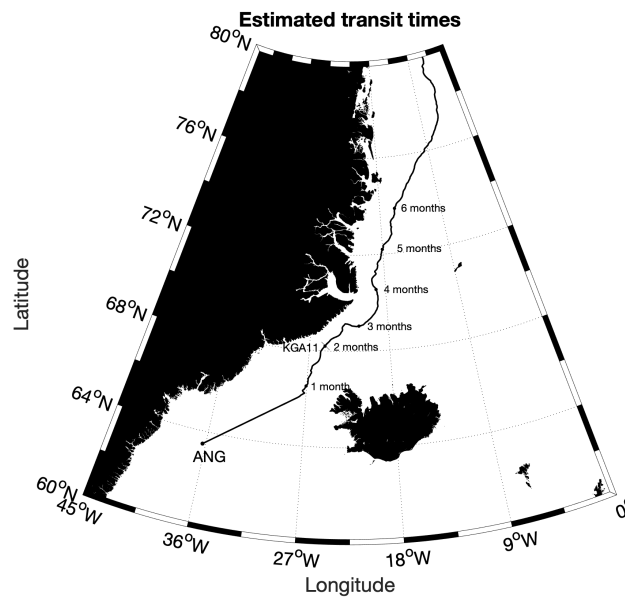


Fig. 5.9 Approximate transit times of salinity anomalies along the east Greenland shelfbreak, north of DS, to ANG, for dense water. The GEBCO 500 m isobath is plotted to indicate the approximate position of the shelfbreak, which indicates the pathway of the Shelfbreak EGC. The transit times from Fram Strait to DS were estimated using velocities from the upper Greenland slope (550 m depth) at KGA11 (location annotated), which is where DSO source water is found. Between DS and ANG, the advection speed is approximated using an estimate of DSO propagation speed.

### 5.3.3 Temporal variability

The correlation between wind and DSO salinity may be dependent on the time period investigated; therefore the temporal variability of the wind-salinity relationship is examined below. Previous investigations make conflicting arguments over what location of wind forcing has the greatest influence on the salinity of the DSO. Whilst Holfort and Albrecht (2007) argue that the wind forcing at DS (66°N) is most important, Hall et al. (2011) contradicted this by arguing that the wind forcing around 75°N over the Greenland shelfbreak is most important. The centre of correlation (between wind and DSO salinity) in this study is located in a third location, at 70°N over the Greenland shelfbreak. All three studies use data from a different time period, when the location of wind forcing most important to the salinity of the DSO, or the centre of correlation (between wind and DSO salinity), may be in different locations. This variability may be subject to changes in large scale atmospheric forcing, associated with different phases of the NAO index and ILD index.

To investigate the interannual variability of wind-DSO salinity correlation, time series of correlation between the wind and salinity of the DSO at ANG are constructed, using the wind time series at two key locations. The two key locations are r2 and r3, which correspond to the correlation maxima of the longer time series (1998-2015) at a two month and three month lag respectively (Figure 5.7). To construct this time series, a 49 month (4 years plus one month) centred sliding window was constructed. Each data point in Figure 5.10 is the centre point of a 49 month window. For example, the data point in January 2005 is the correlation in the period between January 2003 and January 2007 (including the first and last months). The de-seasonalised time series are used to investigate the correlation to preclude correlations resulting from a mutual seasonal cycle, as explained above.

Firstly, the correlations are generally lower between 2008 and 2011, but higher in other periods (Figure 5.10). The correlation at r2 is medium for a sustained six year period from early 2002 until early 2008 (Figure 5.10). Maximum correlation ( $r > 0.45$ ) occurs in May 2007, implying that correlations between the wind at r2 and the DSO salinity are highest between May 2005 and May 2009 (shaded orange window in Figure 5.10). Around this time, medium, statistically significant, correlations also occur at r3, which is perhaps not surprising since r3 is only located 80 km from r2. Sustained medium correlations also occur at r3 from mid 2011 until mid 2013, but not at r2. Maximum correlation in this period occurs in April 2012 - implying that the correlations between the wind at r3 and the DSO salinity are highest between April 2010 and April 2014 (shaded pink window in Figure 5.10). These two periods of higher correlation are investigated further below.

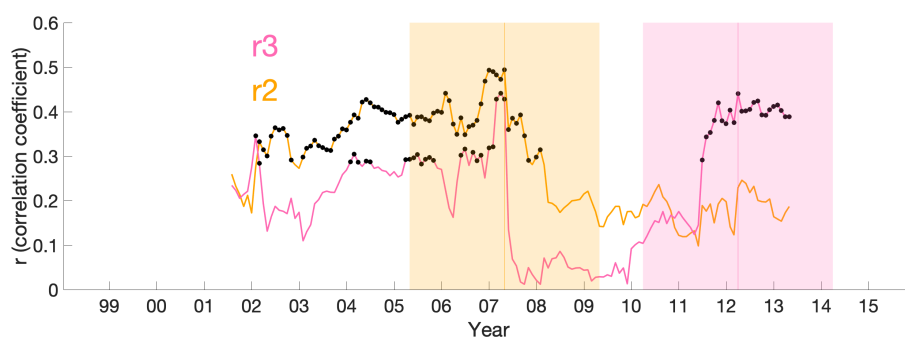


Fig. 5.10 The time series of correlation coefficient ( $r$ ) between the wind at two locations: r2 and r3 (see Figure 5.7 for locations) and the DSO salinity at ANG. The filled black circles indicate correlations that are statistically significant ( $p < 0.05$ ). Each data point is the mid-way point of a 49 month window used to calculate the correlation. The window centred on the r2 peak and r3 peak are shaded in orange and pink respectively.

To investigate the differences between these two periods of medium correlation (highlighted in Figure 5.10), the correlation between the wind field in the entire region and DSO salinity at ANG during the time series subsets was calculated. The correlation maps during this period are shown in Figure 5.11.

The centre of correlation is found in a different location in the two periods. Between 2005 and 2009, the centre of correlation is found off the northeast Greenland coast, whereas the centre of correlation moves southward, and is found at DS in the second period (between 2010 and 2014) (Figure 5.11). In the former period, the correlation of the wind field around DS is not statistically significant. High, statistically significant correlations occur in the wind field over the northeast Greenland shelfbreak ( $r \approx 0.55$ ), with r2 situated around the southern edge of this centre of correlation. Conversely, in the latter period, correlations are not statistically significant over the northeast Greenland shelfbreak, but high, statistically significant, correlations ( $r \approx 0.5$ ) are found around DS, with r3 located around the northern edge of this centre of correlation. Both r2 and r3 ( $\approx 70^\circ\text{N}$ ) are situated on the edge of the centre of correlation in both periods, which explains why the correlation maximum is found here when the full time series (i.e. 1998-2015) is used for the correlation calculation.

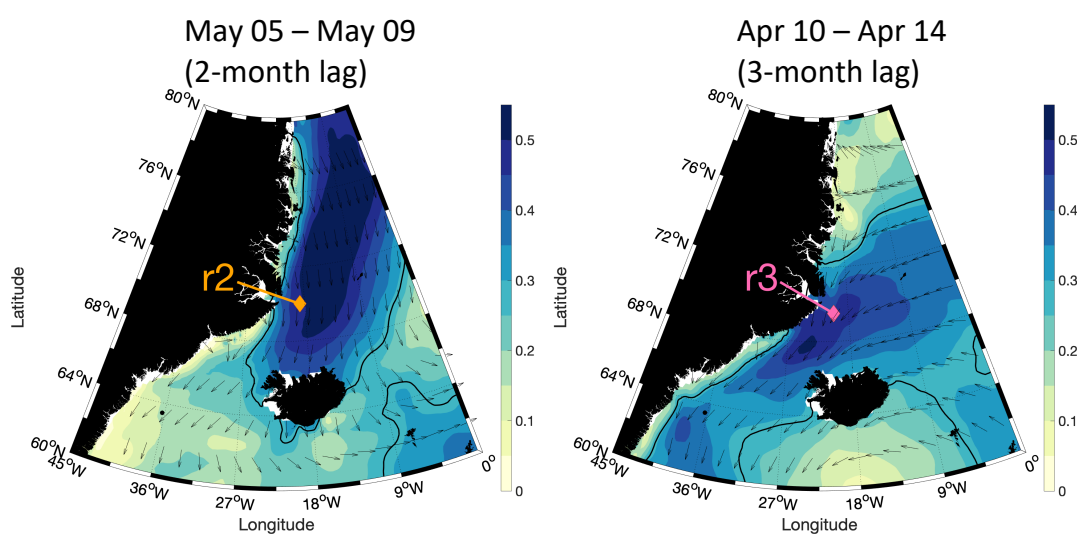


Fig. 5.11 Lagged correlation maps between the wind field and the DSO salinity at ANG (location marked by black circle) during subsets of the 1998-2015 time series. The colours indicate the magnitude of the correlation, whilst the quivers show the wind direction associated with negative salinity anomalies. The thick black line indicates statistically significant correlations ( $p < 0.05$ ). The left panel shows the correlation between May 2005 and May 2009, with a 2 month time lag, and the right panel shows the correlation between April 2010 and April 2014, with a 3 month time lag. These periods correspond to maxima in the correlation time series presented in Figure 5.10.

Time series of the NAO and ILD index are shown in Figure 5.2e and f. Between 2010 and 2014, the NAO index fluctuates between strong negative phases (e.g. winter 2010-11 and winter 2012-13) and strong positive phases (e.g. winter 2011-12 and winter 2013-14). The median absolute magnitude of the NAO index in this period is 1.58, compared with 1.05 between 2005 and 2009. As a result, the NAO pattern is likely the dominant cause of atmospheric variability between 2010 and 2014, and less dominant in the earlier period. Strong positive phases of the NAO index (see composite in Figure 5.3) are associated with particularly strong wind speeds at DS. In contrast, the NAO index is relatively weak between 2005 and 2009, whereas the ILD index is in a sustained negative phase. The ILD pattern influences the wind field off the northeast Greenland coast, but not around DS, and negative ILD phases are associated with intensified northerlies over the northeast Greenland continental margin (Figure 5.4). Intensified northerlies off the northeast Greenland coast, associated with negative ILD index phases, likely drive more intense freshening of the DSO, increasing the correlation between the wind here and the DSO salinity. Consistently, the atmospheric circulation in the correlation map between 2005 and 2009 is similar to the negative phase ILD pattern. The weakness of the NAO index between 2005 and 2009, and the negative phase of the ILD index, likely explains why the centre of correlation is located over the northeast Greenland coast in that period (Figure 5.11).

These results show that the atmospheric variability associated with the NAO and the ILD patterns may both influence the salinity of the DSO. Thus, in different time periods, the relationship between the wind forcing and the DSO salinity is likely different. This explains the contradictory findings of Holfort and Albrecht (2007) and Hall et al. (2011), who analysed the wind forcing of DSO salinity in different time periods. Holfort and Albrecht (2007) used data from the 1990s, when the NAO index was in a strong positive phase (Hurrell, 1995), to argue that the northeasterly winds through DS drive the salinity variability of the DSO. Conversely, Hall et al. (2011) used data from between 1998 to 2005, when the NAO index was generally weak and the ILD index fluctuated between strong negative and strong positive phases (Figure 5.2e and f), to argue that northerly winds at around 75°N drive the salinity variability of the DSO.

## **5.4 Wind stress forcing of intense DSO freshening**

### **5.4.1 Intense DSO freshening events**

The multi-annual variability of large scale atmospheric patterns, discussed above, may determine the intensity of DSO freshening each year. However, there are likely other

important factors, such as variability of sea ice concentration. These variability factors are related to the variability of DSO freshening in this section.

As described in Chapter 3, the DSO at ANG exhibits salinity seasonality characterised by the salinity maximum in December, followed by sustained freshening towards the salinity minimum in May. Intense sustained freshening events, defined by a peak to trough salinity change ( $\Delta S$ ) of below  $-0.05$  are highlighted in Figure 5.12a. Intense freshening occurs in 1999, 2004, 2005, 2009, 2014 and 2015. Of these events, the freshening is most intense in the 1999 and 2004 events, when  $\Delta S < -0.07$  (Figure 5.12a).

Most of the intense freshening events are associated with anomalously high wind speeds at the two locations of the wind-DSO salinity correlation maxima (approximately  $70^\circ\text{N}$ ) (Figure 5.12b). The wind speeds in Figure 5.12b are in the direction of the maximum correlation (Figure 5.7), which is  $182^\circ$  and  $211^\circ$  clockwise from northward for  $r_2$  and  $r_3$  respectively (i.e. the northerly and northeasterly component of wind respectively). Between 1998 and 2015, the highest wind speeds occur in the winter of 2003-04, 2008-09 and 2013-14, during which the monthly mean wind speed exceeded  $11 \text{ m s}^{-1}$  (Figure 5.12b). All three winters precede an intense freshening event in the DSO at ANG (Figure 5.12a). Further, the winters in which the wind speed is anomalously low (e.g. 2002-03, 2005-06 and 2009-10) are associated with weak or no freshening of the DSO.

However, there are some exceptions, with high wind speeds occurring in the winter of 2006-07 and 2011-12 preceding relatively weak DSO freshening ( $\Delta S \approx -0.03$ ), and a winter of relatively weak winds occurring in 2010-11 preceding relatively strong freshening ( $\Delta S \approx 0.04$ ) (Figure 5.12a and b). These exceptions weaken the correlation between the wind and DSO salinity (Figure 5.7), and they demonstrate that the DSO salinity is influenced by other variables.

One variable which can be identified and measured is the momentum exchange across the atmosphere-sea ice/ocean boundary layer, which can change the wind stress acting on the ocean. The momentum exchange is the amount of momentum imparted by the atmosphere on the sea ice/ocean across the boundary layer, or vice versa, to conserve momentum. A key variable which affects momentum exchange is sea ice, which is observed in the study region and is therefore an important factor. Below, the effect of sea ice concentration on wind stress, and thereby the salinity of the DSO at ANG, is investigated.

Alternatively, since the focus of this study is on wind-driven freshening, it may be more appropriate to compare the two time series of wind with the rate of change of salinity (i.e.  $dS/dt$ ) at ANG instead. The time series of these variables are shown in Figure 5.13a. The greatest correlations occur between the wind and the rate of change

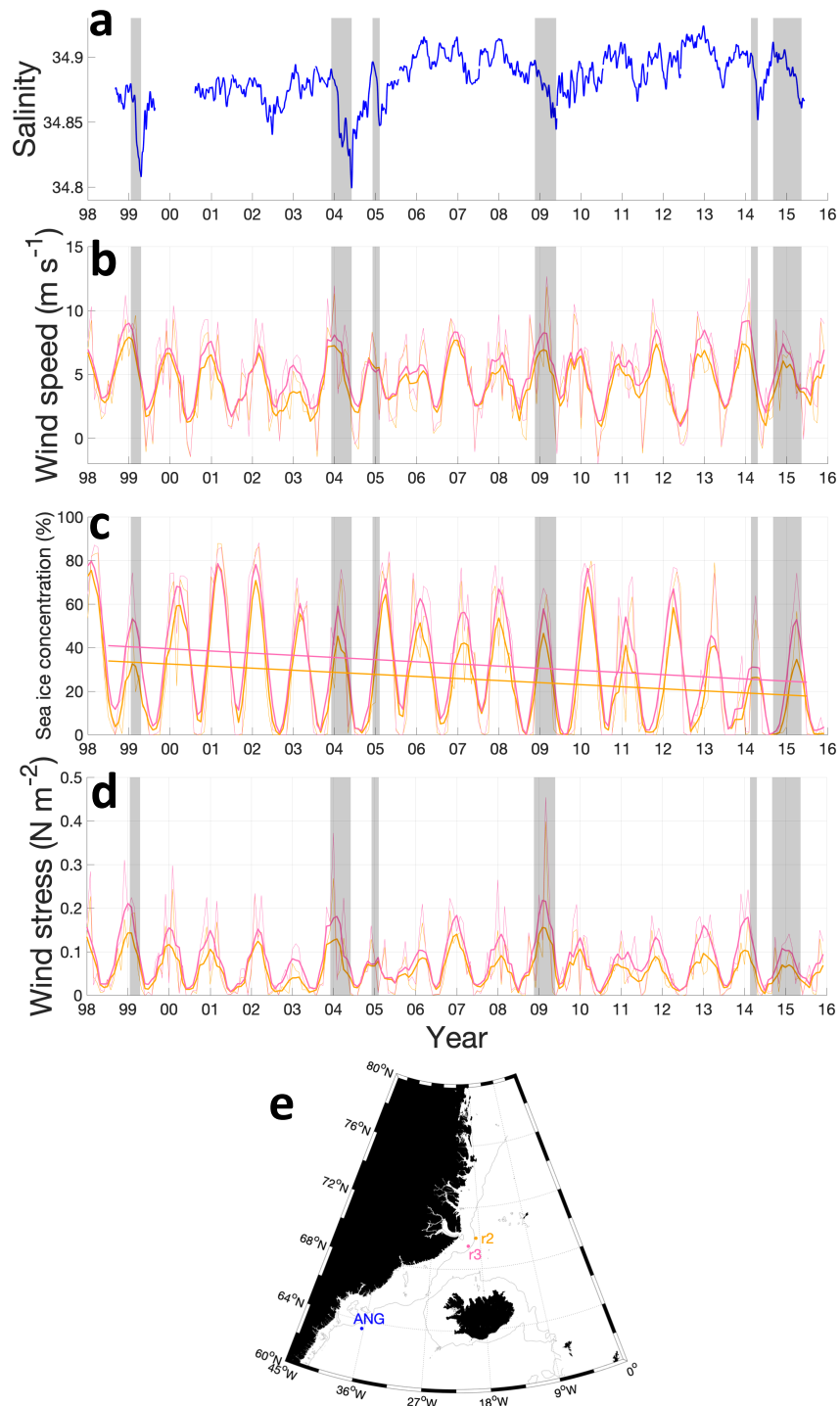


Fig. 5.12 1998-2015 time series of monthly averaged DSO salinity at ANG (a), wind speed ( $\text{m s}^{-1}$ ) (b), sea ice concentration (%) (c), and effective wind stress ( $\text{N m}^{-2}$ ) (d) at r2 and r3, and a map showing the location of the time series (e). The location of the wind and sea ice concentration time series is r3 (pink) and r2 (orange), which are the locations of the correlation maxima (see Figure 5.7). The thin lines are the unsmoothed time series, and the thick lines are smoothed with a 5 month centred moving mean filter. The wind and sea ice concentrations are from ERA5, whilst the salinities are from the UK1 mooring at ANG. The intense freshening events, when the salinity changes by at least  $-0.05$ , are shaded grey in panels a-d. The thick trend lines in (c) are linear models fitted to the annual mean sea ice concentration, and show decrease with time.

of salinity one month after (i.e. with a 1 month lag). The correlation coefficient between the wind at both locations (lagged by 1 month) and rate of change of salinity is  $-0.31$  (Figure 5.13b and c). The correlations are statistically significant at the 99% level. This implies that months of strong winds precede freshening of the DSO by 1 month and, similarly, months of weak winds precede salinity increase by 1 month.

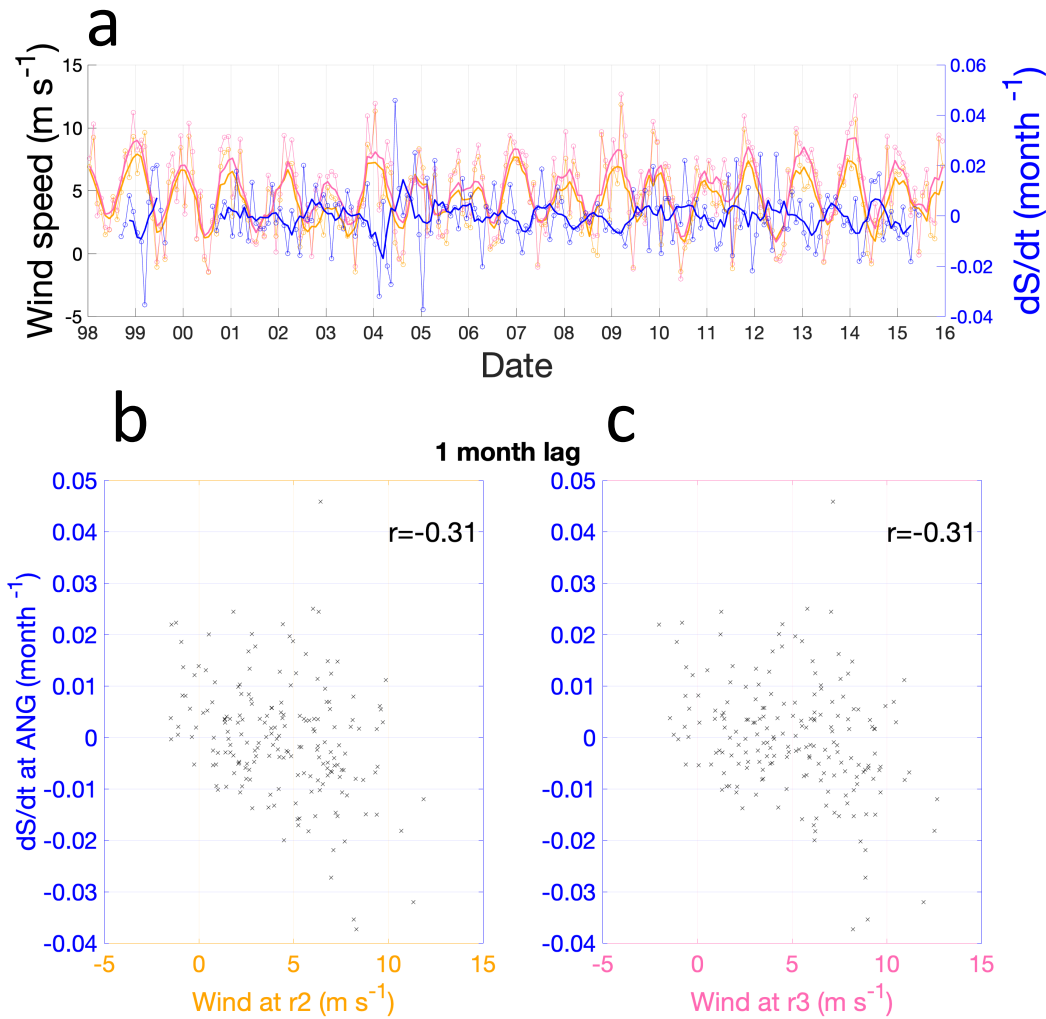


Fig. 5.13 Correlation between the wind at r2 and r3 in  $\text{m s}^{-1}$  and the rate of change of salinity ( $dS/dt$ ) in  $\text{months}^{-1}$  at ANG. Time series of the three variables are shown with the lefthand y-axis corresponding to the winds and the righthand y-axis corresponding to the rate of change of salinity (a). The correlation between the wind at r2 and the rate of change of salinity at ANG (b) and the correlation between the wind at r3 and the rate of change of salinity at ANG (c) are also shown on the bottom two panels. The winds shown are the wind components in the direction corresponding with the maximum correlation in the deseasonalised correlation maps (Figure 5.7).

The mechanism which may explain this relationship is wind driven increased southward volume transport of the Shelfbreak EGC (Mechanism 3 in Chapter 4). Assuming

that when the southward volume transport of the Shelfbreak EGC increases at KGA it also increases consistently at all locations between r2 and r3 and the DS sill. Thus, unlike Mechanisms 1 and 2, Mechanism 3 does not depend on advection of salinity signals from north of DS (at KGA) to ANG, which takes on the order of 2-3 months (Figure 5.9), and therefore the response time is shorter (1 month). When the northerly/northeasterly winds at r2 and r3 are high, the contribution of the fresh water masses of the Shelfbreak EGC to the DSO increase, resulting in the freshening 1 month later, and vice versa. The fact that statistically significant correlations occur between the wind (lagged by 1 month) and the rate of change of salinity and between the wind (lagged by 2-3 months) and the salinity support one of the conclusions drawn in Chapter 4, i.e. that both freshening of the Shelfbreak EGC (Mechanisms 1 and 2) and enhanced southward volume transport of the Shelfbreak EGC (Mechanism 3) contribute to the seasonal freshening of the DSO.

### 5.4.2 The role of sea ice concentration

The mean sea ice concentration in cold season months (October-March), from the ERA5 product, is shown in Figure 5.14. The ERA5 sea ice concentrations are derived from microwave detecting satellite data, as explained in Chapter 2, where the time-mean error of the sea ice concentration estimate was also investigated. The error was shown to be highest on the Greenland shelf to the north of 70°N, where the error was around 5%, and the error on the Greenland shelf around DS and to the south was < 5%, with the error reducing to below 1% offshore. This shows that the ERA5 sea ice concentration estimate is relatively accurate, and provides confidence in the investigation of its variability, which is presented below.

Sea ice covers a large fraction of the east Greenland continental margin, with concentrations on the shelf > 25% north of 66°N and concentrations > 75% north of 72°N. Note that concentrations over the shelfbreak are approximately 50% between 68°N and 78°N. The sea ice melts in most locations in the other half of the year, with the April-September mean sea ice concentrations remaining above 50% only on the Greenland shelf north of 74°N (not shown). The sea ice concentration also varies from year-to-year (Figure 5.12), which may have implications for the relationship between the winds and the DSO salinity. Note that there is a weak (non-statistically significant) negative correlation between the northerly/northeasterly wind speed and the sea ice concentration (not shown), because higher wind speeds from this direction increase the onshore Ekman transport of sea ice and therefore reduce the sea ice concentration over the shelfbreak (where r2 and r3 are located (Figure 5.12e), and thickening the ice on the shelf.

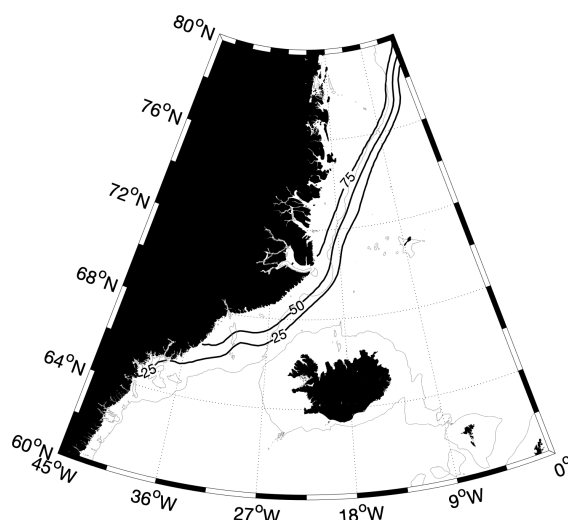


Fig. 5.14 October-March mean sea ice concentration contours (in %) from ERA5 between 1998-2015 (thick black contours: 25%, 50% and 75% contours shown). The thin grey lines indicate the 500 m isobath (from GEBCO), which roughly indicates the location of the shelfbreak.

There is a clear trend of decreasing sea ice concentration between 1998 and 2015 (Figure 5.12c), which is consistent with the larger scale trend of sea ice concentration decrease in the Greenland and Iceland Seas in the same period, reported by Moore et al. (2015). A linear model was fitted to the annual mean sea ice concentration time series at r2 and r3, and these trend lines are shown in Figure 5.12c. The sea ice concentration trend is  $-1\% \text{ year}^{-1}$ , and statistically significant at the 95% level at both locations. This is associated with a weak trend of decreasing effective wind stress (Figure 5.12d), which reduces by around  $0.01 \text{ N m}^{-2}$  over the 18 year period, though this trend is not statistically significant.

The presence of sea ice modifies the momentum exchange across the surface boundary layer. Sea ice has a greater surface roughness than open ocean and thus it may increase the magnitude of the drag coefficient ( $C_D$ ) and thus increase the momentum exchange across the surface boundary layer (Martin et al., 2014). Specifically, skin drag, caused by friction, and form drag, caused by pressure forces resulting from the flow of air interacting with sea ice ridges, floe edges, melt pond edges, and with other types of surface undulations, occur in the atmosphere-sea ice boundary layer (Elvidge et al., 2016). The wind stress is proportional to  $C_D$ , therefore, by increasing  $C_D$ , the wind stress will also increase. Mathematically, the wind stress is approximated by the following equation:

$$\tau = \rho_{air} C_D (U_{wind} - U_{ocean}) \quad (5.1)$$

where  $\tau$  is wind stress,  $\rho_{air}$  is the air density,  $C_D$  is the drag coefficient,  $U_{wind}$  is the wind speed and  $U_{ocean}$  is the ocean speed.  $U_{ocean}$  variability is more than an order of magnitude weaker than the variability of  $U_{wind}$  and can therefore be neglected, to first order.

While acknowledging that the variability of the morphology of sea ice is another potentially important and relevant factor, it is beyond the scope of this thesis, due to a lack of appropriate data. Note that one study of sea ice off the northeast Greenland coast showed that pancake ice is the most common type of sea ice here because the region is exposed to intense wave activity from different directions, which breaks up the sea ice into smaller parts (Wadhams, 1999). Supposing pancake ice is the prevailing sea ice type along the east Greenland coast in all years, this would result in greater drag than would occur over larger ice floes (Elvidge et al., 2016).

The study region is classified as a Marginal Ice Zone (MIZ), which is traditionally defined by sea ice which is fragmented by ocean wave activity, and where the sea ice concentration is between 15% and 80% (Strong and Rigor, 2013). Aircraft observations have shown that, in the Arctic MIZ, the drag coefficient peaks when the sea ice fraction is between 50% and 80%, and the drag decreases at lower fractions (Elvidge et al., 2016; Lüpkes and Birnbaum, 2005). The effect of sea ice concentration on the resulting effective wind stress can be approximated by estimating the dependence of the form drag, on the sea ice concentration, using a simple model which is based on observations (Lüpkes and Birnbaum, 2005), and has been verified by further observations since (Elvidge et al., 2016).

The variability of  $C_D$  as a function of sea ice concentration is shown in Figure 5.15. In this model, the peak drag occurs approximately between sea ice concentrations of 55% and 75%, and maximum  $C_D$  occurs at sea ice concentrations of 63%. This agrees well with the observations presented by Elvidge et al. (2016) of the MIZ in the Barents Sea. The effective wind stress ( $\tau$ ), which uses the model based on observations of the dependence of  $C_D$  on sea ice concentration (Figure 5.15), is calculated, and the resulting time series at r2 and r3 is displayed in Figure 5.12d.

The effective wind stress at r2 and r3 decreased between 1998 and 2015 in response to the decreasing sea ice concentration, despite the fact that the wind speeds do not decrease over the same period (Figure 5.12b-d). Comparing the winters of 1998-99 and 2013-14, the wind speeds are similar, if anything with higher values in the latter period, yet the wind stress is notably lower in 2013-14 (peak values in the smoothed time series between 0.10 and 0.18 N m<sup>-2</sup>) than in 1998-99 (peak values in the smoothed

time series between  $0.14$  and  $0.21 \text{ N m}^{-2}$ ), as a consequence of the sea ice reduction trend (Figure 5.12c). This could explain why the sustained freshening event in 2014 is less intense than the freshening in 1999 and 2004, despite the very high speeds of the preceding winter of the latter period (Figure 5.12a and b). In addition, in the winters of 2003-04 and 2008-09, the high wind speeds coincide with sea ice concentrations of between 40% and 60%, which enhances the effective wind stress and likely causes the intense sustained freshening in 2004 and 2009 (Figure 5.12).

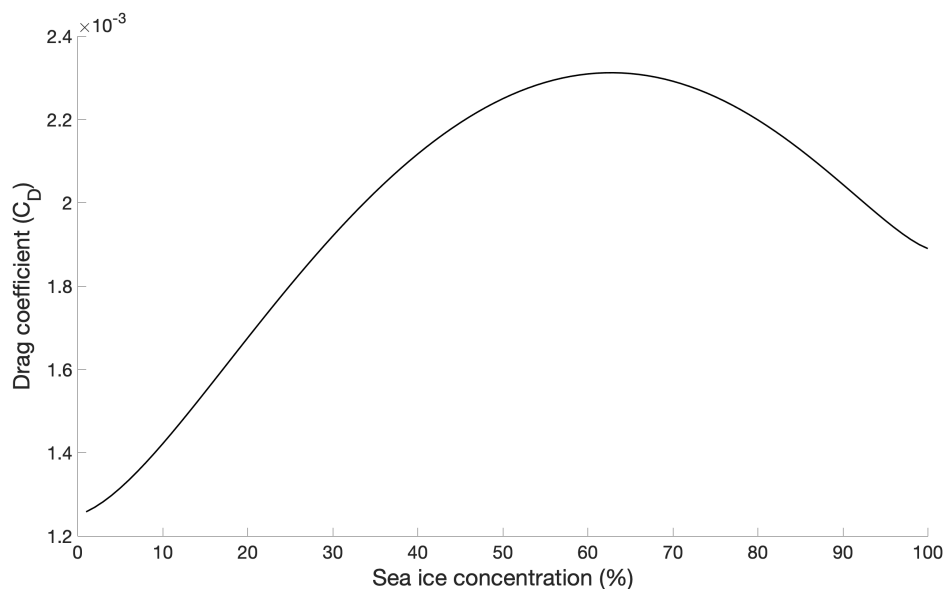


Fig. 5.15 The variability of the drag coefficient ( $C_D$ ) as a function of sea ice concentration in the MIZ, derived from a parameterisation model created by Lüpkes and Birnbaum (2005). This approximation agrees well with observations presented in Elvidge et al. (2016).

## 5.5 Conclusions

In this chapter, the relationship between atmospheric forcing and DSO salinity variability was examined in detail. Four research questions were posed in the introduction:

1. Is wind forcing a controlling factor on the DSO salinity on seasonal to multi-annual timescales?
2. How sensitive is the DSO salinity to wind forcing in particular regions?
3. What is the role of sea ice concentration in the wind-DSO salinity relationship?

4. How does the large scale variability of atmospheric circulation in the North Atlantic influence the salinity of the DSO?

**1. Is wind forcing a controlling factor on the DSO salinity on seasonal to multi-annual timescales?**

Yes, wind forcing does indeed appear to be a key controlling factor on the DSO salinity on these timescales. Remote wind forcing over the Greenland shelf and slope between  $67^{\circ}\text{N}$  and  $75^{\circ}\text{N}$  is correlated with the DSO salinity. The wind forcing is northerly/northeasterly and the correlation is maximised at a time lag of 2-4 months. The correlation is statistically significant whether or not the seasonal cycle is removed. Furthermore the correlations are supported by a strong physical basis. Firstly, the correlations are maximised in the vicinity of the shelfbreak, over the Shelfbreak EGC, where the current may freshen or strengthen in response and drive sustained freshening of the DSO, as argued in Chapter 4. Secondly, the lag times used to maximise correlation are consistent with estimated transit times of property signals, which are advected first by the Shelfbreak EGC and then by the DSO.

**2. How sensitive is the DSO salinity to wind forcing in particular regions?**

There are localised regions where wind forcing appears to be especially important in determining the salinity variability of the DSO. These locations are found over the Greenland shelf and slope at DS and to the north of DS. Specifically, maximum correlation occurs over the Greenland shelfbreak at  $70^{\circ}\text{N}$ , which is situated in the northern Blosseville Basin, around where the EGC bifurcates and forms the Shelfbreak EGC and Separated EGC (Våge et al., 2013). The variability of the ocean circulation in the Blosseville Basin was argued to be the dominant driver of DSO salinity variability at ANG in Chapter 4. Since wind forcing likely controls ocean circulation variability here (as reasoned by Våge et al. (2013) and Harden et al. (2016)), this chapter puts more emphasis on the role of ocean circulation in the Blosseville Basin in the salinity variability of the DSO at ANG. However, the region of wind forcing that is most important to the salinity of the overflow changes in time. For example, between 2005 and 2009 the centre of correlation is found between  $69^{\circ}\text{N}$  and  $75^{\circ}\text{N}$ , whereas the centre of correlation shifts southward towards DS and is found between  $67^{\circ}\text{N}$  and  $73^{\circ}\text{N}$  in 2010-2014. This mobility of the centre of correlation explains why Holfort and Albrecht (2007) and Hall et al. (2011) argued for wind forcing in different locations, to explain the salinity variability of the DS.

### **3. What is the role of sea ice concentration in the wind-DSO salinity relationship?**

Sea ice concentration plays an important role in the relationship between wind forcing and DSO salinity. Firstly, the variation of sea ice concentration modulates the wind stress, by varying the drag coefficient, and thereby modulating the momentum exchange between atmosphere and ocean. Using a model of the variability of the drag coefficient as a function of sea ice concentration, it is demonstrated that maximum drag occurs at sea ice concentrations between 55% and 75%. Secondly, it is argued that the statistically significant  $-1\% \text{ year}^{-1}$  reduction in sea ice concentration between 1998 and 2015 has driven the reduction in effective wind stress forcing over this period. As a result, the sustained freshening event in 2014 is not as intense as freshening events in 1999 and 2004, when the sea ice concentration was higher, despite the fact that the wind speeds were as high if not higher in the winter of 2013-14, compared with the earlier winters. As such, the reduction in sea ice likely has important implications for the wind driven variability of the DSO.

### **4. How does the large scale variability of atmospheric circulation in the North Atlantic influence the salinity of the DSO?**

The NAO is the dominant mode of variability in the atmospheric forcing region, and the number of barrier wind events has been shown to be positively correlated with the NAO index (Harden et al., 2011). Between 2010 and 2014, the NAO fluctuated between strong positive and strong negative phases, and as a result it likely became an even more dominant mode of variability in the region in those years. In this period, the centre of correlation is situated over DS, emphasising the role of barrier winds in controlling the salinity of the DSO in that period. Conversely, between 2005 and 2009, the centre of correlation is found further north, over the Greenland shelfbreak between around  $69^{\circ}\text{N}$  and  $75^{\circ}\text{N}$ . In this period, the NAO was generally much weaker, however the Iceland-Lofoten Difference (ILD) index was in a sustained negative phase. The ILD pattern explains approximately 13% of the atmospheric variability in the region (between 1998 and 2015), and negative phases are associated with strengthened northerlies over the northeast Greenland shelfbreak. It is argued that the ILD index is the dominant driver of atmospheric variability between 2005 and 2009, rather than the NAO index, which is why the centre of correlation is over the northeast Greenland shelfbreak (between around  $69^{\circ}\text{N}$  and  $75^{\circ}$ ), rather than DS, where the winds are not intensified during extreme ILD phases. This implies that, as well as the NAO, the ILD pattern may drive variability of the DSO too.

# Chapter 6

## Discussion and conclusions

This thesis has used unique multi-annual time series of salinity, temperature and velocity variability in the ocean in a region of known climatic importance, and drawn inferences relating to the scale of variability and mechanistic processes by which atmospheric forcing can drive changes in ocean circulation. The ANG mooring array dataset is unique because it comprises sustained observations of a key component of NADW over a long time period (1986-2015). Synthesis of this dataset, with time series from upstream moorings, CTD sections and state of the art atmospheric reanalysis data, has added new understanding of the salinity variability of the DSO on multi-month to multi-annual timescales, as summarised below.

In this light of progress made, several new avenues for investigation have been revealed. These are highlighted as suggested high-priority areas for future research. The potential implications of these new insights for the future ocean circulation of the region, where dramatic climatic changes are anticipated, are also discussed. In the following discussion (Section 6.1), first the limitations of the thesis are identified, the key areas of remaining uncertainty are highlighted and the direction of future work indicated. Finally, the potential impacts of future climatic changes on the ocean circulation are discussed. Lastly, in Section 6.2, the main conclusions of the thesis are listed.

### 6.1 Discussion and future work

The purpose of the following discussion is to place the key findings of this thesis in the wider context of the research area. There are a number of areas of investigation presented in this thesis that could be developed further to advance our understanding of the AMOC, and this is also discussed below. Further, recommendations are made for future work, and the implications of future climatic change on the AMOC are explored.

### 6.1.1 Ocean circulation of DSO source water in the Blosseville Basin

Firstly, in Chapter 4 of this thesis, it was argued that hydrographic changes to the currents which feed the DSO from the north cause the seasonal salinity variability of the DSO, characterised in detail in this thesis. Specifically, winter freshening and acceleration of the Shelfbreak EGC was linked with late winter/spring freshening of the DSO over the Greenland slope and ledge at DS, and in the core of the DSO at ANG.

This is important because it demonstrates that variability of the DSO source water feeding the DSO from the north could cause changes to the composition of the DSO south of DS to the extent that the signal is detected at ANG. This was supported by the fact that the correlation between the wind field and the DSO salinity at ANG is maximised in the northern Blosseville Basin, implying an important role for wind driven circulation changes here in the salinity variability of the DSO (Chapter 5). Furthermore, the variability of the ocean circulation in the Blosseville Basin on seasonal timescales (illustrated in Figure 6.1), which likely causes the salinity anomalies in the DSO, may also drive sustained anomalies in the volume transport of the DSO (see e.g. (Harden et al., 2016)), which could make an important contribution to the net volume transport of the DSO. This demonstrates that there are important implications of the variability of circulation in the Blosseville Basin for the DSO, which are therefore relevant to the AMOC too.

#### Wind driven variability

Firstly, it is not known in detail what forcing mechanisms control the variability in the volume transport of the DSO source water currents (i.e. the Shelfbreak EGC, the separated EGC and the NIJ) on multi-month to seasonal timescales, and this needs to be further investigated. Both Köhl et al. (2007) and Harden et al. (2016) noted an anti-correlation in the southwestward volume transport of the currents on the Greenland and Iceland continental slope. Harden et al. (2016) argue that the wind stress curl in the Blosseville Basin oscillates, from positive to negative, changing the circulation from cyclonic to anti-cyclonic respectively. When the wind stress curl is positive, the circulation is cyclonic, the Shelfbreak EGC is enhanced and the separated EGC is weakened, and vice versa, accounting for the anti-correlation (Harden et al., 2016).

Harden et al. (2016) argued that, as a result of the wind stress curl variability, the volume transport of the Shelfbreak EGC is enhanced in winter and diminished in summer (Figure 6.1). However, this argument was based on only 1 year of mooring data from 2011-12, and more evidence is needed to support this claim, and to show that this year is representative of other years. Furthermore, the percentage of variance

in the volume transport of the current branches explained by this mechanism was not calculated, and it is not known whether other mechanisms, for example the role of freshwater in altering the density structure and thus the baroclinic structure of the current, may also be important.

As shown in this thesis, barrier wind events are associated with intense negative wind stress curl over the Greenland shelf and slope, which drives Ekman pumping there. This could cause important changes to the hydrography of the DSO source water, which may cause variability of the DSO properties downstream. Specifically, sustained Ekman pumping could cause isopycnal heaving, where the water masses over the Greenland slope to deepen below sill depth (650 m). Some fraction of this water would then be too deep to exit the Blosseville Basin to the south, and instead would be bathymetrically steered and would recirculate in the Blosseville Basin to conserve potential vorticity. This may change the volume transport of different water masses and drive hydrographic variability at DS. Specifically, the deeper, denser water masses (RAW and AIW) are likely recirculated in this scenario, while the PW is probably advected to the DS.

Numerical model experiments are also very useful sources of information regarding the role of wind-driven dynamics in the region. For example, Gelderloos et al. (2021) use a high-resolution ocean-sea ice numerical model to show that barrier winds drive fast, long wave length waves on the continental shelf with a period of 5-18 days. Further analysis of numerical model output is an important part of resolving current research questions, especially regarding the nature of the sub-intertidal variability at Denmark Strait (Gelderloos et al., 2021).

The contribution of isopycnal heaving to seasonal hydrographic variability of the DSO at DS could be investigated using moored near-bottom density observations at DS around the east Greenland shelfbreak and slope, as well as the observations in the trough where mooring deployments have mainly been deployed hitherto. However, year round ocean observations on the Greenland continental margin in the vicinity of DS are notoriously difficult to acquire, due to the presence of sea ice, and it might be necessary to deploy upward facing ADCPs to obtain the required velocities in order to calculate volume transports. Nevertheless, this thesis highlights the important contribution of the DSO sources that pass through the Greenland slope to the property variability of DSO.

### **The influence of sea ice concentration**

In addition, this thesis highlights that the role of sea ice in the wind driven hydrographic variability of DSO source water branches upstream of DS is potentially important, yet our knowledge of it remains incomplete. Moore et al. (2015) investigated the important role of sea ice in modulating dense water formation in the Greenland and Iceland Seas.

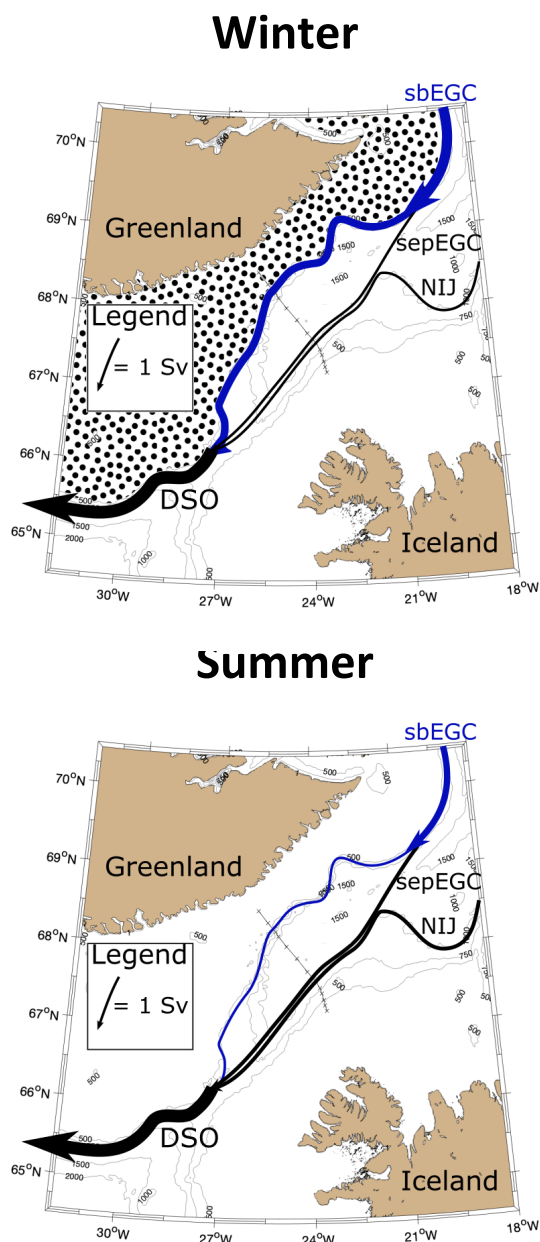


Fig. 6.1 Schematic sketch of the proposed seasonality of ocean circulation in the Blosseville Basin. The black dots represent ice floes, which are found on the Greenland shelf in winter, and may intensify the wind driven seasonality of the ocean circulation. The arrows represent the volume transport of key source water currents of the DSO: the Shelfbreak EGC (sbEGC) in blue, and the separated EGC (sepEGC) and the North Icelandic Jet (NIJ) in black. The width of the arrows is proportional to the volume transport. The thin grey lines show the 500 m, 750 m, 1000 m, 1500 m and 2000 m isoabths, from the GEBCO\_2014 grid. The black crosses indicate the location of KGA moorings. The bifurcation of the EGC at 69°N is based on the theory of Våge et al. (2013), whilst the seasonal changes are based on the findings of Harden et al. (2016) and this thesis.

In particular, Moore et al. (2015) demonstrated that the maximum heat fluxes out of the ocean occur at the edge of the sea ice extent, and the receding of sea ice in the Iceland and Greenland seas was therefore weakening the cooling of the ocean by the atmosphere in important deep convection sites in the central part of the basins. The work in this thesis highlights a further role of sea ice; that of modulating the wind driven component of dense water export from the Nordic Seas, via the DSO.

Specifically, it was argued in this thesis that because the effective wind stress is amplified over the Marginal Ice Zone (MIZ), the wind forced impact on the ocean circulation in the Blosseville Basin is increased when the sea ice concentration is between 55% and 75%. In particular, the sustained freshening of the DSO was weaker in 2014, compared to 2004, despite stronger wind forcing in the later period, which may have been because the sea ice concentration in the winter of 2013-14 was very low ( $\approx 30\%$ ). It may be useful to analyse the response of the ocean circulation to a recurrent pattern of wind forcing during different sea ice concentrations (e.g. partial and 100% ice concentration in winter and ice-free conditions in summer). While Harden et al. (2016) showed that the Shelfbreak EGC was enhanced in winter 2011-12 and weakened in summer, it is not clear what contribution the presence of sea ice made to this seasonality of the circulation (Figure 6.1).

To conduct an investigation on this issue, multiple years of hydrographic section data from around the location of KGA could be investigated in conjunction with atmospheric reanalysis, and sea ice concentration estimates derived from satellite microwave observations. In addition, the acquisition of moored ADCP velocities from the Greenland continental margin would enable a thorough investigation into the Ekman response of the upper part of the ocean to wind forcing. One potential barrier to this investigation is that different types of sea ice will have different impacts on the momentum exchange across the atmosphere-ocean/ice boundary, and regular satellite products do not distinguish between these different types of sea ice. However, a novel processing technique for objectively distinguishing landfast sea ice in satellite observations from other types of sea ice has recently been developed Fraser et al. (2020).

### **Aspiration of dense water into the overflow**

As reasoned by Harden et al. (2016), whilst some fraction of the DSO source water below sill depth is recirculated in the Blosseville Basin, another portion aspirates into the DSO source water between KGA and DS. However, the spatiotemporal variability of the aspiration process has not been thoroughly investigated, despite the large contribution it could make to the volume transport of the DSO. Future studies could quantify the

variability of aspiration using model simulations, verified by observations at KGA and DS.

The type of mixing process which drives aspiration is also not well known at present. Assuming aspiration is driven by diapycnal mixing processes, microstructure measurements using a profiler directly upstream of DS are required to quantify the aspiration rates here. Furthermore, current meters would perhaps be instructive of the relevant mechanisms (e.g. internal tides over rough topography). The acquisition of these data is justified by the contribution aspiration makes to DSO transport, and therefore the AMOC.

### 6.1.2 Role of dense shelf water in the AMOC

In this study, the occurrence of fresh pycnocline water located offshore from the Greenland shelfbreak, in the upper layers of the DSO, at DS, was shown to be seasonal, occurring most clearly in May. This feature has previously been described as a fresh lid of the overflow, by Rudels et al. (2002), who demonstrated its presence in CTD section snapshots at DS, and on the Greenland slope at around 1500 m in the Irminger Basin. In addition to the offshore fresh lid contribution to the DSO, there also exists fresh, but dense, water on the Greenland shelf (Figure 6.2), which is thought to contribute to the DSO after spilling off the shelfbreak downstream of DS (Brearley et al., 2012; Falina et al., 2012; Koszalka et al., 2013).

However, several fundamental questions about the role of dense shelf water in the AMOC still remain, and two vital questions are highlighted here. Firstly, what is the fate of the dense shelf water; what proportion of it feeds the Spill Jet (introduced in Chapter 2) (von Appen et al., 2014) and the DSO (Brearley et al., 2012)? Secondly, how does the contribution of dense shelf water to the DSO vary on daily, to seasonal, to multi-annual timescales?

Using 13-months of sustained observations from a mooring array 250 km downstream of DS, Harden et al. (2014) demonstrated that dense shelf water cascades off the shelf, to feed the Spill Jet (von Appen et al., 2014) and the DSO (Brearley et al., 2012). Using data from the same mooring array, von Appen et al. (2014) characterised the Spill Jet as a bottom intensified current situated upslope from the DSO, associated with a mean volume transport of 3.2 Sv and fed by dense shelf water spilling off the shelf. The Spill Jet primarily transports water that is less dense than the DSO ( $\sigma_\theta < 27.8 \text{ kg m}^{-3}$ ), leading von Appen et al. (2014) to argue that it contributes to the AMOC at intermediate depths in the density class of LSW. Despite this, Brearley et al. (2012) present CTD sections, at the location of the mooring array, where lenses of water dense enough to contribute to the DSO ( $\sigma_\theta > 27.8 \text{ kg m}^{-3}$ ) are found above the core of the

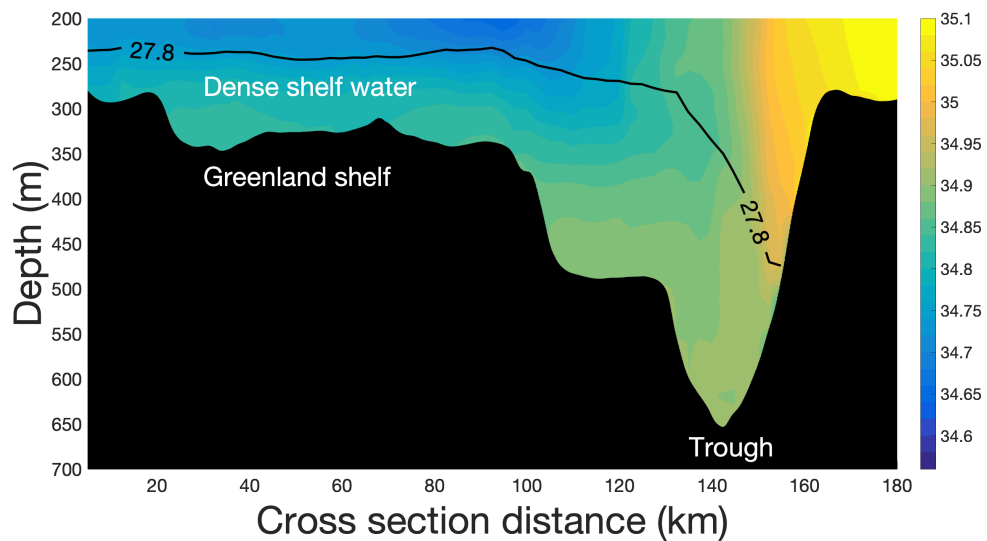


Fig. 6.2 Time-mean salinity cross section at DS between 1990 and 2019, showing the presence of the dense shelf water. The thick black line is the  $27.8 \text{ kg m}^{-3}$  density contour, which is traditionally used as the upper boundary of the DSO. The bathymetry is derived from shipboard echo-sounder data, and key features of the bathymetry are labelled. Also labelled is the dense shelf water, which is the freshest component of the DSO.

DSO, and are advected by the Spill Jet. Sustained seasonal freshening of the DSO is intensified in lighter classes of the DSO ( $27.88 \text{ kg m}^{-3} < \sigma_{\theta} < 27.91 \text{ kg m}^{-3}$ ), and upslope from the DSO at the Spill Jet section, as shown in Chapter 3. This indicates seasonal freshening of the dense shelf water, likely driven by the seasonal changes in hydrography investigated in Chapter 4.

It remains unclear what proportion of the dense shelf water feeds the Spill Jet, and the DSO. Using a numerical particle tracking model, Koszalka et al. (2013) estimate that approximately 25% of the DSO derives from dense shelf water. They also identify the Dohrn Bank (50-100 km downstream of DS) and the mouth of the Kangerdlugssuaq Trough (200 km downstream of DS) as key spilling locations. Falina et al. (2012) estimate the fraction of DSO transport which derives from dense shelf water, using CTD section salinity and dissolved oxygen data. They also attribute 25% of the DSO transport to dense shelf water in some CTD snapshots of the Greenland slope in the southwest Irminger Sea, however, in other snapshots, the contribution was much lower. This demonstrates the high variability of the contribution of dense shelf water to the DSO.

To improve our understanding of the role of dense shelf water in the AMOC, sustained measurements all year round in specific locations where dense shelf water cascades off the Greenland shelf to join the DSO (Koszalka et al., 2013) are a necessity.

A potential mooring array might involve a set of moorings deployed on the outer shelf in a line parallel to the shelfbreak. As the authors make clear, the water on the shelf at the Spill Jet mooring array, observed by Harden et al. (2014), is generally not dense enough ( $\sigma_\theta < 27.8 \text{ kg m}^{-3}$ ) to feed the DSO, and the contribution of the dense shelf water to the DSO likely occurs upstream of this location. The moorings should be equipped with instruments that measure the velocity and the properties of the water. The measurements should focus on near-bottom layers of the water column, and should be deployed on the shelf in locations where numerical models have identified as key spilling locations (Koszalka et al., 2013). Further, process studies could be undertaken using CTDs and microstructure measurements, because turbulent mixing of this water into the DSO plume may be very important.

These observations could provide vital new understanding of the formation of the deep limb of the AMOC, and test the process of dense water spilling off the shelf in ocean models, such as the numerical simulation introduced by Koszalka et al. (2013), which had temperature, salinity and density biases and therefore might misrepresent this process. Refining the modelled representation of this process would lead to improvement in the parameterisation of spilling of dense shelf water in coupled climate models. Furthermore, these observations could be used to determine whether there is a seasonal signal in the salinity and density of the dense shelf water, which would indicate a shelf pathway for the distinct freshening events, originating from Shelfbreak EGC variability, and observed in the core of the DSO at ANG in this thesis.

### 6.1.3 Evolution of the DSO in the Irminger Basin

#### Entrainment

Entrainment of lighter water masses into the DSO is a key area of uncertainty. In particular, the spatiotemporal variability of the entrainment of LSW and MIW into the DSO is still not well understood. One important question is how does the contribution of entrainment to the formation of NADW vary on daily, to seasonal, to inter-annual timescales? Previous studies have identified a location of high entrainment, situated approximately 100 km downstream of DS, where high DSO plume speeds and cyclonic eddies increase the vertical shear of horizontal velocity and thus enhance entrainment (Koszalka et al., 2017; Voet and Quadfasel, 2010). Entrainment around this location drives substantial increases in the temperature and volume transport of the DSO from approximately  $0.25^\circ\text{C}$  (Voet and Quadfasel, 2010) and 3.2 Sv (Jochumsen et al., 2017) respectively, at the sill to  $1^\circ\text{C}$  (Voet and Quadfasel, 2010) and 5 Sv (Dickson and Brown, 1994) 200 km downstream, though spilling of dense shelf water downstream of DS is

responsible for some unknown fraction of the increase in volume transport (Brearley et al., 2012); see Section 6.1.2.

The transport of NADW past Cape Farewell is approximately 13 Sv, due to the convergence of DSO with Iceland Scotland Overflow Water (ISOW) and entrainment of LSW (Dickson and Brown, 1994). However, the two aforementioned DSO mixing studies (Koszalka et al., 2013; Voet and Quadfasel, 2010) focus on the initial 500 km descent of the DSO from DS to ANG. Beyond 200 km downstream of DS, Voet and Quadfasel (2010) argue that horizontal stirring by eddies becomes the dominant mechanism determining the evolution of the DSO. However, Koszalka et al. (2017) do not estimate the contribution from horizontal eddy stirring mechanism, quantified by Voet and Quadfasel (2010). It is of vital importance that this process is quantified between DS and Cape Farewell, as highlighted by Koszalka et al. (2017). It is important to quantify the mixing between NADW source water masses in order to be able to link the meridional advection of signals, and to interpret signals at the different arrays (e.g. OSNAP, RAPID etc).

In general, the spatial resolution of climate models is too coarse to resolve the important process of entrainment of warmer water into cold gravity plumes, such as the DSO and the other Nordic Seas overflows, so parameterisations are used instead (Legg et al., 2009). However, the parameterisations used are approximations, and Danabasoglu et al. (2010) determine that entrainment into the Nordic Seas Overflows is underestimated by climate models. Therefore, there is a pressing need to improve the parameterisation of entrainment. Observations can be used to refine these parameterisations, for example as a reference for process models (Legg et al., 2009). The numerical model used by Koszalka et al. (2017) in their study of entrainment into the DSO, represents the DSO with a positive temperature and salinity bias (Koszalka et al., 2013). The simulated DSO has a mean temperature of 2.5°C and a mean salinity of 34.90 at ANG (Koszalka et al., 2013), compared with the mean observed temperature of 1.8°C and mean salinity of 34.88 (Chapter 3) in the same year (2003). Should this temperature and salinity model bias result in a density bias, it could change the nature of mixing between the DSO and its neighbouring water masses (ISOW and LSW) in the model. For example, a lighter DSO product could result in isopycnal mixing with ISOW, rather than diapycnal mixing. Further work to solve the problem of the model bias may improve the representation of entrainment in climate models.

### **Variability on sub-advective timescales**

The observed advection of property anomalies originating from the DSO demonstrates the connectivity of the basins and deep water masses of the northern North Atlantic.

The coherence of the NADW in the deep limb of the AMOC was investigated on sub-advective timescales by Fischer et al. (2015), in a study associated with OSNAP. This study used moored velocities all along the pathway of the Deep Western Boundary Current, which is the main conduit of NADW in the North Atlantic. The authors demonstrate that topographic Rossby waves, with a period of 10 days (5 days at DS), dominate the variability of the NADW transport in the Irminger and Labrador Seas, on sub-advective timescales (Figure 6.3). The maximum variance is found at longer periods downstream, with peaks in the spectra at Flemish Cap and Grand Banks around 30 days (Figure 6.3). This demonstrates that the topographic Rossby waves are indeed topographically trapped on the continental slope, and therefore are not detected at the Flemish Cap and Grand Banks moorings, which occupy the deep basin (Fischer et al., 2015).

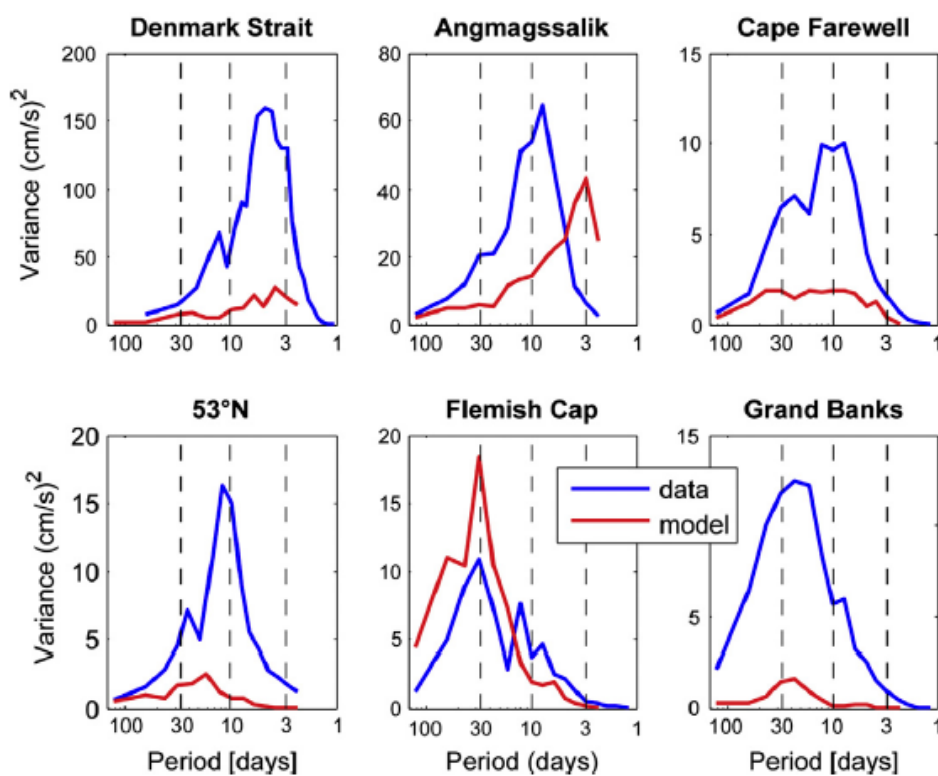


Fig. 6.3 Velocity spectra at mooring arrays in the pathway of the deep boundary current in the subpolar North Atlantic from observations (blue) and a model (red). The arrays are in order of distance downstream from Denmark Strait to Grand Banks. Note the change in scale of the y axis between the different panels. Figure from Fischer et al. (2015): their Figure 13.

### Variability on advective timescales

The sustained seasonal freshening events, characterised for the first time in this study, drive freshening in the deep waters of the central Labrador Sea and in the ISOW (Yashayaev and Dickson, 2008). In their study, Yashayaev and Dickson (2008) used a combination of moored property time series and repeat CTD sections to investigate the advection of water masses and temperature/salinity anomalies in the dense sources of NADW (i.e. the DSO, ISOW, LSW).

Yashayaev and Dickson (2008) showed that negative salinity anomalies in the DSO cause freshening of the ISOW, and appear in the deep ( $> 3000$  m) centre of the Labrador Basin 1 year after passing through ANG (Figure 6.4). Specifically, the property anomalies observed at ANG are advected downstream by the boundary current and are next observed on the southwest Greenland slope, and the eastern Labrador Sea, 3-6 months after, before occurring in the central Labrador Sea a further 6 months later (Figure 6.4), possibly after recirculation of the boundary current into the interior (Clarke and Gascard, 1983). This shows that there is a direct connection between the wind stress forcing north of Denmark Strait (which drive the freshening events) and the property variability in the deep Labrador Sea, and the densest water masses forming NADW (DSO and ISOW), on a 1 - 1.5 year timescale. The contribution of this thesis is therefore highly relevant to the Overturning in the Subpolar North Atlantic Programme (OSNAP); specifically objective three, of five outlined by Lozier et al. (2017), namely to "relate AMOC variability to deep-water mass variability and basin-scale wind forcing".

Moreover, there is a strong case to further investigate the evolution of sustained DSO property anomalies, in order to better understand the evolution of the DSO and how it interacts with ISOW and LSW. As Yashayaev and Dickson (2008) argue in their study, to quantify the rate of mixing between different source water masses of NADW (i.e. LSW, ISOW and the DSO) in different locations, annual CTD sections alone are not adequate, instead mooring observations are required. The evolution of the water masses between ANG and Cape Farewell is vital for the formation of NADW (Dickson and Brown, 1994). The extensive OSNAP observations could be synthesised with concurrent mooring observations upstream (e.g. at ANG and DS) and numerical model simulations to investigate the pathway and evolution of DSO property anomalies. A recent study arising from the OSNAP programme demonstrated that the variability of the AMOC east of Greenland dominates the net volume transport and the variability of the AMOC (Lozier et al., 2019). This places renewed emphasis on understanding the upstream sources of the variability of the volume transport of dense water (i.e. NADW) through the OSNAP line on different timescales, such as the seasonal variability of the DSO investigated in this study.

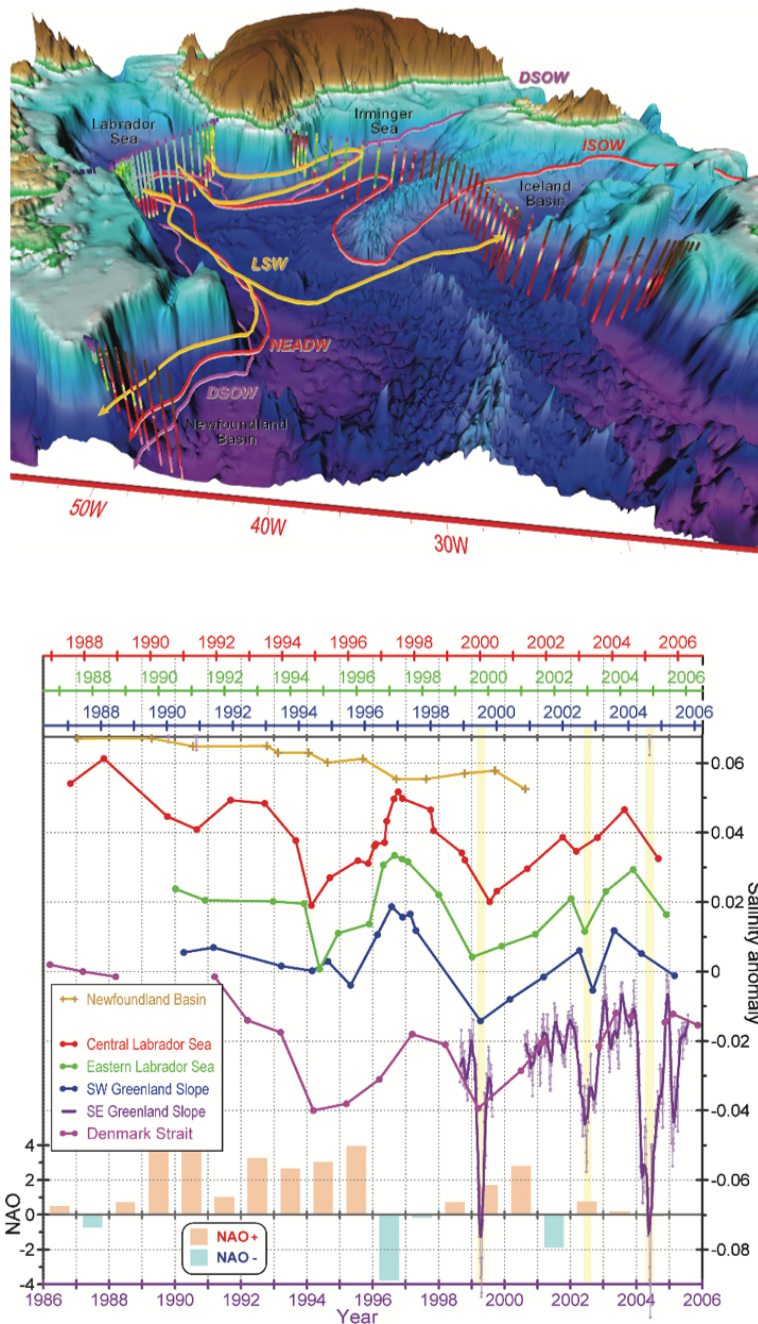


Fig. 6.4 Advection of dense water masses and salinity anomalies in the pathway of NADW source water in the subpolar North Atlantic. Top: schematic map of the pathway of different source water masses of NADW, the acronyms are: DSO Water (DSOW), Iceland Scotland Overflow Water (ISOW), Labrador Sea Water (LSW) and North East Atlantic Deep Water (NEADW), which is a modified form of ISOW. The vertical lines indicate historical CTD stations. Bottom: 1986 to 2006 salinity anomaly time series at different locations within the DSO, from DS to the Newfoundland Basin. Note the time series are associated with different x axes, lagged in time based on the estimated advection time between the observations. The yellow shaded bars indicate negative salinity anomaly events observed at ANG (i.e. the SE Greenland slope). Also shown is a bar graph of the annual NAO index. This figure is adapted from Yashayaev and Dickson (2008): their Figures 21.1 and 21.2.

A number of important research problems could be solved by synthesising the observations of multiple mooring arrays in the pathway of NADW, upstream of Cape Farewell. For example: how do property anomalies evolve between the ANG array and the OSNAP array at Cape Farewell, and what does this reveal about the mixing processes between the DSO and neighbouring water masses in the intervening distance? One approach that could be taken is to examine the transformation of DSO properties along density surfaces (e.g. potential or neutral surfaces) between the arrays, to determine whether anomalies are unchanged, weakened or perhaps mixed out altogether. Furthermore, such an investigation could quantify the effect (if any) of spilling dense Greenland shelf water events on the variability of NADW transport through the OSNAP array at Cape Farewell.

#### **6.1.4 The impacts of future climatic changes**

Climate models predict that the intensity of wind forcing over the east Greenland coast and Iceland will weaken, owing to changes to the North Atlantic storm track (Schwierz et al., 2010). Specifically, the NAO centres of action (presently the Azores high and Icelandic low) are projected to shift northeastward in response to a simulation with increased greenhouse gas forcing (Bacer et al., 2016). This may reduce the number of barrier wind events, which are instigated by the Icelandic low, and positively correlated with the NAO, with its present day centres of action (Harden et al., 2011). In Chapter 4, barrier wind events were shown to cause freshening and enhancement of the Shelfbreak EGC. Therefore, should the number of barrier wind events decrease, the Shelfbreak EGC may weaken around the location of DS as a result. Furthermore, the shifting of the NAO centres of action would change the wind stress curl field in the Blosseville Basin, resulting in changes in the circulation there (Harden et al., 2016). Specifically, the shifting position of the Icelandic low may make the wind stress curl in the Blosseville Basin less negative, and therefore weaken the net volume transport of the Shelfbreak EGC, which may be at a maximum in winter in the present day (Harden et al., 2016) (Figure 6.1).

The volume transport of the DSO on monthly to multi-annual timescales is strongly influenced by the wind driven barotropic transport of DSO source water branches upstream of DS (Köhl et al., 2007). The variability of barotropic transport of the source water branches can cause variability in the height above bottom of the dense water reservoir, which governs the transport of the DSO (Whitehead, 1998). Therefore, future changes to the wind forcing may affect the transport and properties of the DSO.

As demonstrated in this thesis, the sea ice concentration has decreased in an important region of wind forcing of DSO variability, which is part of a larger trend of

sea ice concentration reduction in the Nordic Seas in the past decades (Moore et al., 2015), and this trend is projected to continue (Stroeve et al., 2012) (Figure 6.5). In fact, one third of climate models predict sea ice free conditions in September by the end of the 21st century (Stroeve et al., 2012) (Figure 6.5). Partial sea ice concentration can amplify the momentum transfer from the atmosphere to the ocean by increasing the drag coefficient, as was observed with moorings in the Pacific sector of the Arctic, by Schulze and Pickart (2012), and in the Barents Sea by Elvidge et al. (2016). In this thesis it is argued that reduced sea ice concentration results in weaker effective wind stress, which is connected with weaker wind driven freshening of the DSO downstream. Therefore, should the trend of sea ice concentration reduction continue, this may signal a weakening of the wind driven variability in the ocean circulation in the Blosseville Basin. Further studies, using multiple years of observed and modelled data of the hydrography in the Blosseville Basin, are required to test this theory.

Moreover, the trend of reducing sea ice concentration (Figure 6.5) will expose more of the ocean to the atmosphere in the Nordic Seas in winter months. Whilst this may cause reduced heat fluxes out of the ocean in some locations (Moore et al., 2015), in other locations the heat flux out of the ocean may increase, leading to new locations of dense water formation (Våge et al., 2018). However, the predicted shift of the NAO centres of action in the coming decades (Bacer et al., 2016) may reduce wind speeds in the Iceland and Greenland seas, thus reducing the magnitude of sensible and latent heat fluxes.

Furthermore, as discussed above, another source of DSO is dense water spilling off the Greenland shelf (Brearley et al., 2012; Falina et al., 2012; Koszalka et al., 2013). One of two key mechanisms that cause dense shelf water to cascade is wind forcing, the other being the leading edge of cyclonic eddies (Harden et al., 2014). Should the strength of wind forcing weaken, the contribution of dense shelf water to the DSO might also decrease. Therefore, a weakening of wind forcing in this region may reduce DSO transports in two ways: by reducing the geostrophic transports of the EGC, and by reducing the frequency and/or intensity of spilling of dense shelf water.

However, Köhl et al. (2007) argue that the DSO transport variability on longer timescales (i.e. multi-annual) is dominated by the variability of the height of 27.8 kg m<sup>-3</sup> isopycnal (dense water reservoir) above bottom, to the north of DS. The density gradient between north and south of the sill is associated with a pressure gradient force which drives the volume transport of the DSO (Whitehead, 1998). Whilst the wind-driven barotropic transport contributes to the variability of the reservoir height, other mechanisms are also important Köhl et al. (2007). One key mechanism is the variability of the freshwater budget in the Arctic Ocean. Curry and Mauritzen (2005) describe the

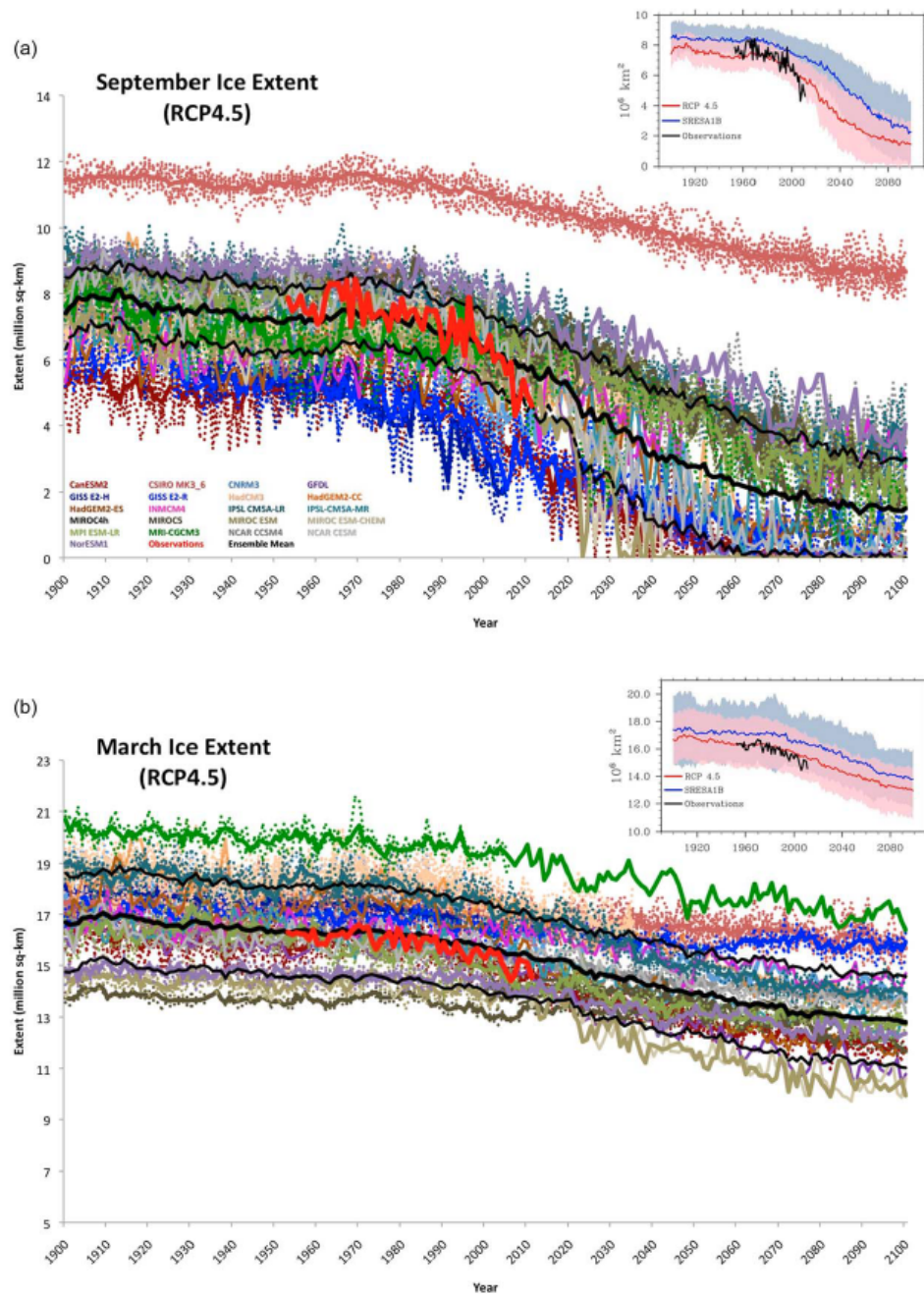


Fig. 6.5 Time series of modelled (coloured lines) and observed (thick red line) sea ice extent in the Arctic in March (top panel) and September (bottom panel) from 1900 to 2100. The model time series are CMIP5 models externally forced by the Representative Concentration Pathway 4.5 (RCP4.5). The coloured dots are the model ensemble member time series, whilst the coloured lines are the individual model ensemble mean time series. The inset panels show the multi-model ensemble mean ( $\pm$  standard deviation) of the CMIP3 time series (externally forced by the business as usual scenario) in blue and the CMIP5 time series in red, with the observational time series shown by the black line. Figure from Stroeve et al. (2012); their Figure 2.

increase in freshwater in the Nordic Seas in the second half of the twentieth century, owing to increased input of freshwater from the Arctic Ocean and into the Nordic Seas, via Fram Strait. If the rate of freshening in the Nordic Seas in the 20th century, described by Curry and Mauritzen (2005), were to resume as a result of increased glacial runoff from Greenland, the DSO is likely to weaken (due to density reduction of the source water and associated reduction of reservoir height), but not for another century at least.

The formation of NADW may be sensitive to large scale surface temperature changes in key dense water formation regions (i.e. the Nordic Seas and Labrador Sea), where temperatures at the ocean and atmospheric surface have increased since 1901 (Rahmstorf et al., 2015). Warming of the surface air temperatures is expected to reduce the amount of heat lost from the ocean, increasing the buoyancy of the ocean surface, and thus reducing the formation of NADW through deep convection and weakening the intermediate and deep limbs of the AMOC (Gregory et al., 2005). These large scale changes to surface temperatures might also change the stratification of the water column, thus affecting the formation of NADW and the strength of the AMOC. Marzeion et al. (2007) argue that, in future, the stratification between the upper 1500 m of the water column and the deep water in high latitudes of the Atlantic Ocean will increase, thus decreasing the amount of vertical diffusion and leading to a reduction in the AMOC. The authors comment that the dependence of AMOC on vertical diffusion is poorly understood at present (Marzeion et al., 2007). Therefore, future work could concentrate on this relationship, perhaps by utilising the unique, near 30 year ANG time series of NADW variability.

The climate in the Arctic and Subpolar North Atlantic is changing rapidly; sea ice is decreasing, increased volumes of glacial meltwater are entering the ocean from Greenland each year, and atmospheric patterns are changing. In this thesis, the DSO was shown to exhibit a statistically significant seasonal salinity cycle, which was linked to atmospheric and sea ice concentration variability driving changes to the ocean circulation around 200 km north of DS. This demonstrates a direct connection between atmospheric and sea ice variability north of DS, and the variability of DSO properties. Therefore, future changes in the ocean circulation north of DS, driven by the climatic changes identified above, may have direct consequences for the DSO, and therefore could be a focus of future work.

## 6.2 Conclusions

1. Observations on the Greenland slope 500 km downstream of DS, at ANG, show that the DSO exhibits a (statistically significant) seasonal salinity cycle, with

maximum in December and minimum in May. The peak to trough amplitude is 0.02, which exceeds the standard deviation (0.016) of the low pass filtered and de-trended time series.

2. Sustained winter-spring freshening of the DSO is intensified in lighter density classes of the DSO and likely originates from fresh lids, found in lighter components of DSO, observed in CTD crossings of DS, but missed by mooring observations hitherto. Future observational efforts to monitor the variability of the DSO at DS should include measurements of lighter classes of DSO.
3. Wintertime barrier wind events induce coastal Ekman downwelling and Ekman pumping over the east Greenland continental margin, to the north of DS. This, in turn, leads to freshening of the Shelfbreak EGC, and contributes to the sustained seasonal freshening of the DSO at ANG.
4. The volume transport of the Shelfbreak EGC was enhanced in winter 2011-12, which was associated with a 63% increase in the volume transport of fresh ( $S < 34.9$ ) water found in the pycnocline, above the RAW, in the Shelfbreak EGC. This mechanism can explain approximately 50% of the salinity seasonality of the DSO at ANG.
5. The DSO salinity is strongly controlled by the northerly/northeasterly along-shore wind forcing over the East Greenland shelfbreak in the northern Blosseville Basin, around  $70^{\circ}\text{N}$ , 2-3 months prior, via the above mechanisms. Both the ILD and NAO patterns influence the salinity variability of the DSO, with the former dominating between 2005 and 2009 and the latter dominating between 2010 and 2014.
6. Sea ice concentration modulates the transfer of momentum from atmosphere to ocean in the wind forcing regions, with maximum effective wind stress occurring over the Marginal Ice Zone (MIZ) where the sea ice concentration is between 55% and 75%. The reduction of sea ice concentration in the northern Blosseville Basin between 1998 and 2015 has reduced the effective wind stress there, and this may have resulted in weaker DSO freshening events later on in the time series, despite strong wind forcing.



# Abbreviations

<b>AAW</b>	Arctic Atlantic Water
<b>ADCP</b>	Acoustic Doppler Current Profiler
<b>AIW</b>	Arctic Intermediate Water
<b>AMOC</b>	Atlantic Meridional Overturning Circulation
<b>ANG</b>	Angmagssalik
<b>CTD</b>	Conductivity Temperature Depth
<b>DS</b>	Denmark Strait
<b>DSO</b>	Denmark Strait Overflow
<b>EGC</b>	East Greenland Current
<b>EOF</b>	Empirical Orthogonal Function
<b>FX9</b>	Faxaflói CTD station 9
<b>ILD</b>	Iceland Lofoten Difference
<b>ISO</b>	Iceland Scotland Overflow
<b>ISOW</b>	Iceland Scotland Overflow Water
<b>KGA</b>	Kögur array
<b>LSW</b>	Labrador Sea Water
<b>MC</b>	MicroCAT
<b>MIW</b>	Middle Irminger Water
<b>MOC</b>	Meridional Overturning Circulation

<b>NAC</b>	North Atlantic Current
<b>NADW</b>	North Atlantic Deep Water
<b>NAO</b>	North Atlantic Oscillation
<b>NIJ</b>	North Icelandic Jet
<b>OSNAP</b>	Overturning in the Subpolar North Atlantic Programme
<b>PC</b>	Principal Component
<b>PSW</b>	Polar Surface Water
<b>PW</b>	Polar Water
<b>RAW</b>	Returning Atlantic Water
<b>RCM</b>	Rotor Current Meter
<b>SST</b>	Sea Surface Temperature

# References

- Aagaard, K., Swift, J., and Carmack, E. (1985). Thermohaline circulation in the arctic mediterranean seas. *Journal of Geophysical Research: Oceans*, 90(C3):4833–4846.
- Alley, R. B. and Clark, P. U. (1999). The deglaciation of the northern hemisphere: a global perspective. *Annual Review of Earth and Planetary Sciences*, 27(1):149–182.
- Arndt, J. E., Schenke, H. W., Jakobsson, M., Nitsche, F. O., Buys, G., Goleby, B., Rebesco, M., Bohoyo, F., Hong, J., Black, J., et al. (2013). The international bathymetric chart of the southern ocean (ibcs) version 1.0 - a new bathymetric compilation covering circum-antarctic waters. *Geophysical Research Letters*, 40(12):3111–3117.
- Bacer, S., Christoudias, T., and Pozzer, A. (2016). Projection of north atlantic oscillation and its effect on tracer transport. *Atmospheric Chemistry and Physics*, 16(24):15581.
- Bakker, P., Schmittner, A., Lenaerts, J., Abe-Ouchi, A., Bi, D., van den Broeke, M., Chan, W.-L., Hu, A., Beadling, R., Marsland, S., et al. (2016). Fate of the atlantic meridional overturning circulation: Strong decline under continued warming and greenland melting. *Geophysical Research Letters*, 43(23):12–252.
- Baringer, M. O. and Price, J. F. (1997). Mixing and spreading of the mediterranean outflow. *Journal of Physical Oceanography*, 27(8):1654–1677.
- Berx, B., Hansen, B., Østerhus, S., Larsen, K., Sherwin, T., and Jochumsen, K. (2013). Combining in-situ measurements and altimetry to estimate volume, heat and salt transport variability through the faroe shetland channel. *Ocean Science Discussions*, 10(1).
- Booth, B. B., Dunstone, N. J., Halloran, P. R., Andrews, T., and Bellouin, N. (2012). Aerosols implicated as a prime driver of twentieth-century north atlantic climate variability. *Nature*, 484(7393):228–232.
- Brakstad, A., Våge, K., Håvik, L., and Moore, G. (2019). Water mass transformation in the greenland sea during the period 1986–2016. *Journal of Physical Oceanography*, 49(1):121–140.
- Brearely, J. A., Pickart, R. S., Valdimarsson, H., Jonsson, S., Schmitt, R. W., and Haine, T. W. (2012). The east greenland boundary current system south of denmark strait. *Deep Sea Research Part I: Oceanographic Research Papers*, 63:1–19.
- Briem, J., Danielsen, M., Gíslason, O., Sveinbjörnsson, S., Sigurðarsson, B., Stefánsson, A., Ólafsson, G., and Gunnarsson, S. (2000). Hydrographic cruise report: B14-2000 (nov/dec 2000). Technical report, Marine Research Institute Iceland.
- Broecker, W. S., Bond, G., Klas, M., Bonani, G., and Wolfli, W. (1990). A salt oscillator in the glacial atlantic? 1. the concept. *Paleoceanography*, 5(4):469–477.

- Bryden, H. L., Longworth, H. R., and Cunningham, S. A. (2005). Slowing of the atlantic meridional overturning circulation at 25 n. *Nature*, 438(7068):655–657.
- Buckley, M. W. and Marshall, J. (2016). Observations, inferences, and mechanisms of the atlantic meridional overturning circulation: A review. *Reviews of Geophysics*, 54(1):5–63.
- Caesar, L., Rahmstorf, S., Robinson, A., Feulner, G., and Saba, V. (2018). Observed fingerprint of a weakening atlantic ocean overturning circulation. *Nature*, 556(7700):191–196.
- Cheng, W., Chiang, J. C., and Zhang, D. (2013). Atlantic meridional overturning circulation (amoc) in cmip5 models: Rcp and historical simulations. *Journal of Climate*, 26(18):7187–7197.
- Clarke, R. A. and Gascard, J.-C. (1983). The formation of labrador sea water. part i: Large-scale processes. *Journal of Physical Oceanography*, 13(10):1764–1778.
- Clement, A., Bellomo, K., Murphy, L. N., Cane, M. A., Mauritsen, T., Rädcl, G., and Stevens, B. (2015). The atlantic multidecadal oscillation without a role for ocean circulation. *Science*, 350(6258):320–324.
- Codiga, D. L. (2011). Unified tidal analysis and prediction using the utide matlab functions.
- Collins, M., Knutti, R., Arblaster, J., Dufresne, J.-L., Fichet, T., Friedlingstein, P., Gao, X., Gutowski, W. J., Johns, T., Krinner, G., et al. (2013). Long-term climate change: projections, commitments and irreversibility. In *Climate Change 2013-The Physical Science Basis: Contribution of Working Group I to the Fifth Assessment Report of the Intergovernmental Panel on Climate Change*, pages 1029–1136. Cambridge University Press.
- Curry, R. and Mauritzen, C. (2005). Dilution of the northern north atlantic ocean in recent decades. *Science*, 308(5729):1772–1774.
- Danabasoglu, G., Large, W. G., and Briegleb, B. P. (2010). Climate impacts of parameterized nordic sea overflows. *Journal of Geophysical Research: Oceans*, 115(C11).
- de Steur, L., Pickart, R. S., Macrander, A., Våge, K., Harden, B., Jónsson, S., Østerhus, S., and Valdimarsson, H. (2017). Liquid freshwater transport estimates from the east greenland current based on continuous measurements north of denmark strait. *Journal of Geophysical Research: Oceans*, 122(1):93–109.
- Dickson, B., Dye, S., Jónsson, S., Köhl, A., Macrander, A., Marnela, M., Meincke, J., Olsen, S., Rudels, B., Valdimarsson, H., et al. (2008). The overflow flux west of iceland: variability, origins and forcing. In *Arctic-Subarctic Ocean Fluxes*, pages 443–474. Springer.
- Dickson, B., Yashayaev, I., Meincke, J., Turrell, B., Dye, S., and Holfort, J. (2002). Rapid freshening of the deep north atlantic ocean over the past four decades. *Nature*, 416(6883):832–837.
- Dickson, R. R. and Brown, J. (1994). The production of north atlantic deep water: sources, rates, and pathways. *Journal of Geophysical Research: Oceans*, 99(C6):12319–12341.

- DiNezio, P. N., Gramer, L. J., Johns, W. E., Meinen, C. S., and Baringer, M. O. (2009). Observed interannual variability of the florida current: Wind forcing and the north atlantic oscillation. *Journal of Physical Oceanography*, 39(3):721–736.
- Eastwood, S., Lavergne, T., and Tonboe, R. (2014). Algorithm theoretical basis document for the osi saf global reprocessed sea ice concentration product. *EUMETSAT Network Satellite Application Facilities*.
- Elvidge, A., Renfrew, I., Weiss, A., Brooks, I., Lachlan-Cope, T., and King, J. (2016). Observations of surface momentum exchange over the marginal ice zone and recommendations for its parametrisation. *Atmospheric Chemistry and Physics*, 16:1545–1563.
- Falina, A., Sarafanov, A., Mercier, H., Lherminier, P., Sokov, A., and Daniault, N. (2012). On the cascading of dense shelf waters in the iringinger sea. *Journal of Physical Oceanography*, 42(12):2254–2267.
- Ferrari, R., Mashayek, A., McDougall, T. J., Nikurashin, M., and Campin, J.-M. (2016). Turning ocean mixing upside down. *Journal of Physical Oceanography*, 46(7):2239–2261.
- Fischer, J., Karstensen, J., Zantopp, R., Visbeck, M., Biastoch, A., Behrens, E., Böning, C. W., Quadfasel, D., Jochumsen, K., Valdimarsson, H., et al. (2015). Intra-seasonal variability of the dwbc in the western subpolar north atlantic. *Progress in Oceanography*, 132:233–249.
- Fogelqvist, E., Blindheim, J., Tanhua, T., Østerhus, S., Buch, E., and Rey, F. (2003). Greenland–scotland overflow studied by hydro-chemical multivariate analysis. *Deep Sea Research Part I: Oceanographic Research Papers*, 50(1):73–102.
- Fraser, A. D., Massom, R. A., Ohshima, K. I., Willmes, S., Kappes, P. J., Cartwright, J., and Porter-Smith, R. (2020). High-resolution mapping of circum-antarctic landfast sea ice distribution, 2000–2018. *Earth System Science Data*, 12(4):2987–2999.
- Freitag, H., McCarty, M., Nosse, C., Lukas, R., McPhaden, M., and Cronin, M. (1999). Coare seacat data: Calibrations and quality control procedures. *NOAA Tech. Memo. ERL PMEL*, 115:89.
- Garabato, A. C. N., Williams, A. P., and Bacon, S. (2014). The three-dimensional overturning circulation of the southern ocean during the woce era. *Progress in Oceanography*, 120:41–78.
- Garraffo, Z. D., Johns, W. E., Chassignet, E. P., and Goni, G. J. (2003). North brazil current rings and transport of southern waters in a high resolution numerical simulation of the north atlantic. In *Elsevier Oceanography Series*, volume 68, pages 375–409. Elsevier.
- Garzoli, S. L. and Matano, R. (2011). The south atlantic and the atlantic meridional overturning circulation. *Deep Sea Research Part II: Topical Studies in Oceanography*, 58(17-18):1837–1847.
- Gelderloos, R., Haine, T. W., and Almansi, M. (2021). Coastal trapped waves and other subinertial variability along the southeast greenland coast in a realistic numerical simulation. *Journal of Physical Oceanography*, 51(3):861–877.

- Gill, A. E. (1982). *Atmosphere-Ocean Dynamics*. Academic Press.
- Goni, G. J. and Johns, W. E. (2001). A census of north brazil current rings observed from topex/poseidon altimetry: 1992–1998. *Geophysical Research Letters*, 28(1):1–4.
- González-Pola, C., Larsen, K., Fratantoni, P., and Beszczynska-Moller, A. (2019). Ices report on ocean climate 2018. *ICES Cooperative Research Report*, (349).
- Gregory, J., Dixon, K., Stouffer, R., Weaver, A., Driesschaert, E., Eby, M., Fichefet, T., Hasumi, H., Hu, A., Jungclaus, J., et al. (2005). A model intercomparison of changes in the atlantic thermohaline circulation in response to increasing atmospheric co2 concentration. *Geophysical Research Letters*, 32(12).
- Hall, S., Dye, S., Heywood, K., and Wadley, M. (2011). Wind forcing of salinity anomalies in the denmark strait overflow. *Ocean Science*, 7(6):821–834.
- Hannachi, A., Jolliffe, I. T., and Stephenson, D. B. (2007). Empirical orthogonal functions and related techniques in atmospheric science: A review. *International Journal of Climatology: A Journal of the Royal Meteorological Society*, 27(9):1119–1152.
- Hansen, B., Hátún, H., Kristiansen, R., Olsen, S., and Østerhus, S. (2010). Stability and forcing of the iceland-faroe inflow of water, heat, and salt to the arctic. *Ocean Science Discussions*, 7(4).
- Hansen, B., Larsen, K. M. H., Hátún, H., and Østerhus, S. (2016). A stable faroe bank channel overflow 1995-2015. *Ocean Science*, 12(6):1205.
- Hansen, B. and Østerhus, S. (2000). North atlantic–nordic seas exchanges. *Progress in oceanography*, 45(2):109–208.
- Harden, B., Renfrew, I., and Petersen, G. (2011). A climatology of wintertime barrier winds off southeast greenland. *Journal of Climate*, 24(17):4701–4717.
- Harden, B. E., Pickart, R. S., and Renfrew, I. A. (2014). Offshore transport of dense water from the east greenland shelf. *Journal of Physical Oceanography*, 44(1):229–245.
- Harden, B. E., Pickart, R. S., Valdimarsson, H., Våge, K., de Steur, L., Richards, C., Bahr, F., Torres, D., Børve, E., Jónsson, S., et al. (2016). Upstream sources of the denmark strait overflow: Observations from a high-resolution mooring array. *Deep Sea Research Part I: Oceanographic Research Papers*, 112:94–112.
- Harvey, J. (1961). Overflow of cold deep water across iceland–greenland ridge. *Nature*, 189(4768):911–913.
- Håvik, L., Almansi, M., Våge, K., and Haine, T. W. (2019). Atlantic-origin overflow water in the east greenland current. *Journal of Physical Oceanography*, 49(9):2255–2269.
- Håvik, L., Pickart, R. S., Våge, K., Torres, D., Thurnherr, A. M., Beszczynska-Möller, A., Walczowski, W., and von Appen, W.-J. (2017). Evolution of the east greenland current from fram strait to denmark strait: synoptic measurements from summer 2012. *Journal of Geophysical Research: Oceans*, 122(3):1974–1994.

- Håvik, L. and Våge, K. (2018). Wind-driven coastal upwelling and downwelling in the shelfbreak east greenland current. *Journal of Geophysical Research: Oceans*, 123(9):6106–6115.
- Hawkins, E. and Sutton, R. (2009). The potential to narrow uncertainty in regional climate predictions. *Bulletin of the American Meteorological Society*, 90(8):1095–1108.
- Henry, L., McManus, J., Curry, W., Roberts, N., Piotrowski, A., and Keigwin, L. (2016). North atlantic ocean circulation and abrupt climate change during the last glaciation. *Science*, 353(6298):470–474.
- Hersbach, H., Bell, B., Berrisford, P., Hirahara, S., Horányi, A., Muñoz-Sabater, J., Nicolas, J., Peubey, C., Radu, R., Schepers, D., et al. (2020). The era5 global reanalysis. *Quarterly Journal of the Royal Meteorological Society*.
- Hogg, N. G. (1992). On the transport of the gulf stream between cape hatteras and the grand banks. *Deep Sea Research Part A. Oceanographic Research Papers*, 39(7-8):1231–1246.
- Holfort, J. and Albrecht, T. (2007). Atmospheric forcing of salinity in the overflow of denmark strait. *Ocean Science*, 3(3):411–416.
- Holliday, N. P., Hughes, S., Bacon, S., Beszczynska-Möller, A., Hansen, B., Lavin, A., Loeng, H., Mork, K., Østerhus, S., Sherwin, T., et al. (2008). Reversal of the 1960s to 1990s freshening trend in the northeast north atlantic and nordic seas. *Geophysical Research Letters*, 35(3).
- Hummels, R., Brandt, P., Dengler, M., Fischer, J., Araujo, M., Veleda, D., and Durgadoo, J. V. (2015). Interannual to decadal changes in the western boundary circulation in the atlantic at 11 s. *Geophysical Research Letters*, 42(18):7615–7622.
- Hurrell, J. W. (1995). Decadal trends in the north atlantic oscillation: regional temperatures and precipitation. *Science*, 269(5224):676–679.
- Jackson, L., Kahana, R., Graham, T., Ringer, M., Woollings, T., Mecking, J., and Wood, R. (2015). Global and european climate impacts of a slowdown of the amoc in a high resolution gcm. *Climate dynamics*, 45(11-12):3299–3316.
- Jacobs, S. S., Amos, A. F., and Bruchhausen, P. M. (1970). Ross sea oceanography and antarctic bottom water formation. In *Deep Sea Research and Oceanographic Abstracts*, volume 17, pages 935–962. Elsevier.
- Jahnke-Bornemann, A. (2019). Iceland-Lofotes-Difference-Index (ILD) 1957-2017 (Version 1.0.0).
- Jahnke-Bornemann, A. and Brümmer, B. (2008). The iceland - lofotes pressure difference: different states of the north atlantic low-pressure zone. *Tellus A: Dynamic Meteorology and Oceanography*, 61(4):466–475.
- Jeansson, E., Olsen, A., and Jutterström, S. (2017). Arctic intermediate water in the nordic seas, 1991–2009. *Deep Sea Research Part I: Oceanographic Research Papers*, 128:82–97.

- Jochum, M. and Malanotte-Rizzoli, P. (2003). On the generation of north brazil current rings. *Journal of Marine research*, 61(2):147–173.
- Jochumsen, K., Köllner, M., Quadfasel, D., Dye, S., Rudels, B., and Valdimarsson, H. (2015). On the origin and propagation of denmark strait overflow water anomalies in the irvinger basin. *Journal of Geophysical Research: Oceans*, 120(3):1841–1855.
- Jochumsen, K., Moritz, M., Nunes, N., Quadfasel, D., Larsen, K. M., Hansen, B., Valdimarsson, H., and Jonsson, S. (2017). Revised transport estimates of the denmark strait overflow. *Journal of Geophysical Research: Oceans*.
- Jochumsen, K., Quadfasel, D., Valdimarsson, H., and Jónsson, S. (2012). Variability of the denmark strait overflow: Moored time series from 1996–2011. *Journal of Geophysical Research: Oceans*, 117(C12).
- Johns, W. E., Shay, T., Bane, J., and Watts, D. (1995). Gulf stream structure, transport, and recirculation near 68 w. *Journal of Geophysical Research: Oceans*, 100(C1):817–838.
- Johnson, G. C. (2008). Quantifying antarctic bottom water and north atlantic deep water volumes. *Journal of Geophysical Research: Oceans*, 113(C5).
- Jones, E. P. (2001). Circulation in the arctic ocean. *Polar Research*, 20(2):139–146.
- Jones, P. D., Jónsson, T., and Wheeler, D. (1997). Extension to the north atlantic oscillation using early instrumental pressure observations from gibraltar and south-west iceland. *International Journal of Climatology: A Journal of the Royal Meteorological Society*, 17(13):1433–1450.
- Jones, S. and Read, J. (1993). *Ministry of Agriculture, Fisheries and Food current meter system and data inventory, 1987-89*. Citeseer.
- Jónsson, S. and Valdimarsson, H. (2004). A new path for the denmark strait overflow water from the iceland sea to denmark strait. *Geophysical Research Letters*, 31(3).
- Jónsson, S. and Valdimarsson, H. (2012). Hydrography and circulation over the southern part of the kolbeinsey ridge. *ICES Journal of Marine Science*, 69(7):1255–1262.
- Joyce, T. (1988). The woce hydrographic program. *Eos, Transactions American Geophysical Union*, 69(5):68–70.
- Jungclaus, J. H., Hauser, J., and Käse, R. H. (2001). Cyclogenesis in the denmark strait overflow plume. *Journal of Physical Oceanography*, 31(11):3214–3229.
- Kageyama, M., Mignot, J., Swingedouw, D., Marzin, C., Alkama, R., and Marti, O. (2009). Glacial climate sensitivity to different states of the atlantic meridional overturning circulation: results from the ipsl model. *Climate of the Past*, 5(3):551–570.
- Kang, S. M., Seager, R., Frierson, D. M., and Liu, X. (2015). Croll revisited: Why is the northern hemisphere warmer than the southern hemisphere? *Climate Dynamics*, 44(5-6):1457–1472.

- Kanzow, T., Cunningham, S., Johns, W. E., Hirschi, J. J., Marotzke, J., Baringer, M., Meinen, C., Chidichimo, M., Atkinson, C., Beal, L., et al. (2010). Seasonal variability of the atlantic meridional overturning circulation at 26.5 n. *Journal of Climate*, 23(21):5678–5698.
- Kanzow, T., Send, U., Zenk, W., Chave, A. D., and Rhein, M. (2006). Monitoring the integrated deep meridional flow in the tropical north atlantic: Long-term performance of a geostrophic array. *Deep Sea Research Part I: Oceanographic Research Papers*, 53(3):528–546.
- Kanzow, T. and Zenk, W. (2014). Structure and transport of the iceland scotland overflow plume along the reykjanes ridge in the iceland basin. *Deep Sea Research Part I: Oceanographic Research Papers*, 86:82–93.
- Karstensen, J. (2013). Overflow, circulation & biodiversity cruise no. m85/2.
- Keeling, R. F., Körtzinger, A., and Gruber, N. (2010). Ocean deoxygenation in a warming world. *Annual review of marine science*, 2:199–229.
- Köhl, A., Käse, R. H., Stammer, D., and Serra, N. (2007). Causes of changes in the denmark strait overflow. *Journal of physical oceanography*, 37(6):1678–1696.
- Koszalka, I. M., Haine, T. W., and Magaldi, M. G. (2013). Fates and travel times of denmark strait overflow water in the irminger basin. *Journal of Physical Oceanography*, 43(12):2611–2628.
- Koszalka, I. M., Haine, T. W., and Magaldi, M. G. (2017). Mesoscale mixing of the denmark strait overflow in the irminger basin. *Ocean Modelling*, 112:90–98.
- Kundu, P. K. (1976). Ekman veering observed near the ocean bottom. *Journal of Physical Oceanography*, 6(2):238–242.
- Lavender, K. L., Davis, R. E., and Owens, W. B. (2000). Mid-depth recirculation observed in the interior labrador and irminger seas by direct velocity measurements. *Nature*, 407(6800):66–69.
- Legg, S., Briegleb, B., Chang, Y., Chassignet, E. P., Danabasoglu, G., Ezer, T., Gordon, A. L., Griffies, S., Hallberg, R., Jackson, L., et al. (2009). Improving oceanic overflow representation in climate models: the gravity current entrainment climate process team. *Bulletin of the American Meteorological Society*, 90(5):657–670.
- Lin, P., Pickart, R. S., Jochumsen, K., Moore, G., Valdimarsson, H., Fristedt, T., and Pratt, L. J. (2020). Kinematic structure and dynamics of the denmark strait overflow from ship-based observations. *Journal of physical oceanography*, 50(11):3235–3251.
- Lozier, M., Bacon, S., Bower, A. S., Cunningham, S. A., Femke de Jong, M., De Steur, L., deYoung, B., Fischer, J., Gary, S. F., Greenan, B. J., et al. (2017). Overturning in the subpolar north atlantic program: A new international ocean observing system. *Bulletin of the American Meteorological Society*, 98(4):737–752.
- Lozier, M., Li, F., Bacon, S., Bahr, F., Bower, A., Cunningham, S., De Jong, M., De Steur, L., Deyoung, B., Fischer, J., et al. (2019). A sea change in our view of overturning in the subpolar north atlantic. *Science*, 363(6426):516–521.

- Lu, P., Li, Z., Cheng, B., and Leppäranta, M. (2011). A parameterization of the ice-ocean drag coefficient. *Journal of Geophysical Research: Oceans*, 116(C7).
- Lüpkes, C. and Birnbaum, G. (2005). Surface drag in the arctic marginal sea-ice zone: a comparison of different parameterisation concepts. *Boundary-layer meteorology*, 117(2):179–211.
- Macrandar, A., Send, U., Valdimarsson, H., Jónsson, S., and Käse, R. H. (2005). Interannual changes in the overflow from the nordic seas into the atlantic ocean through denmark strait. *Geophysical Research Letters*, 32(6).
- Mahajan, S., Zhang, R., and Delworth, T. L. (2011). Impact of the atlantic meridional overturning circulation (amoc) on arctic surface air temperature and sea ice variability. *Journal of Climate*, 24(24):6573–6581.
- Malmberg, S.-A. (1983). Hydrographic investigations in the iceland and greenland seas in late winter 1971-deep water project. *Jokull Reykjavik*, 33:133–140.
- Malmberg, S.-A., Mortensen, J., and Jónsson, S. (2001). Oceanic fluxes in icelandic waters. *ICES CM*.
- Manabe, S. and Stouffer, R. (1988). Two stable equilibria of a coupled ocean-atmosphere model. *Journal of Climate*, 1(9):841–866.
- Marshall, J. and Speer, K. (2012). Closure of the meridional overturning circulation through southern ocean upwelling. *Nature Geoscience*, 5(3):171–180.
- Martin, T., Steele, M., and Zhang, J. (2014). Seasonality and long-term trend of arctic ocean surface stress in a model. *Journal of Geophysical Research: Oceans*, 119(3):1723–1738.
- Marzeion, B., Levermann, A., and Mignot, J. (2007). The role of stratification-dependent mixing for the stability of the atlantic overturning in a global climate model. *Journal of physical oceanography*, 37(11):2672–2681.
- Mastropole, D., Pickart, R. S., Valdimarsson, H., Våge, K., Jochumsen, K., and Girton, J. (2017). On the hydrography of denmark strait. *Journal of Geophysical Research: Oceans*, 122(1):306–321.
- Mauritzen, C. (1996). Production of dense overflow waters feeding the north atlantic across the greenland-scotland ridge. part 1: Evidence for a revised circulation scheme. *Deep Sea Research Part I: Oceanographic Research Papers*, 43(6):769–806.
- McCarthy, G., Smeed, D., Johns, W. E., Frajka-Williams, E., Moat, B., Rayner, D., Baringer, M., Meinen, C., Collins, J., and Bryden, H. (2015). Measuring the atlantic meridional overturning circulation at 26 n. *Progress in Oceanography*, 130:91–111.
- McCartney, M. S. (1992). Recirculating components to the deep boundary current of the northern north atlantic. *Progress in Oceanography*, 29(4):283–383.
- McDougall, T. J. and Barker, P. M. (2011). Getting started with teos-10 and the gibbs seawater (gsw) oceanographic toolbox. *SCOR/IAPSO WG*, 127:1–28.
- Meinen, C. S., Garzoli, S. L., Perez, R. C., Campos, E., Piola, A. R., Chidichimo, M. P., Dong, S., and Sato, O. T. (2017). Characteristics and causes of deep western boundary current transport variability at 34.5 s during 2009-2014.

- Menziel, L., Timmermann, A., Friedrich, T., and England, M. (2014). Hindcasting the continuum of dansgaard-oeschger variability: mechanisms, patterns and timing. *Climate of the Past*, 10(1).
- Mielke, C., Frajka-Williams, E., and Baehr, J. (2013). Observed and simulated variability of the amoc at 26 n and 41 n. *Geophysical research letters*, 40(6):1159–1164.
- Moore, G., Renfrew, I., and Pickart, R. S. (2012). Spatial distribution of air-sea heat fluxes over the sub-polar north atlantic ocean. *Geophysical Research Letters*, 39(18).
- Moore, G. W. K., Våge, K., Pickart, R. S., and Renfrew, I. A. (2015). Decreasing intensity of open-ocean convection in the greenland and iceland seas. *Nature Climate Change*, 5(9):877–882.
- Muir, L. and Fedorov, A. (2015). How the amoc affects ocean temperatures on decadal to centennial timescales: the north atlantic versus an interhemispheric seesaw. *Climate Dynamics*, 45(1-2):151–160.
- Myers, P. G., Kulan, N., and Ribergaard, M. H. (2007). Irminger water variability in the west greenland current. *Geophysical Research Letters*, 34(17).
- Nansen, F. (1902). Oceanography of the north polar basin. the norwegian north polar expedition 1893–1896. scientific results 9 (3): 427.
- Padman, L. and Erofeeva, S. (2004). A barotropic inverse tidal model for the arctic ocean. *Geophysical Research Letters*, 31(2).
- Pickart, R. S., Torres, D. J., and Clarke, R. A. (2002). Hydrography of the labrador sea during active convection. *Journal of Physical Oceanography*, 32(2):428–457.
- Pickart, R. S., Torres, D. J., and Fratantoni, P. S. (2005). The east greenland spill jet. *Journal of Physical Oceanography*, 35(6):1037–1053.
- Pingree, R. and Le Cann, B. (1989). Celtic and armorican slope and shelf residual currents. *Progress in Oceanography*, 23(4):303–338.
- Pinto, J. G., Zacharias, S., Fink, A. H., Leckebusch, G. C., and Ulbrich, U. (2009). Factors contributing to the development of extreme north atlantic cyclones and their relationship with the nao. *Climate dynamics*, 32(5):711–737.
- Price, J. F. and Baringer, M. O. (1994). Outflows and deep water production by marginal seas. *Progress in Oceanography*, 33(3):161–200.
- Quadfasel, D. and Käse, R. H. (2007). Present-day manifestation of the nordic seas overflows. In *Natural Gas Hydrates-Occurrence, Distribution and Detection* (ed. CK Paull and WP Dillon) American Geophysical Union, volume 173, pages 75–89. American Geophysical Union.
- Rahmstorf, S., Box, J. E., Feulner, G., Mann, M. E., Robinson, A., Rutherford, S., and Schaffernicht, E. J. (2015). Exceptional twentieth-century slowdown in atlantic ocean overturning circulation. *Nature climate change*, 5(5):475.
- Read, J. and Pollard, R. (1992). Water masses in the region of the iceland–faeroes front. *Journal of Physical Oceanography*, 22(11):1365–1378.

- Reintges, A., Martin, T., Latif, M., and Keenlyside, N. S. (2017). Uncertainty in twenty-first century projections of the atlantic meridional overturning circulation in cmip3 and cmip5 models. *Climate Dynamics*, 49(5-6):1495–1511.
- Roach, A., Aagaard, K., Pease, C., Salo, S., Weingartner, T., Pavlov, V., and Kulakov, M. (1995). Direct measurements of transport and water properties through the bering strait. *Journal of Geophysical Research: Oceans*, 100(C9):18443–18457.
- Rosby, T. (1996). The north atlantic current and surrounding waters: At the crossroads. *Reviews of Geophysics*, 34(4):463–481.
- Rudels, B. (1989). The formation of polar surface water, the ice export and the exchanges through the fram strait. *Progress in oceanography*, 22(3):205–248.
- Rudels, B., Fahrbach, E., Meincke, J., Budéus, G., and Eriksson, P. (2002). The east greenland current and its contribution to the denmark strait overflow. *ICES Journal of Marine Science*, 59(6):1133–1154.
- Rudels, B., Jones, E., Anderson, L., and Kattner, G. (1994). On the intermediate depth waters of the arctic ocean. *The polar oceans and their role in shaping the global environment*, 85:33–46.
- Rudels, B., Muench, R. D., Gunn, J., Schauer, U., and Friedrich, H. J. (2000). Evolution of the arctic ocean boundary current north of the siberian shelves. *Journal of marine systems*, 25(1):77–99.
- Ruhs, S., Schwarzkopf, F. U., Speich, S., and Biastoch, A. (2019). Cold vs. warm water route-sources for the upper limb of the atlantic meridional overturning circulation revisited in a high-resolution ocean model. *Ocean Science*, 15(3):489–489.
- Saberi, A., Haine, T. W., Gelderloos, R., de Jong, M. F., Furey, H., and Bower, A. (2020). Lagrangian perspective on the origins of denmark strait overflow. *Journal of Physical Oceanography*.
- Sarafanov, A. (2009). On the effect of the north atlantic oscillation on temperature and salinity of the subpolar north atlantic intermediate and deep waters. *ICES Journal of Marine Science*, 66(7):1448–1454.
- Sarafanov, A., Sokov, A., Demidov, A., and Falina, A. (2007). Warming and salinification of intermediate and deep waters in the irvinger sea and iceland basin in 1997–2006. *Geophysical Research Letters*, 34(23).
- Sarnthein, M., Statterger, K., Dreger, D., Erlenkeuser, H., Grootes, P., Haupt, B. J., Jung, S., Kiefer, T., Kuhnt, W., Pflaumann, U., et al. (2001). Fundamental modes and abrupt changes in north atlantic circulation and climate over the last 60 ky - concepts, reconstruction and numerical modeling. In *The Northern North Atlantic*, pages 365–410. Springer.
- Schulze, L. M. and Pickart, R. S. (2012). Seasonal variation of upwelling in the alaskan beaufort sea: Impact of sea ice cover. *Journal of Geophysical Research: Oceans*, 117(C6).
- Schwierz, C., Köllner-Heck, P., Mutter, E. Z., Bresch, D. N., Vidale, P.-L., Wild, M., and Schär, C. (2010). Modelling european winter wind storm losses in current and future climate. *Climatic change*, 101(3-4):485–514.

- Semper, S., Våge, K., Pickart, R. S., Valdimarsson, H., Torres, D. J., and Jónsson, S. (2019). The emergence of the north icelandic jet and its evolution from northeast iceland to denmark strait. *Journal of Physical Oceanography*, 49(10):2499–2521.
- Send, U., Lankhorst, M., and Kanzow, T. (2011). Observation of decadal change in the atlantic meridional overturning circulation using 10 years of continuous transport data. *Geophysical Research Letters*, 38(24).
- Serreze, M. C., Carse, F., Barry, R. G., and Rogers, J. C. (1997). Icelandic low cyclone activity: Climatological features, linkages with the nao, and relationships with recent changes in the northern hemisphere circulation. *Journal of Climate*, 10(3):453–464.
- Smeed, D., Josey, S., Beaulieu, C., Johns, W. E., Moat, B., Frajka-Williams, E., Rayner, D., Meinen, C., Baringer, M., Bryden, H., et al. (2018). The north atlantic ocean is in a state of reduced overturning. *Geophysical Research Letters*, 45(3):1527–1533.
- Spall, M. A. and Price, J. F. (1998). Mesoscale variability in denmark strait: The pv outflow hypothesis. *Journal of Physical Oceanography*, 28(8):1598–1623.
- Sproson, D. A., Renfrew, I. A., and Heywood, K. J. (2008). Atmospheric conditions associated with oceanic convection in the south-east labrador sea. *Geophysical research letters*, 35(6).
- Stommel, H. (1958). The abyssal circulation. *Deep Sea Research*, 5(1):80–82.
- Stroeve, J. C., Kattsov, V., Barrett, A., Serreze, M., Pavlova, T., Holland, M., and Meier, W. N. (2012). Trends in arctic sea ice extent from cmip5, cmip3 and observations. *Geophysical Research Letters*, 39(16).
- Strong, C. and Rigor, I. G. (2013). Arctic marginal ice zone trending wider in summer and narrower in winter. *Geophysical Research Letters*, 40(18):4864–4868.
- Sutton, R. T. and Hodson, D. L. (2005). Atlantic ocean forcing of north american and european summer climate. *science*, 309(5731):115–118.
- Swift, J. H. and Aagaard, K. (1981). Seasonal transitions and water mass formation in the iceland and greenland seas. *Deep Sea Research Part A. Oceanographic Research Papers*, 28(10):1107–1129.
- Swift, J. H. and Koltermann, K. P. (1988). The origin of norwegian sea deep water. *Journal of Geophysical Research: Oceans*, 93(C4):3563–3569.
- Szuts, Z. B. and Meinen, C. S. (2017). Florida current salinity and salinity transport: Mean and decadal changes. *Geophysical Research Letters*, 44(20):10–495.
- Talley, L. D. (2011). *Descriptive physical oceanography: an introduction*. Academic press.
- Talley, L. D. (2013). Closure of the global overturning circulation through the indian, pacific, and southern oceans: Schematics and transports. *Oceanography*, 26(1):80–97.
- Talley, L. D. and McCartney, M. S. (1982). Distribution and circulation of labrador sea water. *Journal of Physical Oceanography*, 12(11):1189–1205.

- Tanhua, T., Olsson, K. A., and Jeansson, E. (2005). Formation of denmark strait overflow water and its hydro-chemical composition. *Journal of Marine Systems*, 57(3):264–288.
- Tanhua, T., Olsson, K. A., and Jeansson, E. (2008). Tracer evidence of the origin and variability of denmark strait overflow water. In *Arctic–Subarctic Ocean Fluxes*, pages 475–503. Springer.
- Timmermann, A., Gildor, H., Schulz, M., and Tziperman, E. (2003). Coherent resonant millennial-scale climate oscillations triggered by massive meltwater pulses. *Journal of Climate*, 16(15):2569–2585.
- Ting, M., Kushnir, Y., Seager, R., and Li, C. (2011). Robust features of atlantic multi-decadal variability and its climate impacts. *Geophysical Research Letters*, 38(17).
- Trenberth, K. E. and Caron, J. M. (2001). Estimates of meridional atmosphere and ocean heat transports. *Journal of Climate*, 14(16):3433–3443.
- Tulloch, R. and Marshall, J. (2012). Exploring mechanisms of variability and predictability of atlantic meridional overturning circulation in two coupled climate models. *Journal of climate*, 25(12):4067–4080.
- Turrell, W., Henderson, E., Slessor, G., Payne, R., Adams, R., and Aberdeen, A. (1992). Hydrographic observations at the continental shelf edge northwest of scotland. *ICES CM*, 100:19.
- Uchida, H., Kawano, T., and Fukasawa, M. (2008). In situ calibration of moored ctds used for monitoring abyssal water. *Journal of Atmospheric and Oceanic Technology*, 25(9):1695–1702.
- Våge, K., Moore, G. W. K., Jónsson, S., and Valdimarsson, H. (2015). Water mass transformation in the iceland sea. *Deep Sea Research Part I: Oceanographic Research Papers*, 101:98–109.
- Våge, K., Papritz, L., Håvik, L., Spall, M. A., and Moore, G. W. K. (2018). Ocean convection linked to the recent ice edge retreat along east greenland. *Nature communications*, 9(1):1–8.
- Våge, K., Pickart, R. S., Spall, M. A., Moore, G., Valdimarsson, H., Torres, D. J., Erofeeva, S. Y., and Nilsen, J. E. Ø. (2013). Revised circulation scheme north of the denmark strait. *Deep Sea Research Part I: Oceanographic Research Papers*, 79:20–39.
- Våge, K., Pickart, R. S., Spall, M. A., Valdimarsson, H., Jónsson, S., Torres, D. J., Østerhus, S., and Eldevik, T. (2011). Significant role of the north icelandic jet in the formation of denmark strait overflow water. *Nature geoscience*, 4(10):723–727.
- Van Aken, H. M. and De Boer, C. (1995). On the synoptic hydrography of intermediate and deep water masses in the iceland basin. *Deep Sea Research Part I: Oceanographic Research Papers*, 42(2):165–189.
- Vellinga, M. and Wood, R. A. (2002). Global climatic impacts of a collapse of the atlantic thermohaline circulation. *Climatic change*, 54(3):251–267.

- Vernet, M., Geibert, W., Hoppema, M., Brown, P. J., Haas, C., Hellmer, H., Jokat, W., Jullion, L., Mazloff, M., Bakker, D., et al. (2019). The weddell gyre, southern ocean: present knowledge and future challenges. *Reviews of Geophysics*, 57(3):623–708.
- Voet, G. and Quadfasel, D. (2010). Entrainment in the denmark strait overflow plume by meso-scale eddies. *Ocean Science*, 6(1):301–310.
- von Appen, W.-J. (2013). *Moored observations of shelfbreak processes at the inflow to and outflow from the Arctic Ocean*. PhD thesis, Massachusetts Institute of Technology and Woods Hole Oceanographic Institution.
- von Appen, W.-J., Koszalka, I. M., Pickart, R. S., Haine, T. W., Mastropole, D., Magaldi, M. G., Valdimarsson, H., Girton, J., Jochumsen, K., and Krahnemann, G. (2014). The east greenland spill jet as an important component of the atlantic meridional overturning circulation. *Deep Sea Research Part I: Oceanographic Research Papers*, 92:75–84.
- von Appen, W.-J., Mastropole, D., Pickart, R. S., Valdimarsson, H., Jónsson, S., and Girton, J. B. (2017). On the nature of the mesoscale variability in denmark strait. *Journal of Physical Oceanography*, 47(3):567–582.
- Wadhams, P. (1999). The odden ice tongue and greenland sea convection. *Weather*, 54(3):91–98.
- Wadhams, P., Holfort, J., Hansen, E., and Wilkinson, J. (2002). A deep convective chimney in the winter greenland sea. *Geophysical research letters*, 29(10):76–1.
- Weaver, A. J., Eby, M., Kienast, M., and Saenko, O. A. (2007). Response of the atlantic meridional overturning circulation to increasing atmospheric co<sub>2</sub>: Sensitivity to mean climate state. *Geophysical Research Letters*, 34(5).
- Whitehead, J. (1998). Topographic control of oceanic flows in deep passages and straits. *Reviews of Geophysics*, 36(3):423–440.
- Woollings, T., Franzke, C., Hodson, D., Dong, B., Barnes, E. A., Raible, C., and Pinto, J. (2015). Contrasting interannual and multidecadal nao variability. *Climate dynamics*, 45(1-2):539–556.
- Yashayaev, I. and Dickson, B. (2008). Transformation and fate of overflows in the northern north atlantic. In *Arctic–Subarctic Ocean Fluxes*, pages 505–526. Springer.
- Zhang, R. and Delworth, T. L. (2006). Impact of atlantic multidecadal oscillations on india/sahel rainfall and atlantic hurricanes. *Geophysical Research Letters*, 33(17).
- Zhao, J. and Johns, W. (2014). Wind-driven seasonal cycle of the atlantic meridional overturning circulation. *Journal of physical oceanography*, 44(6):1541–1562.